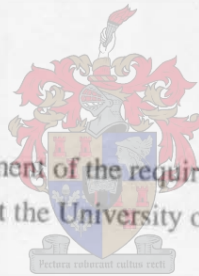


A PREDICTION METHOD FOR FLOW IN AXIAL COMPRESSORS

T. H. Roos

Thesis presented in partial fulfilment of the requirements for the degree of Master of Engineering at the University of Stellenbosch.

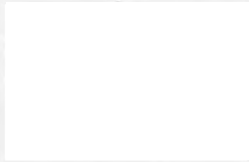


Supervisor: Professor T. W. von Backström

March 1995

DECLARATION

I the undersigned hereby declare that the work contained in this thesis is my own original work and has not previously in its entirety or in part been submitted at any university for a degree.



21/2/95.....
Date:

ABSTRACT

A procedure is presented for predicting the flow through axial compressors. The matrix throughflow equation is transformed to yield an expression of radius dependent on stream function and axial position. The solution of the resultant equation combines the advantages of following streamlines through the calculation domain (as in the streamline curvature method, SCM) with the stability of the matrix throughflow method (MTFM), and is correspondingly called the streamline throughflow method (STFM). The predictions of the method were compared to analytical results for a number of inviscid test cases and gave good results.

As with the SCM and MTFM, using STFM to predict turbomachinery flows requires empirical models for cascade loss and deflection as well as endwall loss. The off-design loss and deflection model of Howell was used as the basis for a new off-design correlation, H2, valid for axial velocity density ratios (AVDR) of unity. The H2 correlation was developed from the NACA 65-Series database as carpet-plotted by Felix.

A simple subcritical Reynolds number correlation for loss and deflection was adapted from a method of Roberts, using inlet blade chord Reynolds number, camber angle, pitch-chord ratio, maximum blade thickness-chord ratio and turbulence factor as parameters. The H2 correlation together with the adapted Roberts correlation gave good predictions of loss and deflection for low-Reynolds number cascade flows at AVDR values of unity.

Measurements were taken at the compressor inlet and behind each blade row of a low speed, three stage axial flow compressor at three flowrates: near-design, near-surge and near-choke. The predictions of STFM using Howell's endwall loss models, the modified low Reynolds number correlation and respectively Howell's original off-design method and H2 were compared with the experimental results. Howell's method predicted pressure rise to within 3% at design and 10% at off-design, compared to 4% at design and 9% at off-design for the H2 method. The prediction of flow angles for H2 were considerably worse than that of Howell. This was deemed to be caused by AVDR effects.

An interim AVDR correlation, dependent on stagger angle, was used together with H2. Choosing values of AVDR for the interim correlation which together with H2 would predict flow angles to match the experimental values, predictions of total pressure rise within 3% at design and 8% at off-design were achieved. As a measure of confidence can be placed in H2 and the modified low Reynolds number correlation, the endwall loss correlation of Howell was determined to be the cause of lack of further gains in accuracy.

Keywords:

axial velocity density ratio, AVDR, cascade, critical Reynolds number, compressor, H2, low Reynolds number, matrix throughflow method, MTFM, NACA-65, SCM, STFM, stream line curvature, streamline throughflow method, throughflow, off-design loss, off-design deflection, subcritical Reynolds number

OPSOMMING

'n Prosedure vir die voorspel van vloeï deur aksiaalkompressors word daargestel. Die matriksdeurvloeivergelyking word getransformeer om 'n uitdrukking van radius, wat afhanklik is van stroomfunksie en aksiale posisie, te gee. Die oplossing van die gevolglike vergelyking span die voordele verbode aan die volg van stroomlyne deur die berekeningsgebied (soos in the stroomlynkrommingsmetode, SKM) met die stabiliteit van die matriksdeurvloeimetode (MDVM), saam. Dienoorkomstig word die prosedure die stroomlyndeurvloeimetode (SDVM) genoem. Die voorspellings van die metode is met analitiese resultate van 'n aantal nie-viskeuse proefgevalle vergelyk en goeie resultate is behaal.

Soos met die SKM en MDVM, genoodsaak die gebruik van SDVM om vloeï deur turbomasjiene te voorspel empiriese kaskade verlies- en defleksiemodelle, asook wandverliesmodelle. Die af-ontwerp verlies- en defleksiemodel van Howell is as 'n basis gebruik vir 'n nuwe af-ontwerp korrelasie, H_2 , wat geldig is vir aksiaalsnelheid-digtheidsverhoudings (ASDV) van een. Die H_2 korrelasie is vanuit die NACA 65-Reeks databasis soos deur Felix geplot, ontwikkel.

'n Subkritiese Reynoldsgetal korrelasie vir verlies en defleksie is vanuit 'n metode van Roberts aangepas. Hierdie metode maak gebruik van inlaat lemkoord Reynoldsgetal, krommingshoek, lempasie-koordverhouding, maksimum lemdikte-koordverhouding en turbulensiefaktor as parameters. Die H_2 korrelasie, saam met die aangepaste Roberts korrelasie, het goeie voorspellings van verlies en defleksie vir lae Reynoldsgetal kaskadevloei met ASDV waardes van een gegee.

Metings is geneem by die kompressorinlaat en agter elke lemry van 'n lae-spoed, driestadium aksiaalvloeïkompressor teen drie massavloei: naby die ontwerp punt, naby die stollyn en naby die wurglyn. Die voorspellings van SDVM met gebruik van Howell se wandverliesmodelle, die gemodifiseerde lae Reynoldsgetal korrelasie en onderskeidelik Howell se oorspronklike af-ontwerp metode en H_2 , is met die eksperimentele resultate vergelyk. Howell se metode het drukstyging tot binne 3% by ontwerp en 10% by af-ontwerp voorspel, in vergeleke met 4% by ontwerp en 9% by af-ontwerp vir die H_2 metode. The voorspelling van vloeïhoeke deur H_2 is heelwat swakker as die van Howell. Dit is as gevolg van ASDV-effekte geag.

'n Interim ASDV korrelasie, afhanklik van lemstelhoek, is saam met H2 gebruik. Deur van ASDV-waardes vir die interim korrelasie te kies wat saam met H2 die eksperimentele vloeihoeke sal voorspel, is totale druk voorspellings binne 3% by ontwerp en 8% by af-ontwerp behaal. Aangesien 'n mate van vertroue in H2 en die aangepasde lae Reynoldsgetal korrelasie geplaas kan word, is die wandverlies korrelasie van Howell uitgesonder as die oorsaak van die gebrek aan verdere verbeterings in akkuraatheid.

Trefwoorde:

aksiaalsnelheid-digtheidsverhouding, ASDV, af-ontwerp defleksie, af-ontwerp verlies, deurvloei, H2, kaskade, kompressor, kritiese Reynoldsgetal, lae Reynoldsgetal, matriksdeurvloeimetode, MDFM, NACA-65, SDVM, SKM, stroomlynkromming, stroomlynkrommingsmetode, subkritiese Reynoldsgetal

DEDICATION

To my late father,

Brigadier Helm Roos

ACKNOWLEDGEMENTS

I would like to thank my supervisor, Professor T. W. von Backström, for his support, guidance and patience during the four years of this thesis.

I am also very grateful to Mrs. Louise Kritzinger for help with the word processing package, to Mr. Donald McLoughlin for illustrative CAD drawings of cascade flows, and to Mr. Trevor Kirsten for insights into fluid flows and time to complete this thesis.

Finally, I would like to thank Stellenbosch 2000, Mr. Harold Crossley and the Department of Mechanical Engineering at the University of Stellenbosch for financial support.

CONTENTS

Chapter	Page
DECLARATION	ii
ABSTRACT	iii
Keywords	iv
OPSOMMING	v
Trefwoorde	vi
DEDICATION	vii
ACKNOWLEDGEMENTS	viii
CONTENTS	ix
LIST OF TABLES	xii
LIST OF FIGURES	xiii
NOMENCLATURE	xxii
ABBREVIATIONS	xxv
1 INTRODUCTION	1
1.1 Background	1
1.2 Scope and Objectives	4
2 EXPERIMENTAL PROCEDURE AND RESULTS	5
2.1 Introduction	5
2.2 Description of Test Bench	5
2.3 Description of Instrumentation	6
2.3.1 Pressure measurement	6
2.3.2 Flow Measurement	7
2.3.3 Rotor Speed Measurement	8
2.4 Calibration	9
2.4.1 Pressure Transducer	9
2.4.2 Angular Potentiometer	10
2.4.3 Cobra Probe	10
2.5 Experimental procedure	11
2.6 Results	12
2.6.1 Mass Balances	13
2.6.2 Flow Angle and Tangential Velocity Profiles	13

	2.6.3	Axial Velocity Profiles	15
	2.6.4	Total Pressure Profiles	15
	2.7	Conclusions	16
3		THE DEVELOPMENT AND TESTING OF THE STREAMLINE THROUGHFLOW METHOD	17
	3.1	Previous work	17
	3.2	Application of Boadway's Transformation to the Matrix Throughflow Equation	18
	3.3	Discretisation and Solution	20
	3.4	Test Case Classification	20
	3.5	Source terms equal to zero	21
	3.5.1	Parallel-walled annulus	21
	3.5.2	Flow over a sphere	23
	3.6	Non-zero Tangential Momentum Gradients across Streamlines, other Terms equal to Zero	24
	3.6.1	Parallel-walled annulus with single actuator disc	25
	3.6.2	Parallel-walled annulus with two actuator discs (blade row interaction)	25
	3.7	Non-zero Total Enthalpy, Tangential Momentum and Entropy Gradients across Streamlines, Incompressible Flow	26
	3.8	Conclusion	29
4		COMPRESSOR CASCADE NOMENCLATURE AND DEFINITIONS	30
	4.1	Introduction	30
	4.2	Cascade Nomenclature	30
	4.3	Cascade Forces	32
	4.4	Cascade Losses	33
	4.5	Lift and Drag	34
5		COMPRESSOR CASCADE CORRELATIONS	37
	5.1	Introduction	37
	5.2	Howell's Correlations	40
	5.2.1	Howell's Nominal Condition	40
	5.2.2	Howell's Off-design Correlation	42
	5.2.3	Howell's Endwall Loss Correlations	42
	5.3	Carter's Deviation Rule	43
	5.4	Lieblein's Loss Correlation	44
	5.5	Jansen and Moffat Loss Correlation	46
	5.5.1	Inlet angles for design, choke and surge	46

5.5.2	Supercritical Mach Number	47
5.5.3	Off-design Loss	47
5.6	NACA Cascade Data	47
5.7	The Correlation of Roberts for Reynolds Number and Turbulence Effects	48
5.8	Comparison and Discussion	50
6	CASCADE CORRELATION DEVELOPMENT	54
6.1	Howell's correlations: curve fits	54
6.2	NACA 65 Data Comparison	55
6.3	Correction Factor Correlation	56
6.4	Modification to the Correlation of Roberts for Reynolds Number and Turbulence Effects	62
6.5	An Interim AVDR Correction	64
6.6	Testing of the Howell Correction Factors and Modified Method of Roberts	65
7	RESULTS	67
7.1	General	67
7.2	Near-design flowrate: 2.54kg/s	69
7.3	Near-choke flowrate: 2.80kg/s	70
7.4	Near-surge flowrate: 1.99kg/s	71
8	CONCLUSIONS	73
9	RECOMMENDATIONS	75
9.1	Numerical Recommendations	75
9.2	Experimental Recommendations	76
	APPENDIX A: BOADWAY'S TRANSFORMATION APPLIED TO CYLINDRICAL CO-ORDINATES	77
	APPENDIX B: DISCRETISATION OF MATRIX THROUGHFLOW EQUATION USING GREYVENSTEIN'S NON-UNIFORM GRID METHOD	81
	REFERENCES	85
	TABLES	90
	FIGURES	95

LIST OF TABLES

Table	Title	Page
2.1:	Details of blade geometry	91
2.2:	Mass balances	92
6.1:	Prediction quality of H2 correlation without gradient correction	93
6.2:	Regions of applicability of gradient correction M	94

LIST OF FIGURES

Figure	Title	Page
2.1:	Schematic diagram of Rofanco low speed compressor testbench (adapted from Lewis)	96
2.2:	Cobra three-hole probe	97
2.3:	HBM pressure transducer calibration	98
2.4:	Angular potentiometer calibration	98
2.5:	Aerodynamic probe calibration facility	99
2.6:	Cobra probe calibration	100
2.7:	Flow angle profiles at near-design flowrate: 2.54 kg/s.	101
2.8:	Tangential velocity profiles at near-design flowrate: 2.54 kg/s.	102
2.9:	Axial velocity profiles at near-design flowrate: 2.54 kg/s. (Zeroes of inlet and rotor rows have been staggered by 40 and 20 m/s respectively).	103
2.10:	Total pressure profiles (relative to inlet mass average) at near-design flowrate: 2.54 kg/s.	104
2.11:	Flow angle profiles at near-choke flowrate: 2.80 kg/s.	105
2.12:	Tangential velocity profiles at near-choke flowrate: 2.80 kg/s.	106
2.13:	Axial velocity profiles at near-choke flowrate: 2.80 kg/s. (Zeroes of inlet and rotor rows have been staggered by 40 and 20 m/s respectively).	107
2.14:	Total pressure profiles (relative to inlet mass average) at near-choke flowrate: 2.80 kg/s.	108
2.15:	Flow angle profiles at near-surge flowrate: 1.99 kg/s.	109
2.16:	Tangential velocity profiles at near-surge flowrate: 1.99 kg/s.	110
2.17:	Axial velocity profiles at near-surge flowrate: 1.99 kg/s. (Zeroes of inlet and rotor rows have been staggered by 40 and 20 m/s respectively).	111
2.18:	Total pressure profiles (relative to inlet mass average) at near-surge flowrate: 1.99 kg/s.	112
3.1:	Effect of $\frac{r_s}{r_N}$ on discretisation error	113
3.2:	Effect of number of internal streamlines (NIS) on error ($r_i = 0$)	113
3.3:	Effect of number of internal streamlines (NIS) on error ($r_i = 0.1 r_o$)	114
3.4:	Effect of number of internal streamlines (NIS) on error ($r_i = 0.2 r_o$)	114
3.5:	Effect of number of internal streamlines (NIS) on error ($r_i = 0.3 r_o$)	115

3.6:	Effect of number of internal streamlines (NIS) on error ($r_i = 0.4 r_o$)	115
3.7:	Flow over a sphere: STFM and potential flow solutions for varying stream function fractions (SFF)	116
3.8:	Error for flow over a sphere at different stream function fractions (SFF)	116
3.9:	Median internal streamline position for actuator disc flow with different numbers of internal streamlines (NIS)	117
3.10:	Error in median internal streamline position for actuator disc flow with different numbers of internal streamlines (NIS)	117
3.11:	Comparison of axial (SRE and STFM) and tangential velocity profiles for actuator disc flow with 7 internal streamlines	118
3.12:	Median internal streamline position for twin actuator disc flow with different numbers of internal streamlines (NIS) (25 equispaced nodes)	119
3.13:	Error in median internal streamline position for twin actuator disc flow with different numbers of internal streamlines (NIS) (25 equispaced nodes)	119
3.14:	Median internal streamline position for twin actuator disc flow with different numbers of internal streamlines (NIS) using sparse non-uniform axial spacing with three nodes between the discs	120
3.15:	Error in median internal streamline position for twin actuator disc flow with different numbers of internal streamlines (NIS) using sparse non-uniform axial spacing with three nodes between the discs	120
3.16:	Median internal streamline position for twin actuator disc flow with different numbers of internal streamlines (NIS) using sparse non-uniform axial spacing with two nodes between the discs	121
3.17:	Error in median internal streamline position for twin actuator disc flow with different numbers of internal streamlines (NIS) using sparse non-uniform axial spacing with two nodes between the discs	121
3.18:	Median internal streamline position for twin actuator disc flow with different numbers of internal streamlines (NIS) using sparse non-uniform axial spacing with a single node between the discs	122
3.19:	Error in median internal streamline position for twin actuator disc flow with different numbers of internal streamlines (NIS) using sparse non-uniform axial spacing with a single node between the discs	122
4.1:	Compressor cascade and blade notation	123
4.2:	Four compressor blade profiles for nominally identical turning, $\alpha_1 = 43.6^\circ$, $\alpha_2 = 23.5^\circ$	124
4.3:	Relationship between isolated aerofoil lift coefficient and equivalent camber for NACA 65-Series profiles	125
4.4:	Forces and velocities in a cascade	126
4.5:	Lift and drag forces exerted by unit span of a cascade blade upon the fluid	127

4.6:	Axial and tangential forces exerted by unit span of a blade upon the fluid	127
5.1:	Total pressure loss coefficient as a function of Reynolds number in region of minimum loss at low speed for various cascade profiles	128
5.2:	Variation of total pressure loss coefficient with incidence angle and Reynolds number for parabolic arc blade 10C4/40P40, α_1 varying from 28° to 40°	129
5.3:	Variation of deviation angle with incidence angle and Reynolds number for parabolic arc blade 10C4/40P40, α_1 varying from 28° to 40°	130
5.4:	Characteristics of an 11C1/45/C50 cascade, showing Howell's nominal condition	131
5.5:	Cascade nominal deflection correlation of Howell	131
5.6:	Nominal deflection as function of nominal outlet angle	132
5.7:	Reynolds number correction for nominal deflection	132
5.8:	Space-chord ratio correction for nominal deflection	132
5.9:	Howell's off-design cascade correlation	133
5.10:	Losses in a compressor stage according to Howell	134
5.11:	Lift-drag ratios for $s/l = 1$	135
5.12:	Carter's deviation rule	136
5.13:	Compressor cascade blade surface velocity distribution	136
5.14:	Compressor cascade blade wake: variation in velocity in a plane normal to axial direction	137
5.15:	Design angles of attack for NACA 65-Series	137
5.16:	Effect of AVDR on deviation angle, loss coefficient and discharge pressure coefficient as a function of incidence	138
6.1:	Howell's nominal deflection correlation data with three curve fit approximations	139
6.2:	Howell's off-design cascade deflection correlation with two curve fit approximations	139
6.3:	Howell's off-design cascade profile drag correlation with polynomial curve fit	140
6.4:	Carter's deviation rule for circular arc with polynomial curve fit	140
6.5:	Comparison of values of m from Carter's deviation rule and Howell's correlation for the NACA test data	141
6.6:	NACA cascade test data non-dimensionalised to Howell's off-design correlation using Howell's deviation rule for ϵ^*	142
6.7:	NACA cascade test data non-dimensionalised to Howell's off-design correlation using Carter's deviation rule for ϵ^*	142
6.8:	NACA cascade test data non-dimensionalised to Howell's off-design correlation and adjusted by the C_1 and C_2 factor correlations	143

6.9:	NACA cascade test data non-dimensionalised to Howell's off-design correlation and adjusted by the C_1 and C_2 factor and M gradient correlations	143
6.10:	Initial correlation applied to the low Reynolds number ε data of Roberts	144
6.11:	Initial correlation applied to the low Reynolds number $\bar{\omega}$ data of Roberts	144
6.12:	Definition of "artificial" bursting Reynolds number	145
6.13:	Final correlation applied to the low Reynolds number ε data of Roberts	146
6.14:	Final correlation applied to the low Reynolds number $\bar{\omega}$ data of Roberts	146
6.15:	Comparison of ε as function of non-dimensionalised incidence and Reynolds number, Re_c , between the data of Roberts and prediction of H2 correlation combined with modified correlation of Roberts, for NACA 65-4(A10)10 profiles in cascade: $s/l = 1.2$, $\beta_1 = 60^\circ$, $TF \sim 0.006$	147
6.16:	Comparison of $\bar{\omega}$ as function of non-dimensionalised incidence and Reynolds number, Re_c , between the data of Roberts and prediction of H2 correlation combined with modified correlation of Roberts, for NACA 65-4(A10)10 profiles in cascade: $s/l = 1.2$, $\beta_1 = 60^\circ$, $TF \sim 0.006$	147
6.17:	Comparison of ε as function of non-dimensionalised incidence and Reynolds number, Re_c , between the data of Roberts and prediction of H2 correlation combined with modified correlation of Roberts, for NACA 65-12(A10)10 profiles in cascade: $s/l = 1.2$, $\beta_1 = 60^\circ$, $TF \sim 0.006$	148
6.18:	Comparison of $\bar{\omega}$ as function of non-dimensionalised incidence and Reynolds number, Re_c , between the data of Roberts and prediction of H2 correlation combined with modified correlation of Roberts, for NACA 65-12(A10)10 profiles in cascade: $s/l = 1.2$, $\beta_1 = 60^\circ$, $TF \sim 0.006$	148
6.19:	Comparison of ε and $\bar{\omega}$ as a function of Reynolds number, Re_c , between the data of Roberts and prediction of H2 correlation combined with modified correlation of Roberts, for NACA 65-12(A2T8b)10 profiles in cascade: $s/l = 1.0$, $\beta_1 = 60^\circ$, $\gamma = 50.4^\circ$, $TF \sim 0.006$	149
6.20:	Comparison of ε and $\bar{\omega}$ as a function of Reynolds number, Re_c , between the data of Roberts and prediction of H2 correlation combined with modified correlation of Roberts, for NACA 65-18(A10)10 profiles in cascade: $s/l = 1.2$, $\beta_1 = 60^\circ$, $\gamma = 45^\circ$, $TF \sim 0.006$	149
6.21:	Comparison of ε and $\bar{\omega}$ as a function of Reynolds number, Re_c , between the data of Roberts and prediction of H2 correlation combined with modified correlation of Roberts, for NACA 65-6(A10)10 profiles in cascade: $s/l = 1.2$, $\beta_1 = 50^\circ$, $\gamma = 40^\circ$, $Tu < 0.01$, TF assumed ~ 0.006	150

6.22:	Comparison of ϵ and $\bar{\omega}$ as a function of Reynolds number, Re_c , between the data of Roberts and prediction of H2 correlation combined with modified correlation of Roberts, for NACA 65-18(A10)10 profiles in cascade: $s/l = 0.55$, $\beta_1 = 60^\circ$, $\gamma = 37.5^\circ$, $TF = -0.006$	150
7.1:	Variation in turbulence level with flowrate for a single stage compressor	151
7.2:	Flow angle profiles at near-design flowrate: 2.54 kg/s. Comparison between experimental data and STFM predictions using Howell's method with and without correction of Roberts	152
7.3:	Flow angle profiles at near-design flowrate: 2.54 kg/s. Comparison between experimental data and STFM predictions using H2 and H2 with correction of Roberts (with and without AVDR correction)	153
7.4:	Tangential velocity profiles at near-design flowrate: 2.54 kg/s. Comparison between experimental data and STFM predictions using Howell's method with and without correction of Roberts	154
7.5:	Tangential velocity profiles at near-design flowrate: 2.54 kg/s. Comparison between experimental data and STFM predictions using H2 and H2 with correction of Roberts (with and without AVDR correction)	156
7.6:	Axial velocity profiles at near-design flowrate: 2.54 kg/s. (Zeroes of inlet and rotor rows have been staggered by 40 and 20 m/s respectively). Comparison between experimental data and STFM predictions using Howell's method	156
7.7:	Axial velocity profiles at near-design flowrate: 2.54 kg/s. (Zeroes of rotor rows have been staggered by 20 m/s). Comparison between experimental data and STFM predictions using Howell's method with and without correction of Roberts	157
7.8:	Axial velocity profiles at near-design flowrate: 2.54 kg/s. (Zeroes of rotor rows have been staggered by 20 m/s). Comparison between experimental data and STFM predictions using H2 and H2 with correction of Roberts (with and without AVDR correction)	158
7.9:	Total pressure profiles (relative to inlet mass average) at near-design flowrate: 2.54 kg/s. Comparison between experimental data and STFM predictions using Howell's methods, using Howell's and Lieblein's profile loss models	159
7.10:	Total pressure profiles (relative to inlet mass average) at near-design flowrate: 2.54 kg/s. Comparison between experimental data and STFM predictions using Howell's method with and without correction of Roberts	160
7.11:	Total pressure profiles (relative to inlet mass average) at near-design flowrate: 2.54 kg/s. Comparison between experimental data and STFM predictions using H2 with and without correction of Roberts	161

7.12:	Total pressure profiles (relative to inlet mass average) at near-design flowrate: 2.54 kg/s. Comparison between experimental data and STFM predictions using H2 with correction of Roberts and <i>AVDR</i> correction for two values	162
7.13:	Flow angle profiles at near-choke flowrate: 2.80 kg/s. Comparison between experimental data and STFM predictions using Howell's method with and without correction of Roberts	163
7.14:	Flow angle profiles at near-choke flowrate: 2.80 kg/s. Comparison between experimental data and STFM predictions using correction of Roberts with Howell's method and H2 (with and without <i>AVDR</i> correction)	164
7.15:	Tangential velocity profiles at near-choke flowrate: 2.80 kg/s. Comparison between experimental data and STFM predictions using Howell's method with and without correction of Roberts	165
7.16:	Tangential velocity profiles at near-choke flowrate: 2.80 kg/s. Comparison between experimental data and STFM predictions using correction of Roberts with Howell's method and H2 (with and without <i>AVDR</i> correction)	166
7.17:	Axial velocity profiles at near-choke flowrate: 2.80 kg/s. (Zeroes of inlet and rotor rows have been staggered by 40 and 20 m/s respectively). Comparison between experimental data and STFM predictions using Howell's method with and without correction of Roberts	167
7.18:	Axial velocity profiles at near-choke flowrate: 2.80 kg/s. (Zeroes of rotor rows have been staggered by 20 m/s). Comparison between experimental data and STFM predictions using correction of Roberts with Howell's method and H2 (with and without <i>AVDR</i> correction)	168
7.19:	Total pressure profiles (relative to inlet mass average) at near-choke flowrate: 2.80 kg/s. Comparison between experimental data and STFM predictions using Howell's method with and without correction of Roberts	169
7.20:	Total pressure profiles (relative to inlet mass average) at near-choke flowrate: 2.80 kg/s. Comparison between experimental data and STFM predictions using correction of Roberts with Howell's method and H2 (with and without <i>AVDR</i> correction)	170
7.21:	Flow angle profiles at near-surge flowrate: 1.99 kg/s. Comparison between experimental data and STFM predictions, with \hat{i}_{adj} limited to 0.6, using Howell's method and H2	171
7.22:	Flow angle profiles at near-surge flowrate: 1.99 kg/s. Comparison between experimental data and STFM predictions, with \hat{i}_{adj} limited to 0.6, using Howell's method without and then with the correction of Roberts at two levels of Tu	172

- 7.23: Flow angle profiles at near-surge flowrate: 1.99 kg/s. Comparison between experimental data and STFM predictions, with \hat{i}_{adj} limited to 0.6, using H2 without and then with the correction of Roberts at two levels of Tu 173
- 7.24: Tangential velocity profiles at near-surge flowrate: 1.99 kg/s. Comparison between experimental data and STFM predictions, with \hat{i}_{adj} limited to 0.6, using Howell's method and H2 174
- 7.25: Tangential velocity profiles at near-surge flowrate: 1.99 kg/s. Comparison between experimental data and STFM predictions, with \hat{i}_{adj} limited to 0.6, using Howell's method without and then with the correction of Roberts at two levels of Tu 175
- 7.26: Tangential velocity profiles at near-surge flowrate: 1.99 kg/s. Comparison between experimental data and STFM predictions, with \hat{i}_{adj} limited to 0.6, using H2 without and then with the correction of Roberts at two levels of Tu 176
- 7.27: Axial velocity profiles at near-surge flowrate: 1.99 kg/s. (Zeroes of inlet and rotor rows have been staggered by 40 and 20 m/s respectively). Comparison between experimental data and STFM predictions, with \hat{i}_{adj} limited to 0.6, using Howell's method and H2 177
- 7.28: Axial velocity profiles at near-surge flowrate: 1.99 kg/s. (Zeroes of rotor rows have been staggered by 20 m/s). Comparison between experimental data and STFM predictions, with \hat{i}_{adj} limited to 0.6, using Howell's method without and then with the correction of Roberts at two levels of Tu 178
- 7.29: Axial velocity profiles at near-surge flowrate: 1.99 kg/s. (Zeroes of rotor rows have been staggered by 20 m/s). Comparison between experimental data and STFM predictions, with \hat{i}_{adj} limited to 0.6, using H2 without and then with the correction of Roberts at two levels of Tu 179
- 7.30: Total pressure profiles (relative to inlet mass average) at near-surge flowrate: 1.99 kg/s. Comparison between experimental data and STFM predictions, with \hat{i}_{adj} limited to 0.6, using Howell's method and H2 180
- 7.31: Total pressure profiles (relative to inlet mass average) at near-surge flowrate: 1.99 kg/s. Comparison between experimental data and STFM predictions, with \hat{i}_{adj} limited to 0.6, using Howell's method without and then with the correction of Roberts at two levels of Tu 181
- 7.32: Total pressure profiles (relative to inlet mass average) at near-surge flowrate: 1.99 kg/s. Comparison between experimental data and STFM predictions, with \hat{i}_{adj} limited to 0.6, using H2 without and then with the correction of Roberts at two levels of Tu 182

- 7.33: Flow angle profiles at near-surge flowrate: 1.99 kg/s. Comparison between experimental data and STFM predictions, with \hat{i}_{adj} limited to 0.4, using Howell's method and H2 183
- 7.34: Flow angle profiles at near-surge flowrate: 1.99 kg/s. Comparison between experimental data and STFM predictions, with \hat{i}_{adj} limited to 0.4, using Howell's method without and then with the correction of Roberts at two levels of Tu 184
- 7.35: Flow angle profiles at near-surge flowrate: 1.99 kg/s. Comparison between experimental data and STFM predictions, with \hat{i}_{adj} limited to 0.4, using H2 without and then with the correction of Roberts at two levels of Tu 185
- 7.36: Tangential velocity profiles at near-surge flowrate: 1.99 kg/s. Comparison between experimental data and STFM predictions, with \hat{i}_{adj} limited to 0.4, using Howell's method and H2 186
- 7.37: Tangential velocity profiles at near-surge flowrate: 1.99 kg/s. Comparison between experimental data and STFM predictions, with \hat{i}_{adj} limited to 0.4, using Howell's method without and then with the correction of Roberts at two levels of Tu 187
- 7.38: Tangential velocity profiles at near-surge flowrate: 1.99 kg/s. Comparison between experimental data and STFM predictions, with \hat{i}_{adj} limited to 0.4, using H2 without and then with the correction of Roberts at two levels of Tu 188
- 7.39: Axial velocity profiles at near-surge flowrate: 1.99 kg/s. (Zeroes of inlet and rotor rows have been staggered by 40 and 20 m/s respectively). Comparison between experimental data and STFM predictions, with \hat{i}_{adj} limited to 0.4, using Howell's method and H2 189
- 7.40: Axial velocity profiles at near-surge flowrate: 1.99 kg/s. (Zeroes of rotor rows have been staggered by 20 m/s). Comparison between experimental data and STFM predictions, with \hat{i}_{adj} limited to 0.4, using Howell's method without and then with the correction of Roberts at two levels of Tu 190
- 7.41: Axial velocity profiles at near-surge flowrate: 1.99 kg/s. (Zeroes of rotor rows have been staggered by 20 m/s). Comparison between experimental data and STFM predictions, with \hat{i}_{adj} limited to 0.4, using H2 without and then with the correction of Roberts at two levels of Tu 191
- 7.42: Total pressure profiles (relative to inlet mass average) at near-surge flowrate: 1.99 kg/s. Comparison between experimental data and STFM predictions, with \hat{i}_{adj} limited to 0.4, using Howell's method and H2 192

7.43:	Total pressure profiles (relative to inlet mass average) at near-surge flowrate: 1.99 kg/s. Comparison between experimental data and STFM predictions, with \hat{i}_{adj} limited to 0.4, using Howell's method without and then with the correction of Roberts at two levels of Tu	193
7.44:	Total pressure profiles (relative to inlet mass average) at near-surge flowrate: 1.99 kg/s. Comparison between experimental data and STFM predictions, with \hat{i}_{adj} limited to 0.4, using H2 without and then with the correction of Roberts at two levels of Tu	194
7.45:	Flow angle profiles at near-surge flowrate: 1.99 kg/s. Comparison between experimental data and STFM predictions, with \hat{i}_{adj} limited to 0.4, using H2 with AVDR correction, without and then with the correction of Roberts at two levels of Tu	195
7.46:	Tangential velocity profiles at near-surge flowrate: 1.99 kg/s. Comparison between experimental data and STFM predictions, with \hat{i}_{adj} limited to 0.4, using H2 with AVDR correction, without and then with the correction of Roberts at two levels of Tu	196
7.47:	Axial velocity profiles at near-surge flowrate: 1.99 kg/s. (Zeroes of rotor rows have been staggered by 20 m/s). Comparison between experimental data and STFM predictions, with \hat{i}_{adj} limited to 0.4, using H2 with AVDR correction, without and then with the correction of Roberts at two levels of Tu	197
7.48:	Total pressure profiles (relative to inlet mass average) at near-surge flowrate: 1.99 kg/s. Comparison between experimental data and STFM predictions, with \hat{i}_{adj} limited to 0.4, using H2 with AVDR correction, without and then with the correction of Roberts at two levels of Tu	198
B.1:	Nomenclature and discretisation grid of Greyvenstein	199

NOMENCLATURE

a	distance along blade chord line to point of maximum camber, Davis and Millar exponent for Reynolds number loss correlation
A	area, determinant of Boadway's transformation matrix
b	maximum camber (measured perpendicular to chord line)
c	velocity
$C_{()}$	constant
C_D	drag coefficient
C_{D_a}	annulus drag coefficient
C_{D_s}	secondary flow drag coefficient
C_L	lift coefficient
D	drag force, diffusion factor
D_{eq}	equivalent diffusion ratio
F	body force
h	enthalpy
H	blade height
i	incidence angle
K	constant in AVDR correlation
l	chord length
L	lift force
L_s	macroscale
m	coefficient of Constant's deviation rule
M	gradient coefficient in H2 correlation
n	exponent for Constant's deviation rule
\mathbf{n}	normal vector
p	pressure
r	radial co-ordinate, radial position of streamline
Re	Reynolds number
Re_c	cascade inlet Reynolds number based on blade chord
s	entropy, blade pitch
S	southern grid point, source terms
\bar{S}	dimensionless angle of correlation of Jansen and Moffat
t	thickness
T	absolute temperature
Tu	turbulence intensity
U	dimensionless axial velocity
v	local velocity

V	magnitude of velocity vector
v_t	component of velocity along streamline
W	dimensionless radial velocity
X	blade force in axial direction
y	displacement in the traverse plane or blade to blade direction
Y	blade force in tangential direction
z	axial co-ordinate (cylindrical coordinates)
α	flow angle (inlet or outlet)
α'	blade angle (inlet or outlet)
α_m	mean flow angle
γ	blade stagger angle
δ	deviation angle, boundary layer thickness
δ_o	deviation angle at $AVDR = 1$
Δ	difference
ϵ	deflection angle
ζ	loss coefficient: $\zeta = \Delta p_o / \left(\frac{1}{2} \rho c_x^2 \right)$
ϕ	dumny variable of r and z for Boadway's transformation
ψ	stream function
ρ	density
ρ_o	far upstream reference density
σ	solidity (l/s)
$\bar{\omega}$	loss coefficient: $\bar{\omega} = \Delta p_o / \left(\frac{1}{2} \rho c_1^2 \right)$
Ω	angular velocity
θ	camber angle

Subscripts

B	bursting
c	choke
cr	critical
e	midpoint between eastern and central points in discretisation grid
E	eastern grid point in discretisation grid
eff	effective
n	midpoint between northern and central points in discretisation grid
N	northern point in discretisation grid
o	stagnation
opt	Carter's optimum condition
p	pressure surface

<i>ref</i>	reference
<i>s</i>	stall, suction surface, midpoint between southern and central points in discretisation grid
<i>S</i>	separation, distance from stagnation point, southern point in discretisation grid
<i>SB</i>	subbursting
<i>w</i>	midpoint between western and central points in discretisation grid
<i>W</i>	western point in discretisation grid
<i>x</i>	axial
<i>y</i>	blade to blade direction
<i>z</i>	axial in cylindrical coordinates
<i>1</i>	upstream, blade inlet
<i>2</i>	downstream, blade exit
θ	tangential

Superscripts

*	nominal condition, design condition
\wedge	non-dimensionalised
"	inches, corrected value for Jansen and Moffat correlation

ABBREVIATIONS

ADT	actuator disc theory
AGARD	Advisory Group for Aerospace Research and Development
ASME	American Society of Mechanical Engineers
AVDR	axial velocity density ratio
CFD	computational fluid dynamics
DC	direct current
DCA	double circular arc
H2	Howell's correlation as modified in this thesis
HBM	Hottinger Baldwin Messtechnik
Hp	horsepower
IGV	inlet guide vanes
K	Kelvin
LE	leading edge
LED	light emitting diode
LHS	left hand side
MTFM	matrix throughflow method
NACA	National Advisory Committee on Aeronautics
NATO	North Atlantic Treaty Organisation
NGTE	National Gas Turbine Establishment
N-S	Navier-Stokes
Pa	Pascal
PC	personal computer
PEP	Propulsion and Energetics Panel
PVD	prescribed velocity distribution
RHS	right hand side
rpm	revolutions per minute
SCM	streamline curvature method
SRE	simple radial equilibrium
STFM	streamline throughflow method
TE	trailing edge
TF	turbulence factor
USSR	Union of Soviet Socialist Republics
VKI	von Karman Institute

1 INTRODUCTION

1.1 Background

Many theoretical methods exist for the simulation of three-dimensional flows through axial-flow turbomachinery. As the flow is inherently three-dimensional, different approaches have historically been taken to arrive at solutions. Initially the calculation methods concentrated on solving two sets of equations describing two-dimensional flows, one set concerning axisymmetric flow in the axial-radial plane, the other flow on a stream surface of revolution. The former set is generally referred to as meridional throughflow methods, the latter as "blade-to-blade" methods. During the last decade, however, emphasis has shifted towards the development and application of computational fluid dynamic (CFD) methods which allow calculation of the full three-dimensional flowfield without two-dimensional assumptions. Initially used for the calculation of three-dimensional flows through blade rows, CFD has more recently allowed the simulation of flows through multistage machines.

Being fully three-dimensional simulations, the CFD methods have formidable computer memory and processing power requirements, and solve either the discretised inviscid Euler equations or the discretised viscous Navier-Stokes (N-S) equations compounded by a relevant turbulence model. At least four equations are solved at each node in both methods, the continuity equation and the three velocity component equations. If the flow modelled is non-isothermal, an energy equation must be solved as well. In the case of the N-S methods additional equations model the effect of turbulence (2 in the case of the $k - \epsilon$ turbulence model).

A disadvantage to N-S is that the number of nodes required greatly exceeds that of the Euler methods, since steep gradients in fluid variables exist at wall boundaries and blade surfaces due to viscous effects. By contrast, the inviscid Euler equations cannot model those secondary flow phenomena that are boundary-layer driven: endwall effects including tip clearance vortices and corner separation; blade boundary layer wakes; spanwise flow along blade boundary layers and separation bubbles. Prediction of blade row exit flow angles is therefore poor compared to N-S.

Blade row interactions using CFD are taken into account by circumferentially averaging the upstream blade row outlet variables at a given radius. Different solution algorithms exist for the CFD methods depending on whether the flow is largely incompressible, subsonic, transonic or supersonic.

Despite the developments in CFD a need still exists for simple meridional flow calculation methods which, when combined with semi-empirical loss and blade deviation models, are reliable preliminary design tools. Meridional methods have much more modest computer memory and processing power requirements compared to CFD, which mean that either simpler machines such as personal computers can be employed or else solution times on advanced machines are greatly reduced.

The most popular meridional throughflow method is the Streamline Curvature Method (SCM) (Novak, 1967; Davis and Millar, 1975; Denton, 1978) which is used in many commercial and in-house codes. The advantages of SCM are that it requires small computer memory and that being streamline based, flow properties are conserved along streamlines as in inviscid flow or else determined by the actual flow path. Since streamlines are used computational results do not need to be interpolated for interpretation. Disadvantages of the SCM are the determination of the streamline curvature since it is dependent on the type of curve fit, the change in blade section properties with streamline shift between iterations and instability caused by uneven spacing of quasi-orthogonals.

An alternative meridional throughflow method is the matrix throughflow method (MTFM) (Marsh, 1968; Davis and Millar, 1975) which solves the tangential vorticity equation expressed in terms of the stream function as independent variable on a fixed irregular grid. Velocities and eventually other variables can be calculated at each grid point from the stream function values. The advantages of the MTFM are the use of standard CFD discretisation schemes and solution methods and its inherent stability, since it is solved as an elliptic Poisson equation of the form:

$$\frac{\partial^2 \psi}{\partial x^2} + \frac{\partial^2 \psi}{\partial y^2} = q \left(x, y, \frac{\partial \psi}{\partial x}, \frac{\partial \psi}{\partial y} \right) \quad 1.1$$

The disadvantages of the MTFM are the requirement of larger computer memory and the advantages of using streamlines as in the SCM are lost. In addition to the advantages and disadvantages of the two methods discussed above, Davis and Millar (1975), comparing the two methods, found that fewer iterations were required for convergence and overall running times were shorter for the MTFM, but the programming was less simple than for the SCM. Denton (1978) adds that the SCM is the natural choice in problems for which regions of supersonic flow are expected, as stream function methods cannot easily be used to analyse flows where patches of supersonic flow exist. For a given value of stream function two

possible velocity fields values exist, one at a Mach number less than and one greater than unity, and there is no *a priori* way of deciding which solution should be chosen. This problem is relatively easily overcome with SCM.

A disadvantage of both the MTFM and the SCM is the axisymmetric inviscid flow assumption itself. Blade rows are modelled by empirical cascade test correlations for fluid deflection and pressure loss dependent on blade loading and geometry, while near-wall viscous effects are taken into account by displacement thicknesses at hub and shroud boundaries, blockage factors or end wall boundary calculation procedures (Davis and Millar, 1975). The effect of secondary flows is accounted for by correlation. Recirculating flows are not calculable.

A consideration of the various methods led to the question of whether the best properties of the two axisymmetric methods could be combined: the stability and lack of streamline curvature assumptions of the MTFM with the streamline property conservation advantages of the SCM. Boadway (1976) described such a method for general irrotational non-turbomachinery flows, transforming the Laplace equation expressed in terms of the stream function,

$$\frac{\partial^2 \psi}{\partial z^2} + \frac{\partial^2 \psi}{\partial r^2} - \frac{1}{r} \frac{\partial \psi}{\partial r} = 0 \quad 1.2$$

by means of a change of variables to:

$$\left[\frac{\partial r}{\partial \psi} \right]^2 \frac{\partial^2 r}{\partial z^2} + \left[1 + \left(\frac{\partial r}{\partial z} \right)^2 \right] \frac{\partial^2 r}{\partial \psi^2} = -\frac{1}{r} \left(\frac{\partial r}{\partial \psi} \right)^2 + 2 \frac{\partial r}{\partial z} \frac{\partial r}{\partial \psi} \frac{\partial^2 r}{\partial z \partial \psi} \quad 1.3$$

Applying the same transformation to the MTFM equation, an equation is arrived at which resembles the SCM in having streamline position as dependent variable, but in general formulation is similar to the MTFM. For this reason the new method is called the Streamline Throughflow Method (STFM) (von Backström and Roos, 1993).

1.2 Scope and Objectives

The purpose of this thesis is to investigate the stability and accuracy of the STFM, and then analyse flow through a low pressure-ratio (essentially incompressible) three stage axial-flow compressor using the STFM for a design flowrate and two off-design flowrates, one each near choke and surge.

Empirical cascade correlations for flow deflection, pressure loss and secondary flow will be used in the STFM code. The results generated by the STFM will be compared to those obtained by experiment. The STFM will be evaluated with respect to its predicted velocity and total pressure distributions. The experimental analysis will serve to indicate how accurately the axisymmetric analysis predicts the real flow.

2 EXPERIMENTAL PROCEDURE AND RESULTS

2.1 Introduction

Experimental compressor data are required to validate the predictions of the STFM and the models of cascade deflection and profile and endwall loss. In this chapter the apparatus and procedure used to generate this data is described. Firstly the compressor testbench layout, assembly, blading and operation is discussed. Sections follow describing the instrumentation and aerodynamic probe used and their calibration. The experimental procedure is given, and finally the results generated by the experiments are presented and discussed.

2.2 Description of Test Bench

The test bench consists of the low pressure ratio three-stage Rofanco axial flow compressor, shown in figure 2.1. At the inlet an annular bellmouth configuration with inner and outer flanges guides the flow from a mixed flow (axial and radial flow) into the axial parallel-walled compressor inlet annulus. Six struts equally spaced circumferentially around the inlet between the hub and the casing provide structural stiffness.

A straightener consisting of six honeycomb sections wedged between the inlet struts removes any swirl from the flow. Attached to the downstream edges of the struts an annular wire mesh removes wakes induced by the honeycomb and generates near isotropic turbulence (Roach, 1987). The honeycomb and mesh were installed by Lewis (1989) to remove low frequency fluctuations observed at the inlet.

The casing is split along the horizontal diameter to allow access to the blades. The rotor blades are bolted onto the rotor drum, and the stator blades are bolted into half rings which fit into circumferential grooves on the inside of the casing. Stagger angles of the rotor and stator blades are fixed using jigs (Roos, 1990). Three builds are possible, giving axial blade pitches of 0.5", 0.75" and 0.875", and this is achieved by three separate rotor drums and three casings. The maximum axial spacing build was used.

The stator rings can be moved circumferentially a distance of 1.5 blade pitches while the compressor is running to allow circumferential traverse of flow behind the stator rows. The compressor blading was designed for 80% reaction using NACA 65 blade profiles on a circular arc camber line by Benadé (1987). The design pressure ratio and mass flow occurs at 3000 rpm, and is 1.03 and 2.66 kg/s respectively at standard sea level conditions, namely static pressure of 101.3 kPa and static temperature of 293 K. The blade design details are given in

table 2.1. The stages are repeating, which is to say that the velocity triangles at a given radius are considered the same for all three stages. Although inlet guide vanes (IGV's) were part of the original design, they were not installed by Lewis (1989) for his single stage tests. Their absence was not regarded as significant due to the high reaction of the blading.

The compressor casing has static pressure tapping points and probe traverse positions at seven axial stations, one at inlet after the IGV's and one after each blade row. At each axial station there are four circumferentially spaced static pressure tapping points to allow circumferentially averaged readings. In addition, at each axial station there are two probe traverse positions, one on the left and the other on the right at equal angles from the vertical, to check for flow asymmetry.

An annular diffuser decelerates the flow after the last blade row, discharging into a dump plenum. Two honeycombs in the plenum straighten the flow before it passes through a measurement Venturi. A lockable throttle plate at the end of the Venturi diffuser permits control of the mass flow.

The compressor is driven by a 15 Hp DC motor. Thyristor speed control ensures speed holding accurate to 0.1% over the range 300-3000 rpm, even at surge.

2.3 Description of Instrumentation

2.3.1 Pressure measurement

Lewis (1989) measured pressures using a single HBM 10 kPa differential pressure transducer linked to an HMB bridge amplifier. The sequential switching of micro-solenoids in a Furness Controls Selector allowed up to 20 individual pressures to be transmitted to the transducer consecutively. A microcomputer equipped with an analog-to-digital converter card controlled the solenoid switching and the measurement of the output from the bridge amplifier. Lewis does not describe the microcomputer, but Gettliffe (1992) made use of an Olivetti M21 PC with analog-to-digital card, and it could have been the same machine.

The same instrumentation as used by Lewis was employed by Gettliffe, but with minor differences for various reasons. Instead of an HBM pressure transducer Gettliffe used a Foxboro transducer linked to the Furness Controls Selector, with the channel selection done manually rather than by computer.

In the present experimental series, the methods of Gettliffe were followed with a few modifications.

Originally, pressures were to be measured using a Foxboro differential pressure transducer, as used by Gettliffe, since it is typically robust and not sensitive enough to register the higher frequency pressure oscillations caused by turbulence. An HBM pressure transducer, however, was used instead for reasons explained in section 2.4.1 under the calibration procedure.

To take out turbulent fluctuations, damping cylinders were used in the pressure lines.

2.3.2 Flow Measurement

Lewis (1989) used a three-hole cobra probe for measuring hub-to-casing profiles of flow velocity, angle and static and total pressure. A diagram of a cobra probe is given in figure 2.2. The assumption was that due to the high hub-to-tip ratio of the blades, the radial component of velocity would be small, and the flow could be assumed approximately two-dimensional in the axial-tangential plane.

Two methods are given by Lewis for determining flow angles using the cobra probe. In the first, the probe is nulled to the flow by rotating the probe until the pressures measured by the two side tubes are equal. The orientation of the probe stem indicates the flow direction. The alternative technique is to fix the probe direction and calibrate a set of k -factors against known flow angles and Reynolds numbers. The details of this technique are given in Lewis' text. Lewis used a combination of the two methods by approximately nulling the probe to the flow and then fixing the probe setting angle. During a traverse, the probe calibration was used to determine the flow parameters. This had the advantage of narrowing the required calibration range of the probe. The probe was mounted in a traversing mechanism which was operated manually.

Lewis also made use of a TSI Intelligent Flow Analyser and hot-film sensor to measure inlet turbulence levels as well as velocity.

The same instrumentation as used by Lewis was employed by Gettliffe, but with minor differences for various reasons.

Gettliffe made use of the nulling technique of flow angle determination for the cobra probe rather than the k -factors used by Lewis for non-nulled probe position. The probe angle was measured using an angular potentiometer fixed to the probe and the traversing mechanism.

The yaw angle as well as the radial traverse position was controlled by stepper motors from the computer. The stepper motors were only able to move in increments of 1.8° , which limited the number of angles at which the probe could be set. At the true flow angle the difference between the pressures in the left and right tubes of the cobra probe would be zero. At each radial station readings were taken at three consecutive angles straddling the true angle, and interpolation was used to obtain the correct flow angle.

The velocities were obtained from the dynamic pressure ratio with the probe nulled to the flow. The dynamic pressure ratio is that ratio of dynamic pressure to quasi-dynamic pressure, where the dynamic pressure is the difference between the total pressure (measured by the central tube of the probe) and the static pressure, and the quasi-dynamic pressure being the difference between the total pressure and the pressure measured by one of the side tubes of the probe.

In the present experimental series, the methods of Gettliffe were followed with a few modifications.

Difficulties arose with the drivers and wiring of the stepper motors. Due to lack of time, their use to control radial and angular traverses was abandoned. Traverses were done manually. To prevent angular drift of the probe during measurement under simultaneous influence of vibration and the weight of the pneumatic piping, the unplugged angular stepper motor was used to hold the probe at the given angle. Interpolation was used to obtain the flow angles.

2.3.3 Rotor Speed Measurement

A geared wheel with 60 teeth is fixed to the main drive shaft. The frequency in Hertz of pulses from a magnetic transducer picking up the passing of each tooth was shown on the LED display of a frequency counter. As there are 60 teeth on the gear, the display in Hertz is equivalent to the number of revolutions per minute. A toggle switch on the counter allowed the display to show exactly half the frequency. This setting was necessary for rotor speeds near 3 000 rpm because the counter could not follow frequencies that high, so a display of 1 500 at the second setting indicated that the compressor was running at design speed.

2.4 Calibration

2.4.1 Pressure Transducer

The analog-to-digital card converts voltage signals between -10V and 9.995V to an integer between $-32\,768$ and $32\,752$. By dividing the resultant integer value by $32\,768$ and multiplying by 10 the original input voltage can be found. Gettliffe calibrated the input pressures and angles to the Foxboro transducer and potentiometer respectively directly against the integer readings from the analog-to-digital card, and not the voltage outputs. The pressure transducer was calibrated by means of a Betz micromanometer.

The same procedure was followed for the current test series. First a Foxboro pressure transducer was calibrated in this way. During calibration the output of the Foxboro was found to be very linear, but displayed a scatter of up to $\pm 25\text{ Pa}$ from the linear fit consistently across the range of calibration.

For a true dynamic pressure of 0 Pa indicating a velocity of 0 m/s a measured dynamic pressure of 25 Pa would yield a measured velocity of 6 m/s , or 15% of the maximum expected velocity in the compressor. This lack of precision was clearly unacceptable. The reason for the scatter was that the Foxboro had a large operating range and the small yet representative differential pressures increments measured during calibration corresponded to threshold voltages increments for the analog to digital card. A Foxboro with a smaller operating range could not be found, so an HBM pressure transducer was used instead.

Two sets of pressure differential readings were taken from -1.75 kPa to 1.75 kPa to check for repeatability, and a linear regression was performed. Figure 2.3 shows the results of the calibration. The repeatability was excellent.

The difference between the true readings and the regression prediction for each reading is shown plotted on the same graph on a different y-axis as the 1st and 2nd set errors. The error has improved from 25 Pa for the Foxboro to about 3 Pa for the HBM in the low pressure region. For a true velocity of 0 m/s this could yield a measured velocity of 2.2 m/s , or 5.5% of the maximum expected velocity in the compressor. At no stage is the velocity expected to fall to zero, but for a true velocity of 10 m/s this imprecision translates to a velocity error of 0.25 m/s , whereas for the Foxboro a velocity error of 1.9 m/s would result.

2.4.2 Angular Potentiometer

The angular potentiometer was calibrated by means of protractor. Two sets of angular readings were taken from 0° to 180° to check for repeatability, and a linear regression was performed. Figure 2.4 shows the results of the calibration. The repeatability was again excellent.

The difference between the true readings and the regression prediction for each reading is shown plotted on the same graph on a different y-axis as the 1st and 2nd set errors. A large error spike of 2° is shown to exist at 80° , but everywhere else the error is only of the order 0.5° and smaller. The 0.5° and smaller errors fall within the range of human judgement error for the protractor used, and were not considered potentiometer inaccuracies. It was decided to use the potentiometer in the range of 180° to 100° , far from the 2° error region.

2.4.3 Cobra Probe

The cobra probe was calibrated in the Calibration Facility as described by Glass (1986). This facility was designed for the calibration of aerodynamic probes and can be described as a small subsonic wind tunnel. Figure 2.5 shows the layout of the facility.

Two methods can be employed to induce air through the test section for probe calibration: a blow-down and an ejector mode. In the ejector mode, the ball valve B_1 is removed from the system leaving the front flange of the plenum open to atmosphere. Opening ball valve B_2 supplies high pressure air to the ejector nozzle downstream of the test section, and so draws air from the atmosphere through the plenum. In the blow-down mode the plenum is supplied with high pressure air from ball valve B_1 , and the ejector is used only when necessary. Higher velocities and Mach numbers can be obtained in the test section for the blow-down mode than the ejector mode, but requires much more air which influences the available calibration time. As the Mach numbers in the compressor are not expected to exceed 0.1, calibration of the probe was performed in the ejector mode.

The Mach number in the test section is determined by a sized nozzle located in the ejector which chokes the flow. The test section Mach number resulting from use of this nozzle is 0.118. This amounts to a velocity of 40 m/s. The compressor velocities are expected to be about 34 m/s but Lewis (1989) found that Reynolds number dependence of a cobra probe is very small in this range, with a slight increase in effect being visible at half this speed, so a calibration of the probe at 40 m/s was regarded as applicable.

The probe calibration procedure followed was the same as that of Gettliffe (1992), with the goal being to determine the dynamic pressure ratio with the probe nullied to the flow. The probe was rotated from a nominal -12° to 12° and the plenum to test section dynamic pressure, the probe dynamic pressure, the quasi-dynamic pressure and the differential pressure between the outer two tubes of the cobra probe were measured at approximately 1.8° angular intervals. The results are shown in figure 2.6. The probe is regarded as nullied to the flow when the differential pressure between the outer two tubes is zero. The position of the zero angle was found by linear interpolation. After fitting a quadratic function through the five closest points, the value of the dynamic pressure ratio was found by quadratic interpolation to be 2.084.

2.5 Experimental procedure

The compressor was run at three different flowrates, near-design, near-surge and near-choke. The near-design flowrate was found by moving the throttle plate until the mass flowrate as indicated by the uncalibrated venturi was approximately 2.66 kg/s. The near-surge flowrate was found by opening the throttle until the gap between the throttle plate and the exit duct was a fraction wider than 0.375", the surge position as mentioned in the manual. For the near-choke flowrate the throttle was simply opened as wide as possible. All tests were performed at 3 000 rpm.

Radial traverses were performed at inlet and behind each blade row at each of the flowrates using the cobra probe. The radial increments grew from 1 mm at the hub and casing to 4 mm at the centre. A varying increment size was used to capture detail in the boundary layers but not waste effort in the centre where gradients in angle and velocity were not expected to be great. At least three measurements were taken at each radial station. This was done to provide points for linear interpolation to determine the flow angles and velocities.

Measurements were taken using only one of the two banks of probe traverse positions. The only exception was at the inlet at the near-design flowrate to ensure a smooth inlet velocity profile. In addition, as explained in section 2.3.2, radial and angular traverses had to be performed manually, greatly increasing the time to complete a single radial traverse. Since three flowrates had to be covered with seven axial stations per flowrate, time constraints dictated that only one radial traverse could be done per blade row. For this reason, use was not made of the circumferentially movable stator rings to obtain a range of readings for a blade-to-blade average at each measurement radius. Measurements behind the stator rows consisted of a single radial traverse behind each stator row.

While beginning testing, it was discovered that the inlet velocity profile was far from smooth, and appeared jagged and uneven. Initially it was thought that the honeycomb segments were not properly inserted, but were in fact distorted, causing flow to be alternatively focussed and dispersed at different radii by respectively convergent and divergent adjacent honeycomb cells. After removal, straightening and careful reinstallation of the honeycomb, the results were no different. The cause was eventually found to be fluff accumulated from years of tests which had been trapped on the upstream side of the inlet mesh. After cleaning the mesh the inlet profiles were much smoother.

After the measurements had been taken, the data on the floppy disk was imported into a spreadsheet and the interpolation was done to obtain the flow angles and velocities. Static pressure values were deduced at each radial station from the total pressures and the quasi-dynamic pressures. Densities were calculated from the static pressures and the external total pressure. Two errors were introduced by this procedure. Firstly the assumption that the stagnation temperature does not change across blade rows gives rise to a cumulative temperature underprediction of 1.4 K per stage at the meanline at the design flowrate, or 4.2 K across the whole compressor. The second error, using the total and not static temperature, gives rise to a constant temperature overprediction of 0.8 K after rotor rows and 0.6 K after stator rows, working against the first error. Density is therefore 1.16% overpredicted at the last rotor row and 1.23% overpredicted at the last stator row. These errors were considered acceptable.

2.6 Results

The results were plotted on graphs displaying flow angle, tangential velocity, axial velocity and total pressure. The axes of the axial velocity graphs were shifted to allow all the stage data to be presented on a single graph for each flowrate. This was done by raising the zeroes of the rotor profiles by 20 m/s and the inlet profiles by 40 m/s. The axes of the total pressure graphs were also shifted. To allow for comparison the total pressures were plotted with respect to the mass average of the inlet total pressure, effectively defining the inlet total pressure as zero for each flowrate. The flow angles were almost all negative by common convention, but were plotted as positive to aid the reader by having the profile above the x-axis.

2.6.1 Mass Balances

Mass balances were done at each axial station for each flowrate, and are shown in table 2.2. The true mass flow for each flowrate was taken as the average of the three rotor flow calculations. This was done because the stator and inlet mass balances are overpredictions due to blockage, as can be seen from the values in table 2.2.

The stator measurements were not made up of pitchwise averages but were single readings at each radial station. Cascade theory dictates that to get true values of turning and pressure loss it is necessary to take several readings across the pitch of the blades in cascade. These readings must then be mass and area averaged. The current set of stator readings, therefore, are overpredictions since they have not been negatively weighted by the blade wake values. The stator mass flows are 24% overpredicted on average for the near-surge flowrate. This is to be expected because the suction surface blade boundary layers are at their largest at this flowrate due to high incidence angles, and present the most blockage. The overpredictions are milder for the near-design and near-choke flowrates, being 8% and 4% respectively.

The inlet mass flows are also overpredicted, although less so than the stator flows. These overpredictions are due to the wakes of the inlet struts causing blockage. The blockage appears to be the same for the near-design and near-choke flowrates, where the inlet flow overprediction is about 3.8%, but at the near-surge flowrate rises to 5.5%.

Comparing the rotor mass averages, the agreement between the different blade rows is very good. For the near-design and near-choke flowrates, differences are less than 1% from the average. For the near-surge flowrate the maximum deviation from average is 1.6%.

2.6.2 Flow Angle and Tangential Velocity Profiles

The inlet flow profile can be seen to be approximately axial from the flow angle and tangential velocity graphs for all three flowrates, except in the casing boundary layer. At the near-design flowrate inlet traverses were taken at the left and right bank, and are shown at figures 2.7 and 2.8. The left and right profiles correspond quite well, except that flow angle of the bulk flow outside the hub boundary is positive for the one bank and negative for the other in a near-symmetrical fashion. This could be as a result of the presence of inlet struts, since the strut position relative to the probe is inverted from one probe bank to the other.

In the hub boundary layer the circumferential entraining effect of the spinning hub is clear for all three flowrates. At the near-choke flowrate the effect is reduced, since the flow is moving faster and has had less time for the viscous forces to drag it circumferentially before it reaches the probe. As expected, the effect is most pronounced at the near-surge flowrate.

At all three flowrates the flow pattern can be seen to be repeatable after the rotor rows, with the rotor flow angle and tangential velocity profiles collapsing onto approximately the same respective lines. The only exception to this is the flow behind the first rotor at the near-surge flowrate (figure 2.15 and 2.16), where the turning of the flow is less than for the other rotor rows. The explanation is simply that the absence of inlet guide vanes means that the flow has not been prerotated before the first row of rotor blades. This lack of prerotation increases the incidence angle "seen" by the first stage rotor. Cumpsty (1989) states that deviation is a weak function of incidence until blade stall is approached. (The deviation angle is the difference between the air outlet angle and the blade outlet angle, and is illustrated in figure 4.1). The absence of prerotation therefore does not affect the rotor outlet flow angle for the near-design and near-choke flowrates, since the flow does not approach stalling incidence. At the near-surge flowrate, however, the flow is very near stall, and so deviation is increased and flow turning is correspondingly decreased for the first stage rotor row.

The flow pattern after the stator rows is also repeatable after all three stages for the near-choke flowrate. The same can be said for the second and third stages for all three flowrates. The first stage stator flow angle and tangential velocity profiles appear lower than for the other two stages for the near-design and the near-surge flowrates. This is possibly due to the probe being near to the suction surface of a first stage stator blade during measurement so that the right side tube of the probe protrudes into the suction surface boundary layer wake of the blade. Since the right tube is not reading a "freestream" quasi-dynamic pressure but a slower boundary layer flow, the probe will under-read the flow angle.

The above scenario is a very plausible explanation for the near-design flowrate static flow measurement results. For the near-surge stator flow the whole probe was probably in the boundary layer wake, since the axial velocity measurement for this stage at this flowrate is lower than for the other two stages, as can be seen in figure 2.17. This is only possible if the central tube of the cobra probe is in the boundary layer wake, underreading the total pressure. The left side tube was probably in the boundary layer wake, as the stator flow angle measurement for this stage at this flowrate does not differ from the other two stages as much as at the near-design flowrate.

At the near-surge flowrate the suction surface boundary layer is expected to be thinner than for the other two flowrates, causing the right side tube of the probe to be outside the suction surface boundary layer of the stator blade.

2.6.3 Axial Velocity Profiles

The inlet axial velocity profiles can be seen to be smooth for the three flowrates from figures 2.9, 2.13 and 2.17, but an interesting gradient exists in these profiles with the velocity decreasing from hub to casing. The same trend was noticed by Lewis (1989) who went to considerable lengths to flatten out the profile by adjusting the honeycomb and the flow coefficient without success.

The velocity gradient can be explained by potential flow theory. The casing flange has greater curvature than the hub flange (see figure 2.1). As the air flows through the bellmouth, potential flow theory dictates that the streamlines lie closer together, and have greater curvature, on the casing (the inside of the bend) than on the hub. Flow near the casing therefore enters the honeycomb at a higher velocity but also greater incidence than at the hub. This leads to the flow experiencing greater losses through the honeycomb at the casing than the hub. At the measuring station at the inlet to the first rotor there is no streamline curvature, due to the combined influence of the parallel walls and the free vortex design of the compressor. There is also no flow rotation due to the straightening effect of the honeycomb. A static pressure gradient is therefore impossible at the inlet measuring station, so the total pressure gradient as described above results in a velocity gradient.

Downstream of the blade rows flow coefficient effects come into play. Outside of the boundary layers at the hub and casing, the axial velocity gradient varies depending on flowrate. Figure 2.13 shows the axial velocity to decrease with increasing radius for the high flowrate, while in figure 2.17 it increases with radius for the low flowrate. At the near-design flowrate the profile is approximately flat. This is because a change in axial velocity causes the rotor velocity triangles to predict varying incidence angles from hub to casing. As a result the thrust imparted to stream tubes varies from hub to casing.

2.6.4 Total Pressure Profiles

The inlet total pressure profiles show the effect of the boundary layers. Figure 2.14 shows that the inlet boundary layers for the near-choke flowrate at the hub and casing are larger than

for the other two flowrates (figures 2.10 and 2.18), since the Reynolds numbers are greater. At the other two flowrates however, the rotational hub boundary layer becomes visible by increasing the total pressure by viscous entrainment.

The total pressure profiles show very little loss between the rotor rows and their corresponding stator rows, and in some cases the total pressure after a stator row exceeds that of the corresponding rotor row. This is another consequence of not pitchwise averaging the stator flows, as the losses are generated in the boundary layers and wakes and have not been transferred to the bulk passage flow as early as the trailing edge.

The measured total pressures do deviate at the hub, however, with the total pressure after the rotors being higher than after the stators. This is due to circumferential viscous entrainment of the flow on the spinning rotor drum boosting total pressure after the rotors but blade tip clearance effects causing losses through the stator hub gap.

The measured total pressures at the casing are higher after the stator rows than after the rotors in all cases except the first stage at the near-design flowrate. In addition to the effect of not pitchwise averaging the stator measurements, this is due to redistribution of total pressure lost due to rotor blade tip clearance effects. This effect can be seen at the edge of the casing boundary layer where the total pressures after the rotors are higher than after the stators in most of the measurements.

Outside the hub and casing boundary layers, the gradient of total pressure after the blade rows follow the same trend as the axial velocity profiles.

2.7 Conclusions

The mass balances show that the rotor flow measurements are reliable and serve a good basis for comparison with numerically predicted results. Acknowledging the detrimental effect of not pitchwise averaging the stator measurements, the stator flow measurements are useful for qualitative comparison. The inlet measurements prove that the flow quality is good and can be numerically modelled by flat profiles.

3 THE DEVELOPMENT AND TESTING OF THE STREAMLINE THROUGHFLOW METHOD

3.1 Previous work

As mentioned in the introduction, the two main inviscid axisymmetric methods are the Streamline Curvature Method and the Matrix Throughflow Method. Oates (1988) derived the following MTFM equation for the stream function ψ for turbomachines:

$$\frac{\partial}{\partial z} \left[\frac{\rho_o}{\rho} \frac{1}{r} \frac{\partial \psi}{\partial z} \right] + \frac{\partial}{\partial r} \left[\frac{\rho_o}{\rho} \frac{1}{r} \frac{\partial \psi}{\partial r} \right] = \frac{1}{v_i} \mathbf{nF} + \frac{\rho}{\rho_o} r \left[\frac{\partial h_o}{\partial \psi} - T \frac{\partial s}{\partial \psi} - \frac{c_\theta}{r} \frac{\partial (rc_\theta)}{\partial \psi} \right] \quad 3.1$$

where the velocity components are given by

$$c_x = \frac{\rho_o}{\rho} \frac{1}{r} \frac{\partial \psi}{\partial z}, \quad c_r = -\frac{\rho_o}{\rho} \frac{1}{r} \frac{\partial \psi}{\partial r} \quad 3.2$$

Owing to the complication introduced by the presence of the body force term F , Oates simplified equation 3.1 by approximating blade rows by infinitely thin actuator discs, with the proviso that the equation does not apply across actuator discs. The effect of the forces upon tangential momentum, stagnation entropy and enthalpy within the actuator disc is the same as that within the blade row, but the forces do not appear in the equation. Equation 3.1 was therefore reduced to

$$\frac{\partial}{\partial z} \left[\frac{\rho_o}{\rho} \frac{1}{r} \frac{\partial \psi}{\partial z} \right] + \frac{\partial}{\partial r} \left[\frac{\rho_o}{\rho} \frac{1}{r} \frac{\partial \psi}{\partial r} \right] = \frac{\rho}{\rho_o} r \left[\frac{\partial h_o}{\partial \psi} - T \frac{\partial s}{\partial \psi} - \frac{c_\theta}{r} \frac{\partial (rc_\theta)}{\partial \psi} \right] \quad 3.3$$

Oates *et al.* (1976) transformed the matrix throughflow equation, equation 3.3, to yield as its dependent variable the radial position of stream function $r = r(z, \psi)$ instead of the value of stream function $\psi = \psi(r, z)$:

$$-\frac{\partial}{\partial z} \left[\frac{1}{\rho r} \left(\frac{\partial r}{\partial z} \right) \right] + \frac{r}{2} \frac{\partial}{\partial \psi} \left[\frac{1 + \left(\frac{\partial r}{\partial z} \right)^2}{\rho \left(r \frac{\partial r}{\partial \psi} \right)^2} \right] + \frac{r}{2} \frac{1 + \left(\frac{\partial r}{\partial z} \right)^2}{\left(r \frac{\partial r}{\partial \psi} \right)^2} \frac{\partial (1/\rho)}{\partial \psi} = \frac{\rho}{\rho_o} r \left[\frac{\partial h_o}{\partial \psi} - T \frac{\partial s}{\partial \psi} - \frac{c_\theta}{r} \frac{\partial (rc_\theta)}{\partial \psi} \right] \quad 3.4$$

The function $r = r(z, \psi)$ was approximated by finite element discretisation and solved as a variational problem. Isentropic compressible flows through a stator-rotor pair were solved using this method.

In this thesis, Boadway's transformation (1976) is applied to the matrix throughflow equation, equation 3.3. A longer, but less contorted expression of the transformed MTFM equation is obtained than that of Oates *et al.* (1976). The function is discretised using the considerably simpler finite difference approach. The method is applied to several exact test cases to determine the characteristics of the method.

3.2 Application of Boadway's Transformation to the Matrix Throughflow Equation

Boadway's transformation (1976) was applied to cylindrical coordinates and is given in appendix A. By making use of this transformation, a different form of equation 3.4 can be derived which, when discretised, gives rise to a rapid solution algorithm. Denote the RHS source terms of equation 3.3 by S . Expanding the LHS terms of equation 3.3 we get

$$\begin{aligned} -\frac{\rho_o}{r\rho^2} \left[\frac{\partial\rho}{\partial z} \frac{\partial\psi}{\partial z} + \frac{\partial\rho}{\partial r} \frac{\partial\psi}{\partial r} \right] - \frac{\rho_o}{r^2\rho} \left[\frac{\partial r}{\partial z} \frac{\partial\psi}{\partial z} + \frac{\partial\psi}{\partial r} \right] \\ + \frac{\rho_o}{r\rho} \left[\frac{\partial^2\psi}{\partial z^2} + \frac{\partial^2\psi}{\partial r^2} \right] = S \end{aligned} \quad 3.5$$

The variables r and z are mutually independent, therefore $\partial r/\partial z = 0$. Equation 3.5 simplifies to

$$\begin{aligned} -\frac{\rho_o}{r\rho^2} \left[\frac{\partial\rho}{\partial z} \frac{\partial\psi}{\partial z} + \frac{\partial\rho}{\partial r} \frac{\partial\psi}{\partial r} \right] - \frac{\rho_o}{r^2\rho} \frac{\partial\psi}{\partial r} \\ + \frac{\rho_o}{r\rho} \left[\frac{\partial^2\psi}{\partial z^2} + \frac{\partial^2\psi}{\partial r^2} \right] = S \end{aligned} \quad 3.6$$

Making use of Boadway's transformation in Appendix A, equation 3.6 becomes

$$\begin{aligned} & \frac{\rho_o}{r\rho^2} \frac{1}{\left(\frac{\partial r}{\partial \psi}\right)^3} \left[\left(\frac{\partial r}{\partial \psi}\right)^2 \frac{\partial r}{\partial z} \frac{\partial \rho}{\partial z} - \frac{\partial r}{\partial \psi} \frac{\partial \rho}{\partial \psi} \left(1 + \left\{\frac{\partial r}{\partial z}\right\}^2\right) \right] - \frac{\rho_o}{r^2 \rho} \frac{1}{\left(\frac{\partial r}{\partial \psi}\right)} \\ & + \frac{\rho_o}{r\rho} \frac{1}{\left(\frac{\partial r}{\partial \psi}\right)^3} \left[2 \frac{\partial r}{\partial \psi} \frac{\partial r}{\partial z} \frac{\partial^2 r}{\partial z \partial \psi} - \left(\frac{\partial r}{\partial \psi}\right)^2 \frac{\partial^2 r}{\partial z^2} - \frac{\partial^2 r}{\partial \psi^2} \left(1 + \left\{\frac{\partial r}{\partial z}\right\}^2\right) \right] = S \end{aligned} \quad 3.7$$

Multiplying by $r \frac{\rho}{\rho_o} \left(\frac{\partial r}{\partial \psi}\right)^3$ we obtain

$$\begin{aligned} & \frac{1}{\rho} \left[\frac{\partial r}{\partial z} \left(\frac{\partial r}{\partial \psi}\right)^2 \frac{\partial \rho}{\partial z} - \frac{\partial \rho}{\partial \psi} \frac{\partial r}{\partial \psi} \left(1 + \left\{\frac{\partial r}{\partial z}\right\}^2\right) \right] - \frac{1}{r} \left(\frac{\partial r}{\partial \psi}\right)^2 + 2 \frac{\partial r}{\partial \psi} \frac{\partial r}{\partial z} \frac{\partial^2 r}{\partial z \partial \psi} \\ & - \left(\frac{\partial r}{\partial \psi}\right)^2 \frac{\partial^2 r}{\partial z^2} - \frac{\partial^2 r}{\partial \psi^2} \left(1 + \left\{\frac{\partial r}{\partial z}\right\}^2\right) = \left[\frac{\rho}{\rho_o} r\right]^2 \left[\frac{\partial r}{\partial \psi}\right]^3 \left[\frac{\partial h_o}{\partial \psi} - T \frac{\partial s}{\partial \psi} - \frac{c_\theta}{r} \frac{\partial (rc_\theta)}{\partial \psi}\right] \end{aligned} \quad 3.8$$

This equation can be seen to be equivalent to that of Oates *et al.*, equation 3.4. The density gradient term can be moved to the RHS since it may be regarded as a form of source term:

$$\begin{aligned} & 2 \frac{\partial r}{\partial \psi} \frac{\partial r}{\partial z} \frac{\partial^2 r}{\partial z \partial \psi} - \left(\frac{\partial r}{\partial \psi}\right)^2 \frac{\partial^2 r}{\partial z^2} - \frac{\partial^2 r}{\partial \psi^2} \left(1 + \left\{\frac{\partial r}{\partial z}\right\}^2\right) - \frac{1}{r} \left(\frac{\partial r}{\partial \psi}\right)^2 \\ & = \left[\frac{\rho}{\rho_o} r\right]^2 \left[\frac{\partial r}{\partial \psi}\right]^3 \left[\frac{\partial h_o}{\partial \psi} - T \frac{\partial s}{\partial \psi} - \frac{c_\theta}{r} \frac{\partial (rc_\theta)}{\partial \psi}\right] - \frac{1}{\rho} \left[\frac{\partial r}{\partial z} \left(\frac{\partial r}{\partial \psi}\right)^2 \frac{\partial \rho}{\partial z} - \frac{\partial \rho}{\partial \psi} \frac{\partial r}{\partial \psi} \left(1 + \left\{\frac{\partial r}{\partial z}\right\}^2\right) \right] \end{aligned} \quad 3.9$$

If the flow is incompressible, then $\rho/\rho_o = 1$ and $\frac{\partial \rho}{\partial \psi}, \frac{\partial \rho}{\partial z} = 0$. Equation 3.9 then simplifies to

$$\begin{aligned} & 2 \frac{\partial r}{\partial \psi} \frac{\partial r}{\partial z} \frac{\partial^2 r}{\partial z \partial \psi} - \left(\frac{\partial r}{\partial \psi}\right)^2 \frac{\partial^2 r}{\partial z^2} - \frac{\partial^2 r}{\partial \psi^2} \left(1 + \left\{\frac{\partial r}{\partial z}\right\}^2\right) - \frac{1}{r} \left(\frac{\partial r}{\partial \psi}\right)^2 \\ & = r^2 \left[\frac{\partial r}{\partial \psi}\right]^3 \left[\frac{\partial h_o}{\partial \psi} - T \frac{\partial s}{\partial \psi} - \frac{c_\theta}{r} \frac{\partial (rc_\theta)}{\partial \psi}\right] \end{aligned} \quad 3.10$$

Examining the LHS of equation 3.10 the same terms as Boadway's transformed Laplace equation for cylindrical coordinates (equation 1.3) can be seen. The first four terms on the

LHS of equation 3.10 are equivalent to the terms in x and y coordinates of Boadway's transformed Laplace equation for Cartesian coordinates. The last term on the LHS of equation 3.10 is therefore the transformed extra term for cylindrical coordinates.

3.3 Discretisation and Solution

The efficiency of application of the stream function equation after Boadway's transformation is greatly improved if use is made of non-uniform grid spacing. This allows fine spacing in areas of extreme velocity gradients and coarse spacing in areas of very gradual gradients. The former is to improve accuracy, the latter to reduce the amount of computer memory and computation time required.

Greyvenstein (1981) extended the Boadway numerical method to non-uniform grids for the above reasons. Appendix B contains the method used to discretise equation 3.9. Compressible flow was not investigated in this thesis, so the simpler equation 3.10 was discretised. To solve equation 3.10, initial radial positions are found from the stream function definition

$$\Psi = \int_{r_{hub}}^r \frac{\rho}{\rho_0} c_x r dr = \int_{r_{hub}}^r c_x r dr \quad 3.11$$

where c_x is the component of velocity in the axial direction, and c_x was assumed constant for all radial stations at a given axial station.

Successive iterations employ a relaxation factor of less than unity to prevent instabilities, typically 0.9. The code was written in Pascal for a personal computer with a 80286 processor. The convergence criterion was that streamlines should move less than 0.001% of the distance between neighbouring streamlines per iteration.

3.4 Test Case Classification

The test cases required to investigate the behaviour of the incompressible STFM fall into four categories, and involve sequentially activating each of the source terms in the last bracket on the RHS of equation 3.10.

Firstly, all the source terms are set equal to zero. These test cases depend entirely on boundary conditions and do not have tangential momentum, entropy or enthalpy gradients across

streamlines. These test cases investigate the basic tendencies of the method, and explore the behaviour of the extra term for cylindrical coordinates, $\frac{1}{r} \left(\frac{\partial r}{\partial \psi} \right)^2$, mentioned at the end of section 3.2.

Secondly, non-zero tangential momentum gradients across streamlines are introduced with the stagnation enthalpy and entropy gradients kept equal to zero. These test cases compare the known effect of certain vortex distribution manipulations from actuator disc theory with the STFM results for the same vortex distribution manipulations.

Thirdly, non-zero stagnation enthalpy and tangential momentum gradients across streamlines are tested assuming isentropic flows. These test cases add the effect of non-uniform work input to the vortex distribution effects mentioned in the previous class of test cases. This class of flows will not be investigated in this thesis.

Lastly, all the source terms are non-zero, representing general classes of bounded inviscid flows with losses such as turbomachinery flows.

3.5 Source terms equal to zero

3.5.1 Parallel-walled annulus

In this test case, the streamlines will be parallel since the walls are parallel and radial equilibrium is undisturbed by blade rows. Slug flow with no swirl is assumed. The inlet and outlet boundary conditions are specified by zero gradient in radial position of streamlines, i.e.

$$\left[\frac{\partial r}{\partial z} \right]_{\psi} = 0 \quad 3.12$$

Since the above gradient will become zero, the first two terms on the LHS of equation 3.10 effectively disappear, r becomes a variable in ψ only, and the LHS becomes an ordinary second order differential equation. First the effect of hub-tip ratios on discretisation error was examined by taking an even-spaced nine-point grid (see figure B.1), with

$$r_W = r_P = r_E \quad 3.13$$

and

$$r_N = r_o$$

$$r_S = r_i$$

3.14

These were non-dimensionalised by dividing all the radii by the outer radius r_o . The solution was compared with the exact solution from equation 3.11 and both are plotted in figure 3.1 as a function of r_S/r_N . The difference between the two, expressed as a percentage of the exact solution, is also shown. The largest error occurs when r_S equals zero.

Next the effect of the number of nodes in the grid in the radial direction was investigated. To make the error as visible as possible, the inner radius r_i was chosen to be zero. The grid was evenly spaced in the stream function direction, again with three nodes in the axial direction. Calculations were done with grids containing 1, 3, 7, 15 and 31 internal streamlines to examine the effect of halving the stream function spacing. The resultant values are shown in figure 3.2 as fractions of the exact values. The procedure was repeated for different values of r_i and are shown in figures 3.3, 3.4, 3.5 and 3.6.

From the figures it can be seen that if calculations have to be made involving low hub-tip ratios, the grid must be made finer in the smaller radius regions, or else the cylindrical coordinate term, $\frac{1}{r} \left(\frac{\partial r}{\partial \psi} \right)^2$, should be modelled differently.

3.5.2 Flow over a sphere

This test case is useful since it gives a means of assessing the flow over the nose cone of the hub of a turbomachine. It differs from the previous test case in that $\frac{\partial r}{\partial z}$ is no longer zero, so the first two terms on the LHS of equation 3.10 come into play.

A sphere of radius 0.4 units was chosen for the internal bounding streamline. To eliminate the complication of taking blockage into account, an exact potential flow solution was taken for the external bounding streamline, with a radius of unity at the widest point.

Non-uniform increments were used in the stream function direction to avoid using too many grid points and still examine a streamline close to the centreline, and in the axial direction to be able to follow the curvature of the sphere relatively accurately.

Figure 3.7 shows the comparison between the STFM and potential flow solutions. Only one half of the solution is displayed since the streamlines are symmetrical about the $z = 0$ axis. The error is shown in figure 3.8. It can be seen that the error at all streamlines is less than 1% at $z = 0$. This shows that the STFM yields accurate velocity distributions after nose cones.

3.6 Non-zero Tangential Momentum Gradients across Streamlines, other Terms equal to Zero

Actuator disc theory (ADT), as discussed by Dixon (1978), provides a model for introducing tangential momentum changes in the flow for the STFM, as well as an analytical method against which to compare the predictions of the STFM. An actuator disc is an idealised blade row, infinitely thin, which provides a stepwise change in tangential momentum and stagnation enthalpy but not axial velocity.

As applied to the STFM, the actuator disc is not part of the flowfield and values upstream and downstream of the disc must be calculated to satisfy stepwise changes across the disc. This may be done in one of two ways: either the disc lies between two axial STFM stations, so that the full step in tangential momentum and stagnation enthalpy is implemented at the downstream station relative to the upstream station for a given streamline; or the disc is situated at an STFM station where the change in tangential momentum and stagnation enthalpy is the average of the upstream and downstream STFM stations for a given streamline.

Two compatibility conditions must be satisfied at the discontinuity, mass conservation and radial momentum conservation. Mass conservation amounts to the radial position of a streamline being the same immediately after as immediately before the disc. Since the STFM procedure under discussion in this thesis is incompressible, this requires the axial velocity across the disc to remain the same. Radial momentum conservation requires that the radial velocity component be conserved across the disc. Combined with the constant axial velocity condition of mass conservation, this means that streamline slope cannot change across the actuator disc. These conditions of continuous streamlines and streamline slopes are automatically satisfied by equation 3.10.

3.6.1 Parallel-walled annulus with single actuator disc

Using actuator disc theory (ADT) as discussed by Dixon (1978), flow was analysed through an actuator disc in a parallel-walled annulus with hub-tip ratio of 0.4. Simple radial equilibrium (SRE) first power vortex distributions were chosen up and downstream. The radial positions of streamlines were found with equation 3.12. The calculations were repeated using the STFM with grids containing 1, 3 and 7 internal streamlines to examine the effect of halving the stream function spacing.

The resultant positions of the median streamline are shown on figure 3.9. The radial error varies from an acceptable 0.9% for a single internal streamline to an excellent 0.24% for 7 internal streamlines, as can be seen on figure 3.10. The corresponding velocity profiles for 7 internal streamlines are given in figure 3.11 where the agreement is seen to be excellent.

3.6.2 Parallel-walled annulus with two actuator discs (blade row interaction)

Dixon (1978) discusses blade row interaction effects using ADT for a repeating stage. A parallel-walled annulus with hub-tip ratio of 0.4 with actuator discs one blade length apart was used to analyse flow through a blade row using ADT. The same first power vortex distributions as for the single actuator disc were chosen, one up and downstream and the other between the discs. The calculations were repeated using the STFM, again with grids containing 1, 3 and 7 internal streamlines.

The resultant positions of the median streamline are shown on figure 3.12. Figure 3.13 shows that the radial error varies from an acceptable 0.95% for a single internal streamline to an excellent 0.05% for 7 internal streamlines.

The calculations were repeated for sparse, non-uniform grid spacing. Whereas figures 3.12 and 3.13 show the results for 5 stations between the actuator discs, figures 3.14 and 3.15 illustrate the results for 3 stations between the discs, 3.16 and 3.17 for 2 stations between the discs and 3.18 and 3.19 for a single station between the discs. For 3 stations between the discs the radial error varied from 1% for a single streamline to 0.35% for 7 internal streamlines. For 2 stations between the discs the radial error varied from 1.25% for a single streamline to 0.2% for 7 internal streamlines. For a single station between the discs the radial error varied from 1.1% for a single streamline to 0.15% for 7 internal streamlines.

3.7 Non-zero Total Enthalpy, Tangential Momentum and Entropy Gradients across Streamlines, Incompressible Flow

These test cases are, in effect, the results from the experiments performed on the Rofanco compressor. Since the STFM is inviscid, losses will have to be introduced by correlation. The comparisons with the experimental results will not be presented in this chapter as they are expected to be quite dependent upon the different correlations employed. The substitutions within the source term to remove the entropy gradient will, however, be presented here.

From thermodynamics the following equation is obtained:

$$Tds = dh - \frac{dp}{\rho} \quad 3.15$$

Since the flow is incompressible, the following relations apply:

$$\begin{aligned} p_o &= p + \frac{1}{2}\rho V^2 \\ h_o &= h + \frac{1}{2}V^2 \end{aligned} \quad 3.16$$

After combining the two above equations, it is clear that

$$h_o - h = \frac{p_o}{\rho} - \frac{p}{\rho} \quad 3.17$$

so therefore

$$dh_o - \frac{dp_o}{\rho} = dh - \frac{dp}{\rho} \quad 3.18$$

Substituting 3.15 into 3.18 yields

$$Tds = dh_o - \frac{dp_o}{\rho} \quad 3.19$$

Applying finite instead of differential differences, 3.19 becomes

$$T\Delta s = \Delta h_o - \frac{\Delta p_o}{\rho} \quad 3.20$$

Applying 3.20 across a blade row, the notation changes:

$$T\Delta s_{1,2} = \Delta h_{o1,2} - \frac{\Delta p_{o1,2}}{\rho} \quad 3.21$$

The Euler turbomachinery equation is

$$\Delta h_{o1,2} = \Omega(r_2 c_{\theta 2} - r_1 c_{\theta 1}) \quad 3.22$$

where Ω is the angular velocity of the blade row and r_1 and r_2 are the upstream and downstream radii of the streamline. The change in total pressure across a blade row can be broken down as follows:

$$\begin{aligned} \Delta p_{o1,2} &= p_{o2} - p_{o1} \\ &= p_{o1} + \Delta p_{o1,2ideal} - \Delta p_{o1,2loss} - p_{o1} \\ &= \Delta p_{o1,2ideal} - \Delta p_{o1,2loss} \end{aligned} \quad 3.23$$

In an actual blade row $\Delta p_{o1,2loss}$ results from viscous boundary layer losses on the blades and endwalls as well as secondary flows. These can be obtained by correlation. Substituting 3.22 and 3.23 into 3.21 we obtain

$$T\Delta s_{1,2} = \Omega(r_2 c_{\theta 2} - r_1 c_{\theta 1}) - \frac{(\Delta p_{o1,2ideal} - \Delta p_{o1,2loss})}{\rho} \quad 3.24$$

If the flow is isentropic and ideal, then it follows that

$$\Delta s_{1,2} = 0, \Delta p_{o1,2loss} = 0 \quad 3.25$$

Inserting 3.25 into 3.24 yields

$$\Delta p_{o1,2ideal} = \rho \Omega (r_2 c_{\theta 2} - r_1 c_{\theta 1}) \quad 3.26$$

On combining 3.26 and 3.24 we get

$$T\Delta s_{1,2} = \frac{(\Delta p_{o1,2loss})}{\rho} \quad 3.27$$

Considering 3.22 and 3.27 alongside 3.20, it is clear that

$$\begin{aligned} \Delta h_{o1,2} - T\Delta s_{1,2} &= \frac{\Delta p_{o1,2}}{\rho} \\ &= \Omega(r_2 c_{\theta 2} - r_1 c_{\theta 1}) - \frac{(\Delta p_{o1,2loss})}{\rho} \\ &= \frac{(\rho\Omega(r_2 c_{\theta 2} - r_1 c_{\theta 1}) - \Delta p_{o1,2loss})}{\rho} \end{aligned} \quad 3.28$$

and

$$\Delta p_{o1,2} = \rho\Omega(r_2 c_{\theta 2} - r_1 c_{\theta 1}) - \Delta p_{o1,2loss} \quad 3.29$$

Rearranging 3.19 yields

$$dh_o - Tds = \frac{dp_o}{\rho} \quad 3.30$$

Since

$$\begin{aligned} dh_o &= \frac{\partial h_o}{\partial \psi} d\psi + \frac{\partial h_o}{\partial z} dz \\ ds &= \frac{\partial s}{\partial \psi} d\psi + \frac{\partial s}{\partial z} dz \\ dp_o &= \frac{\partial p_o}{\partial \psi} d\psi + \frac{\partial p_o}{\partial z} dz \end{aligned} \quad 3.31$$

and (except across actuator disks)

$$\begin{aligned}\frac{\partial h_o}{\partial z} &= 0 \\ \frac{\partial s}{\partial z} &= 0 \\ \frac{\partial p_o}{\partial z} &= 0\end{aligned}\tag{3.32}$$

equation 3.30 is equivalent to

$$\frac{\partial h_o}{\partial \psi} - T \frac{\partial s}{\partial \psi} = \frac{1}{\rho} \frac{\partial p_o}{\partial \psi}\tag{3.33}$$

This substitution removes the entropy gradient term in equation 3.10 which in turbomachinery flows is inconvenient. The use instead of the total pressure gradient allows use of two-dimensional empirical correlations from which the amount of fluid turning and the total pressure loss across blade rows due to profile drag and secondary flows can be calculated. The values of stagnation enthalpy h_o , total pressure p_o , entropy s and tangential momentum rc_θ in inviscid flow are all conserved along streamlines until changed by external influences such as blade rows. Given initial profiles of total pressure p_o and tangential momentum rc_θ , the method will calculate all the downstream values.

3.8 Conclusion

The test cases have systematically examined the behaviour of the STFM, gradually including more of the source terms. A substitution for the turbomachinery test case was introduced replacing the $\frac{\partial h_o}{\partial \psi} - T \frac{\partial s}{\partial \psi}$ term with a $\frac{1}{\rho} \frac{\partial p_o}{\partial \psi}$ term, where p_o is affected by the Euler turbomachinery equation and loss correlations. No attempt was made to investigate compressible flows. The STFM has shown to yield accurate results for inviscid, incompressible flows determined by external boundaries alone, external boundaries and actuator disks and interference between actuator disks.

4 COMPRESSOR CASCADE NOMENCLATURE AND DEFINITIONS

4.1 Introduction

The correlations referred to in the previous chapter depend upon a thorough understanding of the compressor cascade nomenclature, definitions and derivations. Horlock (1958), Dixon (1978) and Cumpsty (1989) all give the derivation of the relevant compressor cascade equations, but for the sake of completeness and to assist the reader they are repeated here.

One assumption in the use of cascade correlations is that hub and casing boundary layers do not extend a great deal into the calculation domain which is regarded as inviscid. Furthermore, it is assumed that there is not a great radial variation in the flow properties being calculated, since the correlations were developed from two-dimensional flows. Where the blades being modelled do contain such a large variation, the flows are still calculable but the number of radial calculation stations must increase to decrease the differences between adjacent radial stations, making the region under examination at each radial station still at least approximately two-dimensional.

4.2 Cascade Nomenclature

In figure 4.1 the basic nomenclature of the compressor blade in cascade is illustrated. The blade surface coordinates result from a thickness distribution symmetrically "wrapped" around a curved camber line. The camber line is usually a circular or parabolic arc, defined by the maximum camber b at a distance a from the blade leading edge. The thickness distribution might be of a known family of blades, notably the British C-series, the NACA 65 series and the double circular arc (DCA), or else it may have been designed to a prescribed velocity distribution (PVD) also known as a supercritical profile. Figure 4.2 shows a comparison of the four profile types designed for the same nominal turning (Cumpsty, 1989).

The DCA blade is meant for the transonic regime and is completely described by the suction and pressure surface radii as well as the leading and trailing edge radii.

The NACA 65 series was not originally intended for cascade applications but for a low drag aircraft wing profile. This is borne out by its numbering convention: for a blade profile designated 65-(12)10, the number in brackets refers to the lift coefficient of the isolated aerofoil in tenths, i.e. $C_L = 1.2$. Figure 4.3 shows a relationship between the isolated aerofoil lift coefficient and the equivalent camber. The last two digits in the number give the maximum

thickness of the blade in hundredths of the chord. The "6" refers to the series and the "5" refers to the fraction in chord lengths for which the static pressure was to remain constant in tenths of the chord for the isolated aerofoil.

The C-series sections were calculated mathematically and then modified to give better performance in cascade (Cumpsty, 1989). The numbering convention of the C-series is analogous to the NACA series: For a blade profile numbered 10C4/30C50, 10 refers to the thickness-chord ratio in percent, C4 describes the thickness distribution, 30 is the camber angle in degrees, C refers to a circular arc camber line and 50 the percent chord at which the maximum camber occurs.

The leading and trailing edge points of a blade profile are the forward and rear intersections of the camber line with the outer surface of the blade. The blade chord l is the length of the chord line, which is the straight line joining the profile leading and trailing edge points. In figure 4.1 the camber line y and the thickness distribution t are shown as functions of the distance x along the chord l . Having described the individual blade, the cascade is completely described by the spacing of the blades and their setting angle. This setting angle is known as the stagger angle γ , being, in the case of a tuomachine, the angle between the chord line and the machine axis of rotation, and in the case of a cascade, the angle between the chord line and the line perpendicular to the cascade front. The blade spacing is denoted in British terminology as the pitch-chord ratio s/l , and in American terminology by its inverse, solidity ($\sigma = l/s$). The blade inlet and outlet angles are denoted by α'_1 and α'_2 . The camber angle θ is the change in angle of the camber line between inlet and outlet

$$\theta = \alpha'_1 - \alpha'_2 \quad 4.1$$

and is an indication of the loading of the blade. For circular arc camber lines the stagger angle is simply the mean of the inlet and outlet blade angles

$$\gamma = (\alpha'_1 + \alpha'_2)/2 \quad 4.2$$

For parabolic arc camber lines the relationship between α'_1 , α'_2 and γ depends on the location from the leading edge a of the maximum camber point, and is given by

$$\alpha'_1 = \gamma + \tan^{-1} \frac{b/l}{(a/l)^2}, \quad \alpha'_2 = \gamma - \tan^{-1} \frac{b/l}{(1-a/l)^2} \quad 4.3$$

The compressor analysed in this thesis is fitted with NACA 65 profiles on a circular arc camber line, so no more attention will be paid to parabolic arc camber lines. Three more angle definitions complete the cascade nomenclature: incidence, deviation and deflection. The incidence angle i is the difference between the air inlet angle α_1 and the blade inlet angle α'_1 :

$$i = \alpha_1 - \alpha'_1 \quad 4.4$$

The deviation angle δ is the difference between the air outlet angle α_2 and the blade outlet angle α'_2 :

$$\delta = \alpha_2 - \alpha'_2 \quad 4.5$$

The deflection angle ε is the difference between the entry and exit air angles:

$$\varepsilon = \alpha_1 - \alpha_2 \quad 4.6$$

4.3 Cascade Forces

Figure 4.4 illustrates flow through a cascade entering the control volume from the far upstream boundary at velocity c_1 at an angle α_1 and leaving the cascade at the far downstream boundary of the control volume at velocity c_2 at an angle α_2 . The side boundaries of the control volume are median streamlines. The flow is assumed to be steady and incompressible. The forces X and Y are exerted upon the fluid by unit depth of blade, and are exactly equal and opposite to the forces exerted by the fluid upon unit length of blade.

Applying continuity to a unit depth of span and assuming incompressibility, the axial velocity is constant through the cascade:

$$c_1 \cos \alpha_1 = c_2 \cos \alpha_2 = c_x \quad 4.7$$

The momentum equation applied in the x and y directions with constant axial velocity gives

$$X = (p_2 - p_1)s \quad 4.8$$

$$Y = \rho s c_x (c_{y1} - c_{y2}) \quad 4.9$$

or

$$Y = \rho s c_x^2 (\tan \alpha_1 - \tan \alpha_2) \quad 4.10$$

4.4 Cascade Losses

Total pressure losses are incurred as a real fluid passes through a cascade as a result of skin friction and other effects. From Bernoulli's equation we get

$$\begin{aligned} \frac{\Delta p_o}{\rho} &= \frac{p_1 - p_2}{\rho} + \frac{c_1^2 - c_2^2}{2} \\ &= \frac{p_1 - p_2}{\rho} + \frac{(c_{y1}^2 + c_x^2)}{2} - \frac{(c_{y2}^2 + c_x^2)}{2} \\ &= \frac{p_1 - p_2}{\rho} + \frac{(c_{y1}^2 - c_{y2}^2)}{2} \\ &= \frac{p_1 - p_2}{\rho} + \frac{1}{2} (c_{y1} + c_{y2})(c_{y1} - c_{y2}) \end{aligned} \quad 4.11$$

(If the flow is through a rotor row, the above derivation is not applicable, and use must be made of equation 3.29 to take Euler's pump equation into account. The derivation is nonetheless useful for describing the origin of loss coefficients). Substituting equations 4.8 and 4.9 into 4.11 yields

$$\frac{\Delta p_o}{\rho} = -\frac{X}{\rho s} + \frac{Y(c_{y1} + c_{y2})}{2\rho s c_x} \quad 4.12$$

Now

$$c_{y1} + c_{y2} = c_x (\tan \alpha_1 + \tan \alpha_2) \quad 4.13$$

Let

$$\tan \alpha_m = \frac{1}{2} (\tan \alpha_1 + \tan \alpha_2) \quad 4.14$$

Substitute equation 4.13 and 4.14 into 4.12 to obtain

$$\frac{\Delta p_o}{\rho} = \frac{1}{\rho s} (-X + Y \tan \alpha_m) \quad 4.15$$

Pressure losses are most often presented in dimensionless form. Two commonly used loss coefficients are

$$\zeta = \frac{\Delta p_o}{\frac{1}{2} \rho c_x^2} \quad 4.16$$

and

$$\bar{\omega} = \frac{\Delta p_o}{\frac{1}{2} \rho c_1^2} \quad 4.17$$

4.5 Lift and Drag

Figure 4.5 shows a single cascade blade with the lift and drag forces it exerts on the fluid. Define a mean velocity c_m as

$$c_m = \frac{c_x}{\cos \alpha_m} \quad 4.18$$

where α_m is defined by equation 4.14. A lift force L acts in a direction perpendicular to c_m along a unit depth of blade, and a drag force D similarly acts in a direction parallel to c_m . Experimental data presented in terms of lift and drag can be resolved in terms of axial and tangential forces. From figure 4.6 it can be seen that

$$L = X \sin \alpha_m + Y \cos \alpha_m \quad 4.19$$

$$D = Y \sin \alpha_m - X \cos \alpha_m \quad 4.20$$

On combining equation 4.15 and 4.20 we get

$$D = \cos \alpha_m (Y \tan \alpha_m - X) = s \Delta p_o \cos \alpha_m \quad 4.21$$

Rearranging equation 4.21 to solve for X and then substituting into 4.19 gives

$$\begin{aligned} L &= (Y \tan \alpha_m - s \Delta p_o) \sin \alpha_m + Y \cos \alpha_m \\ &= Y \sec \alpha_m - s \Delta p_o \sin \alpha_m \end{aligned} \quad 4.22$$

Inserting equation 4.10 into 4.22 yields

$$L = \rho s c_x^2 (\tan \alpha_1 - \tan \alpha_2) \sec \alpha_m - s \Delta p_o \sin \alpha_m \quad 4.23$$

Coefficients for lift and drag based on the chord l and the mean velocity c_m may now be introduced:

$$C_L = \frac{L}{\frac{1}{2} \rho c_m^2 l} \quad 4.24$$

$$C_D = \frac{D}{\frac{1}{2} \rho c_m^2 l} \quad 4.25$$

Considering equations 4.16, 4.17 and 4.21 alongside 4.25 we can write

$$C_D = \frac{s \Delta p_o \cos \alpha_m}{\frac{1}{2} \rho c_m^2 l} = \zeta \frac{s}{l} \cos^3 \alpha_m = \omega \frac{s}{l} \frac{\cos^3 \alpha_m}{\cos^2 \alpha_1} \quad 4.26$$

Substituting 4.23 into 4.24 results in

$$C_L = \frac{\rho s c_x^2 (\tan \alpha_1 - \tan \alpha_2) \sec \alpha_m - s \Delta p_o \sin \alpha_m}{\frac{1}{2} \rho c_m^2 l} \quad 4.27$$

Inserting 4.21 into 4.27 we obtain

$$C_L = 2 \frac{s}{l} \cos \alpha_m (\tan \alpha_1 - \tan \alpha_2) - C_D \tan \alpha_m \quad 4.28$$

Values of C_D are very much less than C_L within the normal range of operation of a cascade. In addition, since α_m is unlikely to exceed 60° , it is normal practice to drop the $C_D \tan \alpha_m$ term in equation 22. Within the STFM code, however, it was decided to retain the term as it would not be detrimental to calculate, and extreme flow conditions may well result necessitating a more accurate approach.

5 COMPRESSOR CASCADE CORRELATIONS

5.1 Introduction

As mentioned in the introduction to this thesis, in axisymmetric inviscid methods such as the MTFM and the SCM, the effects of blade rows are modelled by empirical two-dimensional cascade test correlations for fluid deflection and pressure loss dependent on blade loading and geometry. It is assumed that in axial compressors of high hub-tip ratio, radial velocities are small, justifying the two-dimensional approach. Endwall losses exceed the profile losses in the design regime (Cumpsty, 1989), and comprise annulus skin friction and secondary losses (three-dimensional flow losses). Near-wall viscous effects are taken into account by end wall boundary layer calculation procedures, displacement thicknesses at hub and casing boundaries, or by blockage factors (Davis and Millar, 1975). The effect of secondary flows is accounted for by correlation. This chapter will introduce different low speed cascade data sets and correlations for deviation, profile loss and endwall loss from the literature.

Reviews of compressor cascade correlations are given by Cumpsty (1989), Dixon (1978), Hirsch and Denton (1981) and Horlock (1958). There is a fair degree of overlap between Horlock (1958) and Dixon (1978), the former for many years having been the standard reference on axial flow compressors and the latter an introductory student textbook to all classes of turbomachinery, including relevant work that is more current and omitting outdated methods. Cumpsty (1989) does not attempt to be a design manual, but is very comprehensive in reviewing papers and reports on relevant work in many disciplines within the field. Hirsch and Denton (1981) edited the work carried out by Working Group 12 of the Propulsion and Energetics Panel (PEP) of the Advisory Group for Aerospace Research and Development (AGARD) of NATO, which reviewed all the loss, deviation and endwall correlations from the literature or from sources not subject to commercial or military restrictions, collected test cases and compared the predictive capability of the correlations.

Dixon (1978) presents two sets of compressor blade correlations: those of Lieblein (1959, 1965) and Howell (1942, 1945). Dixon gives only Lieblein's correlation for pressure loss at design point and at positive incidence angles in the low loss region, but in Lieblein (1965) correlations for design-point deviation and incidence are given. Howell's correlation allows for operation of the cascade at conditions noticeably removed from the design point. Generalised curves predict the blade profile drag and generalised fluid deflection for a given generalised blade incidence angle. Howell also adds two endwall loss correlations - one to account for secondary flow losses and one for annulus frictional losses.

As well as Howell's correlations, Horlock (1958) presents the correlation of Carter (1950) for "optimum" incidence and deviation (defined later), and the NACA 65 low speed cascade data (Herrig *et al.*, 1951) plotted by Mellor (1956). The same NACA 65 low speed cascade data is plotted by Felix (1957), but a different convention is used. Dixon (1978) also references the work of Herrig *et al.*, but refers to a later report (Herrig *et al.*, 1957), while Cumpsty (1989) refers to a later report still (Emery *et al.*, 1958). Cumpsty (1989) gives a review of the above correlations and data plots.

Hirsch and Denton (1981) present the loss correlations of Swan (1961), Monsarrat (1969), Jansen and Moffat (1967), Fottner (1979), Strinning (1977) and Koch and Smith (1976). The correlation of Monsarrat (1969) is only valid for the design case, although it includes the effects of tip clearance, secondary and endwall boundary layer losses to some degree by increasing the losses from midspan of the blade to hub and tip. The methods of Strinning (1977) and Koch and Smith (1976) are both intended only for design conditions. The method of Swan (1961), while ingenious, bases its off-design momentum-thickness parameter θ/l on a cubic expression of the inlet Mach number, and as the title of the paper suggests, appears to be meant for the high subsonic to transonic regime. The methods of Jansen and Moffat (1967) and Fottner (1979) are very similar, with Fottner (1979) introducing a blade thickness to chord ratio modification. At a t/l ratio of 0.1 the methods are practically identical. Both methods use the same off-design loss prediction procedure.

Concerning deviation prediction, Hirsch and Denton (1981) mention the National Gas Turbine Establishment (NGTE) correlation (otherwise known as Carter's rule), the NACA correlation (Lieblein's deviation correlation) and the USSR correlation. No discussion is given of the USSR correlation.

Hirsch and Denton (1981) and Cumpsty (1989) give reviews of endwall boundary layer methods, and Cumpsty (1989) gives a history of the development of spanwise mixing calculation in turbomachines. The incorporation of these methods was considered beyond the scope of this thesis.

Compressor blades are designed to have a turbulent boundary layer on the suction surface to allow deceleration of the flow without major separation (Cumpsty, 1989). At low Reynolds number, laminar separation bubbles are quite common near the leading edge, and the separated layer in most cases undergoes transition and reattaches almost immediately as a turbulent boundary layer. If the separation region grows to a significant portion of the blade chord, deviation and pressure loss increase markedly. These two effects work together to greatly reduce the pressure rise across a compressor stage in the low Reynolds number regime.

Many workers have reported the effect of Reynolds number variation on cascade performance, and the reader is referred to Cumpsty (1989) and Roberts (1975) for reviews on work done on cascades at low Reynolds numbers, some of which include turbulence level variation. Figure 5.1 (Lieblein, 1965) shows the combined effects of Reynolds number and turbulence on pressure loss for a range of compressor cascades, and figures 5.2 and 5.3 (Lawson, 1953) show the effects of Reynolds number on pressure loss and deviation for a 10C4/40PS40 blade cascade of solidity 1.333. Since the Rofanco compressor rotor blade chord Reynolds number at design point is 1.3×10^5 (Lewis, 1989), Reynolds number effects are expected to be significant and have to be accounted for.

Very few prediction methods seem to exist to account for compressor cascade flow in the low Reynolds number regime. In their comparison of the SCM and the MTFM, Davis and Millar (1975) compounded the off-design transonic loss correlations of Swan (1961) by a Reynolds number correction of the form

$$\bar{\omega} = \bar{\omega} \left[\frac{3 \times 10^5}{Re} \right]^a \quad 5.1$$

where $Re \leq 3 \times 10^5$, using figures 5.1 and 5.2 as justification. This correlation does not appear to have been validated for the combined effects of camber, solidity and turbulence intensity as the critical Reynolds number is held constant (as with Howell's method). The equation for the exponent a was not given, and may be dependant on a number of parameters. Roberts (1975) states that the only available prediction method generally known at the time of writing is the "power relation" of Howell (1942), which he dismisses as primitive. Hirsch and Denton (1981) quote only the work of Roberts (1975) for low Reynolds number effects in the chapter "Review of Loss and Deviation Prediction Methods" in the section dealing with axial compressors, PART II.

5.2 Howell's Correlations

Howell (1942, 1945) has laid much of the basis of compressor cascade work, at design and off-design conditions. In this section three sets of correlations are presented; correlations for the nominal condition (design point) deviation and incidence, off-design loss and deflection and endwall losses.

5.2.1 Howell's Nominal Condition

Howell (1942) defined nominal conditions of cascade operation as those pertaining to a cascade deflection which is 80% of its maximum stalling deflection ϵ_s , (see figure 5.4). Howell found that the nominal deflection ϵ^* of various cascades are a function of the nominal outlet air angle α_2^* , space-chord ratio s/l and the Reynolds number Re

$$\epsilon^* = f(s/l, \alpha_2^*, Re) \quad 5.2$$

This correlation is independent of camber within its normal range of choice ($20^\circ < \theta < 40^\circ$) (Dixon (1978)). The correlation, based on C-Series profiles, is shown in figure 5.5 as a function of α_2^* and s/l , as dependence on Reynolds number is small for $Re > 3 \times 10^5$. This is borne out by Howell's original graphs: figure 5.5 originated from figures 5.6 and 5.7, while figure 5.8 shows the low-Reynolds number deflection behaviour as an s-shaped curve with values of

$$\Phi = \frac{\epsilon^*}{\epsilon_{Re=3 \times 10^5}^*} \quad 5.3$$

varying from 0.84 at $Re = 1 \times 10^5$ to 1.0 at $Re = 3 \times 10^5$.

To obtain the value of α_2^* , it is first necessary to obtain the nominal deviation δ^* , which is the deviation the flow experiences at the nominal condition explained above, since

$$\alpha_2^* = \alpha_2' + \delta^* \quad 5.4$$

Howell used an empirical deviation rule by Constant (1939) relating deviation to camber θ and space-chord ratio s/l :

$$\delta^* = m\theta(s/l)^n \quad 5.5$$

where $n = \frac{1}{2}$ for compressor cascades and $n = 1$ for inlet guide vanes. Constant originally suggested $m = 0.26$, but Howell modified m to allow it to vary with α_2^*

$$m = 0.23 \left(2 \frac{a}{l} \right)^2 + \frac{\alpha_2^*}{500} \quad 5.6$$

where a/l is the fraction of chord from the leading edge to the point at which maximum camber occurs (see figure 4.1). For inlet guide vanes, the flow is accelerated as in turbine passages and

$$m = 0.19 \quad 5.7$$

From equations 5.4, 5.5 and 5.6, for a circular arc camber line compressor cascade, $\left(2 \frac{a}{l} \right)^2$ reduces to 1, and:

$$\begin{aligned} \delta^* &= \left[0.23 + \frac{\alpha_2^*}{500} \right] \theta \sqrt{\frac{s}{l}} \\ &= \left[0.23 + \frac{(\alpha_2' + \delta^*)}{500} \right] \theta \sqrt{\frac{s}{l}} \\ \therefore \frac{\delta^*}{\theta \sqrt{\frac{s}{l}}} &= \left[0.23 + \frac{(\alpha_2' + \delta^*)}{500} \right] \\ \therefore \frac{\delta^*}{\frac{\theta}{500} \sqrt{\frac{s}{l}}} &= [500 \times 0.23 + \alpha_2' + \delta^*] \\ \therefore \delta^* \left(\frac{1}{\frac{\theta}{500} \sqrt{\frac{s}{l}}} - 1 \right) &= [500 \times 0.23 + \alpha_2'] \\ \therefore \delta^* &= \frac{[500 \times 0.23 + \alpha_2']}{\left(\frac{1}{\frac{\theta}{500} \sqrt{\frac{s}{l}}} - 1 \right)} \quad 5.8 \end{aligned}$$

Having obtained α_2^* from equations 5.4 and 5.8, ϵ^* may be obtained from figure 5.5. Equation 4.6

$$\epsilon = \alpha_1 - \alpha_2 \quad 4.6$$

allows α_1^* to be calculated, and the design incidence i^* follows from equation 4.4:

$$i^* = \alpha_1^* - \alpha'_1 \quad 5.9$$

5.2.2 Howell's Off-design Correlation

The off-design deflection and pressure loss may now be calculated from the generalised curves shown in figure 5.9 as a function of i , since i^* and ϵ^* are already known, and the ordinate $(i - i^*)/\epsilon^*$ can be calculated. The effect of Reynolds number is included by adding 0.007 to the value of C_D obtained in figure 5.9 for flows at $Re < 1 \times 10^5$. For flows at Reynolds numbers between 1×10^5 and 3×10^5 linear interpolation can be used. Low-Reynolds number deflection has been dealt with in the previous section.

All the Reynolds numbers referred to in Howell's methods are *effective* Reynolds numbers Re_{eff} , where test Reynolds numbers are multiplied by a turbulence factor TF to obtain the equivalent Reynolds number where similar results would be obtained in a turbulence-free tunnel (Howell, 1942). Modern trends are to correlate turbulence intensity Tu and Reynolds number independently instead of together in an effective Reynolds number.

5.2.3 Howell's Endwall Loss Correlations

Howell (1945) assumed that two distinct sources combined to produce endwall loss, being frictional drag from the annulus wall and secondary loss, and correlated both by means of drag coefficients. The annulus loss drag coefficient scales on the blade spacing to height ratio

$$C_{D_a} = 0.20 \frac{s}{H} \quad 5.10$$

Cumpsty (1989) states that Howell derived the secondary loss by analogy with the trailing vortex loss behind aircraft. Additional incidence would be induced over the whole span of

a blade as a result of trailing vortices shed by the blades due to circulation variation along the length. Secondary loss was therefore believed to be linked to the reduction in blade circulation in the blade end region and represented by

$$C_{D_s} = 0.018(C_L)^2 \quad 5.11$$

where C_L is the blade lift coefficient outside the endwall region. The loss over a blade row is then obtained by summation

$$\begin{aligned} C_D &= C_{D_p} + C_{D_a} + C_{D_s} \\ &= C_{D_p} + 0.02 \frac{s}{H} + 0.018(C_L)^2 \end{aligned} \quad 5.12$$

where C_{D_p} is the profile loss drag coefficient. Howell (1945) gives an illustration of the relative magnitudes of the different loss sources as they vary with stage flow coefficient in figure 5.10.

5.3 Carter's Deviation Rule

Carter produced correlations which, unlike Howell, include the effect of camber (Horlock, 1958). An "optimum" condition of incidence and deflection is defined, being the point of maximum lift-drag ratio. Figure 5.11 shows lines of constant L/D on a graph of deflection ϵ against outlet angle α_2 for cascades at a space-chord ratio of 1.0. Also included in the figure is a stall line (twice minimum drag), a nominal line and an optimum line. Similar figures can be drawn for other space-chord ratios.

For a detailed explanation of the workings of Carter's correlation the reader is advised to consult Horlock (1958). Of interest here, however, is Carter's modification to Constant's deviation rule. The constant m is related to stagger γ for cascades with circular and parabolic arc camber lines. Figure 5.12 shows the variation of m with γ .

Horlock (1958) also refers to, but does not supply, an off-design deflection curve of Carter similar in nature to that of Howell, linking $(\epsilon - \epsilon_{opt})/(i_s - i_{opt})$ to $(i - i_{opt})/(i_s - i_{opt})$ where i_s is the stalling incidence and i_{opt} is the optimum incidence. No off-design loss curve is mentioned, however.

5.4 Lieblein's Loss Correlation

Dixon (1978) states that the correlation of Lieblein (1959, 1965) is based on an experimental observation: A large amount of velocity diffusion on blade surfaces tends to produce thick boundary layers and eventually separation. Conventional compressor blade suction surface boundary layers are considerably larger than the pressure surface boundary layers, and as a result dominate the compressor blade wake formation. The growth of the boundary layer on the suction surface is controlled by the diffusion in velocity on the suction surface of the blade. Lieblein's hypothesis therefore is that the total pressure loss can be correlated by the suction surface velocity distribution in the region of minimum loss.

A typical compressor cascade blade velocity distribution where the blade is operating in the minimum loss region is shown in figure 5.13. The ratio of maximum suction surface velocity to outlet velocity, $c_{\max,s}/c_2$, can be used as an expression of the diffusion in velocity. The wake momentum thickness to chord ratio θ_2/l for NACA 65 and C4 circular arc camber line blades at the reference incidence (mid-point of working range) was found by Lieblein to be correlated by $c_{\max,s}/c_2$. The wake momentum thickness is defined as

$$\theta_2 = \int_{-\delta_p}^{\delta_s} \frac{v}{V} \left(1 - \frac{v}{V} \right) dy \quad 5.13$$

where δ_s and δ_p are the suction and pressure surface boundary layer thickness, V is the freestream velocity and v is the velocity at distance y above the wake centreline. These parameters are illustrated in figure 5.14. This correlation between θ_2/l and $c_{\max,s}/c_2$ is considered to be fitted by the equation

$$\frac{\theta_2}{l} = \frac{0.004}{\left\{ 1 - 1.17 \ln \left(\frac{c_{\max,s}}{c_2} \right) \right\}} \quad 5.14$$

As θ_2/l tends to infinity, the diffusion ratio $c_{\max,s}/c_2$ tends to an upper limit of 2.35. Efficient operation confines the practical upper bound of diffusion ratio to a value between 1.9 and 2.0. From chapter 4, losses can be presented as drag coefficient C_D or as either of the two total pressure loss coefficients,

$$\zeta = \frac{\Delta p_o}{\frac{1}{2} \rho c_x^2} \quad 4.16$$

and

$$\bar{\omega} = \frac{\Delta p_o}{\frac{1}{2} \rho c_1^2} \quad 4.17$$

Lieblein and Roudebush (1956) have shown a simplified relationship between θ_2/l and total pressure coefficient, valid for unstalled blades,

$$\bar{\omega} = 2 \left(\frac{\theta_2}{l} \right) \left(\frac{l}{s} \right) \frac{\cos^2 \alpha_1}{\cos^3 \alpha_2} \quad 5.15$$

Substituting equation 5.15 into 4.26,

$$C_D = \bar{\omega} \left(\frac{s}{l} \right) \frac{\cos^3 \alpha_m}{\cos^2 \alpha_1} = 2 \left(\frac{\theta_2}{l} \right) \left(\frac{\cos \alpha_m}{\cos \alpha_2} \right)^3 = \zeta \left(\frac{s}{l} \right) \cos^3 \alpha_m \quad 5.16$$

Since values of $c_{\max,s}/c_2$ will not be known without detailed cascade data or flowfield calculation results, an equivalent diffusion ratio D_{eq} has been correlated for NACA 65 and C4 blades from inlet and outlet cascade conditions:

$$D_{eq} = \frac{c_{\max,s}}{c_2} = \frac{\cos \alpha_2}{\cos \alpha_1} \left\{ 1.12 + 0.61 \left(\frac{s}{l} \right) \cos^2 \alpha_1 (\tan \alpha_1 - \tan \alpha_2) \right\} \quad 5.17$$

At incidence angles greater than the reference incidence i_{ref} (either mid-point of working range or position of minimum loss) Lieblein extended the above correlation to

$$D_{eq} = \frac{\cos \alpha_2}{\cos \alpha_1} \left\{ 1.12 + k(i - i_{ref})^{1.43} + 0.61 \left(\frac{s}{l} \right) \cos^2 \alpha_1 (\tan \alpha_1 - \tan \alpha_2) \right\} \quad 5.18$$

where $k = 0.0117$ for NACA 65 blades and $k = 0.007$ for C4 blades on a circular arc camber line.

Lieblein (1965) also developed a complicated but accurate method of determining the minimum-loss incidence angle i_{ref} and deviation angle δ as a function of solidity σ , maximum blade thickness-chord ratio, thickness distribution (profile), air inlet angle α_1 and camber θ . No off-design deflection calculation method is given, however.

5.5 Jansen and Moffat Loss Correlation

In the correlation of Jansen and Moffat (1967) it is the design diffusion factor incorporating streamline radial shift which is the parameter determining design loss $\bar{\omega}$:

$$D = 1 - \frac{V_1}{V_2} + \frac{r_1 V_{\theta 1} - r_2 V_{\theta 2}}{(r_1 + r_2) V_1 \sigma} \quad 5.19$$

The wake momentum thickness to chord ratio θ/l is linked to the design diffusion factor D by the expression

$$\left(\frac{\theta}{l}\right)^* = 0.003 + 0.02375D - 0.05D^2 + 0.125D^3 \quad 5.20$$

In Hirsch and Denton's (1981) review of Jansen and Moffat (1967), Lieblein's loss expression is then used

$$\bar{\omega} = 2 \left(\frac{\theta}{l}\right) \left(\frac{l}{s}\right) \frac{\cos^2 \alpha_1}{\cos^3 \alpha_2} \quad 5.15$$

Jansen and Moffat (1967) originally used a simplification in their paper of

$$\bar{\omega} = \frac{2\sigma}{\cos^{\alpha_2^*}} \left(\frac{\theta}{l}\right)^* \quad 5.21$$

The method of Wiggins (1963) is used to account for Mach number effects and incidence effects at off-design:

5.5.1 Inlet angles for design, choke and surge

If the inlet Mach number exceeds 0.7, the inlet flow angles are corrected by the following equations

$$\begin{aligned}\beta_{1s}^* &= \beta_{1s} \\ \beta_{1c}^* &= \beta_{1c} + 1.5\Delta\beta \\ \beta_{1s}^* &= \beta_1^* + \Delta\beta\end{aligned}\quad 5.22$$

where s represents surge, c represents choke, $*$ indicates a corrected value and $\Delta\beta$ is given by

$$\Delta\beta = 10M_1 - 7 \quad 5.23$$

5.5.2 Supercritical Mach Number

If the inlet Mach number exceeds its critical value, the design loss coefficient is corrected by

$$\bar{\omega}^{**} = \bar{\omega}^* [2(M_1 - M_{1cr}) + 1] \quad 5.24$$

5.5.3 Off-design Loss

A parabolic variation of loss with incidence is assumed for off-design operation, with choke or surge being achieved at twice the minimum value:

$$\bar{\omega} = \bar{\omega}^{**} (0.8333\bar{S}^2 + 0.1667\bar{S} + 1.0) \quad 5.25$$

where \bar{S} is defined as

$$\begin{aligned}\beta_1 < \beta_1^* & \quad \bar{S} = \frac{\beta_1 - \beta_1^*}{\beta_{1c} - \beta_1^*} \\ \beta_1 > \beta_1^* & \quad \bar{S} = \frac{\beta_1 - \beta_1^*}{\beta_{1s} - \beta_1^*}\end{aligned}\quad 5.26$$

5.6 NACA Cascade Data

Herrig *et al.* (1951) systematically tested the NACA 65 family of profiles (65-0-10 to 65-(27)10) from positive to negative stall and solidities from 0.5 to 1.5 at low speed. The data has been summarised respectively by Mellor (1956) and Felix (1957).

In the case of Mellor the data was plotted in the form of graphs of α_2 against α_1 , as a mesh of intersecting lines of constant stagger and lines of constant angle of attack ($\alpha_1 - \gamma$). Each separate graph displays data for a different camber θ and solidity σ combination. The work of Mellor was never published but the complete set of diagrams is shown in Horlock (1958). No information concerning pressure loss is given other than the positive and negative stall lines which bracket each block of results. Mellor defined stall as when the drag coefficient increased by 50% above the minimum value.

Felix (1957) presented the data in the form of "carpet plots" of deflection ϵ as a mesh of intersecting lines of constant air inlet angle α_1 and lines of constant angle of attack. As with the work of Mellor, separate graphs display data for different camber θ and solidity σ combinations. Pressure loss information was not given explicitly, but by inspection of the constant α_1 lines the values of ϵ often form clear maxima and then decrease at high values of angle of attack ($\alpha_1 - \gamma$), indicating blade stall and post-stall conditions.

Herrig *et al.* (1951) give "design points" for each cascade which represent the angle of attack at which the smoothest pressure distribution is observed on the blade surfaces. Figure 5.15 shows that the curves of design angle of attack ($\alpha_1 - \gamma$) against solidity σ and camber θ to be consistent despite the subjective nature of their definition (Horlock, 1958).

5.7 The Correlation of Roberts for Reynolds Number and Turbulence Effects

Roberts (1975) performed several low-speed cascade test series on 3 NACA 65-Series profiles in cascade where in each series the blade chord Reynolds number Re_c was varied in steps from ~250 000 down to ~40 000 by varying the tunnel speed and blade chord. The three profiles were NACA 65-4(A_{10})10, NACA 65-12(A_{10})10 and NACA 65-18(A_{10})10, representing camber angles of 10°, 30° and 45° respectively. The tests were performed at a constant inlet air angle α_1 of 60° and at a s/l ratio of 1.2, except for one series of tests on the NACA 65-18(A_{10})10 profile done at a s/l ratio of 0.55. The blade stagger angle γ for the NACA 65-4(A_{10})10 and NACA 65-12(A_{10})10 profiles was varied between positive and negative stall to give a wide range of data at various blade loadings, while for the NACA 65-18(A_{10})10 profile tests were performed at a single γ , chosen near the minimum loss point for each of the two s/l ratios. Roberts displays his results graphically.

In addition to his own results, Roberts displays graphical results for cascade tests at varying Reynolds numbers from Schlichting and Das (1970) and Erwin *et al* (1956). These data sets

comprise cascade tests done on a NACA 65-6(A_{10})10 (15° camber) cascade with α_1 of 50° and NACA 65-12(A_{10})10 (30° camber) cascade with α_1 of 60° respectively. Each of the two sets were performed at a single stagger angle and a s/l ratio of 1.0.

Roberts (1975) modified a semiempirical theory of Horton (1969) for predicting the behaviour of the shear layer across a laminar separation bubble. The method can be used to predict the length of the laminar bubble, the Reynolds number below which a short laminar bubble "bursts" into a long laminar bubble and the development of the shear layer in the separated region. Combined with a boundary layer method the losses of compressor and turbine cascades where separation bubbles are present can be predicted, and Roberts obtained good agreement with experimental compressor cascade results.

For Reynolds numbers below "bursting" the semiempirical theory does not apply, so Roberts developed a wholly empirical correlation to calculate compressor cascade performance in the subbursting regime. The correlation was derived from the data Roberts obtained in the low Reynolds number cascade tests. The empirical correlations were of the form

$$\bar{\omega}_{1_{SB}} = K_1(\hat{\theta}f\hat{s})\Delta RX + \bar{\omega}_{1_B} \quad 5.27$$

$$\epsilon_{SB} = \epsilon_B - K_2\theta(s/l)\Delta RX \quad 5.28$$

where

$$\begin{aligned} \Delta RX &= \left[\frac{Re_{\theta_s^*}}{(S/l)_S} \right]_{SB} - \left[\frac{Re_{\theta_s^*}}{(S/l)_S} \right]_B \\ \hat{\theta} &= \theta/\theta_{ref}, \quad \theta_{ref} = 10^\circ \\ f &= (t/l)/(t/l)_{ref}, \quad (t/l)_{ref} = 0.1 \\ \hat{s} &= (s/l)/(s/l)_{ref}, \quad (s/l)_{ref} = 1.0 \end{aligned} \quad 5.29$$

and θ_s^* is the separation momentum thickness, $(S/l)_S$ is the fraction of chord at which separation occurs, B refers to bursting, i.e. $Re_c = Re_{c_B}$, and SB refers to subbursting, i.e. $Re_c < Re_{c_B}$.

In addition, Roberts developed a correlation for the bursting blade chord Reynolds number

$$Re_{\tau\theta} = \left[\frac{(D + 0.4)}{7.5\sqrt{TF}} \right] \times 10^5 + 10000 \quad 5.30$$

as a function of the NACA diffusion factor

$$D = 1 - \frac{V_1}{V_2} + \frac{\Delta V_\theta}{2\sigma V_1} \quad 5.31$$

and Taylor's turbulence factor

$$TF = Tu \left(\frac{l}{L_x} \right)^{\frac{1}{3}} \quad 5.32$$

where

$$Tu = \frac{\sqrt{\overline{u'^2}}}{V_1} \quad 5.33$$

$$L_x = \int_0^{x_p} \frac{\overline{u'_1 u'_2}}{\sqrt{\overline{u'^2_1}} \sqrt{\overline{u'^2_2}}} d(X_p) \quad 5.34$$

If TF is not available then Tu can be used as an approximation. No bursting takes place at values of D below 0.14.

5.8 Comparison and Discussion

Cumpsty (1989) gives a substantive review of the correlations mentioned in the sections above in terms of incidence, deviation and loss.

Concerning reference incidence (variously called nominal, optimum, design and minimum-loss by Howell (1945), Carter (1950), Emery *et al.* (1958) and Lieblein (1960, 1965) respectively), Cumpsty comments on the philosophies of the different approaches and concludes that very similar predictions are obtained by using the different approaches for moderate to high camber blades, but for low camber blades Carter's predictions diverge from those of the other methods. Carter's method predicts the incidence to give the highest lift-drag ratio for a given camber, but for a given flow deflection the lift-drag ratio is not the highest and is regarded by Cumpsty to be the incorrect approach.

Of the deviation correlations, Cumpsty comments only on the prediction methods of Carter and Lieblein, but not on Howell's correlation. As Howell's method is a precursor to Carter's rule, the comments on the latter are regarded as applicable on the former. Although Carter's method was intended for use at "optimum incidence" and Lieblein's method for minimum-loss incidence, as has been pointed out these incidences are quite close together. In addition Cumpsty remarks that deviation is quite a weak function of incidence until stalling incidence is approached. Carter's method is the simpler of the two but Lieblein's is more accurate and reliable, being based on the NACA data at constant axial velocity. Carter's rule typically predicts between about 1° and 2° less deviation than Lieblein's correlation. Carter's rule was based on data from British cascades in which the axial velocity-density ratio

$$AVDR = \frac{\rho_2 c_{x2}}{\rho_1 c_{x1}} \quad 5.35$$

was not held at unity but typically varied between 1.1 and 1.2 (Gostelow, 1984). The NACA data, upon which Lieblein's correlation is based, had been obtained with careful attention being paid to maintaining $AVDR$ at 1.0. Cumpsty quotes Felix and Emery (1953) as writing that up to 3° more turning (or 3° less deviation) can be attributed to the fact that British tests were performed at $AVDR > 1$. A number of correlations exist in the literature for taking $AVDR$ variations into account.

Pollard and Gostelow (1967) developed the following expression for a cascade of 10C4/30C50 blades set at a stagger of 36°, a space-chord ratio of 0.875 and a nominal air inlet angle of 52°50′:

$$\delta = \delta_0 - 10(AVDR - 1) \quad 5.36$$

where δ_0 is the deviation at $AVDR = 1.0$. Cumpsty (1989) disputes the universality of this rule, and presents similar expressions with different coefficients for two calculated cascades:

$$\delta = \delta_0 - 8(AVDR - 1) \quad 5.37$$

for a cascade of 40° camber and 15° stagger, and

$$\delta = \delta_0 - 20(AVDR - 1) \quad 5.38$$

for a cascade of 20° camber and 45° stagger. Both cascades were of C4 blades at $\sigma = 1.0$, 10% thickness and zero incidence.

Jansen and Moffat (1967) quote the work of Pollard and Horlock (1962) and Kubota (1959) for correcting techniques, and then present their own method, similar to that of Kubota (1959), more suitable for rotating cascades. Gostelow (1984) mentions the work of Pollard and Horlock (1962) as well as two equations of Schultze *et al* (1957), and then compares the predictions of the two methods to the experimental results upon which Pollard and Gostelow (1967) based their correlation (equation 5.36). Gostelow (1984) also supplies a figure showing the variation of effect of *AVDR* on deviation, loss and pressure coefficient with incidence angle using data from Liverpool University and German sources (figure 5.16). Stagger angle γ is noted to be a very significant variable, and high incidence angles on high stagger blades such as compressor rotors effect deviation angle markedly. From the above it can be concluded that *AVDR* effects are significant, although at the time of writing (1989) Cumpsty stated that there was no comparably accurate method for introducing the effects of *AVDR* $\neq 1.0$.

Comparing Howell's and Carter's correlations, Horlock (1958) comments that Carter's curves of optimum deflection against α_2 are close to Howell's nominal deflection for $Re_{eff} = 3 \times 10^5$, but at lower effective Reynolds numbers the optimum deflections of Carter may be closer to the stalling deflections.

Gettliffe (1992) used Lieblein's correlation for loss and Howell's correlation for nominal deviation in his analysis of the Rofanco compressor using the STFM. Despite the absence of inlet guide vanes for which the blading was designed, he decided that due to the high reaction of 80%, the blades would be operating at or very near to the design point for the design flow rate. In the light of Cumpsty's remarks concerning variation of deviation with incidence this approach appears to have been justified.

For the present analysis, off-design flows (a near-surge flowrate and a near-choke flowrate) will be analysed as well as a design flowrate. Of the reviewed loss correlations, only those of Howell and Jansen and Moffat (1967) provide off-design capabilities, since Lieblein's loss correlation is only valid in the low-loss region. For the sake of consistency it was decided to make use of the generalised off-design correlation curves of Howell. NACA 65-Series data would be used to check for predictive errors as a result of exceeding camber range (greater than 40° and less than 20°, Dixon, 1978), profile change (NACA 65 and not C-series), and *AVDR*, and correction factors would be developed.

For the low Reynolds number regime the correlations of Howell (1942) and Davis and Millar (1975) appear too simplistic. Neither the semi-empirical correlation nor the empirical correlation of Roberts (1975) are useful in a method such as the STFM since the blade velocity distribution and a boundary layer method are required. Since Roberts provides the data from which the correlation was derived in graphical format, however, it is possible to create correlations of loss and turning versus the difference in bursting and subbursting blade chord Reynolds numbers

$$\Delta Re_c = Re_{c_B} - Re_{c_{SB}} \quad 5.39$$

in the same manner as Roberts' empirical correlation. From section 5.7 it can be seen that Roberts had based his original correlation on the difference in bursting and subbursting separation momentum thickness Reynolds number to separation position blade chord fraction ratios

$$\Delta RX = \left[\frac{Re_{\theta_s^*}}{(S/l)_S} \right]_{SB} - \left[\frac{Re_{\theta_s^*}}{(S/l)_S} \right]_B \quad 5.29$$

6 CASCADE CORRELATION DEVELOPMENT

6.1 Howell's correlations: curve fits

Figure 5.5 shows Howell's correlation for nominal fluid deflection versus fluid outlet angle. Two approximating formulae for this relation are mentioned by Dixon (1978): the tangent-difference rule, quoted by Howell

$$\tan \alpha_2^* - \tan \alpha_1^* = \frac{1.55}{1 + 1.5s/l} \quad 6.1$$

for the range $0 \leq \alpha_2^* \leq 40^\circ$ and a linear approximation for student use

$$\varepsilon^* = (16 - 0.2\alpha_2^*)(3 - s/l)^\circ \quad 6.2$$

These two approximating formulae are shown plotted in figure 6.1, as well as isolated data points digitised from Howell's graph in figure 5.5. Although useful as simple approximations, they were considered to be too inaccurate for the purpose at hand. A polynomial curve fit through the Howell data points was obtained to remove range and inaccuracy problems and is also plotted in the figure. The fit can be seen to be very good, with a correlation coefficient of 0.999 775. The equation for the polynomial fit is

$$\begin{aligned} \varepsilon^* = & 54.668880 - 0.795123 \alpha_2^* + 0.00261660 \alpha_2^{*2} \\ & - 26.0804 \frac{s}{l} + 5.09697 \left(\frac{s}{l} \right)^2 + 0.254166 \alpha_2^* \frac{s}{l} \\ & - 0.000554660 \left(\alpha_2^* \frac{s}{l} \right)^2 \end{aligned} \quad 6.3$$

A polynomial was fitted through the relative deflection data points in figure 5.9. Figure 6.2 shows the relative deflection data and approximating curves. The correlation coefficient of the polynomial is 0.990 918. Since at values of non-dimensionalised incidence $\hat{i} = (i - i^*)/\varepsilon^*$ below -0.6 the polynomial values start dropping considerably below those of the linear approximation that Howell (1942) gives, it was decided to use the linear approximation for $\hat{i} < 0$, and the polynomial for $\hat{i} \geq 0$:

$$\begin{aligned}
 \hat{i} < 0 & \quad \frac{\epsilon}{\epsilon^*} = 1.0 + \hat{i} \\
 \hat{i} \geq 0 & \quad \frac{\epsilon}{\epsilon^*} = 0.994648 + 0.879105 \hat{i} - 0.235132 \hat{i}^2 \\
 & \quad - 0.958304 \hat{i}^3 - 1.01317 \hat{i}^4 + 0.687731 \hat{i}^5 \quad 6.4
 \end{aligned}$$

A polynomial with 2 variables, \hat{i} and s/l , was fitted to data points taken from the profile drag coefficient curves in figure 5.9. The resultant fit in figure 6.3 can be seen to be good, and the correlation coefficient is 0.997 324. The polynomial is given by

$$\begin{aligned}
 C_D = & 0.0244835 - 0.0253888 \hat{i} + 0.0304050 \hat{i}^2 \\
 & + 0.019518 \hat{i}^3 + 0.0931483 \hat{i}^4 + 0.446040 \hat{i}^5 \\
 & + 0.508065 \hat{i}^6 - 0.00809064 \frac{s}{l} + 0.0137634 \hat{i} \frac{s}{l} \\
 & + 0.0229892 \hat{i} \left(\frac{s}{l} \right)^2 - 0.0125055 \hat{i} \left(\frac{s}{l} \right)^3 \quad 6.5
 \end{aligned}$$

6.2 NACA 65 Data Comparison

Seeing that Carter's deviation rule (figure 5.14) was developed subsequent to Howell's deviation rule

$$m = 0.23 \left(2 \frac{a}{l} \right)^2 + \frac{\alpha_2^*}{500} \quad 5.5$$

it was logical to compare the effects of the two rules to see if either was to be preferred before applying correction factors to one of them. Firstly, the NACA 65 data as "carpet plotted" by Felix (1957) was digitised and typed into a spreadsheet. A polynomial was fitted through Carter's curve for m for a circular arc camber line for values of stagger angle γ between 0° and 70° , obtained from Robbins *et al* (1965), and is shown in figure 6.4. The polynomial fitting the data is a simple quadratic equation, being

$$m = 0.215188 + 0.000969877 \gamma + 2.4512 \times 10^{-5} \gamma^2 \quad 6.6$$

Then the values of m from the two rules for a circular arc camber line were compared as a function of γ for all the cascades in the database. The results are shown in figure 6.5. The two correlations exhibit the same trends and approximate values, with Howell's correlation showing a fair amount of scatter in the midrange, generally predicting more deviation than Carter's rule. For values of γ greater than 45° and less than 5° , Carter predicts more deviation, although Carter's values for γ less than 0° are extrapolations. It is to be expected that Carter's rule would be more accurate, having been developed later, but Howell's nominal condition correlation relating ϵ^* to α_2^* and s/l was based on Howell's deviation correlation.

To make a meaningful decision regarding which of the two correlations to use as a basis for development, the NACA 65 database was non-dimensionalised to $\hat{\epsilon} = \epsilon/\epsilon^*$ as a function of $\hat{i} = (i - i^*)/\epsilon^*$, where ϵ^* was obtained from Howell's and Carter's deviation rules respectively, using Howell's nominal condition correlation. The results are shown in figures 6.6 and 6.7. Each dotted line curve represents a series of tests performed at constant inlet air angle α_1 and solidity σ , with stagger angle γ varied. Plotted on the same system of axes on both graphs was Howell's off-design deflection correlation. The two graphs can be seen to be very similar. Since neither of the two graphs stood out clearly as better collapsed onto Howell's off-design curve, it was decided to use Howell's deviation rule for the sake of consistency.

6.3 Correction Factor Correlation

The data in figure 6.6 does not collapse very well onto Howell's off-design curve. The difference between the NACA point values and Howell's predictions are quantified by an average error in $\hat{\epsilon}$ of 0.018 196 and a standard deviation of the error of 0.116 902. Two constants, C_1 and C_2 , were introduced to move the stall point of each of the NACA data lines to Howell's stall point of $\hat{i} = 0.4$ and $\hat{\epsilon} = 1.25$. The philosophy behind this approach was that if the data could be made to collapse on Howell's line by correlation, then by starting with Howell's curve the NACA data could be reproduced by applying the correlation in reverse. The values of ϵ^* were adjusted by

$$\epsilon_{adj}^* = C_1 \epsilon^* \quad 6.7$$

resulting in i^* becoming i_{adj}^* from equations 4.4 and 4.6

$$i_{adj}^* = \epsilon_{adj}^* + \alpha_2^* - \alpha_1' \quad 6.8$$

and \hat{i} becoming \hat{i}_{adj}

$$\hat{i}_{adj} = (i_{data} - i_{adj}^*) / \epsilon_{adj}^* \quad 6.9$$

Values of C_1 were chosen so that the \hat{i}_{adj} values of the stall points would be 0.4. The C_1 values found in this manner were then correlated by the expression

$$C_1 = 0.720467 - 0.154903 \sigma - 0.00446029 \alpha_1 \\ + 0.00459836 \theta + 0.000152596 \alpha_1^2 \quad 6.10$$

with a correlation constant of 0.946 775. The values of $\hat{\epsilon} = \epsilon_{data} / \epsilon_{adj}^*$ were adjusted by

$$\hat{\epsilon}_{adj} = \frac{\epsilon_{data}}{C_2 \times \epsilon_{adj}^*} \quad 6.11$$

choosing values of C_2 which lined up the $\hat{\epsilon}_{adj}$ points at stall to 1.25. The C_2 values were less easy to correlate, requiring more terms and yielding a lower correlation constant of 0.922 307:

$$C_2 = 0.410688 - 1.06448 \sigma - 0.00505307 \alpha_1 \\ + 0.00292760 \theta - 0.379925 \sigma^2 + 0.00048433 \theta \alpha_1 \\ - 4.19067 \times 10^{-6} \theta \alpha_1^2 + 0.0150439 \theta \sigma + 0.00511456 \theta \sigma^2 \quad 6.12$$

The NACA data was adjusted using the correlations of C_1 and C_2 , and the result is shown in figure 6.8. The spread of data has narrowed noticeably, with the average error in $\hat{\epsilon}$ dropping to 0.010 241 and the standard deviation of the error to 0.073 736. Unfortunately the adjusted NACA data still diverges as \hat{i}_{adj} decreases from the stall point value of 0.4.

A third constant, M , was then introduced to adjust the gradient of the NACA data lines to converge to the off-design correlation of Howell:

$$M = \frac{\hat{\epsilon}_{adj} - \hat{\epsilon}_{Howell}}{\hat{i} - 0.4} \quad 6.13$$

for values of $\hat{\varepsilon}_{adj}$ where $\hat{i}_{adj} < 0.4$. Correlating M proved to be the least straightforward. Success was ultimately only achieved by dividing the data into two ranges, $30^\circ \leq \alpha_1 \leq 50^\circ$ and $50^\circ < \alpha_1 \leq 70^\circ$:

$$\begin{aligned} \hat{\alpha}_1 \leq \frac{50}{30} & & M = M_1 \\ \hat{\alpha}_1 > \frac{50}{30} & & M = M_2 \end{aligned} \quad 6.14$$

M_1 and M_2 are given by

$$\begin{aligned} 30^\circ \leq \alpha_1 \leq 50^\circ & & M_1 = & 1.051072 + 0.867436 \hat{\theta} + 1.11147 \hat{\sigma} \\ & & & + 0.524389 \hat{\alpha}_1 - 0.0389094 \hat{\alpha}_1^2 - 0.351642 \hat{\sigma}^2 \\ & & & - 0.209736 \hat{\theta}^2 - 0.535405 \hat{\theta} \hat{\sigma} - 0.415628 \hat{\sigma} \hat{\alpha}_1 \\ & & & - 0.202516 \hat{\alpha}_1 \hat{\sigma} + 0.0893002 (\hat{\theta} \hat{\sigma})^2 + 0.0173806 (\hat{\theta} \hat{\alpha}_1)^2 \\ & & & - 0.0148907 (\hat{\alpha}_1 \hat{\sigma})^2 + 0.215056 \hat{\theta} \hat{\sigma} \hat{\alpha}_1 + 0.0263945 \hat{\theta}^3 \\ & & & - 0.00778454 \hat{\theta} \hat{\sigma}^3 \end{aligned} \quad 6.15$$

$$\begin{aligned}
50^\circ < \alpha_1 \leq 70^\circ \quad M_2 = & -22.886694 + 12.1308 \hat{\Gamma} + 28.6134 \hat{\sigma} \\
& + 11.1523 \hat{\alpha}_1 - 0.207618 \hat{\alpha}_1^2 - 5.58370 \hat{\sigma}^2 \\
& - 1.31375 \hat{\theta}^2 - 6.88576 \hat{\theta} \hat{\sigma} - 5.09887 \hat{\sigma} \hat{\alpha}_1 \\
& - 12.9649 \hat{\alpha}_1 \hat{\sigma} + 0.531582 (\hat{\theta} \hat{\sigma})^2 + 0.165805 (\hat{\theta} \hat{\alpha}_1)^2 \\
& - 1.19605 (\hat{\alpha}_1 \hat{\sigma})^2 + 2.33333 \hat{\theta} \hat{\sigma} \hat{\alpha}_1 + 0.0785607 \hat{\theta}^3 \\
& - 0.0345338 \hat{\theta} \hat{\sigma}^3
\end{aligned} \tag{6.16}$$

where

$$\begin{aligned}
\hat{\theta} &= \frac{\theta}{\theta_{ref}}, \quad \theta_{ref} = 10^\circ \\
\hat{\alpha}_1 &= \frac{\alpha_1}{\alpha_{ref1}}, \quad \alpha_{ref1} = 30^\circ \\
\hat{\sigma} &= \frac{\sigma}{\sigma_{ref}}, \quad \sigma_{ref} = 1.0
\end{aligned} \tag{6.17}$$

The correlation coefficients for the two ranges are 0.866 199 and 0.923 300 respectively.

Using these interpolation equations, the M correlations were used to modify $\hat{\epsilon}_{adj}$ in the following way:

$$\hat{\epsilon}_{mod} = \hat{\epsilon}_{adj} - M(\hat{i}_{adj} - 0.4) \tag{6.18}$$

for the values of $\hat{\epsilon}_{adj}$ where $\hat{i}_{adj} < 0.4$. Application of the correlation for M had the effect of reducing the average error to 0.008 44 and the standard deviation of the error to 0.060 252. Qualitatively, the spread of the worst diverging NACA data lines was reduced, but some of

the data lines that converged well to the Howell correlation line to start with, such as those with low θ , low σ and low α_1 , were more dispersed. This is due to the correlation of M being imperfect and over-predicting values of M in regions where it should become very small.

To overcome this effect, table 6.1 was drawn up showing the regions where the values of $\hat{\epsilon}_{adj}$, the NACA data adjusted only by C_1 and C_2 , were considered good (with acceptably small deviation from Howell's curve). Using table 6.1, table 6.2 was drawn up showing zones of applicability of the two M correlations. In the non-applicable regions M was assumed to equal zero. Linear interpolation was used to ensure smooth transitions between the different regions. Therefore

$$\begin{aligned} \hat{\alpha}_1 \leq \frac{50}{30} & & M = M_1 \\ \hat{\alpha}_1 \geq \frac{55}{30} & & M = M_2 \\ \frac{50}{30} < \hat{\alpha}_1 < \frac{55}{30} & & M = M_1 + \frac{(M_2 - M_1)}{\left(\frac{55}{30} - \frac{50}{30}\right)} \left(\hat{\alpha}_1 - \frac{50}{30}\right) \end{aligned} \quad 6.19$$

M_1 and M_2 are altered by

$$\begin{aligned} M_1 &= M_1(1 - C_{\theta 2}(1 - C_{\theta 1}C_{\sigma})) \\ M_2 &= M_2(1 - C_{\sigma}(1 - C_{\theta 1})) \end{aligned} \quad 6.20$$

where

$$\begin{aligned}
\hat{\sigma} \leq 1.0 & & C_{\sigma} &= 1 \\
\hat{\sigma} \geq 1.2 & & C_{\sigma} &= 0 \\
1.0 < \hat{\sigma} < 1.2 & & C_{\sigma} &= 1 + \frac{(0-1)}{(1.2-1.0)}(\hat{\sigma}-1.0) \\
\hat{\theta} \leq 1.5 & & C_{\theta_1} &= 0 \\
\hat{\theta} \geq 2.5 & & C_{\theta_1} &= 1 \\
1.5 < \hat{\theta} < 2.5 & & C_{\theta_1} &= 0 + \frac{(1-0)}{(2.5-1.5)}(\hat{\theta}-1.5) \\
\hat{\theta} \leq 3.8 & & C_{\theta_2} &= 1 \\
\hat{\theta} \geq 4.2 & & C_{\theta_2} &= 0 \\
3.8 < \hat{\theta} < 4.2 & & C_{\theta_2} &= 1 + \frac{(0-1)}{(4.2-3.8)}(\hat{\theta}-3.8) \tag{6.21}
\end{aligned}$$

The NACA data was again modified using equation 6.18, this time with M having been altered by equations 6.19, 6.20 and 5.21. The average error is now 0.005 89 and the standard deviation of the error is 0.052 933. The exercise was repeated, this time applying equation 6.18 for all values of \hat{i}_{adj} , collapsing the data lines at $\hat{i}_{adj} > 0.4$ by

$$\begin{aligned}
\hat{i} \leq 0.4 & & M &= M \\
\hat{i} > 0.4 & & M &= -M \tag{6.22}
\end{aligned}$$

The resultant values of $\hat{\epsilon}_{mod}$ are shown plotted in figure 6.9. The spread has been successfully narrowed and the divergence minimised, and the values for average and standard deviation of the error are 0.003 54 and 0.054 261 respectively.

To regenerate the NACA results, firstly the values of ϵ^* and C_1 must be found from θ , σ (or s/l) and α_1 . Then, C_1 and ϵ^* produce ϵ_{adj}^* and, with i , \hat{i}_{adj} . From \hat{i}_{adj} , use is made of Howell's off-design correlation to obtain $\hat{\epsilon}_{mod}$ and, with s/l , C_D . After finding M from equation 6.22 and C_2 , the deflection ϵ is finally found from

$$\epsilon = C_2 \epsilon_{adj}^* [\hat{\epsilon}_{mod} + M(\hat{i}_{adj} - 0.4)] \tag{6.23}$$

6.4 Modification to the Correlation of Roberts for Reynolds Number and Turbulence Effects

As mentioned in section 5.6, the correlations of Roberts (1975) are not directly applicable to the cascade correlation requirements of the STFM, since the blade velocity distribution and a boundary layer method are required. The data in the graphs of the two papers of Roberts (1975), however, were used to create correlations of loss and turning versus the difference in bursting and subbursting blade chord Reynolds numbers

$$\bar{\omega}_{1,q} = K_1(\hat{\theta}f\hat{s})\Delta Re_c + \bar{\omega}_{1_B} \quad 6.24$$

$$\varepsilon_{SB} = \varepsilon_B - K_2\theta(s/l)\Delta Re_c \quad 6.25$$

where

$$\Delta Re_c = Re_{c_B} - Re_{c_{SB}} \quad 5.39$$

$$\hat{\theta} = \theta/\theta_{ref}, \quad \theta_{ref} = 10^\circ$$

$$f = (t/l)/(t/l)_{ref}, \quad (t/l)_{ref} = 0.1$$

$$\hat{s} = (s/l)/(s/l)_{ref}, \quad (s/l)_{ref} = 1.0 \quad 6.26$$

The subbursting and superbursting values of $\bar{\omega}_1$ and ε were digitised from the graphs in the two papers of Roberts (1975). By means of the modified Howell correlation (sections 6.1 to 6.3), a spreadsheet was used to calculate the values of diffusion factor D for each of the test points.

The bursting Reynolds numbers were then obtained from Roberts' correlation equation

$$Re_{c_B} = \left[\frac{(D + 0.4)}{7.5\sqrt{TF}} \right] \times 10^5 + 10000 \quad 5.30$$

and Taylor's turbulence factor

$$TF = Tu \left(\frac{l}{L_s} \right)^{\frac{1}{5}} \quad 5.32$$

where Roberts gives the turbulence intensity Tu of the VKI cascade tunnel as 0.48% (or 0.0048) and the macroscale L_x as ~ 15 mm. The blade chord l was 127mm for the tests at $Re_c \geq 200\,000$ and 60mm for lower values of Re_c , giving TF values of 0.0063 and 0.0074 respectively. In practice, however, none of the bursting Reynolds numbers from the correlation reached 200 000, so the TF value of 0.0074 was never used. Since Roberts refers to the value of TF as ~ 0.006 , it was decided to drop the fourth decimal place.

The bursting values of $\bar{\omega}_1$ and ϵ were not available, so the superbursting values were used.

Figure 6.10 shows values of

$$\frac{\bar{\omega}_{1SB} - \bar{\omega}_{1B}}{\theta l \xi} = f(\Delta Re_c) \quad 6.27$$

and 6.11 values of

$$\frac{\epsilon_B - \epsilon_{SB}}{\theta \frac{s}{l}} = f(\Delta Re_c) \quad 6.28$$

Linear regressions were fitted to the data in both graphs, and in both cases the lines do not pass through the origin but pass above it as can be seen in figures 6.10 and 6.11. This is because of the use of superbursting values for bursting ones. The exact value of the bursting $\bar{\omega}_1$ and ϵ can be calculated by Roberts' semi-empirical correlation, but since the inviscid solution augmented by a boundary layer method is required for each data point, a different course of action was decided upon. The values of $\bar{\omega}_1$ and ϵ for the highest Reynolds number in each test series was assumed to be equal to those for a Reynolds number high enough for transition to occur before separating into a laminar bubble. This assumption is shown to be reasonable by examination of Roberts' data in figures 6.15 to 6.22. The rate of decay of $\bar{\omega}_1$ and ϵ with decreasing Reynolds number is very mild in the superbursting regime compared to the subbursting regime, and in some cases is imperceptible.

The linear regressions were extrapolated backward until they crossed the x-axis. The average of the negatives of the ordinates of the two intercepts was taken, and added to the RHS of the bursting Reynolds number equation (5.21) as an additional constant. New values of bursting Reynolds number were calculated, and using updated values of ΔRX a new linear regression was formed. This cycle was repeated until the intercepts on the x-axis of the two regressions were equidistant from the origin on both sides.

The newly modified bursting Reynolds number equation predicts an "artificial" bursting Reynolds number with the same rate of decay of $\bar{\omega}_1$ and ϵ in the subbursting regime, but occurring at a higher Reynolds number to account for superbursting $\bar{\omega}_1$ and ϵ without having to calculate the Reynolds number at which laminar separation begins. This is illustrated in figure 6.12. The "artificial" bursting Reynolds number equation is

$$Re_{c_B} = \left[\frac{(D+0.4)}{7.5\sqrt{TF}} \right] \times 10^5 + 10000 + 17766 \quad 6.29$$

Having found the "artificial" bursting Reynolds number equation, linear regressions of equations 6.28 and 6.29 were performed, with the lines forced to go through the origin as seen in figures 6.13 and 6.14. The resultant equations to obtain subbursting $\bar{\omega}_1$ and ϵ are

$$\bar{\omega}_{1_{SB}} = \bar{\omega}_{1_B} + 2.45826 \times 10^{-7} (\hat{\theta} f \hat{s}) \Delta Re_c \quad 6.30$$

$$\epsilon_{SB} = \epsilon_B - 1.72523 \times 10^{-6} \theta (s/l) \Delta Re_c \quad 6.31$$

6.5 An Interim AVDR Correction

Since the NACA data (from which the adjustments to the Howell correlation were done) were of cascade tests done at *AVDR* of unity an *AVDR* correction was added to the Howell adjustments. This would allow the effect on the STFM predictions of *AVDR* variations to be analysed qualitatively, since the Rofanco compressor blade rows are expected to operate at *AVDR* > 1.

Different techniques for taking *AVDR* variations were listed in section 5.8. Curupsty (1989) stated that there was no comparably accurate method for introducing the effects of *AVDR* \neq 1.0. The effort required to compile a representative *AVDR* correlation dependent on stagger, solidity, incidence and camber would not be justified if no endwall boundary layer method was incorporated into the STFM to predict the endwall displacement thicknesses, and hence the actual *AVDR* values. The *AVDR* correction was therefore not intended to be accurate, but to be simple and to indicate the trends.

The three rules for *AVDR*-affected deviation mentioned in section 5.8 (equations 5.36 to 5.38) were incorporated into a piecewise-linear interpolated correlation with stagger as the independent variable

$$\delta = \delta_0 - K(AVDR - 1) \quad 6.32$$

where δ_0 the deviation at $AVDR = 1.0$. K is given by

$$\begin{aligned} 15^\circ > \gamma & \quad K = 8 \\ 15^\circ < \gamma < 36^\circ & \quad K = 8 + \frac{(\gamma - 15)}{(36 - 15)} \times (10 - 8) \\ 36^\circ > \gamma & \quad K = 10 + \frac{(\gamma - 36)}{(45 - 36)} \times (20 - 10) \end{aligned} \quad 6.33$$

The reason the high-stagger portion of the correlation is allowed to extrapolate beyond the top limit while the low-stagger portion is bounded by the lower limit is that the three points seem to suggest an exponential-type curve. Figure 5.16 from Gostelow (1984) provides some justification for values of K above 20 for high stagger blades, even though the values in the figure are incidence-dependent. The value of 20 was obtained from a cascade at zero incidence.

6.6 Testing of the Howell Correction Factors and Modified Method of Roberts

The method of Howell using the adjustment factors was used together with the low Reynolds number modified Roberts' method to predict the $\bar{\omega}_1$ and ϵ of the data presented by Roberts (1975). The results are shown in figures 6.15 to 6.22.

Howell's method with adjustment factors is shown to be quite accurate for all the test cases by comparing the highest Reynolds number data with the solid lines indicating most turning or least loss.

The turning ϵ for the $10^\circ \theta$ and $1.2 s/l$ cascade (figure 6.15) was consistently overpredicted by about 1° for all incidence angles, whereas greater variation was evident for the $30^\circ \theta$ and $1.2 s/l$ cascade (figure 6.17). At highly positive incidence ϵ was underpredicted by 1° whereas at highly negative incidence ϵ was overpredicted by 1.5° and 2.5° . For both cascades at design point ϵ was predicted to within 1° . The prediction of ϵ for the other, single-incidence, four cascades was within 1.75° .

The prediction of loss $\bar{\omega}_1$ was very good, being everywhere within 2 percentage points and mostly within 1 percentage point, with the exception of the highly negative incidence on the

$10^\circ \theta$ and 1.2 s/l cascade (figure 6.16), where the loss was overpredicted by 8 percentage points. This is to be expected since from figure 6.3 it can be seen that a \hat{i} value of -0.84 is far from the given data range and extrapolation is always dangerous.

The prediction of subbursting ϵ and $\bar{\omega}_1$ was very good, given the simplicity of the correlation and the accuracy bounds of Howell's adjusted method. The two methods were then deemed acceptable for use in the STFM.

7 RESULTS

7.1 General

For all the compressor runs, the computational domain consisted of 52 axial stations and 11 stream function stations. The axial station positions were chosen such that:

- a) The expansion ratio would never exceed 1.30. The expansion ratio is defined as the ratio between the distances to the upstream and downstream station from a given station.
- b) The axial stations would coincide with the mean blade inlet and exit positions as well as the experimental position of the nose of the cobra probe at inlet and after the blade rows. The probe nose position behind the stator row was found to be so close to the stator blade exit plane that the two stations were made coincident.
- c) Each blade row consisted of 4 axial stations. Values of change of total pressure and tangential momentum were calculated at the blade exit and linearly interpolated from the full value at the blade exit to zero at the blade inlet.

The STFM equation has no term dealing with total pressure values, only total pressure gradients. For this reason gauge pressure, measured against any reference, may be used for total pressure values instead of absolute pressure. Compressor inlet values for total pressure and tangential momentum were assumed to be zero. The downstream outlet streamline gradient was held at zero by making the outlet radius of a streamline equal to the radius calculated for the adjacent upstream node at the previous iteration.

The maximum stream function values were calculated from the mass averaged velocity for the flow outside of the hub and casing boundary layers from the experimental velocity profiles. These velocities were then corrected to remove the effect of inlet blockage presented by the six struts circumferentially distributed about the inlet. This was done by multiplying the thus-calculated inlet velocity by the ratio of the average of the three experimental rotor mass flows at a given flowrate to the implied inlet flowrate from the experimental inlet velocity profile.

The STFM program was run simulating the three mass flowrates at which the Rofanco compressor was tested. The different cascade correlations fitted and modified in chapter 6 were used, namely: Howell's nominal and original off-design correlation for deflection and loss; the off-design correlation of Howell as adjusted in section 6.3 (hereafter referred to as

H2); the modified low Reynolds number correlation of Roberts; and the interim *AVDR* correction. Lieblein's correlation was also used at the design flowrate as an alternate profile loss prediction. The STFM predictions were plotted on the same graphs as the experimental data for comparison. The inlet flow angle and tangential velocity profiles were not plotted as they were assumed zero for the STFM purposes, and their comparison with the experimental values is not meaningful. The zeroes in the axial velocity profiles are staggered for clarity. The rotor profiles have had their zeroes raised by 20 m/s, and the inlet flows by 40 m/s.

When applying Roberts' correction, the value of Taylor's turbulence factor *TF* was not available since no turbulence or macroscale measurements had been taken. Use was made of the turbulence measurements of Lewis (1989) at the inlet to the first rotor, downstream of the honeycomb and mesh screen, at a flow coefficient of 0.6. Lewis' build of the compressor differed from the current one by being only one stage. The turbulence intensity from figure 5.3 of Lewis (1989) in the bulk flow outside the annulus boundary layers is 1.38%. At this point two assumptions were made: firstly that the value of *Tu* remained approximately unchanged from inlet to outlet (not very physical, given that the effect of wake passing probably overrides the decay of turbulence), and secondly that the value of *TF* was close that of *Tu* (reasonable, given the 1/5th power of the chord to macroscale ratio in the scaling factor in equation 5.32). The value of *TF* was therefore assumed constant at 0.0138.

At the near-surge flowrate, Roberts' correction was also applied for a higher value of *TF*. Justification for this is a figure from Gostelow (1984) showing that turbulence intensity increases as flow coefficient decreases (figure 7.1). A value of *TF* of 2.5% was arbitrarily chosen to investigate the effect.

In all the tangential and axial velocity graphs the values after the stator rows appear to be badly underpredicted. The explanation for this anomaly is that the experimental stator measurements were not mass and area averaged across the pitch of the stator passages a chord length downstream (as is customary for cascade testing) but were single measurements at each radial station at the trailing edge axial position, approximately midway pitchwise between the stator trailing edges. The result of this was that the probe read the velocity of the bulk passage flow accelerated by the blockage caused by the blades and their boundary layers. Had the wakes been taken into account by pitchwise averaging, the velocities would have been lower.

The stator flow angles also appear underpredicted due to the deviation being greater (hence the turning being less) in the passage bulk flow than in the blade suction or pressure surface

boundary layer wakes. The flow has been given tangential velocity by the rotors, and if the straightening by the stators is less in the passage bulk flow than in the blade boundary layer wakes, then the flow angles will be greater there.

For a similar reason the inlet flows seem underpredicted. As pointed out in chapter 2, the blockage presented by the inlet struts and their wakes accelerate the flow locally, giving a falsely high reading if the wakes are not taken into account.

The near-wall velocities, pressures and angles are inaccurately predicted because the STFM is an inviscid method, and no endwall method has been incorporated together with a mixing model.

7.2 Near-design flowrate: 2.54kg/s

Howell's original loss and deflection correlations give good predictions of flow angle and tangential velocity after the rotor rows (figures 7.2 and 7.4), which together with Howell's endwall correlation, predict the total pressure distribution very well, to within 3% (figure 7.9). Lieblein's loss correlation was used at this flowrate with Howell's original correlations, and predicts less pressure loss (greater pressure rise), particularly near the casing. The differences are not remarkable, being of the order of 3% at most. Both simulations were done with Roberts' correction switched off.

The effect of Roberts' correlation was very mild on the tangential velocity and flow angle profiles (figures 7.2 and 7.4) but shows up most clearly on the pressure distribution (figure 7.10). A laminar bubble is predicted across the span of the rotor blades, most clearly visible in the 20mm closest to the hub of the rotors, and corresponds to a drop in total pressure in the experimental results in the same region.

The H2 method fared poorly at this flowrate, underpredicting turning (figures 7.3 and 7.5) and therefore pressure rise (figure 7.11) in the top two-thirds of the rotor blades. The inclusion of Roberts' correlation alleviated overprediction of pressure rise at the hub (figure 7.11).

Since it is primarily *AVDR* effects that separate Howell's correlation from H2, the interim *AVDR* correlation was applied to the rotors in H2. The stators were not corrected for *AVDR* effects for two reasons. Firstly, the effect of *AVDR* on stator blades with their lower stagger angles is much less than on rotor blades (compare equations 5.37 and 5.38). Secondly, it would be difficult to make comparisons since the experimental data taken behind the stator rows are not mass and area averaged.

The *AVDR* value was taken to be constant for the three rotor rows, and was varied until the predicted rotor flow angle equalled the experimental angle at mid-height (see figure 7.3), and was settled at 1.05. The flow angle and tangential velocity distributions improved (figures 7.3 and 7.5), not surprisingly, and therefore so did the total pressure distribution. Figure 7.12 shows very good predictions for stages 1 and 2 and overprediction for stage 3 (about 3%), instead of underprediction for all three. Also plotted is the pressure distribution for an *AVDR* of 1.03, to show the effect of an intermediate value.

It must be borne in mind that the interim *AVDR* correlation does not account for *AVDR*-dependent pressure loss. For *AVDR* values of greater than unity pressure loss is most often less than for two-dimensional flows (*AVDR* = 1.0), but can be greater for negative incidence and high stagger, as can be seen from figure 5.16.

7.3 Near-choke flowrate: 2.80kg/s

Howell's original loss and deflection correlations, with and without Roberts' correction (*TF* at 1.38%), underpredict the flow angle and tangential velocity profiles after the rotor rows at this flowrate (figures 7.13 and 7.15). Predictably, this leads to poor total pressure distribution prediction, too low by 10% at midspan using Roberts' correction (figure 7.19). The effect of Roberts' correction is much less visible than in the design flowrate, and only makes a noticeable difference at the hub in the pressure distribution graph at the hub (figure 7.19). The reason for this drop in influence is not so much that the rotor blade inlet Reynolds number has increased from the design case (merely from 1.24×10^5 to 1.27×10^5) but that the value of the diffusion factor *D* has decreased with the decrease in incidence angle, dropping the bursting Reynolds number.

The H2 method fared worse than Howell's method with both compounded by Roberts' correction, underpredicting turning (figures 7.14 and 7.16) and therefore pressure rise (figure 7.20). In the top two-thirds of the rotor blades, the pressure rise prediction is worse than Howell's and Roberts' correlation predictions.

In the same manner as the design flowrate case, the *AVDR* value was varied until the *AVDR* interim correlation accurately predicted the mid-height rotor flow angle (see figure 7.14), and was settled at 1.07. Figure 7.20 shows the *AVDR*-correction to yield a fair prediction of total pressure for stage 1, slight overprediction for stage 2 and about 7% overprediction for stage 3.

As mentioned in the previous case, for *AVDR* values of greater than unity, as can be seen from figure 5.16, pressure loss can be greater for negative incidence and high stagger. There is reason to believe that an *AVDR*-dependent pressure loss correction would yield a better pressure prediction.

Whereas the predictions of axial velocity profiles were flat for the design flowrate (figures 7.6, 7.7 and 7.8), for the near-choke flowrate the flow is predicted to accelerate at the hub and decelerate at the casing. Although not evident from the experimental rotor profiles, the experimental stator profiles clearly show this trend outside of the boundary layers.

7.4 Near-surge flowrate: 1.99kg/s

Problems arose in the low flowrate prediction in that streamline shift became pronounced and was unstable. Changing the relaxation factor only delayed the instability that prevented convergence. It was suspected that the problem lay in Howell's correlation with the turning rather than the drag coefficient correlation, since two values of \hat{i}_{adj} will give the same value of \hat{e} , a possible cause of instability.

To reach a converged solution it was thought necessary to put limits on Howell's correlation at $\hat{i}_{adj} = \pm 0.6$ instead of at $\hat{i}_{adj} = \pm 0.7$ (see figure 6.2 and 6.3). By this is meant that if the predicted value of \hat{i}_{adj} lay outside the limits, the value of \hat{e} returned by the correlation would be the value at the limit, not the extrapolated value. The limit was set on \hat{e} only and not on C_D , but the problem was not solved and the instability continued. Limits were set on both \hat{e} and C_D , and convergence was achieved. In a real compressor, either the blade row would stall or viscous effects would damp out streamline shift by increasing frictional drag on the accelerating casing streamtube.

The upper limit of \hat{i}_{adj} was first set at 0.6 (the first limit at which a converged solution was possible) so that the tendencies of the method could be investigated. Thereafter it was set at 0.4, Howell's stalling condition, since beyond that point in practice stall would be very likely.

With the limit set at 0.6, the effect of streamline shift can be clearly seen from the axial velocities predicted by both Howell and H2 (figure 7.27), which are underpredicted at the hub and overpredicted at the casing, and the flow angles which are overpredicted at the hub and underpredicted at the casing (figures 7.21). Roberts' correlation aggravates the situation (figures 7.22, 7.23, 7.25, 7.26, 7.28 and 7.29). In all cases, Howell's method appears worse, except for the flow angle prediction behind the third stator for H2 at Tu of 1.38%. Both

methods overpredict total pressure (figure 7.30), but Howell's method overpredicts by more since it predicts more turning. No *AVDR* correction was attempted for this situation as it was clearly unrealistic.

Setting the upper limit of \hat{i}_{adj} to 0.4 improved matters considerably. The prediction of flow angle, tangential velocity and axial velocity more closely approximated the experimental values for both methods at this setting, although Howell's method gave better profiles. Figure 7.33 shows Howell's prediction of flow angle. The slopes of the rotor flow angles for the three stages are quite well predicted. The same comments apply to the axial and tangential velocity profiles (figures 7.39 and 7.36). The H2 method underpredicts the flow angles and tangential velocities (figures 7.35 and 7.38), as well as the variation in slope of the axial velocity profiles (figure 7.41). This is all explained by the fact that the H2 method is calculating flow at an *AVDR* of unity.

Examining figures 6.2 and 6.3, it can be seen that by setting the limit of \hat{i}_{adj} at 0.6, the profile losses were higher and the amount of turning was lower than for the case at stalling incidence at 0.4, yet the total pressure is still overpredicted for all stages using both methods at both incidence limits, including Roberts' correction at two turbulence intensities. This implies that somewhere a loss generating mechanism is being underpredicted and probably concerns the endwall losses, since the blade losses and turning have been varied and accounted for.

As with the other two flowrates, the H2 method was augmented by the interim *AVDR* correlation. More or less correct rotor flow angle prediction was obtained with an *AVDR* value of 1.1, as shown by figure 7.45. The variation in slope of the axial velocity profiles improved (figure 7.47). The total pressure rise (with Roberts' correction with a turbulence intensity of 1.38%) was overpredicted by 9%, emphasising the pressure loss problem. A turbulence intensity value of 1.38% appears to have consistently given better results than the 2.5% value.

8 CONCLUSIONS

The STFM procedure appears to give good results for internal flows in general. The test cases chosen in chapter 3 show that for inviscid flows the method compares well with classical methods. Inaccuracies result from the use of very few streamlines in regions of hub-to-tip ratios less than about 0.2, but increasing the number of streamlines soon suppresses this effect. As can be expected, for compressor flows the method was shown to be very dependent on the cascade models chosen.

The H2 method (the adjustment factors correlated for Howell's method in chapter 6) gave much better predictions of the NACA data than Howell's method. The H2 method together with the Roberts-type low-Reynolds number correction (as modified in chapter 6) were shown to give good flow turning and profile loss predictions for Roberts' low-Reynolds number data. Both sets of test cases had *AVDR* values of unity.

Measurements were taken at three different flowrates of the low-speed Rofanco compressor; near-design point, near-surge and near-choke. The STFM program was run at the three experimental flowrates, using Howell's nominal and off-design methods, compounded by Howell's endwall loss correlations and the Roberts-type correction. Compared to the experimental results, the STFM program using these correlations performed well at the design point and acceptably at off-design. The pressure rise was underpredicted by 3% at a near-design flowrate, underpredicted by 9% at a near-choke flowrate and overpredicted by 10% at a near-surge flowrate. In the absence of any capability of predicting *AVDR* values in blade rows, there is no option but to use this collection of correlations.

When the STFM was used together with H2 combined with Howell's endwall loss correlations and the Roberts-type correlation, the flow angle predictions were not as good as those of Howell. This gave rise to a 4% total pressure underprediction for design, 9% underprediction for near-choke and 8% overprediction for near-surge flowrates respectively.

Making guesses of rotor row *AVDR* values to match the flow angles, the adjustment factors correlated for Howell's method in chapter 6 combined with the Roberts-type correlation gave total pressure overpredictions of 3%, 7% and 8% for design, near-choke and near-surge flowrates respectively. Since a lot of confidence can be placed in H2 and the Roberts-type correlation, it would appear that Howell's endwall loss correlations are the bottleneck in improvement of pressure prediction.

In neither of the two methods is mass flow comparable with experimental values because no annulus blockage capability has been built into the method. A better comparison would be possible if a reliable endwall boundary layer technique were employed to predict blockage (especially in blade rows to yield *AVDR* values) and endwall losses.

9 RECOMMENDATIONS

9.1 Numerical Recommendations

In order to improve the capability of the STFM program, a number of modifications are necessary to predict compressor flows.

The philosophy behind the correlations has been proved, but use of Howell's deviation rule should be abandoned because of the *AVDR* inaccuracy. The deviation prediction graphs of Lieblein (1965) should be curve fitted and used instead, since the definitions of reference incidence produce similar angles, and deviation is a very weak function of incidence when blade stall is approached (Cumpsty, 1989). A new Howell-type nominal condition should be developed using the NACA data. Using these two new correlations, new C_1 , C_2 and M adjustments should prove less difficult to correlate and should yield simpler expressions, since most of the variations should have been taken care of by the deviation and nominal condition correlations.

The values of the losses found in the NACA investigations should be compared with the predictions of Howell and Jansen and Moffat (1967) to establish which is preferable.

An endwall loss prediction method (including the effect of tip clearance) combined with a spanwise mixing procedure should be implemented to replace Howell's endwall loss prediction method. A great deal of work has been done in this field, and Cumpsty (1989) presents a review of papers up to 1989, and Dunham (1994) presents a method as well as reviewing more recent work.

A better correlation should be found or developed to predict both deviation and loss modifications as a result of *AVDR* variations, having incorporated an endwall method which should yield the value of *AVDR* for each blade row and streamline intersection.

A correlation predicting turbulence intensity variation behind compressor blade rows incorporating wake passing and turbulence decay should be developed as input to the modified Roberts' low Reynolds number correlation.

Lastly, the STFM procedure can be upgraded to calculate compressible flows, and the method of Swan (1961) may be used for off-design transonic loss prediction. Lieblein's (1965) Mach number correction for deviation prediction can be implemented.

9.2 Experimental Recommendations

The experimental runs should be repeated incorporating a number of important modifications.

The traversing in the radial and yaw plane should be automated to decrease the time taken to complete measurements. This will allow more tests to be taken in a reasonable amount of time.

Measurements should be taken at several pitchwise stations behind each stator row to allow mass and area averaging for comparison with predicted values of pressure, velocity and angle.

The cobra probe should also be calibrated for errors in angle prediction in flow with pitchwise velocity gradients.

Detailed turbulence measurements, including calculations of macroscale L_y , should be done at inlet and behind each blade row.

APPENDIX A: BOADWAY'S TRANSFORMATION APPLIED TO CYLINDRICAL CO-ORDINATES

The stream function ψ is a function of radius and axial position and hence its differential is given as

$$d\psi = \frac{\partial\psi}{\partial r} dr + \frac{\partial\psi}{\partial z} dz \quad A.1$$

Introducing a dummy variable $\phi = \phi(r, z)$ another differential is found:

$$d\phi = \frac{\partial\phi}{\partial r} dr + \frac{\partial\phi}{\partial z} dz \quad A.2$$

New functions are required, such that:

$$z = z(\phi, \psi), \quad r = r(\phi, \psi) \quad A.3$$

$$dz = \frac{\partial z}{\partial\phi} d\phi + \frac{\partial z}{\partial\psi} d\psi \quad A.4$$

$$dr = \frac{\partial r}{\partial\phi} d\phi + \frac{\partial r}{\partial\psi} d\psi \quad A.5$$

Substituting A.1 and A.2 into A.4 and A.5 we obtain

$$dz = \frac{\partial z}{\partial\phi} \left[\frac{\partial\phi}{\partial r} dr + \frac{\partial\phi}{\partial z} dz \right] + \frac{\partial z}{\partial\psi} \left[\frac{\partial\psi}{\partial r} dr + \frac{\partial\psi}{\partial z} dz \right] \quad A.6$$

and

$$dr = \frac{\partial r}{\partial\phi} \left[\frac{\partial\phi}{\partial r} dr + \frac{\partial\phi}{\partial z} dz \right] + \frac{\partial r}{\partial\psi} \left[\frac{\partial\psi}{\partial r} dr + \frac{\partial\psi}{\partial z} dz \right] \quad A.7$$

Collecting the dz terms the following set of simultaneous equations, expressed in matrix form, can be derived:

$$\begin{bmatrix} \frac{\partial z}{\partial \phi} & \frac{\partial z}{\partial \psi} \\ \frac{\partial r}{\partial \phi} & \frac{\partial r}{\partial \psi} \end{bmatrix} \begin{bmatrix} \frac{\partial \phi}{\partial z} \\ \frac{\partial \psi}{\partial z} \end{bmatrix} = \begin{bmatrix} 1 \\ 0 \end{bmatrix} \quad \text{A.8}$$

from which it follows that

$$\frac{\partial \phi}{\partial z} = \frac{\partial r / \partial \psi}{A}, \quad \frac{\partial \psi}{\partial z} = -\frac{\partial r / \partial \phi}{A} \quad \text{A.9}$$

where A is the determinant of the matrix. Similarly, collecting dr terms one obtains:

$$\begin{bmatrix} \frac{\partial z}{\partial \phi} & \frac{\partial z}{\partial \psi} \\ \frac{\partial r}{\partial \phi} & \frac{\partial r}{\partial \psi} \end{bmatrix} \begin{bmatrix} \frac{\partial \phi}{\partial r} \\ \frac{\partial \psi}{\partial r} \end{bmatrix} = \begin{bmatrix} 0 \\ 1 \end{bmatrix} \quad \text{A.10}$$

from which

$$\frac{\partial \phi}{\partial r} = -\frac{\partial z / \partial \psi}{A}, \quad \frac{\partial \psi}{\partial r} = \frac{\partial z / \partial \phi}{A} \quad \text{A.11}$$

The second partial derivatives can be obtained in an analogous fashion:

$$\begin{aligned} \frac{\partial^2 \psi}{\partial z^2} &= \frac{\partial(\partial \psi / \partial z)}{\partial z} = \frac{\partial(\partial \psi / \partial z)}{\partial \phi} \frac{\partial \phi}{\partial z} + \frac{\partial(\partial \psi / \partial z)}{\partial \psi} \frac{\partial \psi}{\partial z} \\ &= \frac{\partial \left[\frac{-\partial r / \partial \phi}{A} \right]}{\partial \phi} \frac{\partial r / \partial \psi}{A} + \frac{\partial \left[\frac{-\partial r / \partial \phi}{A} \right]}{\partial \psi} \frac{-\partial r / \partial \phi}{A} \end{aligned} \quad \text{A.12}$$

$$\frac{\partial \left[\frac{-\partial r / \partial \phi}{A} \right]}{\partial \phi} = -\frac{1}{A^2} \left[A \frac{\partial^2 r}{\partial \phi^2} - \frac{\partial r}{\partial \phi} \frac{\partial A}{\partial \phi} \right] \quad \text{A.13}$$

$$\frac{\partial \left[\frac{-\partial r / \partial \phi}{A} \right]}{\partial \psi} = -\frac{1}{A^2} \left[A \frac{\partial^2 r}{\partial \phi \partial \psi} - \frac{\partial r \partial A}{\partial \phi \partial \phi} \right] \quad \text{A.14}$$

Inserting A.13 and A.14 into A.12 yields

$$\frac{\partial^2 \psi}{\partial z^2} = -\frac{1}{A^3} \left[\frac{\partial r}{\partial \phi} \left[\frac{\partial r \partial A}{\partial \phi \partial \psi} - A \frac{\partial^2 r}{\partial \phi \partial \psi} \right] - \frac{\partial r}{\partial \psi} \left[\frac{\partial r \partial A}{\partial \phi \partial \phi} - A \frac{\partial^2 r}{\partial \phi^2} \right] \right] \quad \text{A.15}$$

By a similar process $\frac{\partial^2 \psi}{\partial r^2}$ can be found:

$$\frac{\partial^2 \psi}{\partial r^2} = -\frac{1}{A^3} \left[\frac{\partial z}{\partial \phi} \left[\frac{\partial z \partial A}{\partial \phi \partial \psi} - A \frac{\partial^2 z}{\partial \phi \partial \psi} \right] - \frac{\partial z}{\partial \psi} \left[\frac{\partial z \partial A}{\partial \phi \partial \phi} - A \frac{\partial^2 z}{\partial \phi^2} \right] \right] \quad \text{A.16}$$

If one lets $\phi = z$, then:

$$\frac{\partial z}{\partial \phi} = 1, \quad \frac{\partial z}{\partial \psi} = 0, \quad \frac{\partial r}{\partial \phi} = \frac{\partial r}{\partial z}$$

$$A = \frac{\partial z \partial r}{\partial \phi \partial \psi} - \frac{\partial z \partial r}{\partial \psi \partial \phi} = \frac{\partial r}{\partial \psi}$$

$$\frac{\partial A}{\partial \psi} = \frac{\partial^2 r}{\partial \psi^2}$$

$$\frac{\partial A}{\partial \phi} = \frac{\partial A}{\partial z} = \frac{\partial^2 r}{\partial z \partial \psi} \quad \text{A.17}$$

Considering A.17 alongside A.15 and A.16 it is clear that

$$\frac{\partial^2 \psi}{\partial z^2} = \frac{1}{(\partial r / \partial \psi)^3} \left[\frac{\partial r}{\partial \psi} \left[\frac{\partial r \partial^2 r}{\partial z \partial z \partial \psi} - \frac{\partial r \partial^2 r}{\partial \psi \partial z^2} \right] - \frac{\partial r}{\partial z} \left[\frac{\partial r \partial^2 r}{\partial z \partial \psi^2} - \frac{\partial r \partial^2 r}{\partial \psi \partial z \partial \psi} \right] \right]$$

$$\frac{\partial^2 \psi}{\partial r^2} = \frac{1}{(\partial r / \partial \psi)^3} \left[\frac{\partial^2 r}{\partial \psi^2} \right]$$

$$\frac{\partial \psi}{\partial r} = \frac{(\partial z / \partial \phi)}{A} = \frac{1}{(\partial r / \partial \psi)} \quad \text{A.18}$$

Density gradients are handled in the same manner:

$$\begin{aligned}
 \rho &= \rho(\phi, \psi) \\
 \frac{\partial \rho}{\partial z} &= \frac{\partial \rho}{\partial \phi} \frac{\partial \phi}{\partial z} + \frac{\partial \rho}{\partial \psi} \frac{\partial \psi}{\partial z} \\
 &= \frac{\partial \rho}{\partial \phi} \frac{(\partial r / \partial \psi)}{A} + \frac{\partial \rho}{\partial \psi} \left[-\frac{\partial r / \partial \phi}{A} \right] \\
 &= \frac{\partial \rho}{\partial \phi} \frac{(\partial r / \partial \psi)}{(\partial r / \partial \psi)} + \frac{\partial \rho}{\partial \psi} \left[-\frac{\partial r / \partial \phi}{\partial r / \partial \psi} \right] \\
 &= \frac{\partial \rho}{\partial \phi} + \frac{\partial \rho}{\partial \psi} \left[-\frac{\partial r / \partial z}{\partial r / \partial \psi} \right] \\
 &= \frac{\partial \rho}{\partial \phi} - \frac{1}{(\partial r / \partial \psi)} \frac{\partial \rho}{\partial \psi} \frac{\partial r}{\partial z}
 \end{aligned} \tag{A.19}$$

$$\begin{aligned}
 \frac{\partial \rho}{\partial r} &= \frac{\partial \rho}{\partial \phi} \frac{\partial \phi}{\partial r} + \frac{\partial \rho}{\partial \psi} \frac{\partial \psi}{\partial r} = \frac{\partial \rho}{\partial \phi} \left[-\frac{\partial z / \partial \psi}{\partial r / \partial \psi} \right] + \frac{\partial \rho}{\partial \psi} \frac{(\partial z / \partial \phi)}{(\partial r / \partial \psi)} \\
 &= 0 + \frac{1}{(\partial r / \partial \psi)} \frac{\partial \rho}{\partial \psi} = \frac{\partial \rho / \partial \psi}{\partial r / \partial \psi}
 \end{aligned} \tag{A.20}$$

APPENDIX B: DISCRETISATION OF MATRIX THROUGHFLOW EQUATION USING GREYVENSTEIN'S NON-UNIFORM GRID METHOD

Equation 7 is reproduced for convenience:

$$\begin{aligned}
 & 2 \frac{\partial r}{\partial \psi} \frac{\partial r}{\partial z} \frac{\partial^2 r}{\partial z \partial r} - \left(\frac{\partial r}{\partial \psi} \right)^2 \frac{\partial^2 r}{\partial z^2} - \frac{\partial^2 r}{\partial \psi^2} \left(1 + \left\{ \frac{\partial r}{\partial z} \right\}^2 \right) - \frac{1}{r} \left(\frac{\partial r}{\partial \psi} \right)^2 \\
 & = \left[\frac{\rho}{\rho_0} r \right]^2 \left[\frac{\partial r}{\partial \psi} \right]^3 \left[\frac{\partial h_0}{\partial \psi} - T \frac{\partial s}{\partial \psi} - \frac{c_0}{r} \frac{\partial(r c_0)}{\partial \psi} \right] - \frac{1}{\rho} \left[\frac{\partial r}{\partial z} \left(\frac{\partial r}{\partial \psi} \right)^2 \frac{\partial \rho}{\partial z} - \frac{\partial \rho}{\partial \psi} \frac{\partial r}{\partial \psi} \left(1 + \left\{ \frac{\partial r}{\partial z} \right\}^2 \right) \right] \quad B.1
 \end{aligned}$$

Analogous to the method of Greyvenstein (1981), but in axisymmetric co-ordinates, the equation is discretised for a rectangular (ψ, z) grid. The equation is then numerically solved.

Figure B.1 shows a section of the (ψ, z) grid. N, S, E and W indicate neighbouring grid points, while n, s, e and w are the midpoints between the neighbouring points and the point P, the point being examined. The grid is not necessarily evenly spaced.

Using linear interpolation, the term $\frac{\partial r}{\partial z}$ at the point P can be written as

$$\begin{aligned}
 \left[\frac{\partial r}{\partial z} \right]_P &= \frac{(r_P - r_W)}{\delta z_w} + \frac{\delta z_w}{2\delta z} \left[\frac{(r_E - r_P)}{\delta z_e} - \frac{(r_P - r_W)}{\delta z_w} \right] \\
 &= ZG1(r_E - r_P) + ZG2(r_P - r_W) \\
 &= i' \quad B.2
 \end{aligned}$$

where

$$ZG1 = \frac{\delta z_w}{2\delta z \delta z_e} \quad B.3$$

and

$$ZG2 = \frac{\delta z_e}{2\delta z \delta z_w} \quad B.4$$

The term $\frac{\partial r}{\partial \psi}$ at the point P can be expressed in a similar fashion as

$$\begin{aligned} \left[\frac{\partial r}{\partial \psi} \right]_P &= PG1(r_N - r_P) + PG2(r_P - r_S) \\ &= A \end{aligned} \quad B.5$$

where

$$PG1 = \frac{\delta \psi_s}{2\delta \psi \delta \psi_n} \quad B.6$$

and

$$PG2 = \frac{\delta \psi_n}{2\delta \psi \delta \psi_s} \quad B.7$$

The remaining terms in equation B.1 are discretised in the same way. The following expressions are used:

$$\left[\frac{\partial r}{\partial \psi} \right]_W = PG1(r_{NW} - r_W) + PG2(r_W - r_{SW}) = B \quad B.8$$

$$\left[\frac{\partial r}{\partial \psi} \right]_E = PG1(r_{NE} - r_E) + PG2(r_E - r_{SE}) = C \quad B.9$$

$$\left[\frac{\partial^2 r}{\partial z \partial \psi} \right]_P = ZG1(C - A) + ZG2(A - B) = D \quad B.10$$

$$\left[\frac{\partial \rho}{\partial z} \right]_P = ZG1(\rho_E - \rho_P) + ZG2(\rho_P - \rho_W) = F \quad B.11$$

$$\left[\frac{\partial \rho}{\partial \psi} \right]_P = PG1(\rho_N - \rho_P) + PG2(\rho_P - \rho_S) = G \quad B.12$$

The second-order partial derivatives in *B.1* can be written as

$$\left[\frac{\partial^2 r}{\partial z^2} \right]_P = \frac{1}{\delta z} \left[\frac{(r_E - r_P)}{\delta z_e} - \frac{(r_P - r_W)}{\delta z_w} \right] \quad B.13$$

$$\left[\frac{\partial^2 r}{\partial \psi^2} \right]_P = \frac{1}{\delta \psi} \left[\frac{(r_N - r_P)}{\delta \psi_n} - \frac{(r_P - r_S)}{\delta \psi_s} \right] \quad B.14$$

Using equations *B.3* to *B.14* in the LHS of equation *B.1* yields

$$\begin{aligned} & 2 \frac{\partial r}{\partial \psi} \frac{\partial r}{\partial z} \frac{\partial^2 r}{\partial z \partial r} - \left(\frac{\partial r}{\partial \psi} \right)^2 \frac{\partial^2 r}{\partial z^2} - \frac{\partial^2 r}{\partial \psi^2} \left(1 + \left\{ \frac{\partial r}{\partial z} \right\}^2 \right) - \frac{1}{r} \left(\frac{\partial r}{\partial \psi} \right)^2 \\ & = 2AHD - \frac{A^2}{\delta z} \left[\frac{(r_E - r_P)}{\delta z_e} - \frac{(r_P - r_W)}{\delta z_w} \right] - \frac{(1-H^2)}{\delta \psi} \left[\frac{(r_N - r_P)}{\delta \psi_n} - \frac{(r_P - r_S)}{\delta \psi_s} \right] - \frac{A^2}{r_P} \end{aligned} \quad B.15$$

In a similar manner, the RHS of equation *B.1* can be expressed as

$$\begin{aligned} & \left[\frac{\rho}{\rho_o} r \right] \left[\frac{\partial r}{\partial \psi} \right]^3 \left[\frac{\partial h_o}{\partial \psi} - T \frac{\partial s}{\partial \psi} - \frac{c_\theta}{r} \frac{\partial (rc_\theta)}{\partial \psi} \right] - \frac{1}{\rho} \left[\frac{\partial r}{\partial z} \left(\frac{\partial r}{\partial \psi} \right)^2 \frac{\partial \rho}{\partial z} - \frac{\partial \rho}{\partial \psi} \frac{\partial r}{\partial \psi} \left(1 + \left\{ \frac{\partial r}{\partial z} \right\}^2 \right) \right] \\ & = \left[\frac{\rho_P}{\rho_o} r_P \right]^2 A^3 \left[L - \frac{c_{\theta P}}{r_P} N \right] - \frac{1}{\rho_P} [HA^2 F - AG(1+H^2)] \\ & = SO \end{aligned} \quad B.16$$

where

$$L = \left[\frac{\partial h_o}{\partial \psi} - T \frac{\partial s}{\partial \psi} \right]_P \quad B.17$$

and

$$\begin{aligned} N &= \left[\frac{\partial (rc_\theta)}{\partial \psi} \right]_P \\ &= PG1(r_N c_{\theta N} - r_P c_{\theta P}) + PG2(r_P c_{\theta P} - r_S c_{\theta S}) \end{aligned} \quad B.18$$

If flow is incompressible,

$$\frac{\partial h_o}{\partial \psi} - T \frac{\partial s}{\partial \psi} = \frac{1}{\rho} \frac{\partial p_o}{\partial \psi} \quad B.19$$

Inserting *B.19* into *B.17* results in

$$\begin{aligned} L &= \left[\frac{1}{\rho} \frac{\partial p_o}{\partial \psi} \right]_F \\ &= \frac{1}{\rho} [PG1(p_{oN} - p_{oP}) + PG2(p_{oP} - p_{oS})] \quad B.20 \end{aligned}$$

Substituting equations *B.15* and *B.16* into *B.1*, we obtain:

$$2AHD - \frac{A^2}{\delta z} \left[\frac{(r_E - r_P)}{\delta z_e} - \frac{(r_P - r_W)}{\delta z_w} \right] - \frac{(1+H^2)}{\delta \psi} \left[\frac{(r_N - r_P)}{\delta \psi_n} - \frac{(r_P - r_S)}{\delta \psi_s} \right] - \frac{A^2}{r_P} = SO \quad B.21$$

Substituting $Q = \frac{A^2}{r_P}$ and rearranging, the following identity emerges:

$$r_P = \frac{\frac{A^2}{\delta z} \left[\frac{r_E}{\delta z_e} + \frac{r_W}{\delta z_w} \right] + \frac{(1+H^2)}{\delta \psi} \left[\frac{r_N}{\delta \psi_n} + \frac{r_S}{\delta \psi_s} \right] + Q + SO - 2AHD}{\frac{A^2}{\delta z} \left[\frac{1}{\delta z_e} + \frac{1}{\delta z_w} \right] + \frac{(1+H^2)}{\delta \psi} \left[\frac{1}{\delta \psi_n} + \frac{1}{\delta \psi_s} \right]} \quad B.22$$

Equation *B.22* is solved by iteration, with *A*, *D*, *H*, *Q* and *SO* calculated from values of *r_P* obtained from the previous iteration.

REFERENCES

- Benadé, J. G., "Die Herontwerp van die Rofanco Kompressor", B. Eng. Project Report, University of Stellenbosch. April 1987.
- Boadway, J. D., "Transformation of elliptic partial differential equations for solving two-dimensional boundary value problems in fluid flow", *International Journal for Numerical Methods in Engineering*, Vol. 10, 1976, pp. 527-533.
- Carter, A. D. S., "Low Speed Performance of Related Aerofoils in Cascade", *Aeronautical Research Council CP No. 29*, 1950.
- Constant, H., "Performance of Cascades of Aerofoils", *RAE Note No. E3696; ARC Report No. 4155*, 1939.
- Cumpsty, N. A., *Compressor Aerodynamics*, Longman Scientific and Technical, Harlow, 1989.
- Davis, W. R. and Millar, D. A. J., "A Comparison of the Matrix and Streamline Curvature Methods of Axial Flow Turbomachinery Analysis, From a User's Point of View", *Trans ASME, Journal of Engineering for Power*, October 1975, pp. 549-560.
- Denton, J. D., "Throughflow Calculations for Transonic Axial Flow Turbines", *Trans ASME, Journal of Engineering for Power*, Vol 100, April 1978, pp. 212-218.
- Dixon, S. L., *Fluid Mechanics, Thermodynamics of Turbomachinery*, Third Edition, Pergamon Press, Oxford, 1978.
- Dunham, J., "A New Approach to Predicting Annulus Wall Boundary Layers in Axial Compressors", *Proc Instn Mech Engrs*, Volume 207, 1994, pp. 413-425.
- Emery, J. C., Herrig, L. J., Erwin, J. R. And Felix, A. R., "Systematic Two-dimensional Cascade Tests of NACA 65-Series Compressor Blades at Low Speeds", *NACA Report 1368*, 1958.
- Erwin, J. R., Salvage and Emery, J. C., "Two-Dimensional Low Speed Cascade Investigation of NACA Compressor Blade Sections Having a Systematic Variation in Mean-Line Loading", *NACA TN 3817*, 1956.

- Felix, A. R., "Summary of 65-Series Compressor Blades Low-speed Cascade Data by Use of the Carpet-plotting Technique", *NACA TN 3913*, 1957.
- Felix, A. R., and Emery, J. C., "A Comparison of Typical Gas Turbine Establishment and NACA Axial-flow Compressor Blade Sections in Cascade of Low Speed, *NACA TN 3937*, 1953.
- Fottner, L., "Kennfeldrechnung für Axialverdichter", *Technischer Bericht 72/008*, MTU, 1972.
- Fottner, L., Answer to Questionnaire on Compressor Loss and Deviation Angle Correlations, AGARD-PEP, Working Group 12, 1979.
- Gettliffe, K. M., "Experimental and Theoretical Analysis of Flow through an Axial Flow Compressor", B. Eng. Final Year Project Report, University of Stellenbosch, November 1992.
- Glass, S. J., "Commissioning and Testing the Probe Calibration Facility", B. Eng. Final Year Project Report, University of Stellenbosch, November 1986.
- Greyvenstein, G. P., *Snelheidsdruk Numeriese metode vir die Berekening van Tweedimensionele Elliptiese Vloei (Velocity-pressure Numerical Method for the Computation of Two-dimensional elliptic Flow)*, Private communication, December 1981.
- Gostelow, J. P., *Cascade Aerodynamics*, Pergamon Press, Oxford, 1984.
- Herrig, L. J., Emery, J. C. and Erwin, J. R., "Systematic Two-dimensional Cascade Tests of NACA 65-Series Compressor Blades at Low Speeds", *NACA RM L51G31*, 1951.
- Herrig, L. J., Emery, J. C. and Erwin, J. R., "Systematic Two-dimensional Cascade Tests of NACA 65-Series Compressor Blades at Low Speeds", *NACA TN 3916*, 1957.
- Hirsch, C. and Denton, J. D., "Through Flow Calculations in Axial Turbomachines", *AGARD-AR-175*, 1981
- Hirsch, C. and Warzee, G., "A Finite-element Method for Through Flow Calculations in Turbomachines", *Journal of Fluids Engineering*, Sept 1976, pp. 403-421.
- Horlock, J. H., *Axial Flow Compressors*, Butterworths Scientific Publications, London, 1958

- Howell, A. R., "The Present Basis of Axial Flow Compressor Design: Part 1 - Cascade Theory and Performance", *Aeronautical Research Council Reports and Memoranda No. 2095*, 1942.
- Howell, A. R., "Design of Axial Compressors", *Proceedings of the Institution of Mechanical Engineers*, London, 153, 1945.
- Howell, A. R., "Fluid Dynamics of Axial Compressors", *Proceedings of the Institution of Mechanical Engineers*, London, 153, 1945.
- Jansen, W., and Moffat, W. C., "The Off-Design Analysis of Axial-Flow Compressors", *Trans ASME, Journal of Engineering for Power*, Oct. 1967, pp. 453-462.
- Koch, C. C., and Smith, L. H., "Loss Sources and Magnitudes in Axial-Flow Compressors", *Trans ASME, Journal of Engineering for Power*, July 1976, pp. 411-424.
- Kubota, S., "Cascade Performance with Accelerated or Decelerated Axial Velocity", *Gas Turbine Laboratory Report 56*, MIT, September 1959.
- Lawson, T. V., "An Investigation into the Effect of Reynolds Number on a Cascade of Blades With Parabolic Arc Camber Line", *British NGTE, Memo M 195*, 1953.
- Lewis, K. L., "Prediction of Stall Inception in an Axial Flow Compressor", M.Sc Project Report, University of the Witwatersrand, 1989.
- Lieblein, S., "Loss and Stall Analysis of Compressor Cascades", *Trans ASME, Journal of Basic Engineering*, 81, September 1959, pp. 387-400.
- Lieblein, S., "Incidence and Deviation-angle Correlations for Compressor Cascades", *Trans ASME, Journal of Basic Engineering*, 82, September 1960, pp. 575-587.
- Lieblein, S., "Experimental Flow in Two-dimensional Cascades", Chapter IV, *Aerodynamic Design of Axial-flow Compressors*, NASA SP 36, 1965
- Lieblein, S. and Roudebush, W. H., "Theoretical Loss Relation for Low-Speed 2D Cascade Flow", *NACA TN 3662*, 1956.

Marsh, H., "A Digital Computer Program for the Through-Flow Fluid Mechanics in an Arbitrary Turbomachine, Using a Matrix Method", *Aeronautical Research Council Reports and Memoranda No. 3509*, 1968.

Mellor, G., *The 65-Series Cascade Data*, Gas Turbine Laboratory, MIT (unpublished), 1956.

Monsarrat, N. T., *et al.*, "Design Report Single Stage Evaluation of Highly Loaded High-Mach-Number Compressor Stages", *NASA N69-30869*, 1969.

Novak, R. A., "Streamline Curvature Computing Procedures", *Trans ASME, Journal of Engineering for Power*, Vol 89 No 4, October 1957, pp. 478-490.

Oates, G. C., *Aerothermodynamics of Gas Turbine and Rocket Propulsion*, Revised and Enlarged, 2nd Edition, AIAA Education Series, New York, 1988.

Oates, G. C., Knight, C. J. and Carey, G. F., "A Variational Formulation of the Compressible Throughflow Problem", *Trans ASME, Journal of Engineering for Power*, Jan 1976, pp. 1-8.

Pollard, D., and Gostelow, J. P., "Some Experiments at Low Speed on Compressor Cascades", *Trans ASME, Journal of Engineering for Power*, 89, 1967, pp. 427-436.

Pollard, D., and Horlock, J. H., "A Theoretical Investigation of the Effect of Change in Axial Velocity on the Potential Flow Through a Cascade of Aerofoils", *Aeronautical Research Council CP 619*, June 1962.

Roach, P. E., "The Generation of nearly isotropic turbulence by means of grids", *Int J Heat Fluid Flow*, Vol 8 No 2, June 1987, pp. 82-92.

Robbins, W. H., Jackson, R. J., and Lieblein, S., "Blade-Element Flow in Annular Cascades", Chapter VII, *Aerodynamic Design of Axial-flow Compressors*, NASA SP 36, 1965

Roberts, W. B., "The Effect of Reynolds Number and Laminar Separation on Axial Cascade Performance", *Trans ASME, Journal of Engineering for Power*, April 1975, pp. 261-274

Roberts, W. B., "The Experimental Cascade Performance of NACA Compressor Profiles at Low Reynolds Number", *Trans ASME, Journal of Engineering for Power*, April 1975, pp. 454-459.

- Roos, T. H., "Reblading and Testing the Rofanco Low Speed Axial Compressor", B. Eng. Mechanical Project Report, University of Stellenbosch, November 1990.
- Schlichting, H. and Das, A., "On the Influence of Turbulence Level on the Aerodynamic Losses of Axial Turbomachines", From *Flow Research on Blading*, L. S. Dzung, ed., Elsevier Publ. Co., 1970.
- Schulze, W. M., Erwin, J. R. and Ashby, G. C. Jr., "NACA 65-Series Compressor Rotor Performance With Varying Annulus-Area Ratio, Solidity, Blade Angle, and Reynolds Number and Comparison with Cascade Results", *NACA TN 4130*, October 1957.
- Strinning, P., and Dunker, R., "Grundlagen des Auslegungsverfahrens und Vergleich Messung/Rechnung", *Forschungsberichte Verbrennungskraftmaschinen*, Heft 235, 1977.
- Swan, W. C., "A Practical Method of Predicting Transonic-Compressor Performance", *Trans ASME, Journal of Engineering for Power*, July 1961, pp. 322-330
- Wiggins, J. O. "A Procedure for Determining the Off-Design Characteristics of Multistage Axial Flow Compressors", MSc. dissertation, University of Cincinnati, Ohio, 1963.
- von Backström, T. W., and Roos, T. H., "The Streamline Throughflow Method for Axial Turbomachinery Flow Analysis", Presented at ISABE XI, Tokyo, Japan, September 1993.

TABLES

Table 2.1: Details of blade geometry

Rotor blades

Blade number: 41

Blade chord: 30 mm

Radius (mm)	Stagger (degrees)	Camber (degrees)	Solidity	Maximum Thickness	Position of Maximum Camber
150.0	38.00	31.04	1.3051	0.10	0.5
165.0	45.00	23.48	1.1864	0.10	0.5
180.0	49.40	17.93	1.0876	0.10	0.5
195.0	53.00	13.85	1.0039	0.10	0.5
210.0	56.10	10.90	0.9322	0.10	0.5

Stator blades

Blade number: 43

Blade chord: 30 mm

Radius (mm)	Stagger (degrees)	Camber (degrees)	Solidity	Maximum Thickness	Position of Maximum Camber
150.0	20.38	46.28	1.3687	0.10	0.5
165.0	18.18	43.39	1.2443	0.10	0.5
180.0	16.61	41.05	1.1406	0.10	0.5
195.0	14.90	40.57	1.0529	0.10	0.5
210.0	14.32	40.00	0.9777	0.10	0.5

Table 2.2: Mass balances

Near-surge flowrate:
Density = 1,1757 kg/m³ $\dot{m} = 1,9892$ kg/s

Measured inlet velocity 27,413 m/s
Corrected inlet velocity 25,984 m/s

Stage No.	Rotor			Stator			Inlet
	1	2	3	1	2	3	left
\dot{m}	2,0093	1,9573	2,0010	2,2949	2,5651	2,5579	2,0986
$\frac{\dot{m}}{\dot{m}_{ave}}$	1,0101	0,9840	1,0059	1,1537	1,2895	1,2859	1,0550

Near-design flowrate:
Density = 1,1664 kg/m³ $\dot{m} = 2,5378$ kg/s

Measured inlet velocity 34,631 m/s
Corrected inlet velocity 33,384 m/s

Stage No.	Rotor			Stator			Inlet	
	1	2	3	1	2	3	left	right
\dot{m}	2,5601	2,5140	2,5394	2,7877	2,6854	2,7623	2,6356	2,6296
$\frac{\dot{m}}{\dot{m}_{ave}}$	1,0088	0,9906	1,0006	1,0984	1,0581	1,0884	1,0385	1,0362

Near-choke flowrate:
Density = 1,1602 kg/m³ $\dot{m} = 2,8036$ kg/s

Measured inlet velocity 38,367 m/s
Corrected inlet velocity 36,924 m/s

Stage No.	Rotor			Stator			Inlet
	1	2	3	1	2	3	left
\dot{m}	2,7850	2,8309	2,7949	2,8917	2,8959	2,9686	2,9131
$\frac{\dot{m}}{\dot{m}_{ave}}$	0,9934	1,0097	0,9969	1,0314	1,0329	1,0589	1,0391

Table 6.1: Prediction quality of H2 correlation without gradient correction

+ good
 - poor
 * not applicable

Camber angle	Solidity	Inlet angle				
		30°	40°	50°	60°	70°
10°	0,5	+	+	+	+	+
	0,75	+	+	+	+	+
	1	+	+	+	+	+
	1,25	+	+	+	-	-
	1,5	+	+	+	-	-
20°	1	+	+	+	+	+
	1,5	+	+	+	-	-
30°	0,5	-	-	-	-	-
	0,75	+	-	-	-	-
	1	+	+	+	+	+
	1,25	+	+	+	-	-
	1,5	+	+	+	-	-
37,5°	1	+	+	+	-	-
	1,5	+	+	+	-	-
45°	0,5	-	-	-	-	*
	0,75	+	+	+	+	*
	1	+	-	-	-	*
	1,25	+	-	-	-	*
	1,5	+	+	-	-	*

Table 6.2: Regions of applicability of gradient correction correlation M

+ applicable
- not applicable

$M_1: 30^\circ \leq \alpha_1 \leq 50^\circ$				
Solidity	Camber angle			
	$10^\circ - 20^\circ$	$20^\circ - 30^\circ$	$30^\circ - 37,5^\circ$	$37,5^\circ - 45^\circ$
0,5 - 0,75	-	+	+	+
0,75 - 1	-	+	+	+
1 - 1,25	-	-	-	+
1,25 - 1,5	-	-	-	+
$M_2: 50^\circ \leq \alpha_1 \leq 70^\circ$				
Solidity	Camber angle			
	$10^\circ - 20^\circ$	$20^\circ - 30^\circ$	$30^\circ - 37,5^\circ$	$37,5^\circ - 45^\circ$
0,5 - 0,75	-	+	+	+
0,75 - 1	-	+	+	+
1 - 1,25	+	+	+	+
1,25 - 1,5	+	+	+	+

FIGURES

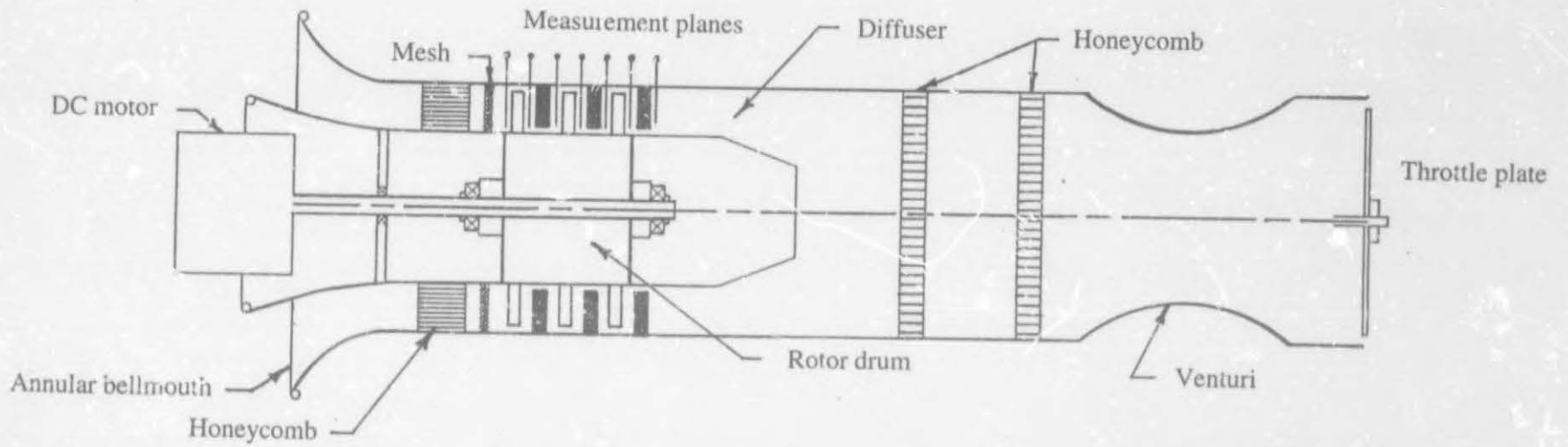


Figure 2.1: Schematic diagram of Rofanco low speed compressor testbench (adapted from Lewis)

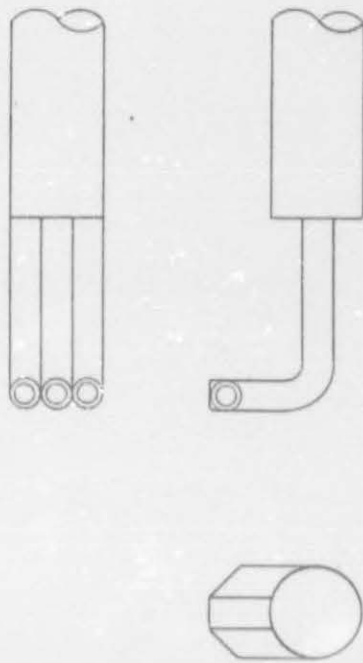


Figure 2.2: Cobra three-hole probe

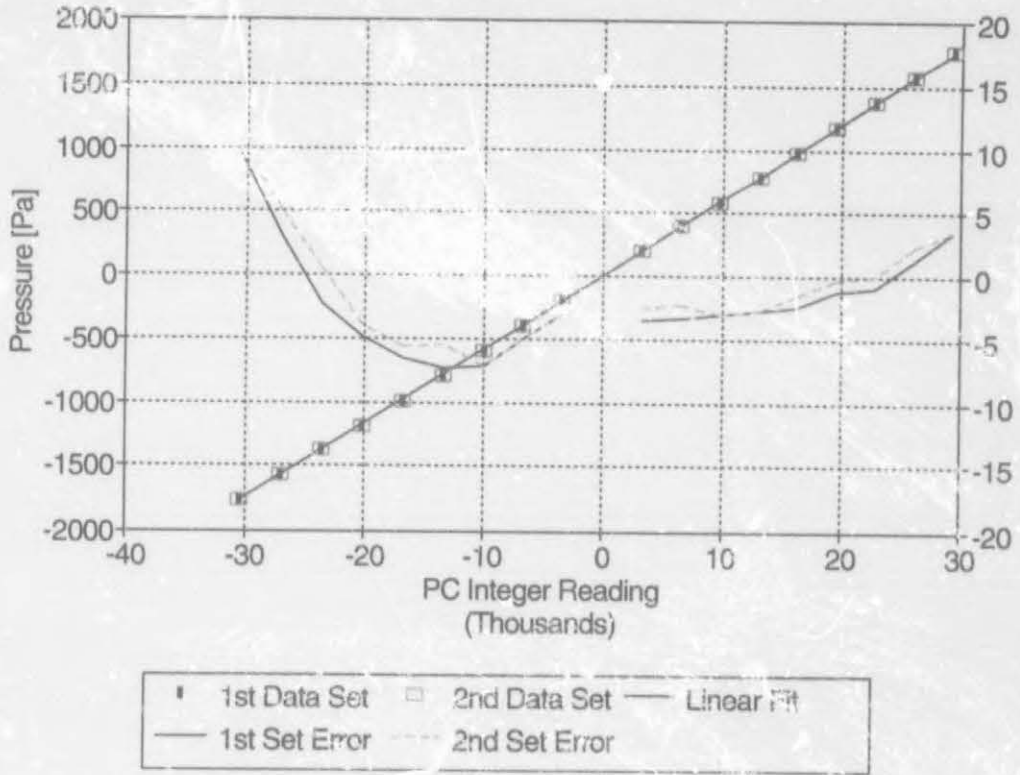


Figure 2.3: HBM pressure transducer calibration

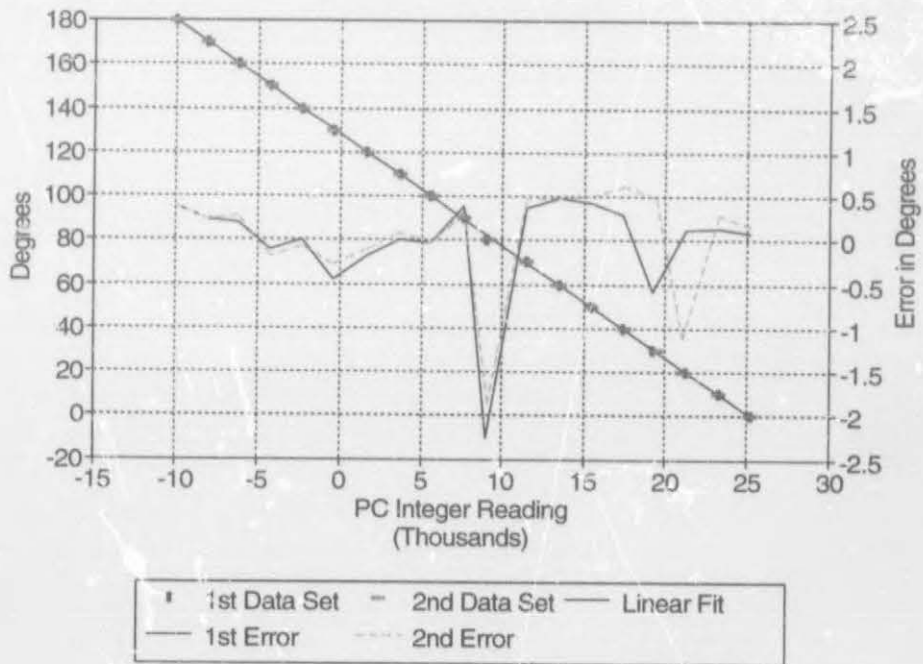


Figure 2.4: Angular potentiometer calibration

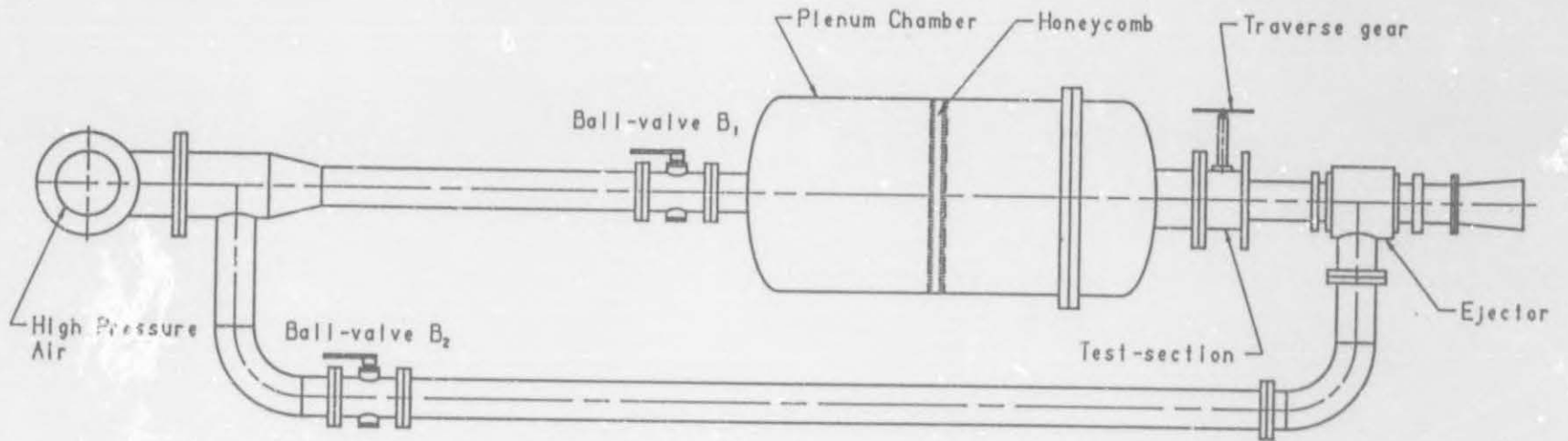


Figure 2.5: Aerodynamic probe calibration facility

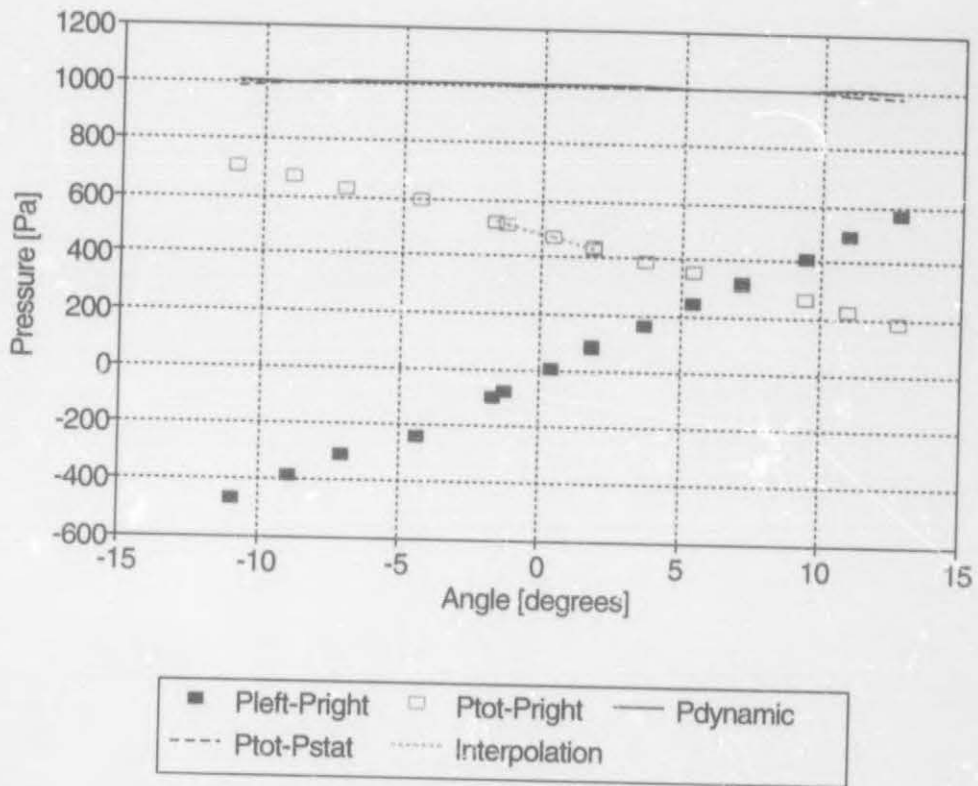


Figure 2.6: Cobra probe calibration

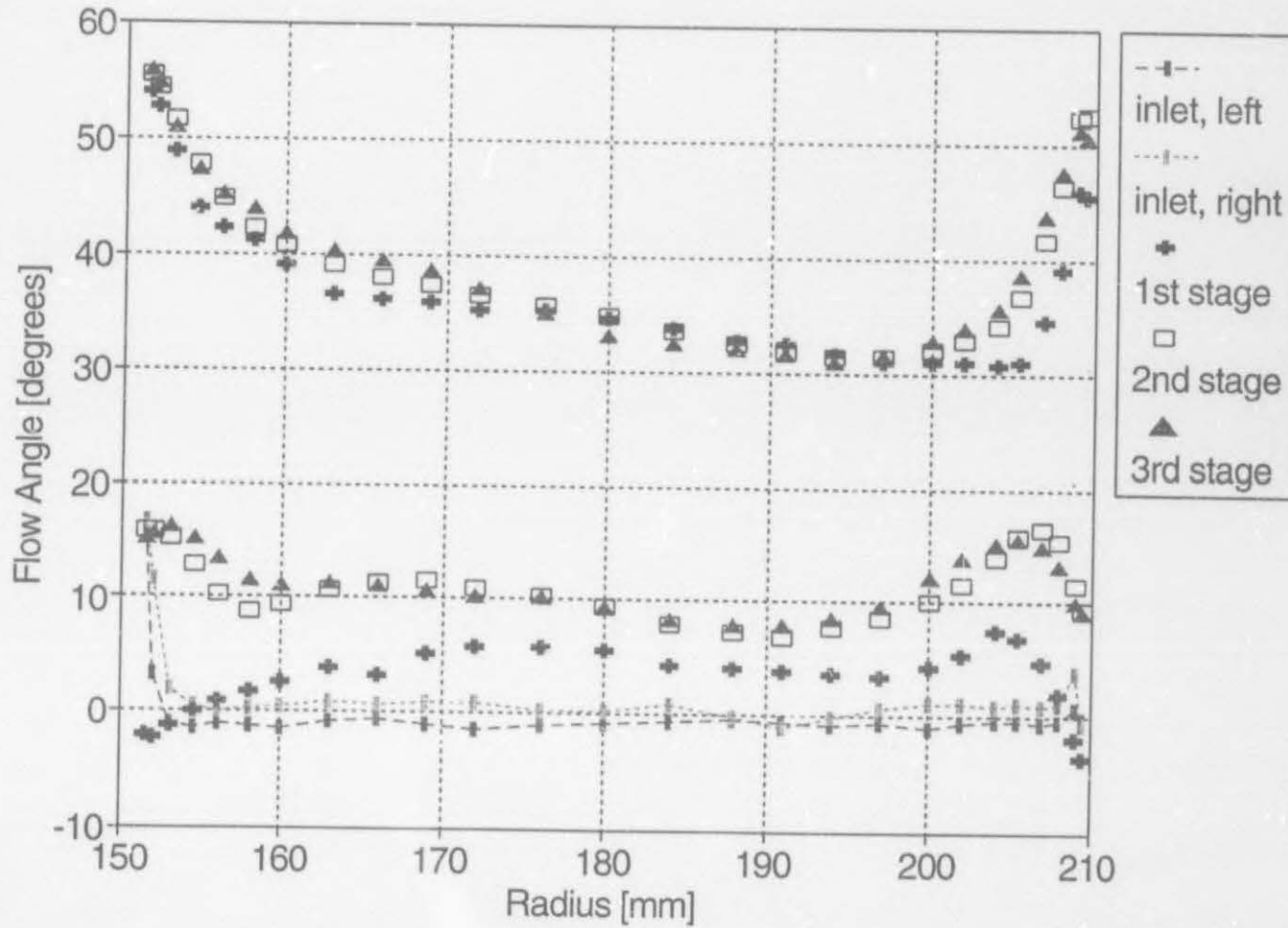


Figure 2.7: Flow angle profiles at near-design flowrate: 2.54 kg/s.

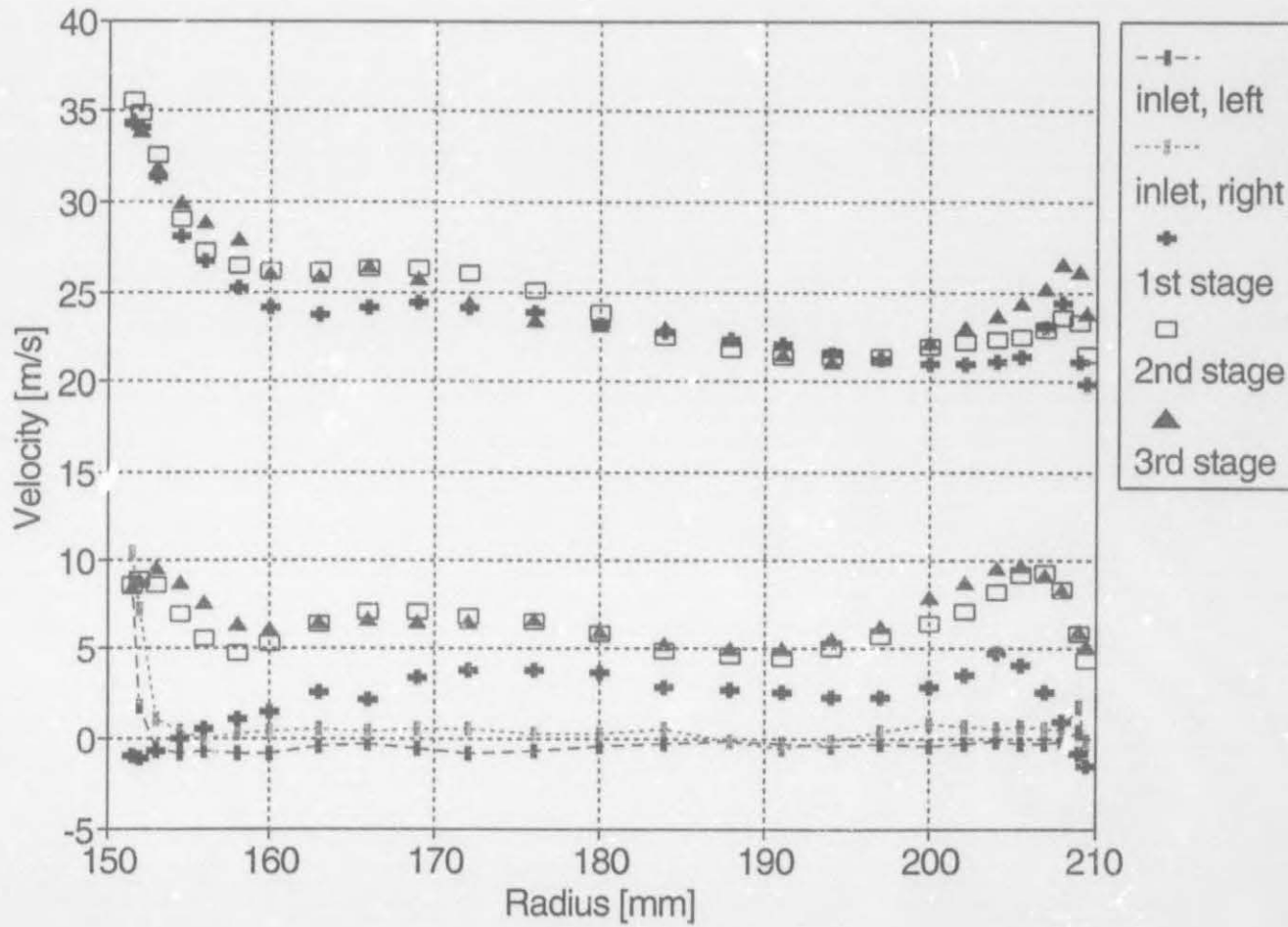


Figure 2.8: Tangential velocity profiles at near-design flowrate: 2.54 kg/s.

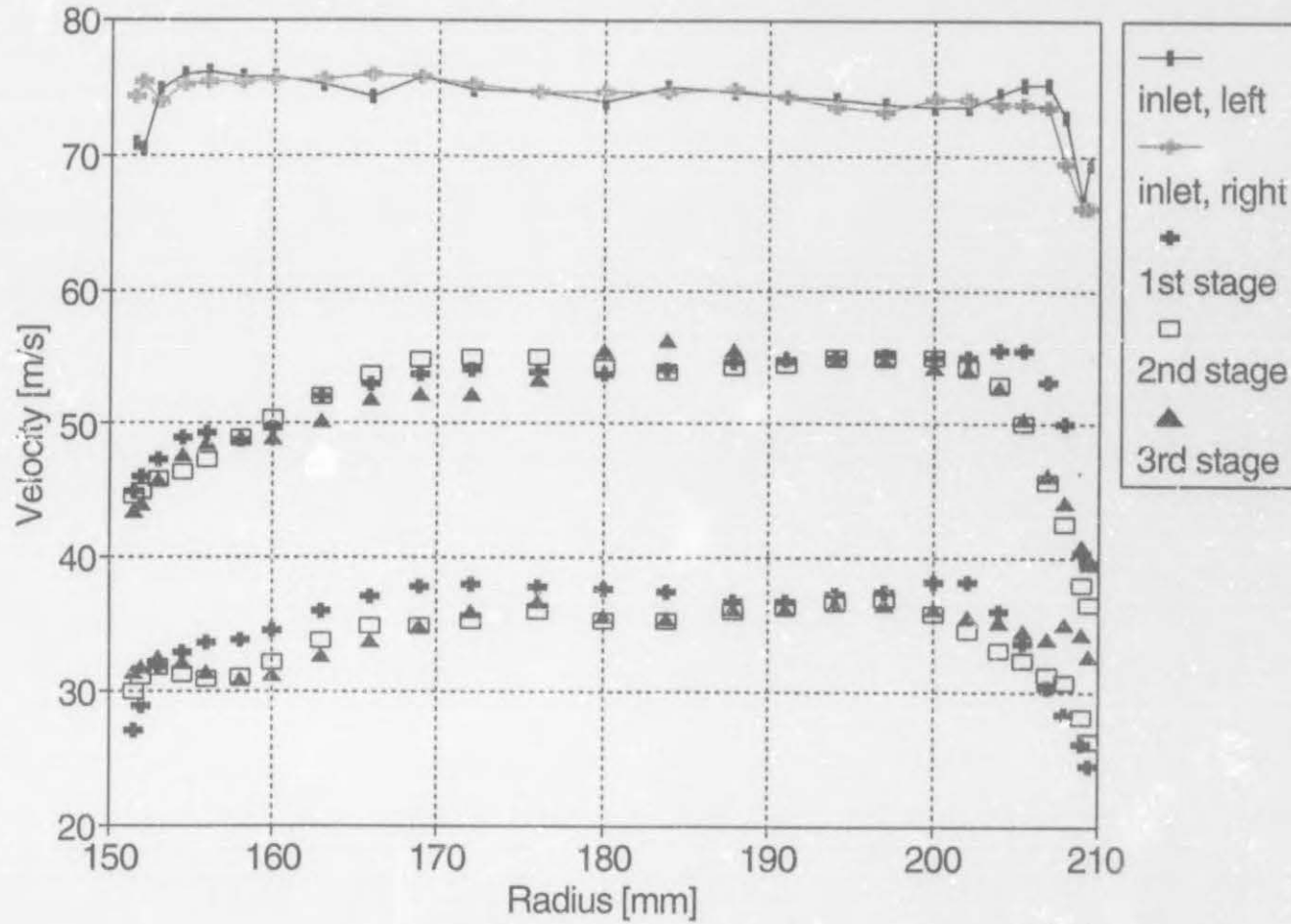


Figure 2.9: Axial velocity profiles at near-design flowrate: 2.54 kg/s. (Zeroes of inlet and rotor rows have been staggered by 40 and 20 m/s respectively).

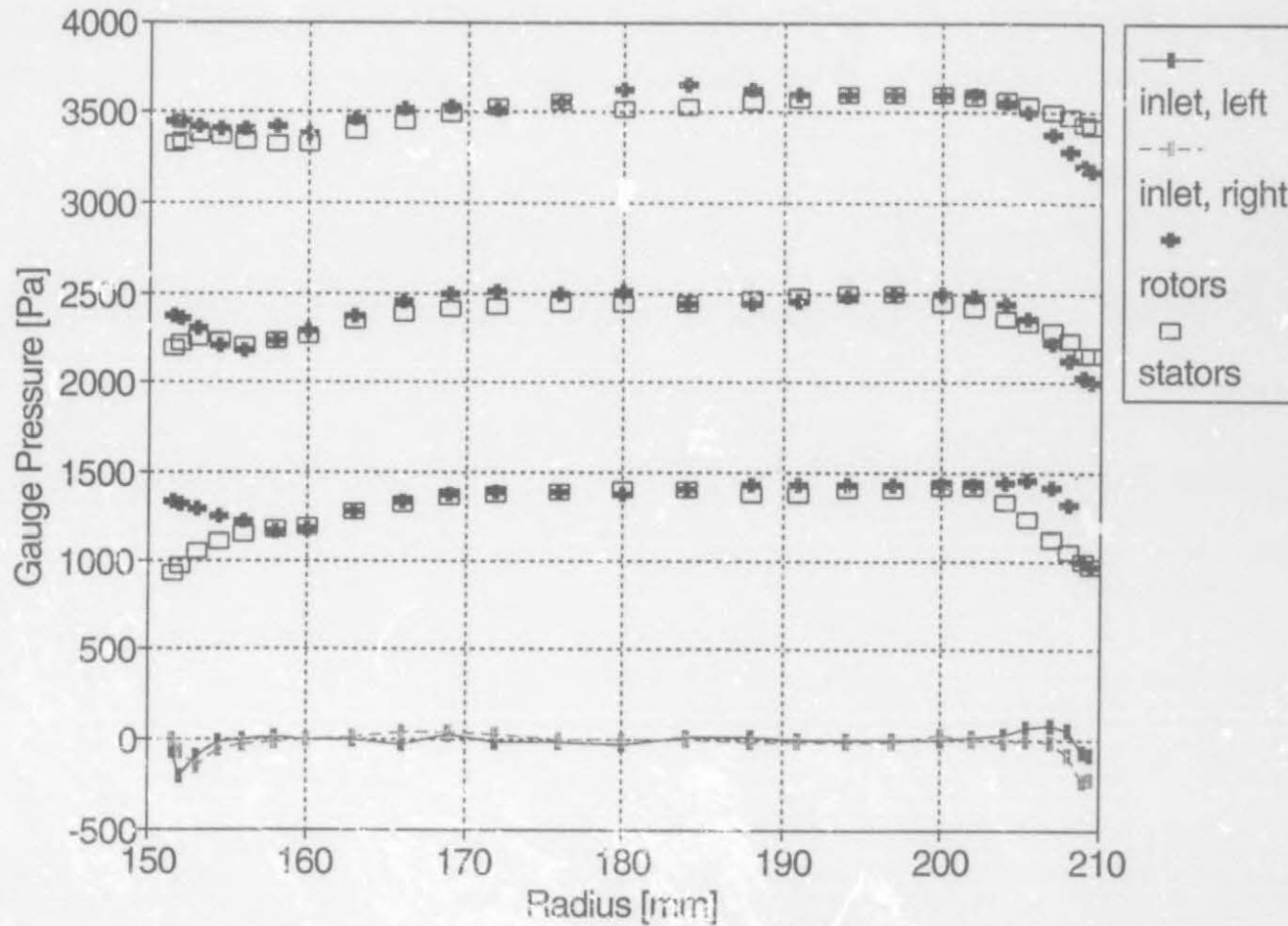


Figure 2.10: Total pressure profiles (relative to inlet mass average) at near-design flowrate: 2.54 kg/s.

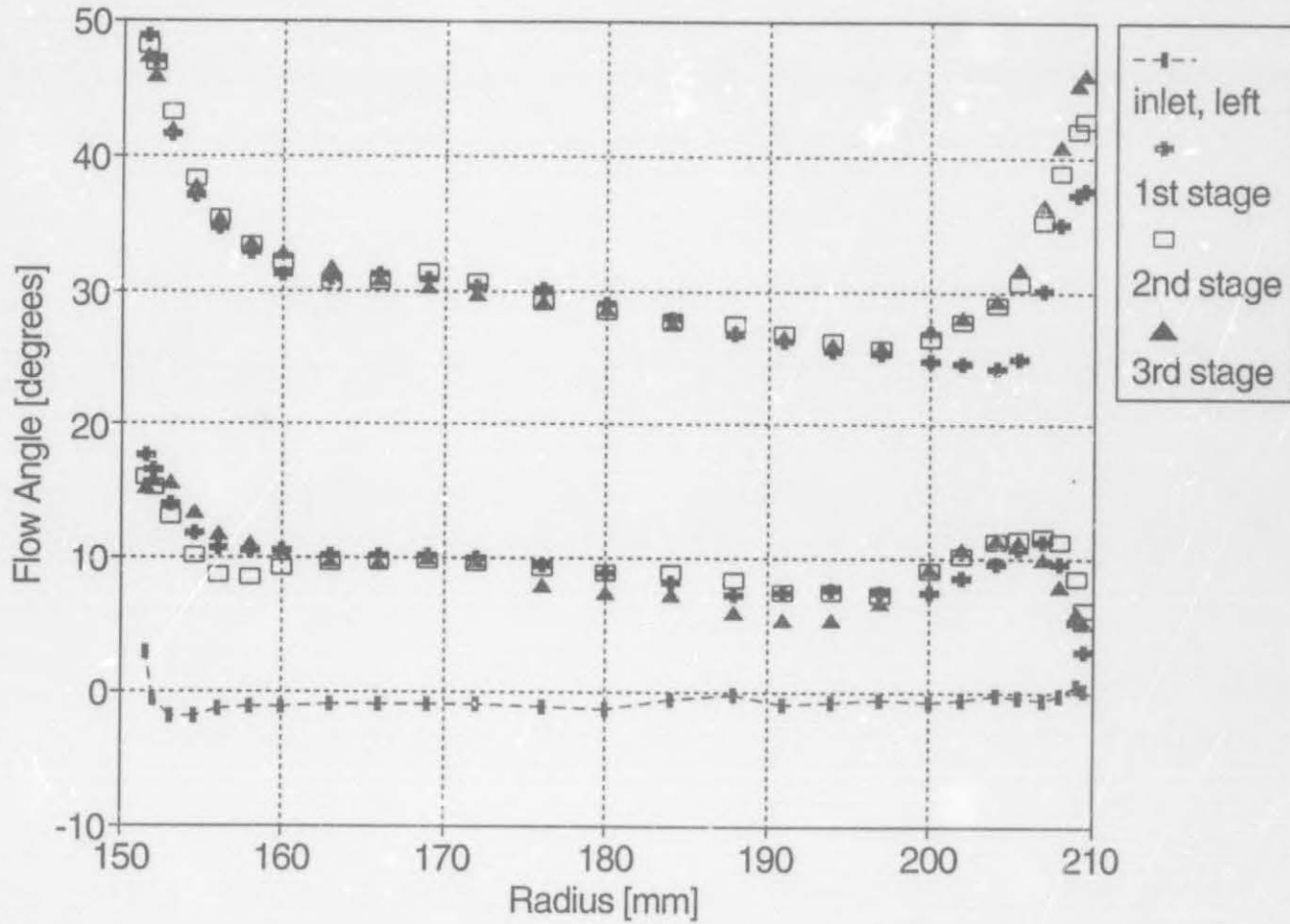


Figure 2.11: Flow angle profiles at near-choke flowrate: 2.80 kg/s.

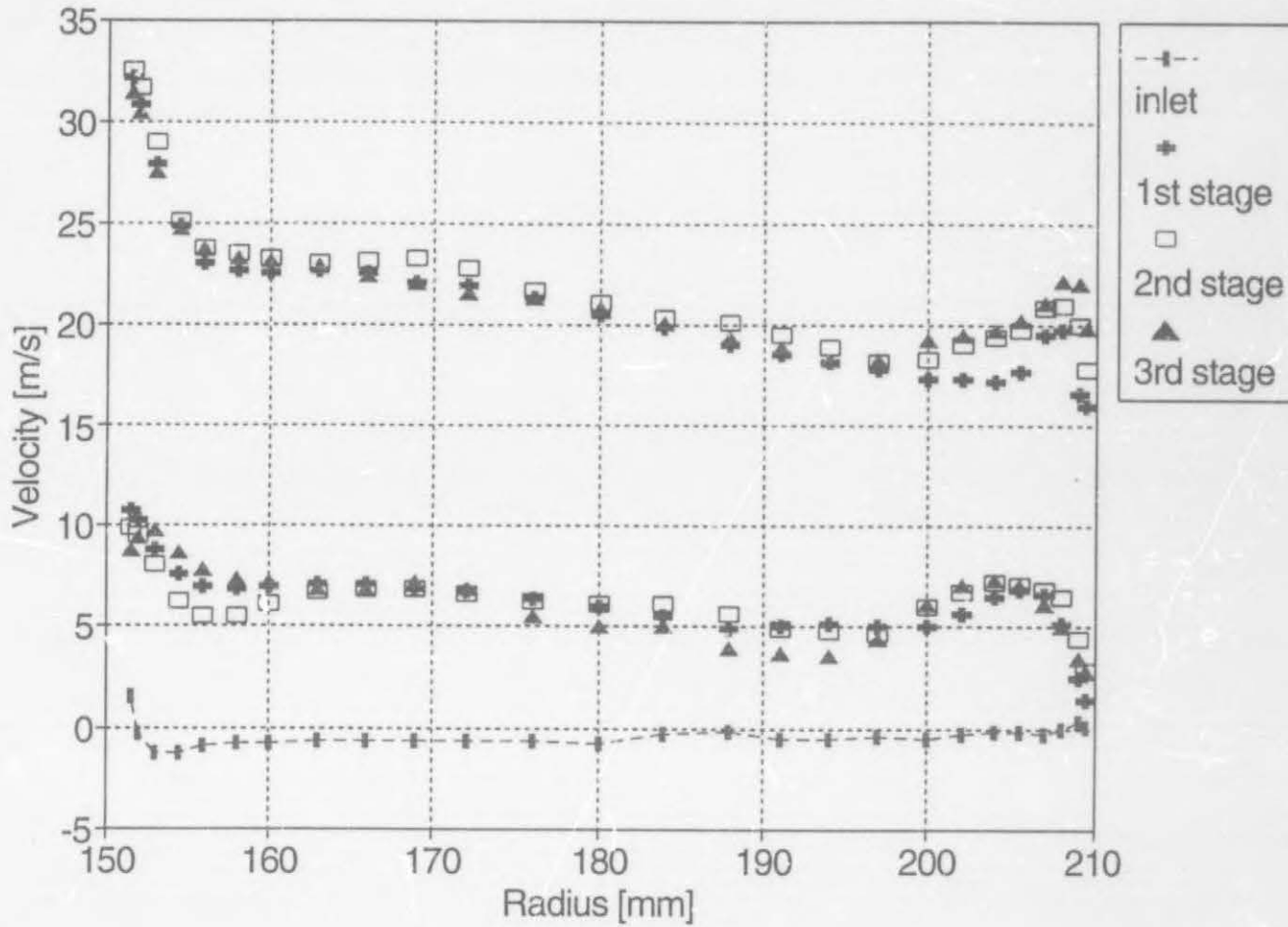


Figure 2.12: Tangential velocity profiles at near-choke flowrate: 2.80 kg/s.

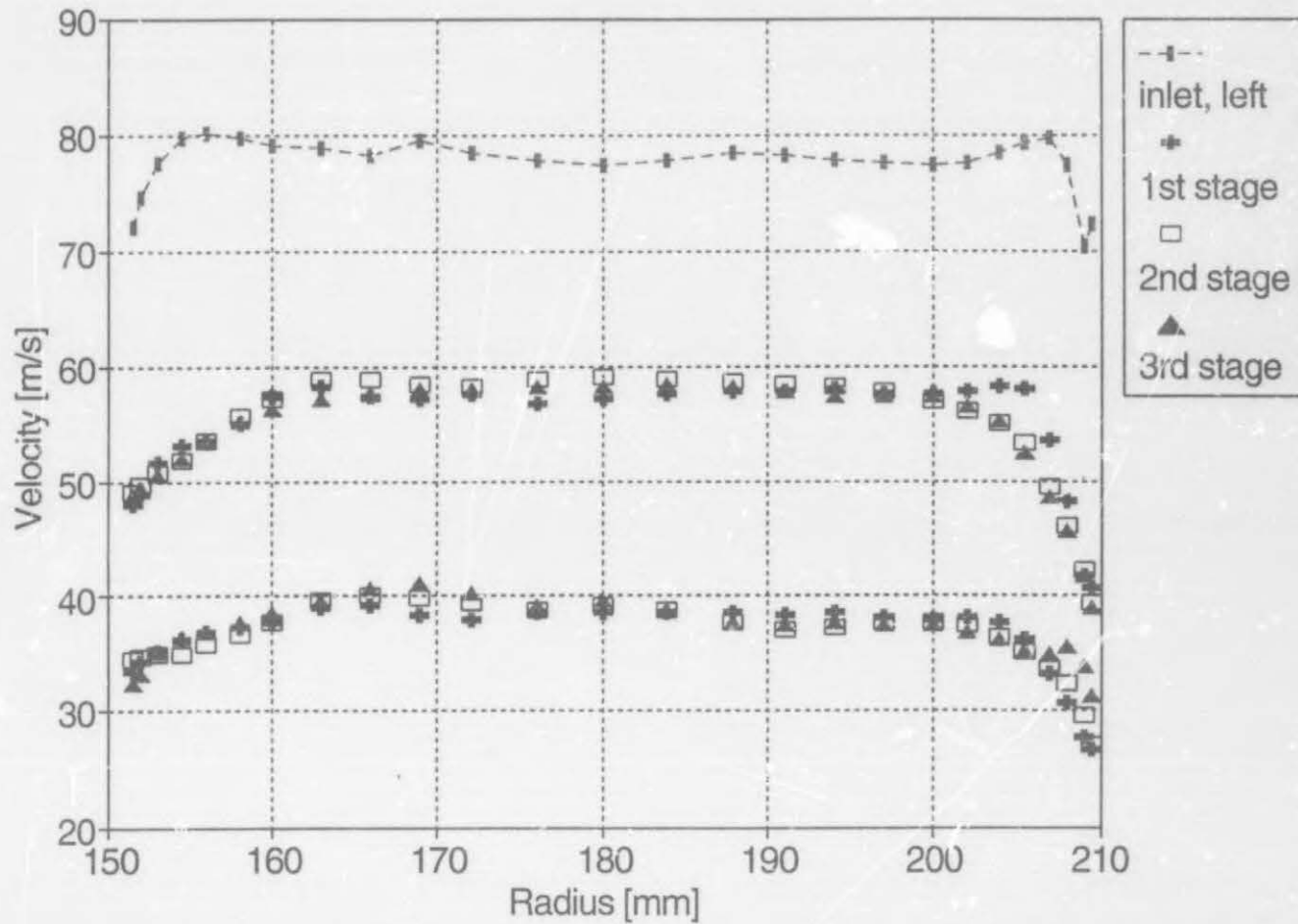


Figure 2.13: Axial velocity profiles at near-choke flowrate: 2.80 kg/s. (Zeroes of inlet and rotor rows have been staggered by 40 and 20 m/s respectively).

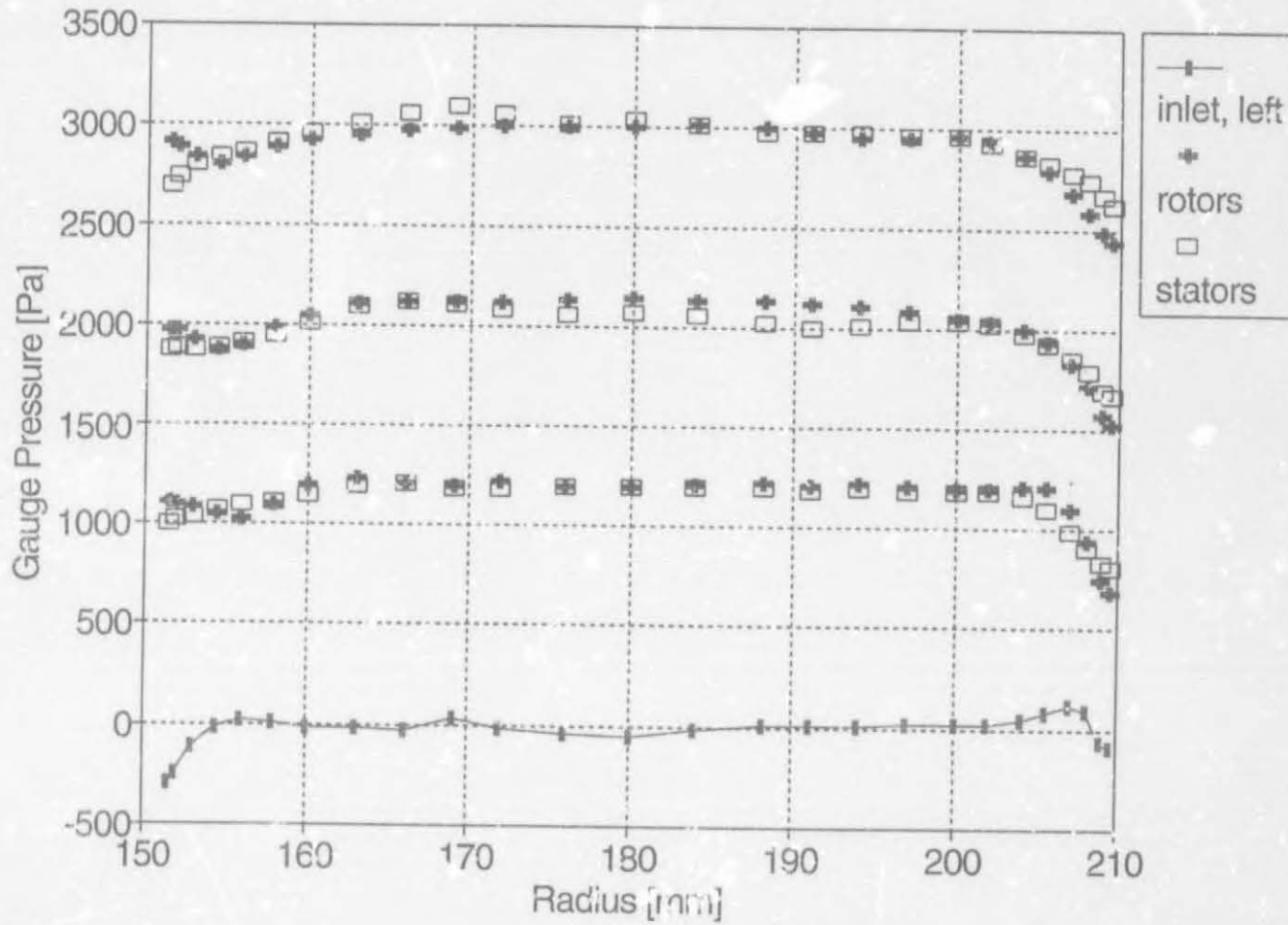


Figure 2.14: Total pressure profiles (relative to inlet mass average) at near-choke flowrate: 2.80 kg/s.

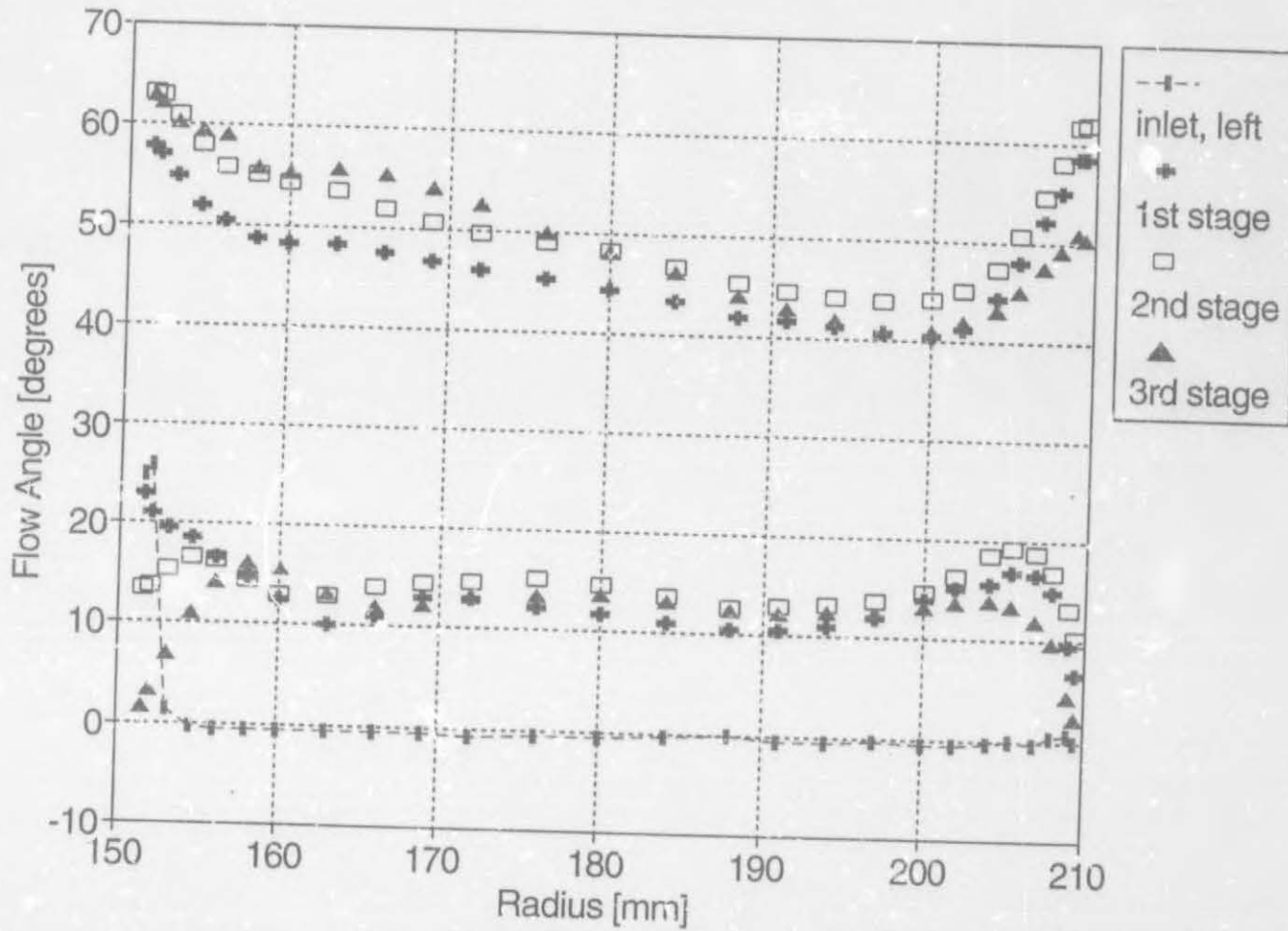


Figure 2.15: Flow angle profiles at near-surge flowrate: 1.99 kg/s.

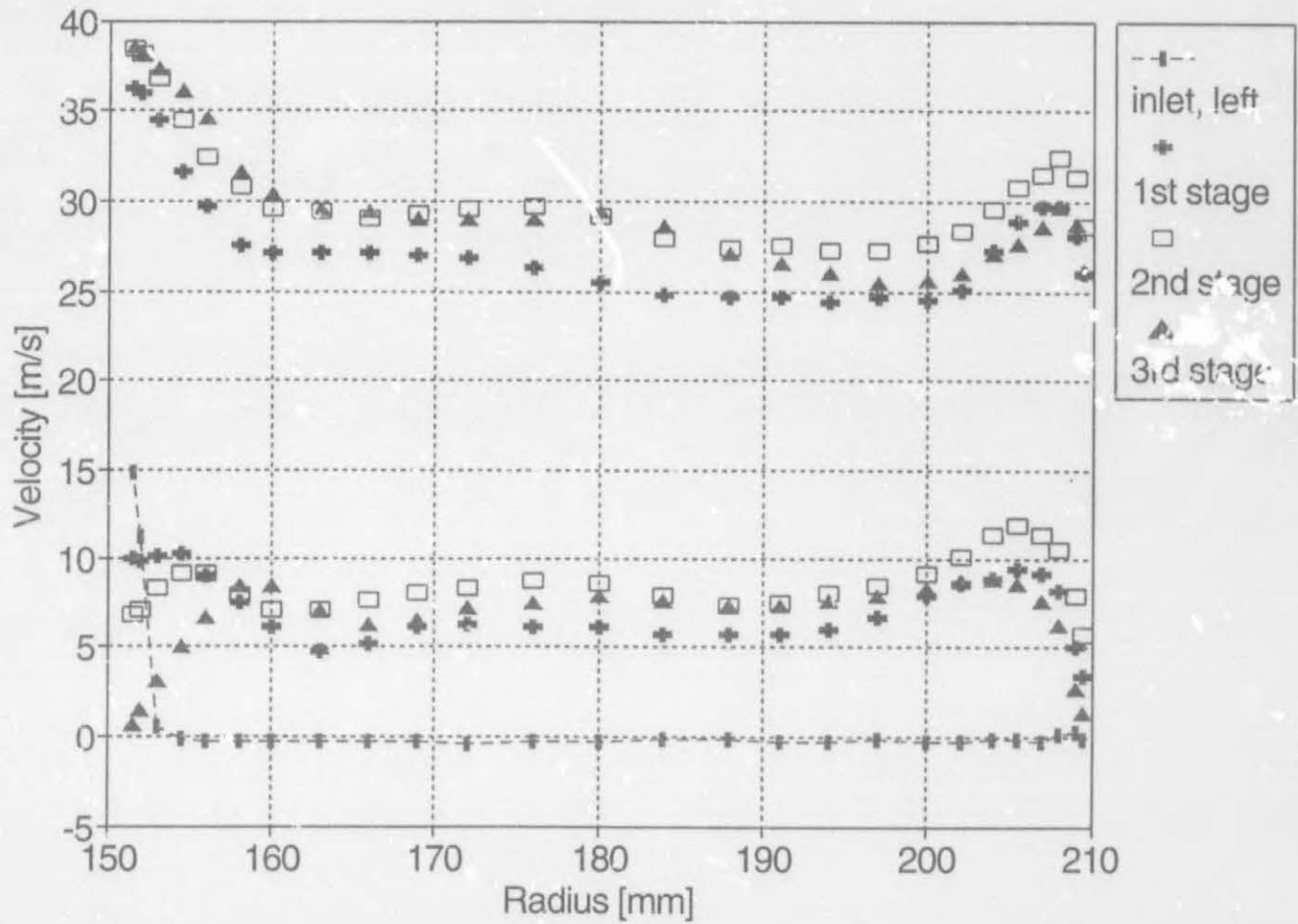


Figure 2.16: Tangential velocity profiles at near-surge flowrate: 1.99 kg/s.

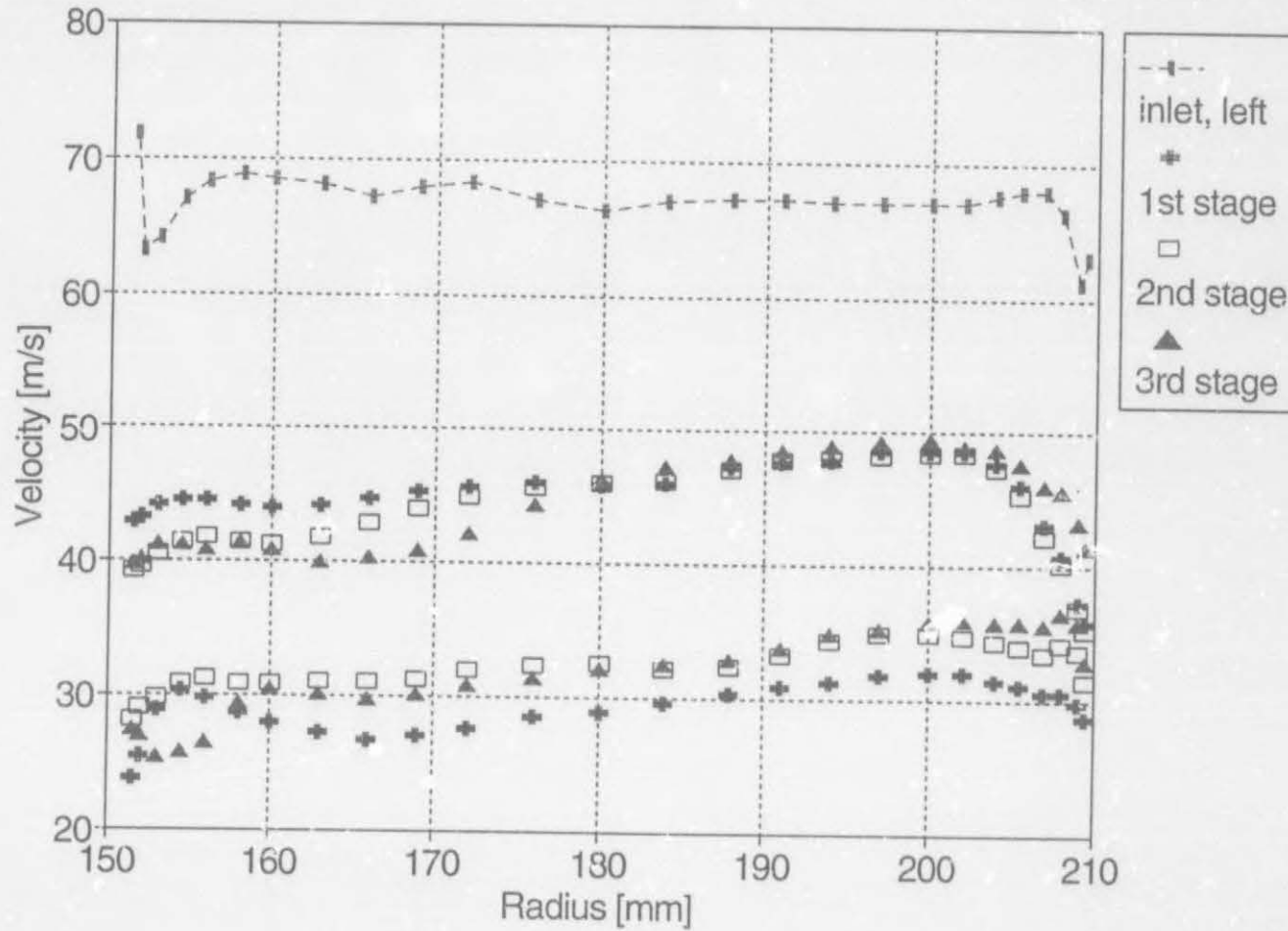


Figure 2.17: Axial velocity profiles at near-surge flowrate: 1.99 kg/s. (Zeroes of inlet and rotor rows have been staggered by 40 and 20 m/s respectively).

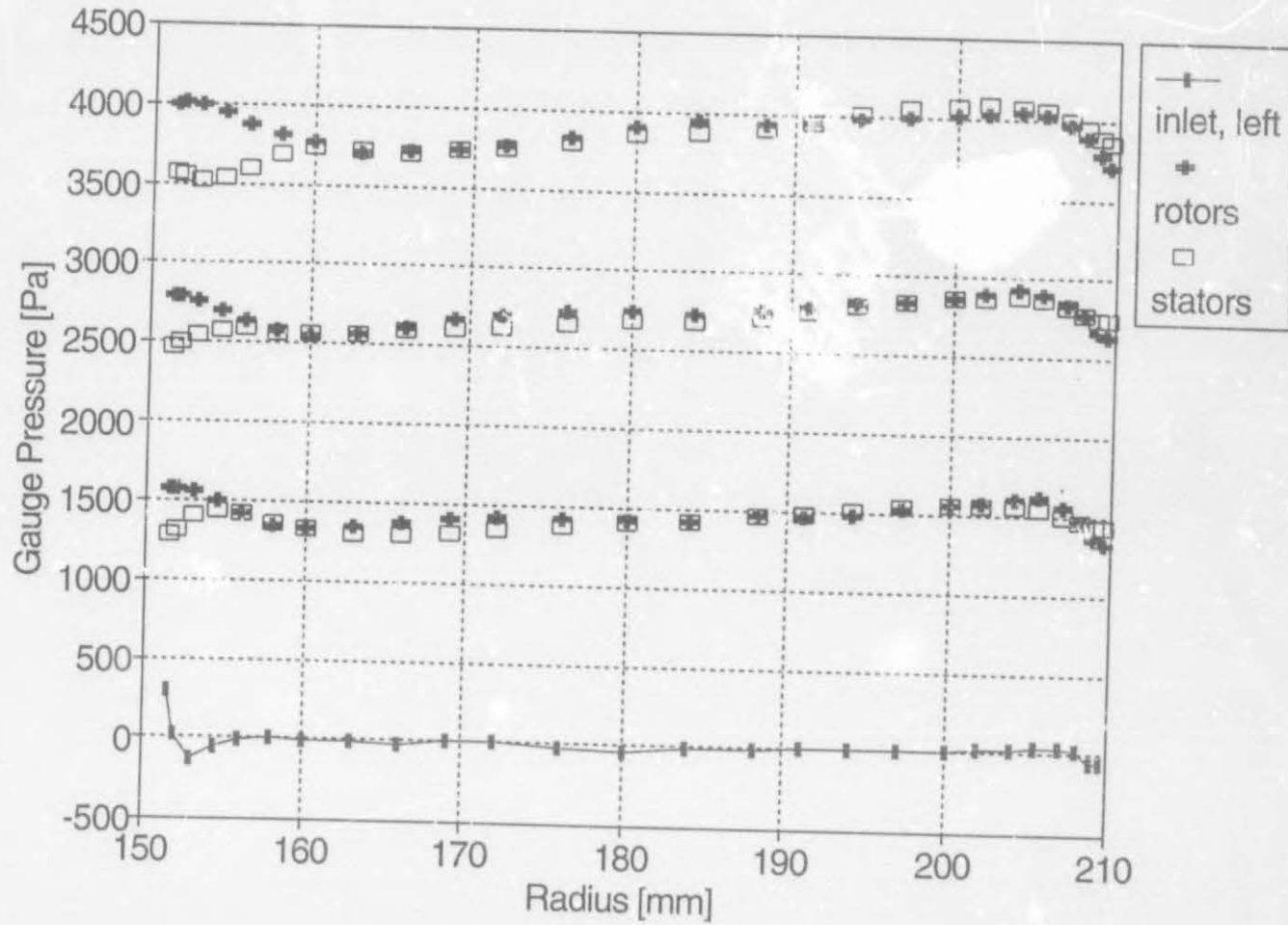


Figure 2.18: Total pressure profiles (relative to inlet mass average) at near-surge flowrate: 1.99 kg/s.

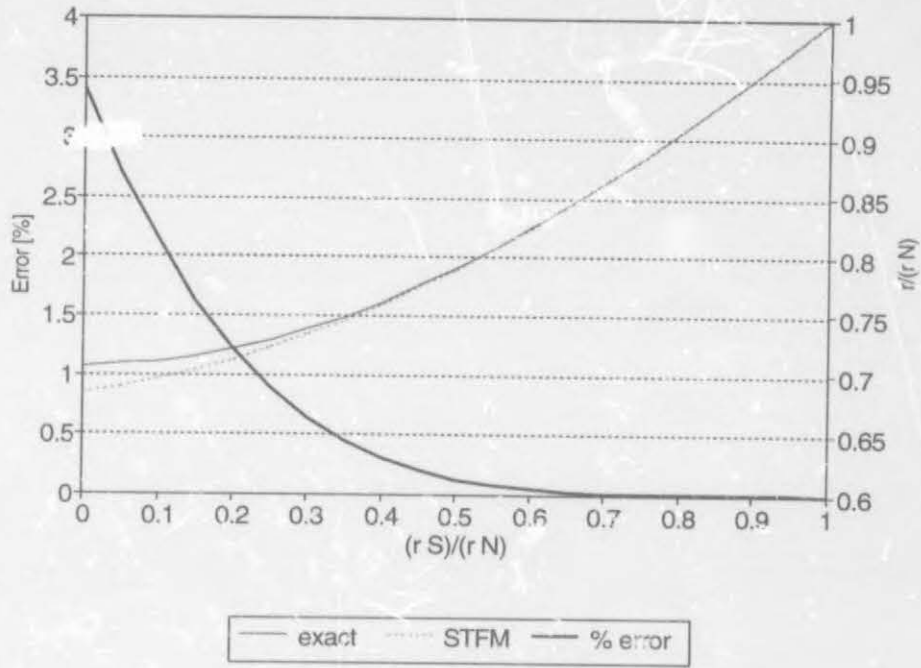


Figure 3.1: Effect of $\frac{r_s}{r_N}$ on discretisation error

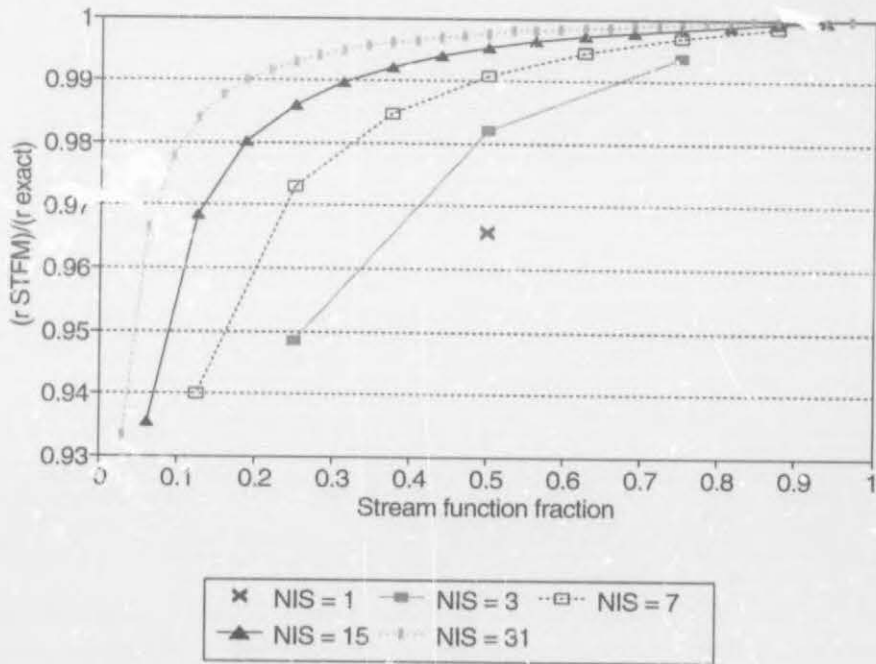


Figure 3.2: Effect of number of internal streamlines (NIS) on error ($r_i = 0$)

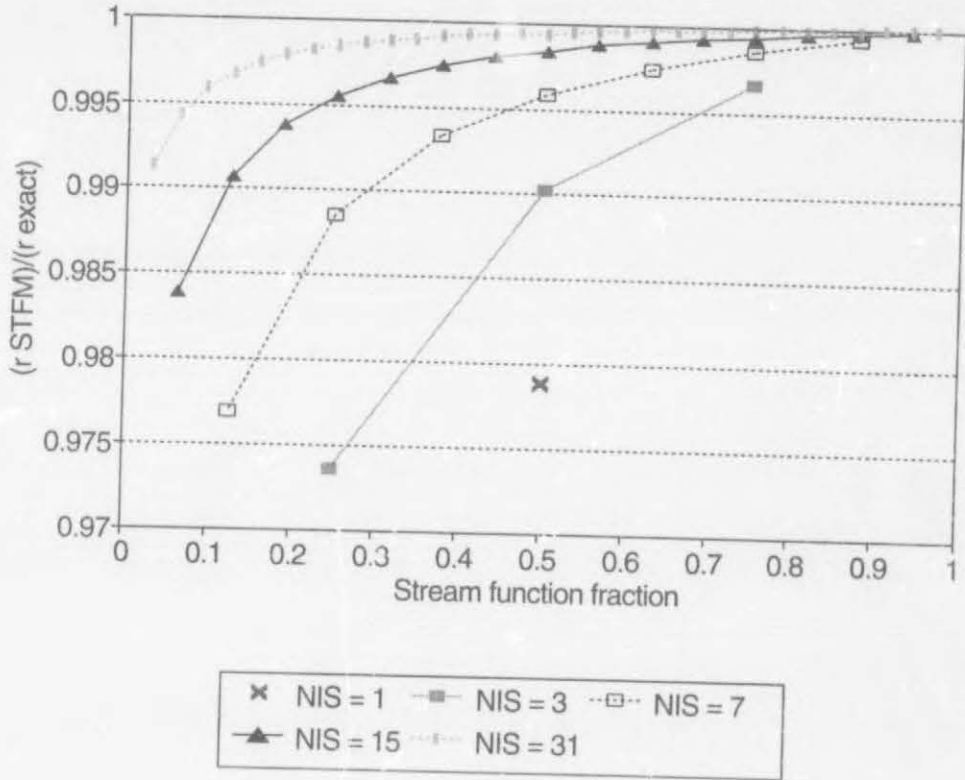


Figure 3.3: Effect of number of internal streamlines (NIS) on error ($r_i = 0.1 r_o$)

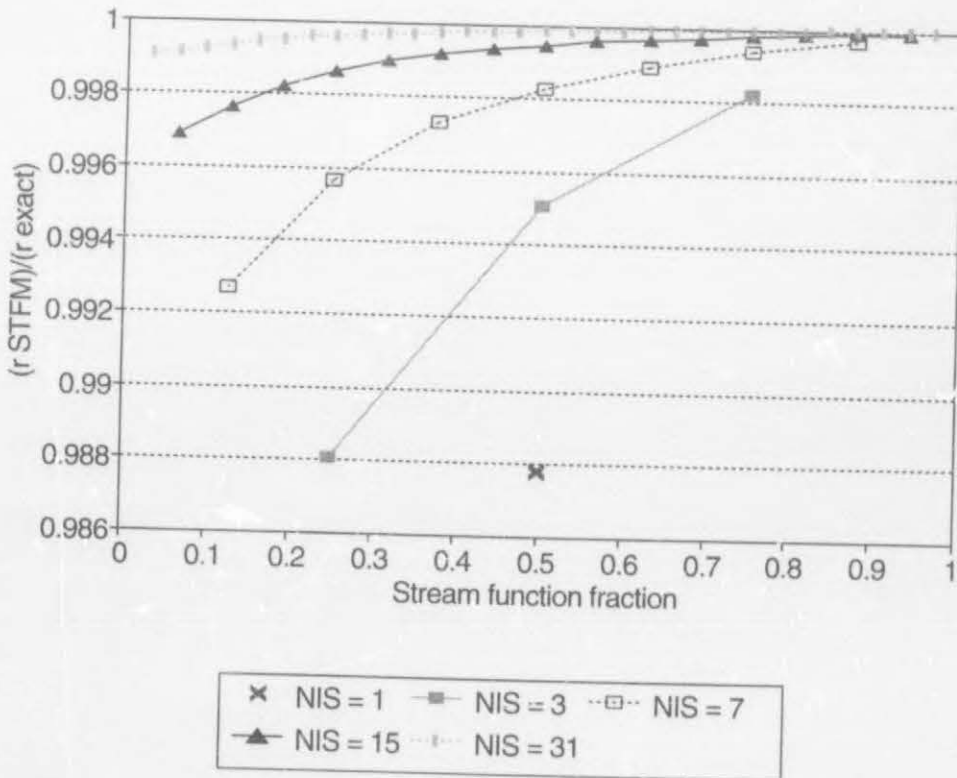


Figure 3.4: Effect of number of internal streamlines (NIS) on error ($r_i = 0.2 r_o$)

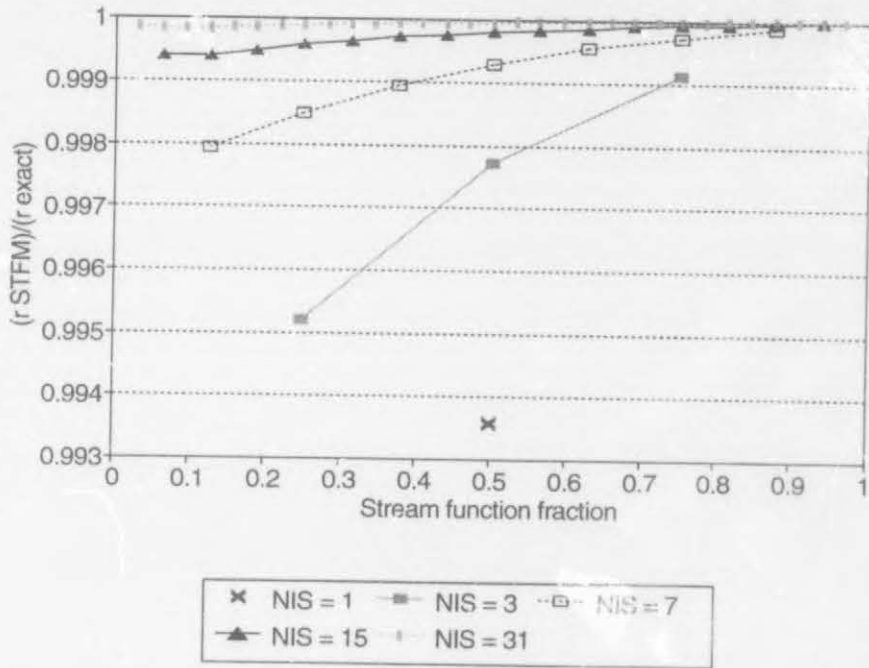


Figure 3.5: Effect of number of internal streamlines (NIS) on error
 $(r_i = 0.3 r_o)$

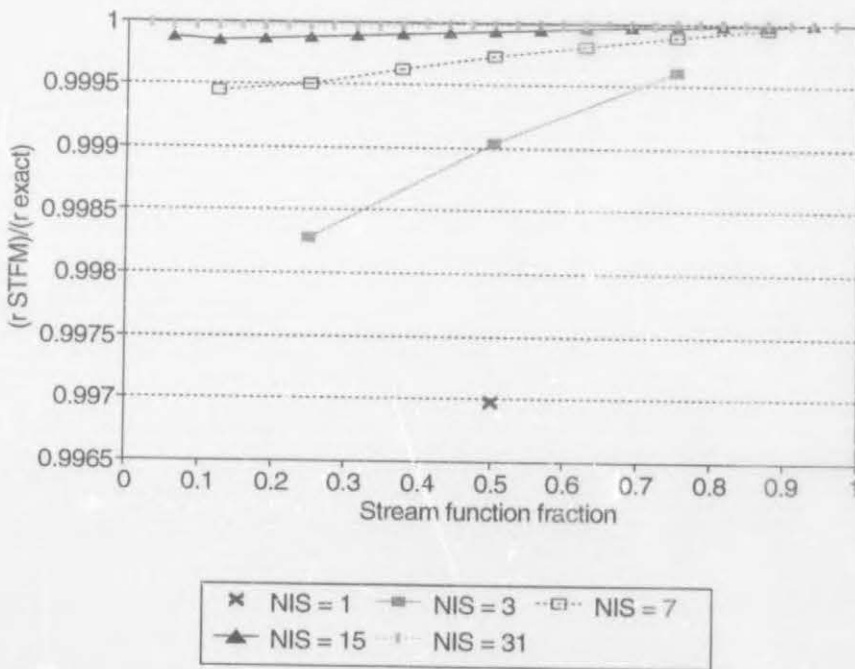


Figure 3.6: Effect of number of internal streamlines (NIS) on error
 $(r_i = 0.4 r_o)$

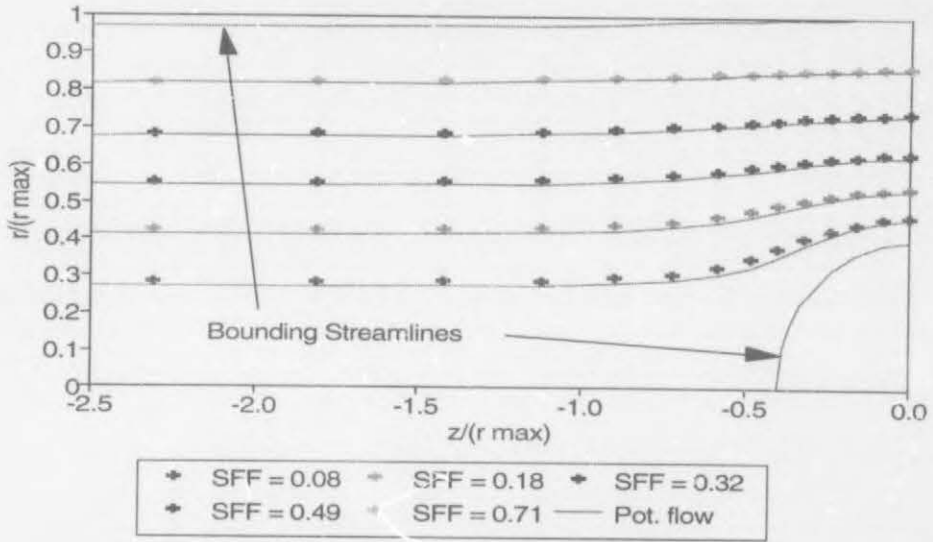


Figure 3.7: Flow over a sphere: STFMs and potential flow solutions for varying stream function fractions (SFF)

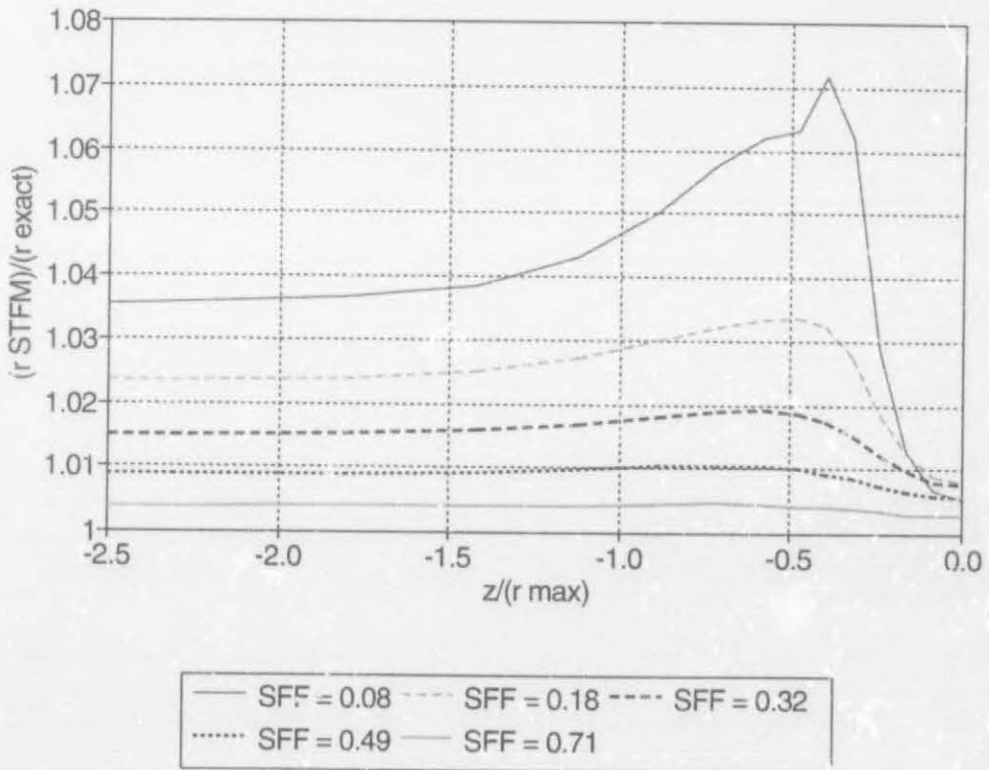


Figure 3.8: Error for flow over a sphere at different stream function fractions (SFF)

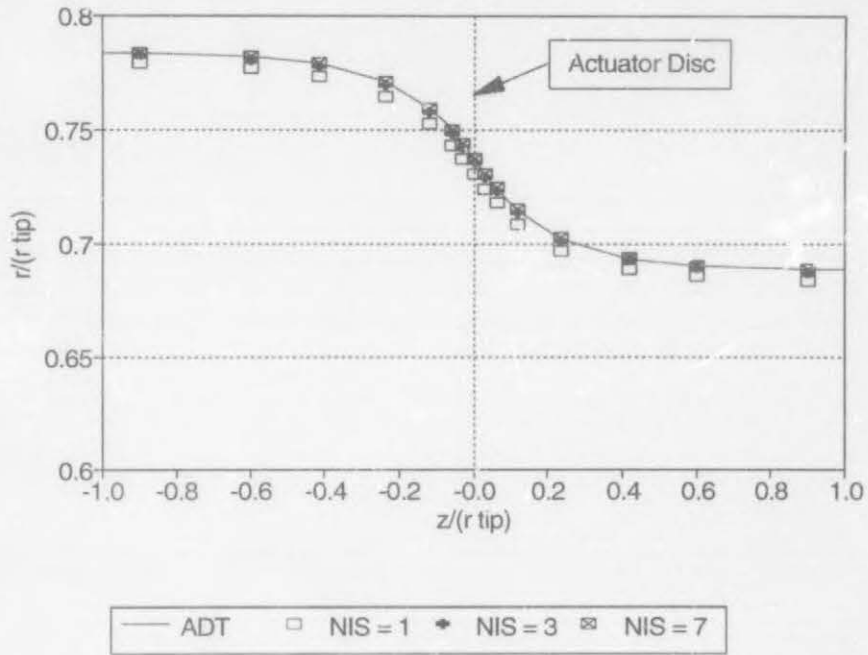


Figure 3.9: Median internal streamline position for actuator disc flow with different numbers of internal streamlines (NIS)

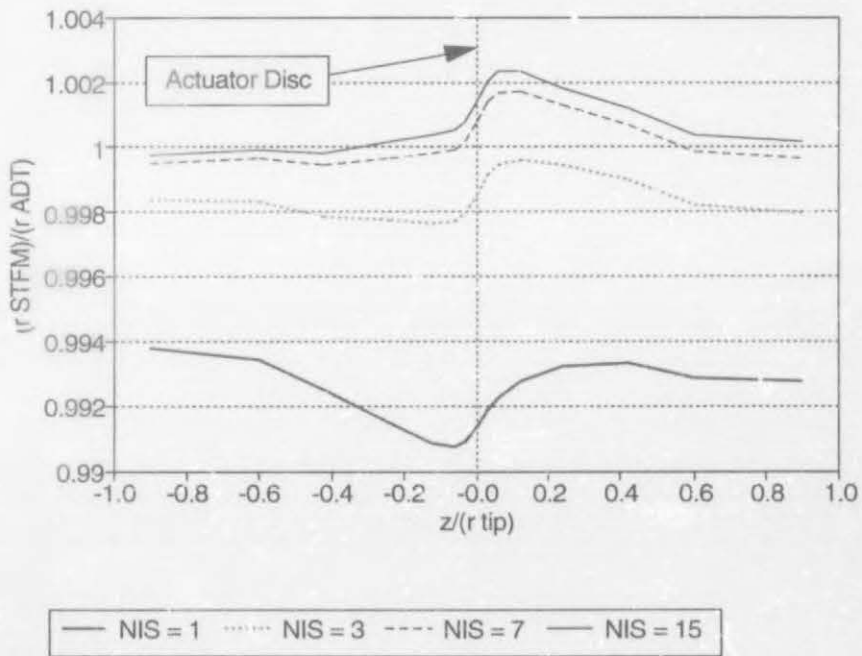


Figure 3.10: Error in median internal streamline position for actuator disc flow with different numbers of internal streamlines (NIS)

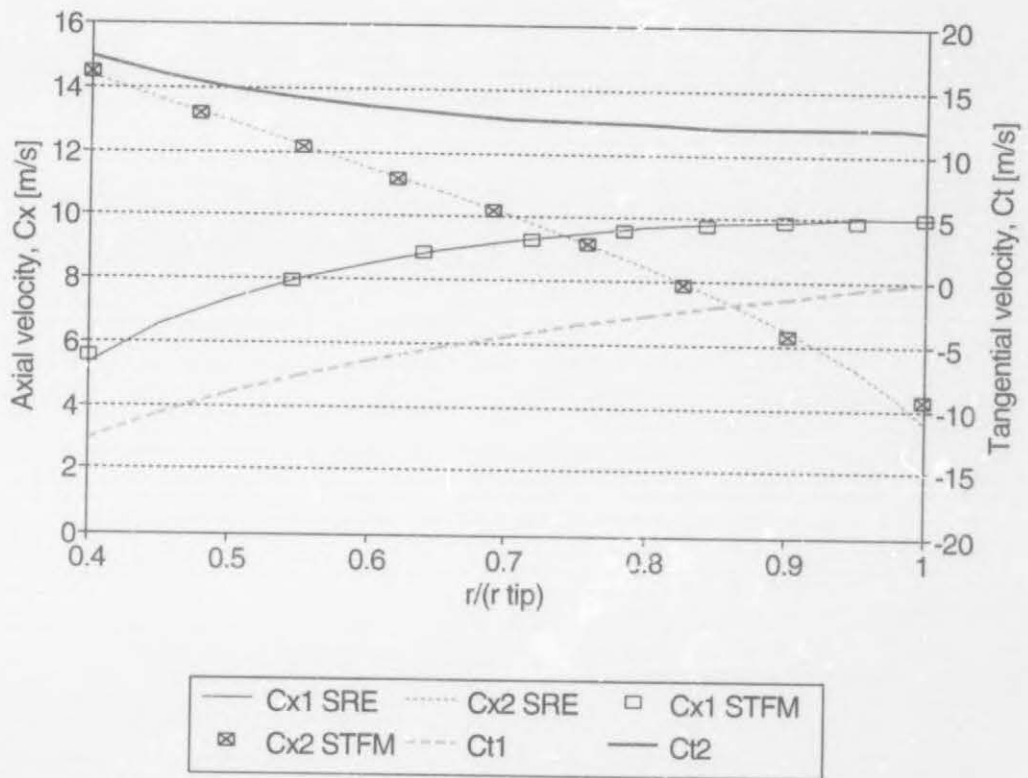


Figure 3.11: Comparison of axial (SRE and STFM) and tangential velocity profiles for actuator disc flow with 7 internal streamlines

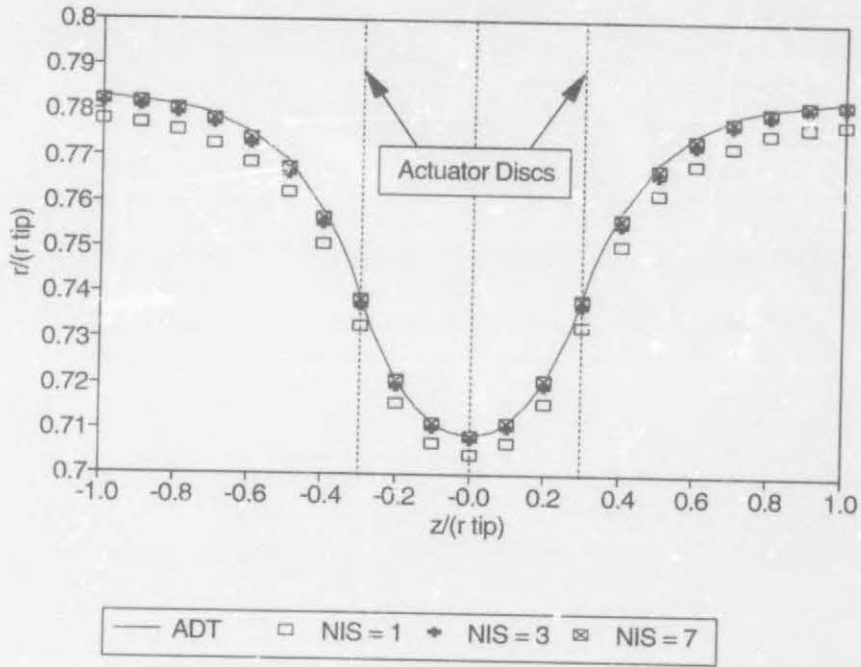


Figure 3.12: Median internal streamline position for twin actuator disc flow with different numbers of internal streamlines (NIS) (25 equispaced nodes)

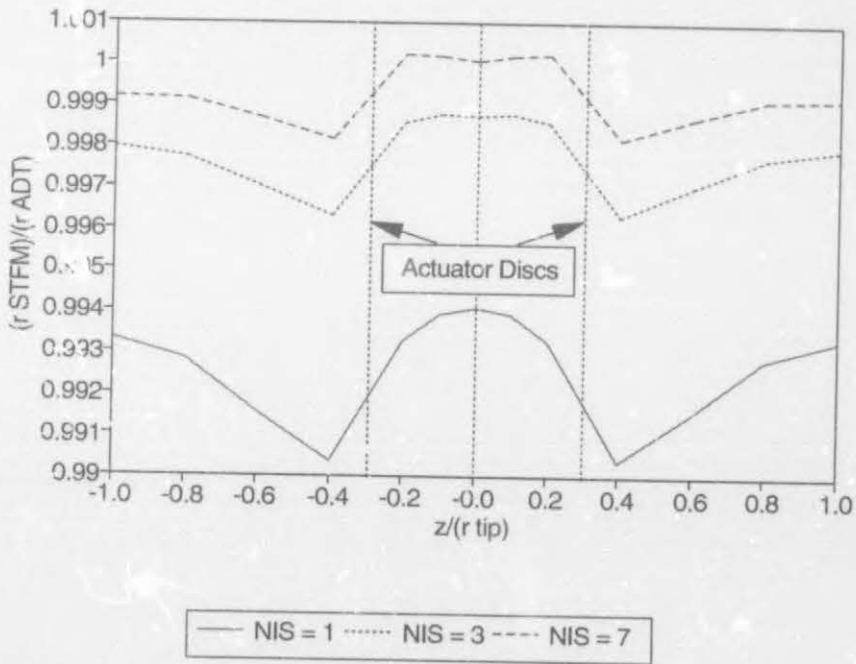


Figure 3.13: Error in median internal streamline position for twin actuator disc flow with different numbers of internal streamlines (NIS) (25 equispaced nodes)

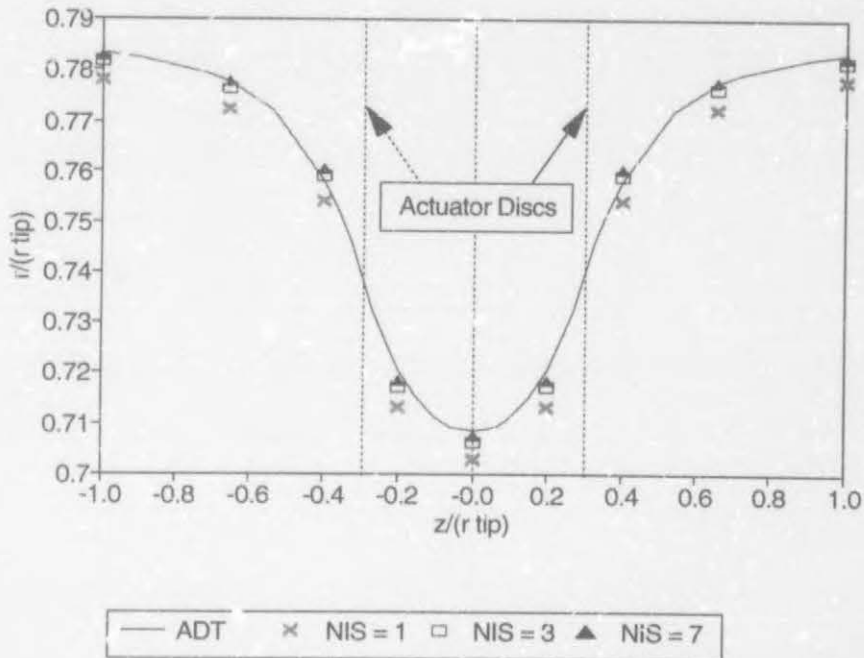


Figure 3.14: Median internal streamline position for twin actuator disc flow with different numbers of internal streamlines (NIS) using sparse non-uniform axial spacing with three nodes between the discs

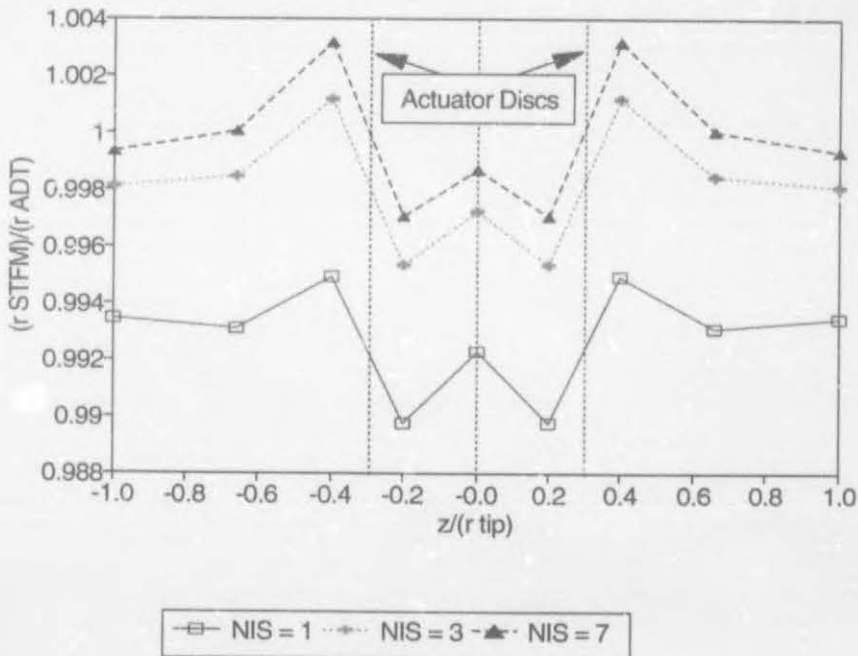


Figure 3.15: Error in median internal streamline position for twin actuator disc flow with different numbers of internal streamlines (NIS) using sparse non-uniform axial spacing with three nodes between the discs

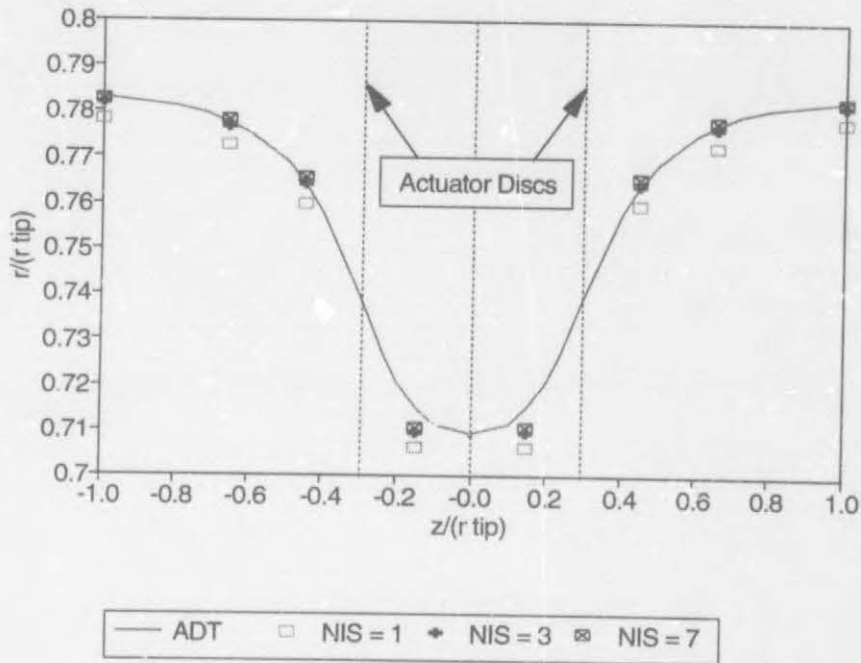


Figure 3.16: Median internal streamline position for twin actuator disc flow with different numbers of internal streamlines (NIS) using sparse non-uniform axial spacing with two nodes between the discs

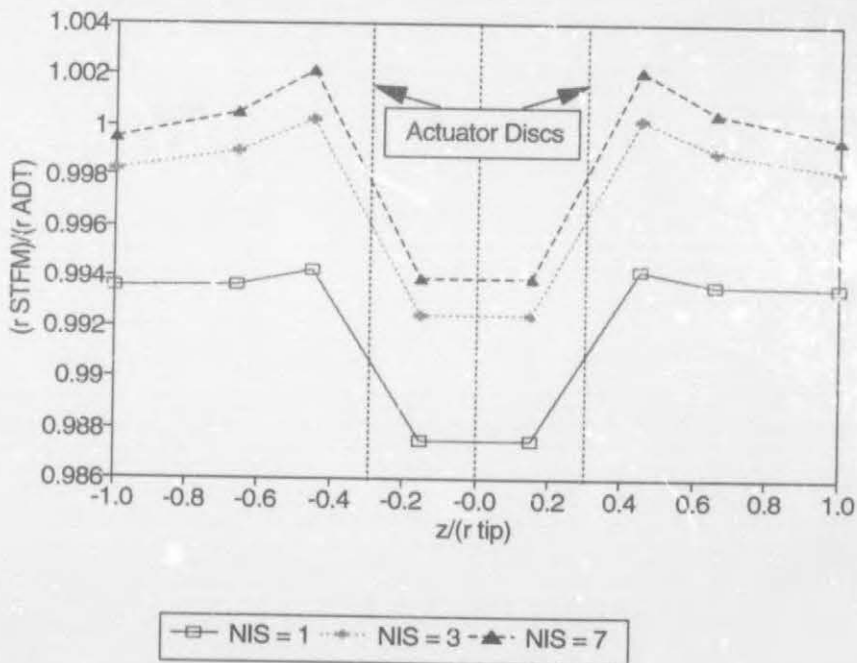


Figure 3.17: Error in median internal streamline position for twin actuator disc flow with different numbers of internal streamlines (NIS) using sparse non-uniform axial spacing with two nodes between the discs

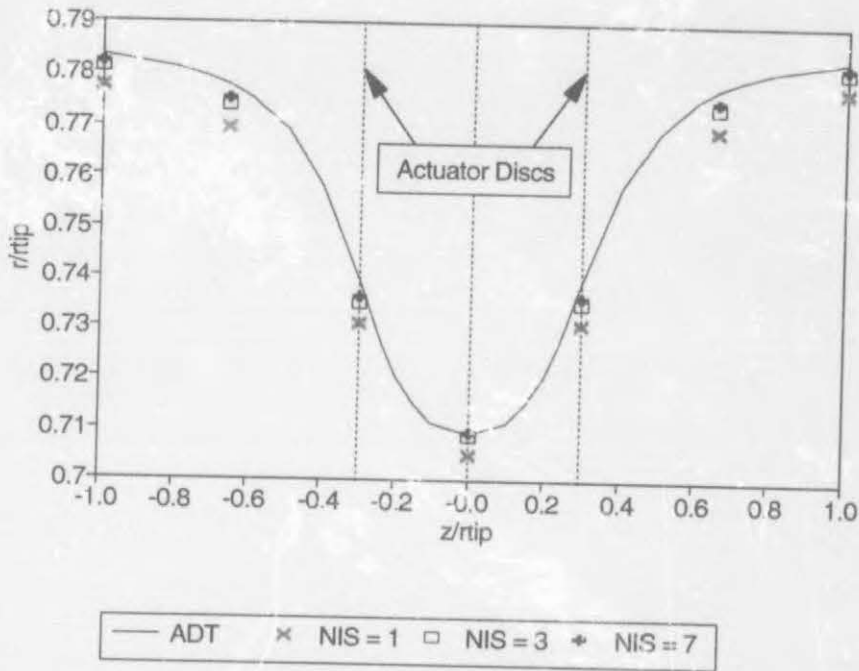


Figure 3.18: Median internal streamline position for twin actuator disc flow with different numbers of internal streamlines (NIS) using sparse non-uniform axial spacing with a single node between the discs

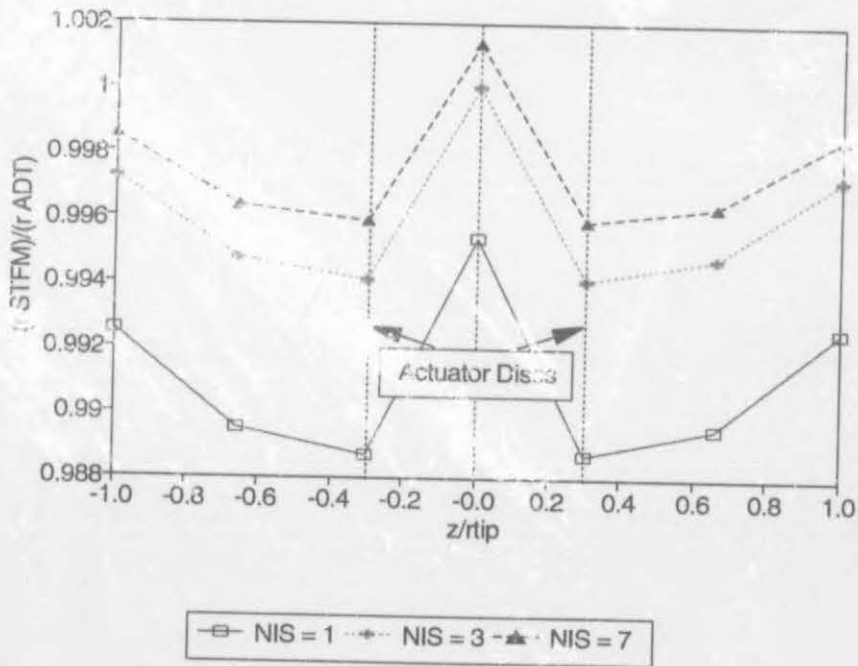


Figure 3.19: Error in median internal streamline position for twin actuator disc flow with different numbers of internal streamlines (NIS) using sparse non-uniform axial spacing with a single node between the discs

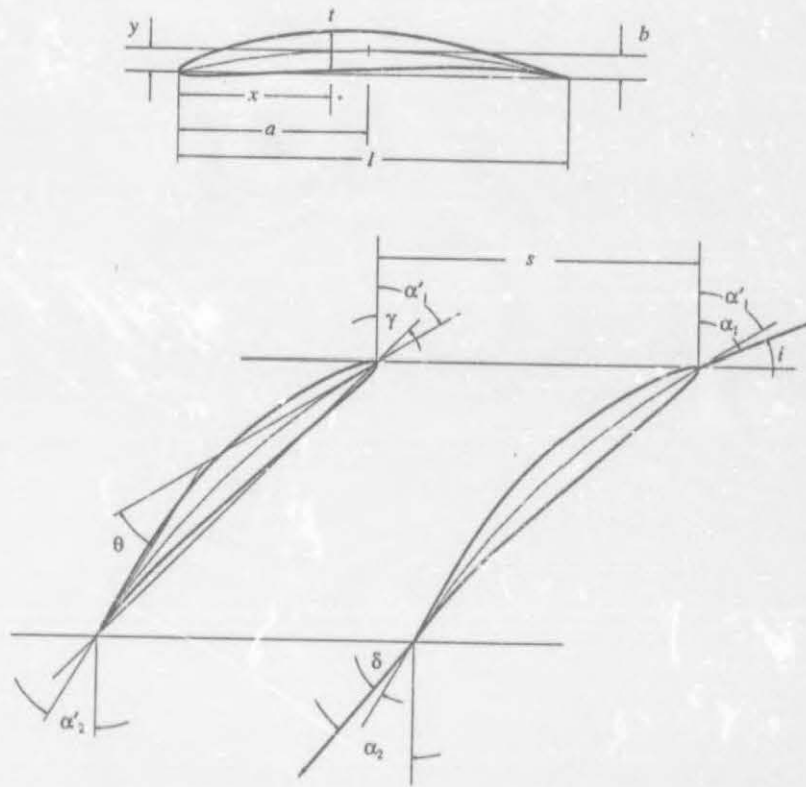


Figure 4.1: Compressor cascade and blade notation

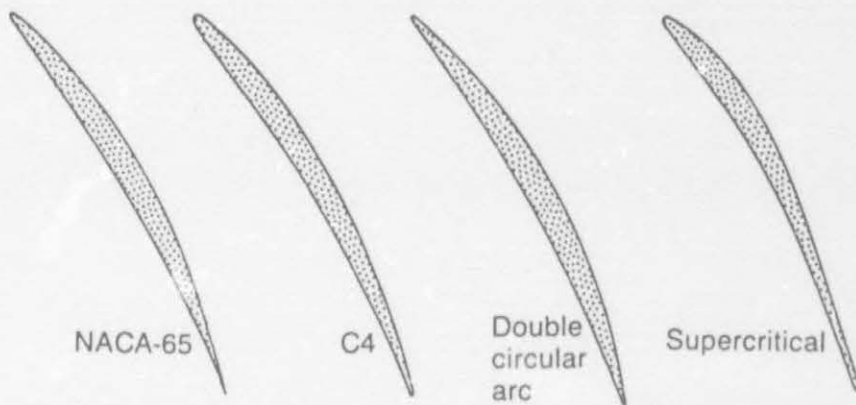


Figure 4.2: Four compressor blade profiles for nominally identical turning,
 $\alpha_1 = 43.6^\circ$, $\alpha_2 = 23.5^\circ$

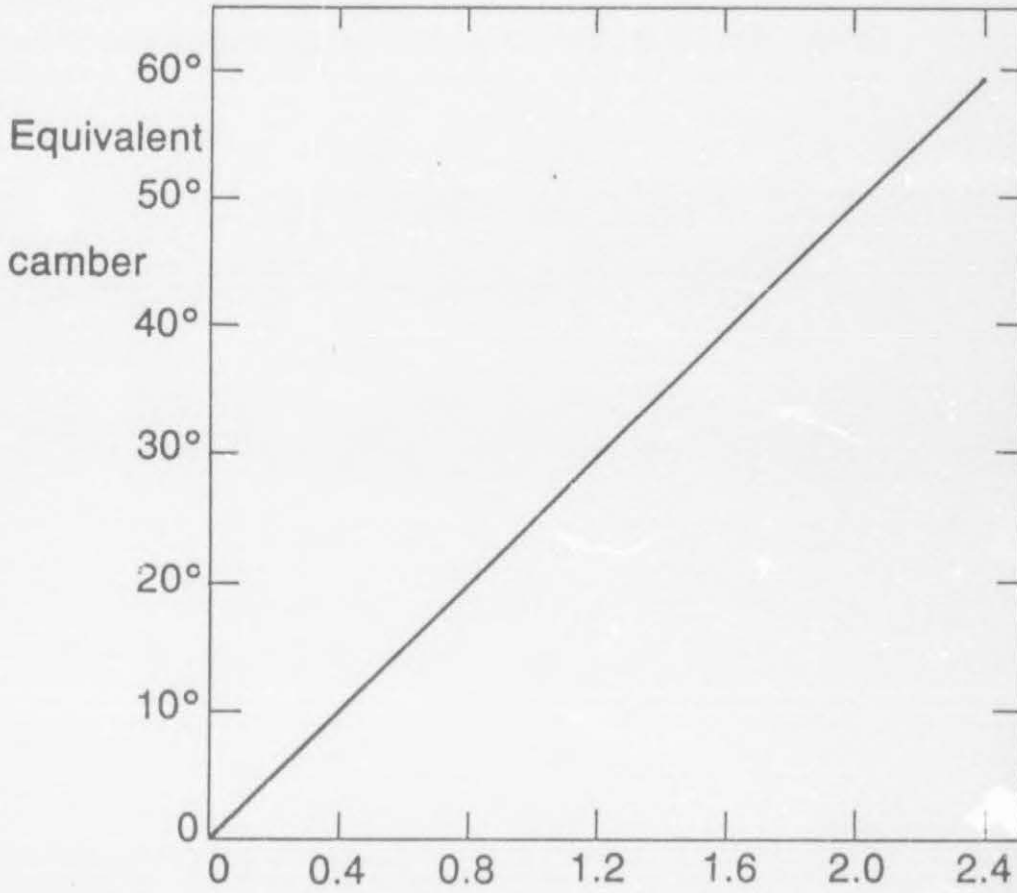


Figure 4.3: Relationship between isolated aerofoil lift coefficient and equivalent camber for NACA 65-Series profiles

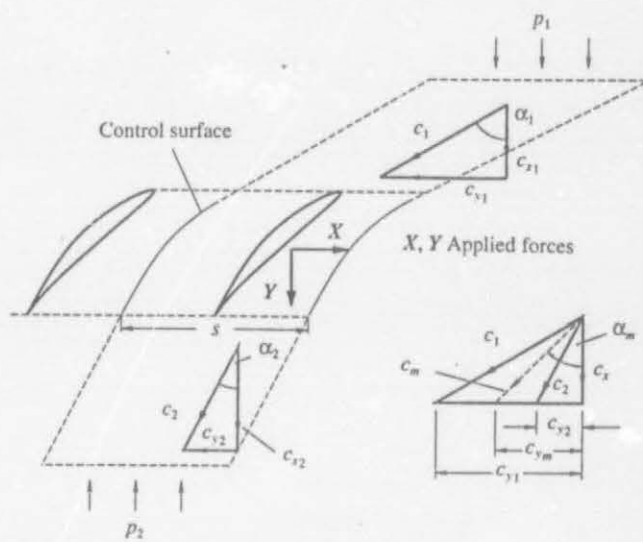


Figure 4.4: Forces and velocities in a cascade

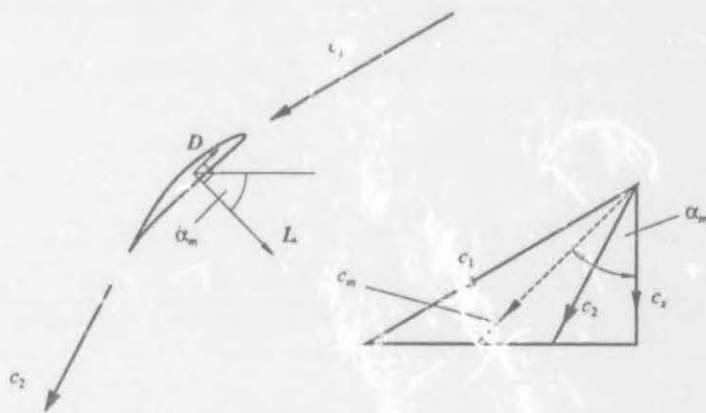


Figure 4.5: Lift and drag forces exerted by unit span of a cascade blade upon the fluid

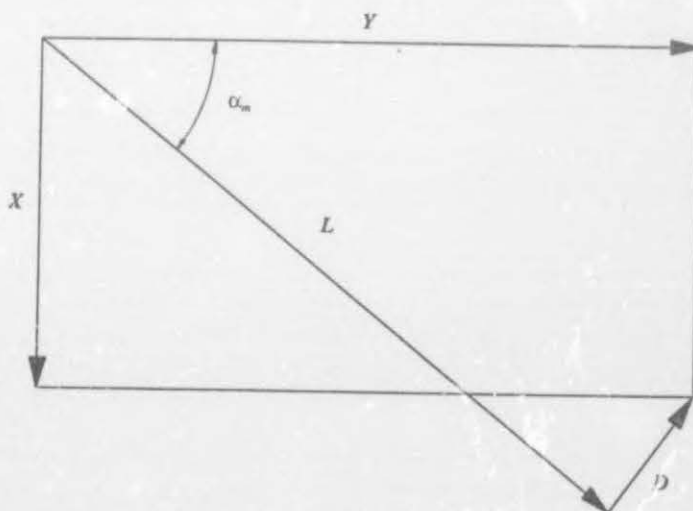


Figure 4.6: Axial and tangential forces exerted by unit span of a blade upon the fluid

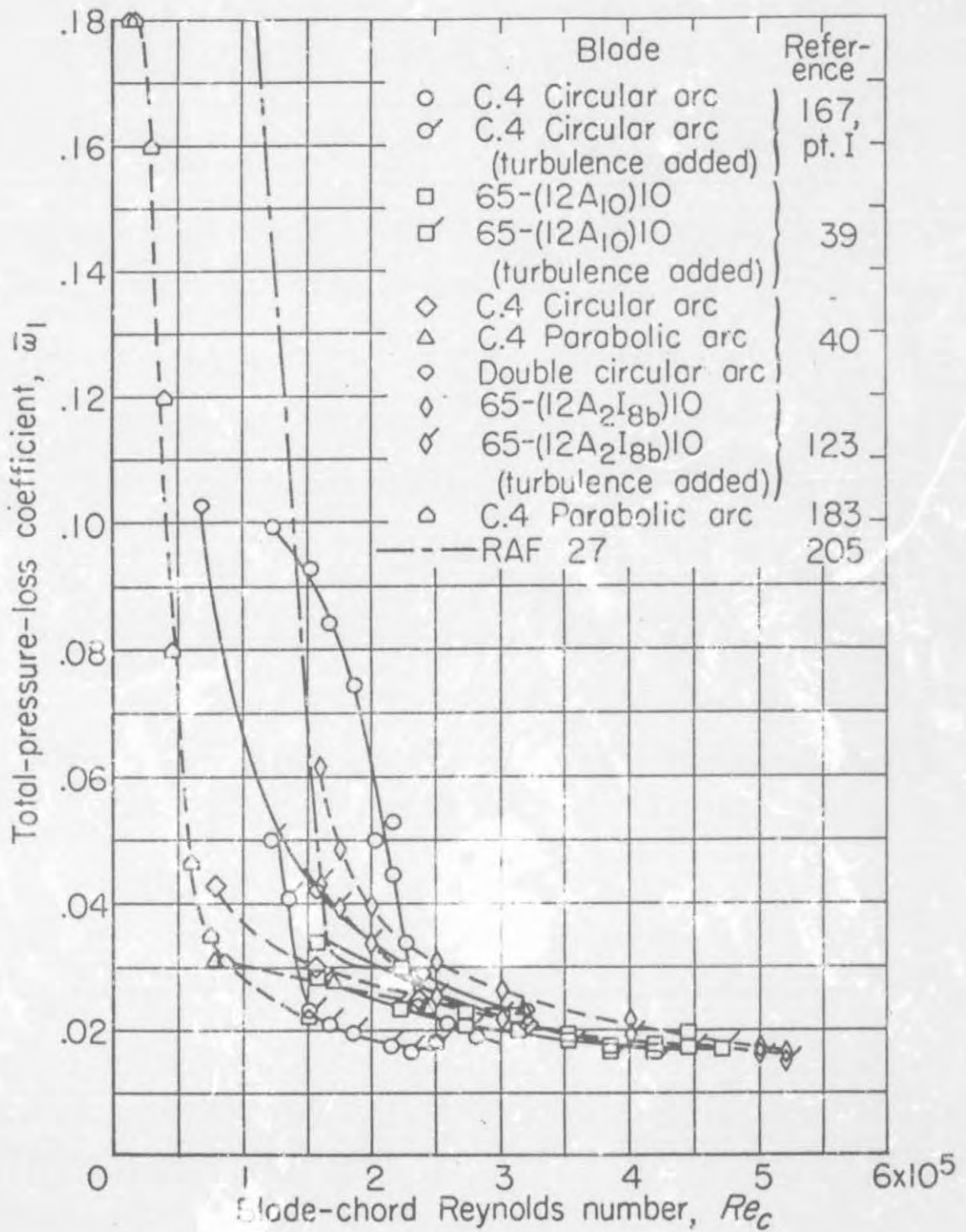


Figure 5.1: Total pressure loss coefficient as a function of Reynolds number in region of minimum loss at low speed for various cascade profiles.

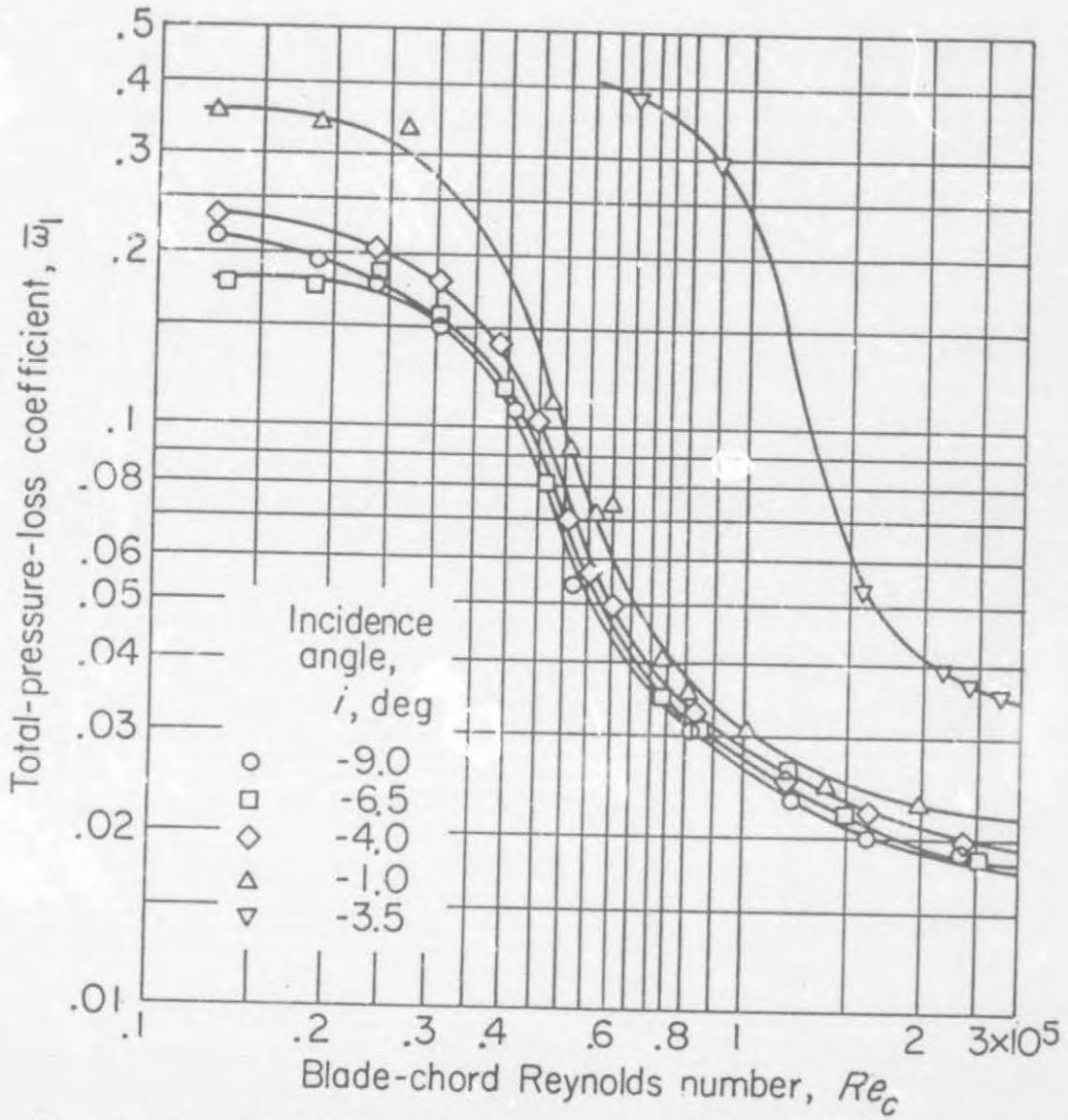


Figure 5.2: Variation of total pressure loss coefficient with incidence angle and Reynolds number for parabolic arc blade 10C4/40P40, α_1 varying from 28° to 40°

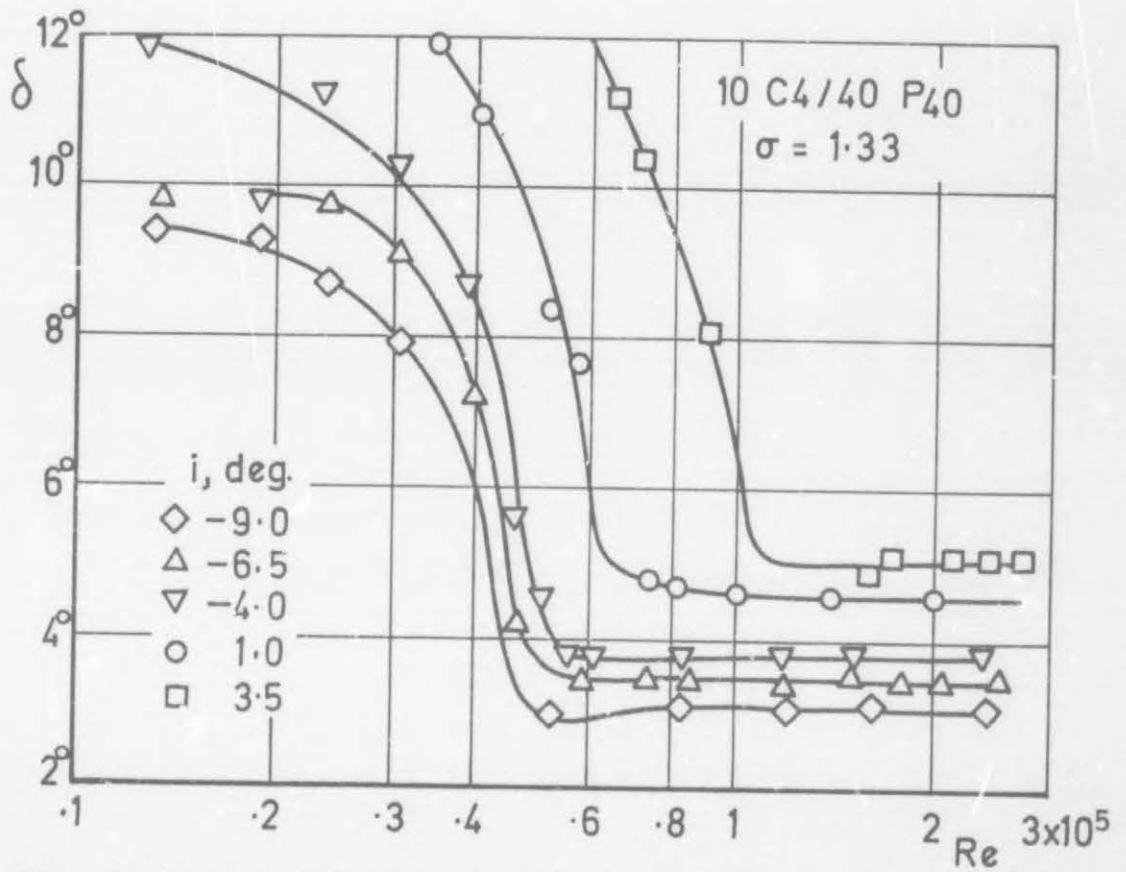


Figure 5.3: Variation of deviation angle with incidence angle and Reynolds number for parabolic arc blade 10C4/40P40, α_1 varying from 28° to 40°

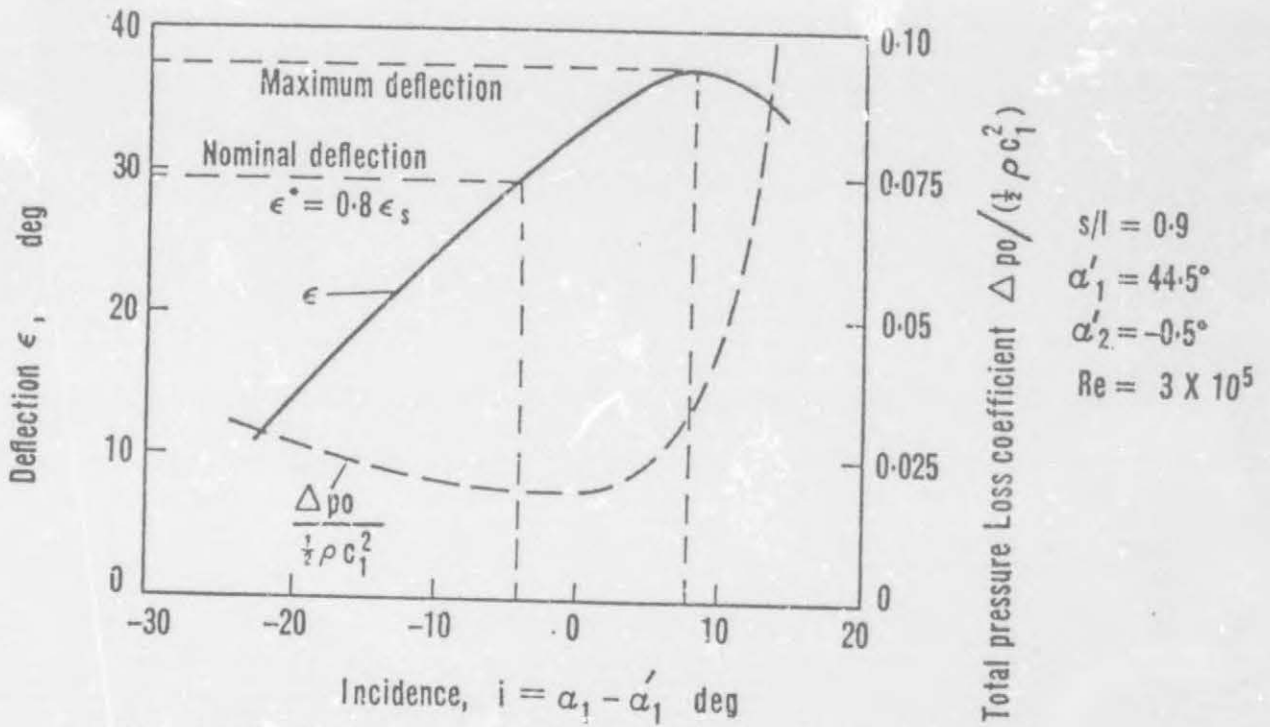


Figure 5.4: Characteristics of an 11C1/45/C50 cascade, showing Howell's nominal condition

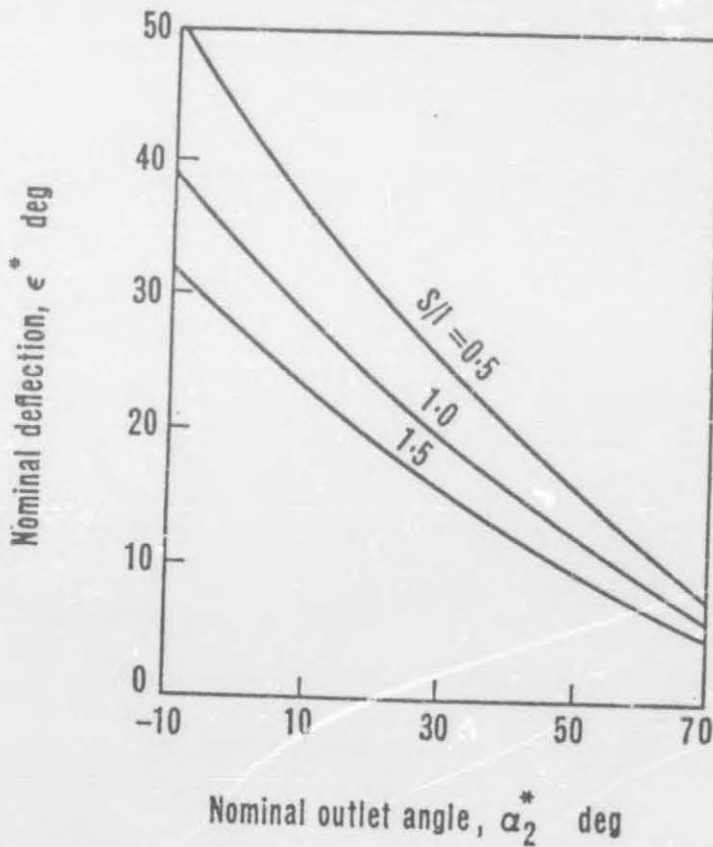


Figure 5.5: Cascade nominal deflection correlation of Howell

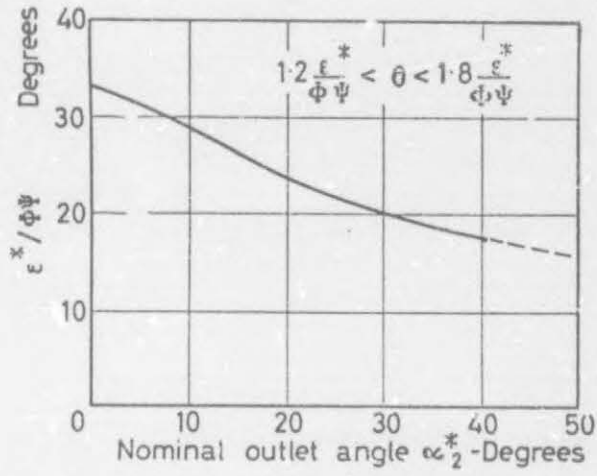


Figure 5.6: Nominal deflection as function of nominal outlet angle

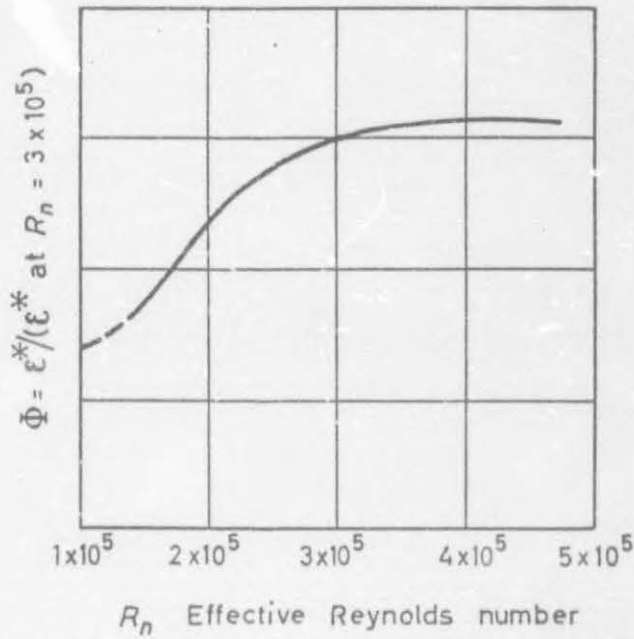


Figure 5.7: Reynolds number correction for nominal deflection

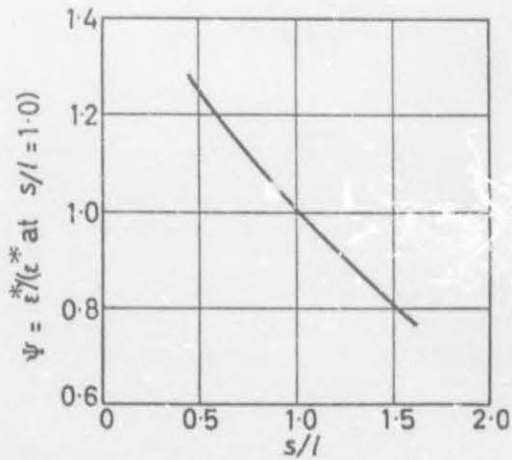


Figure 5.8: Space-chord ratio correction for nominal deflection

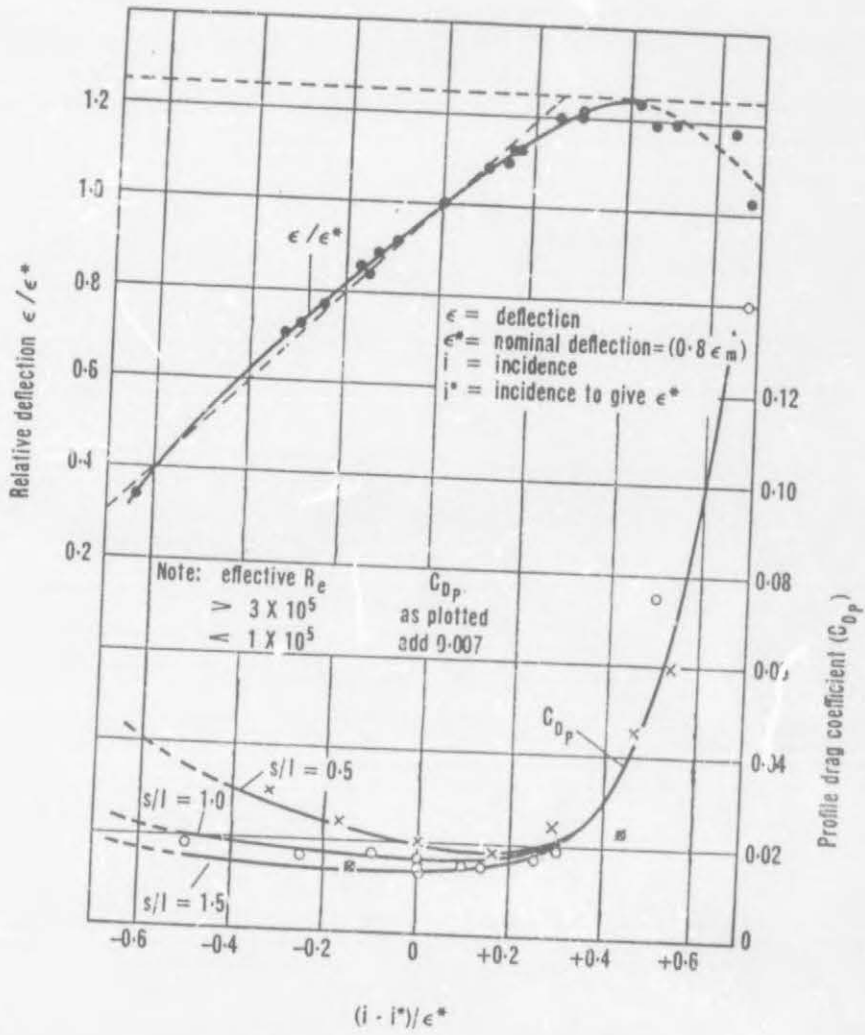


Figure 5.9: Howell's off-design cascade correlation

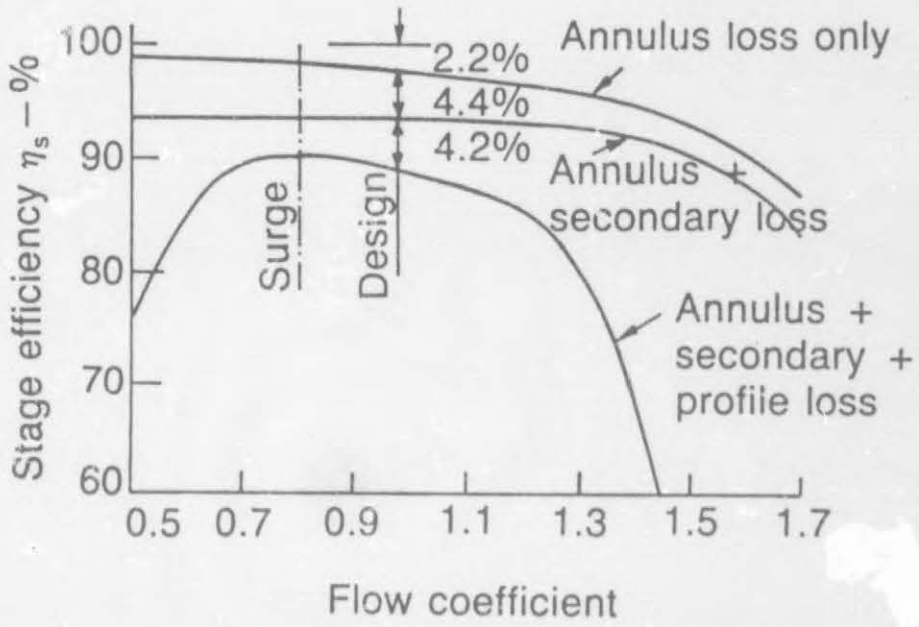


Figure 5.10: Losses in a compressor stage according to Howell

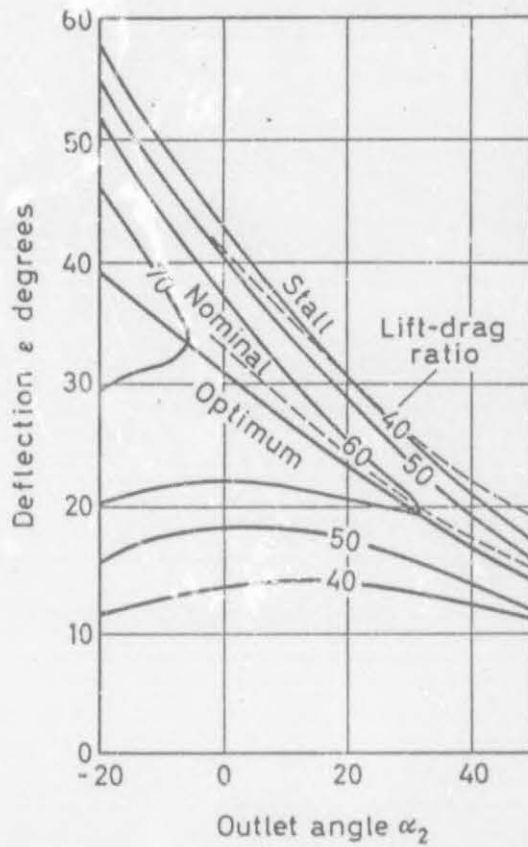


Figure 5.11: Lift-drag ratios for $s/l = 1$

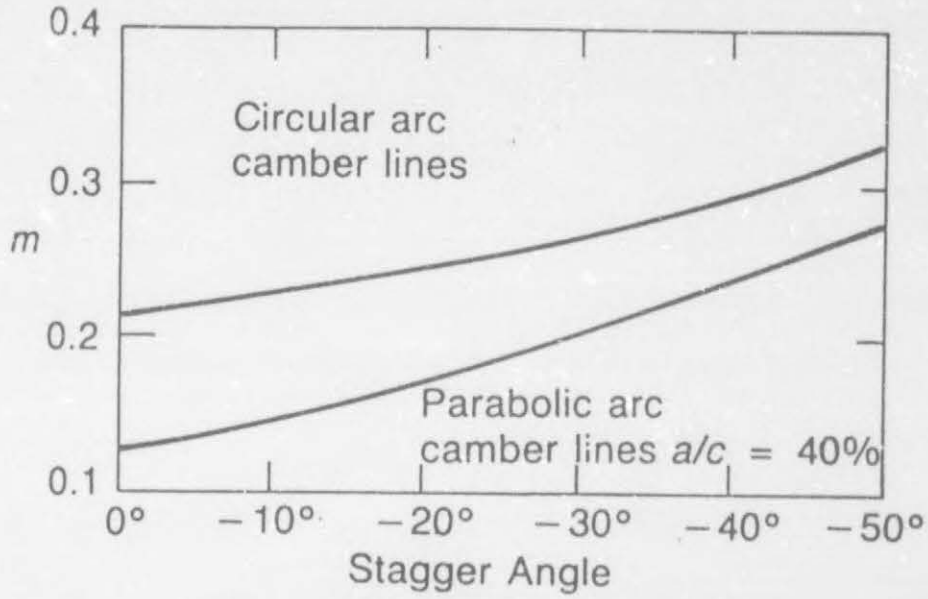


Figure 5.12: Carter's deviation rule

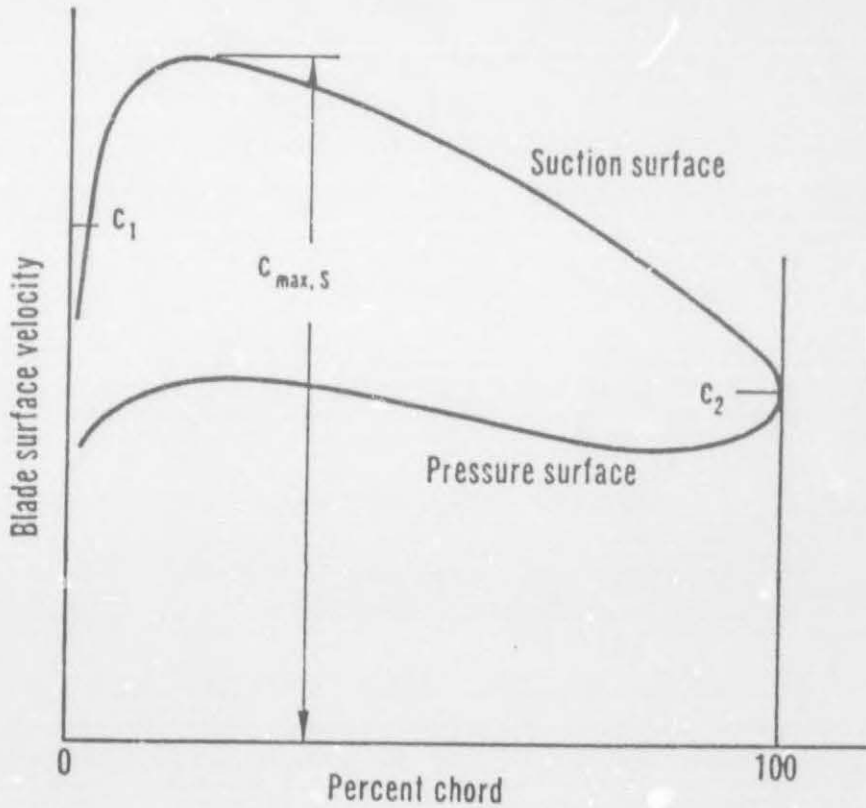


Figure 5.13: Compressor cascade blade surface velocity distribution

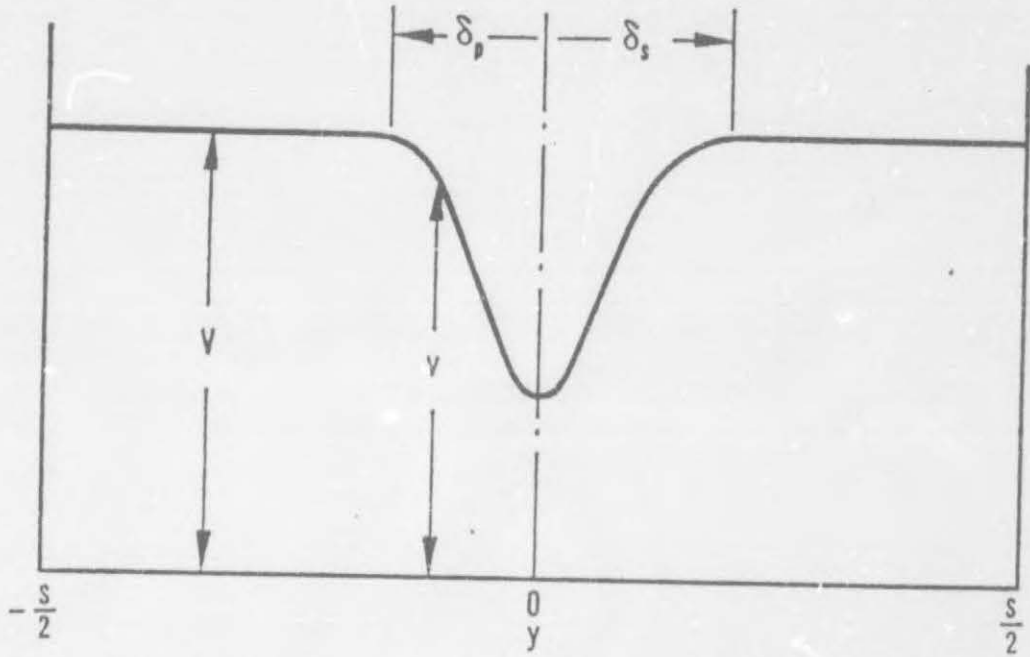


Figure 5.14: Compressor cascade blade wake: variation in velocity in a plane normal to axial direction

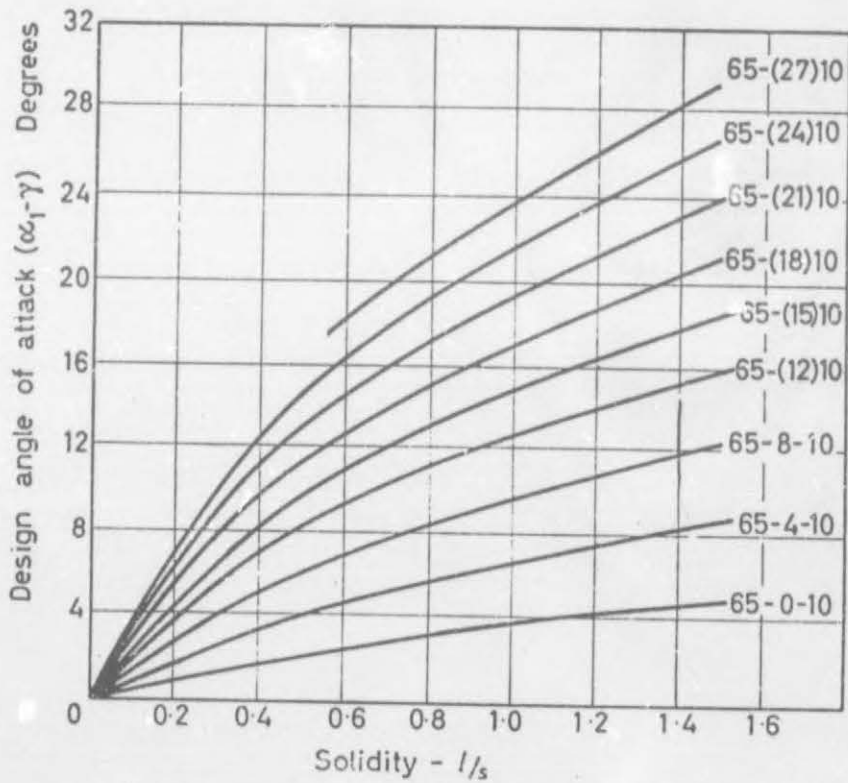


Figure 5.15: Design angles of attack for NACA 65-Series

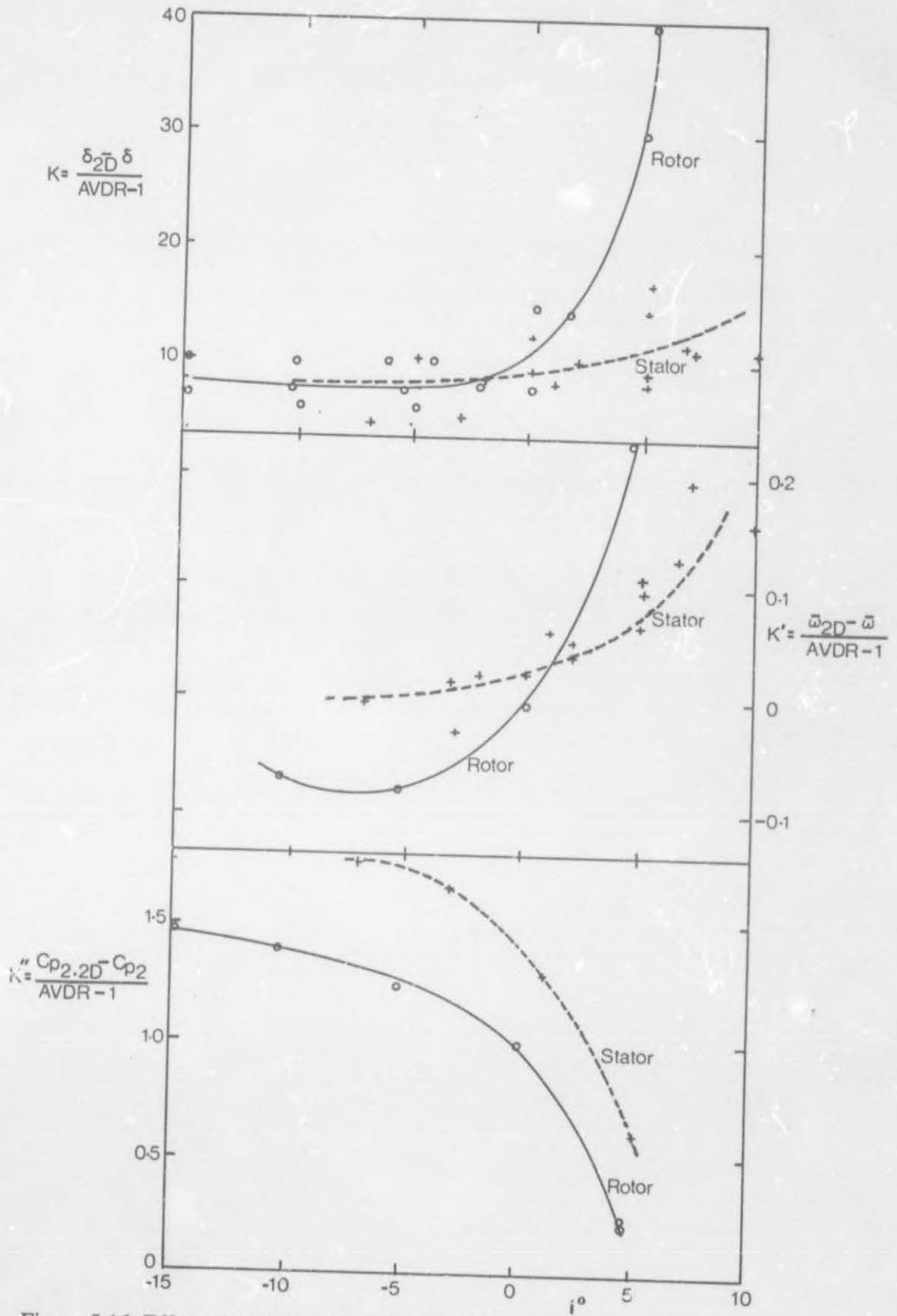


Figure 5.16: Effect of AVDR on deviation angle, loss coefficient and discharge pressure coefficient as a function of incidence

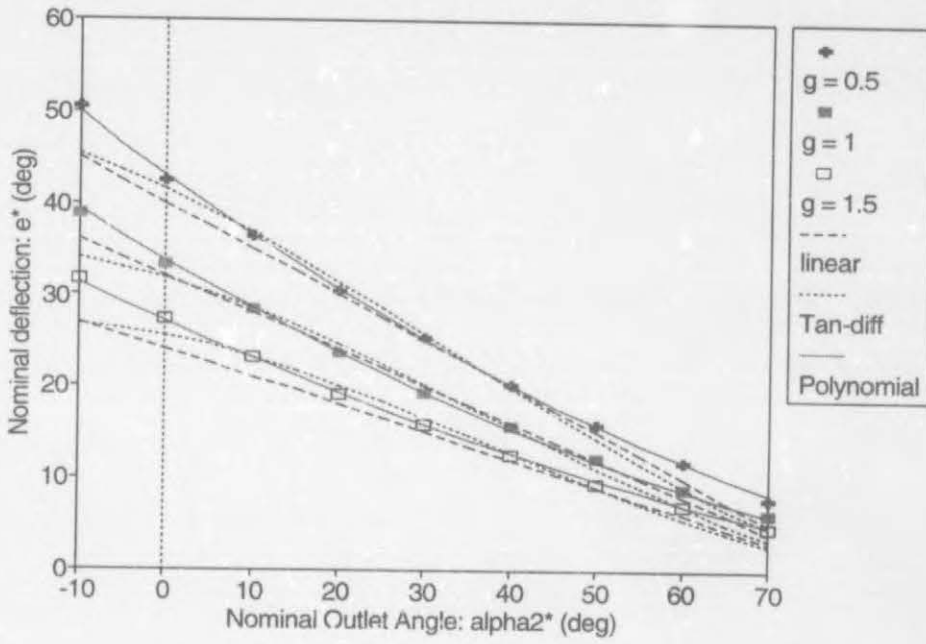


Figure 6.1: Howell's nominal deflection correlation data with three curve fit approximations

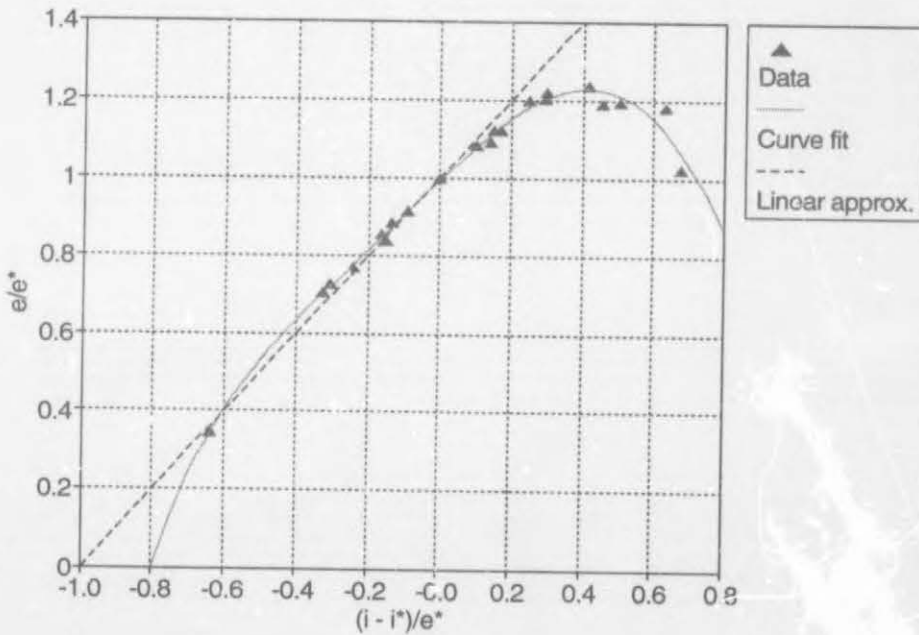


Figure 6.2: Howell's off-design cascade deflection correlation with two curve fit approximations

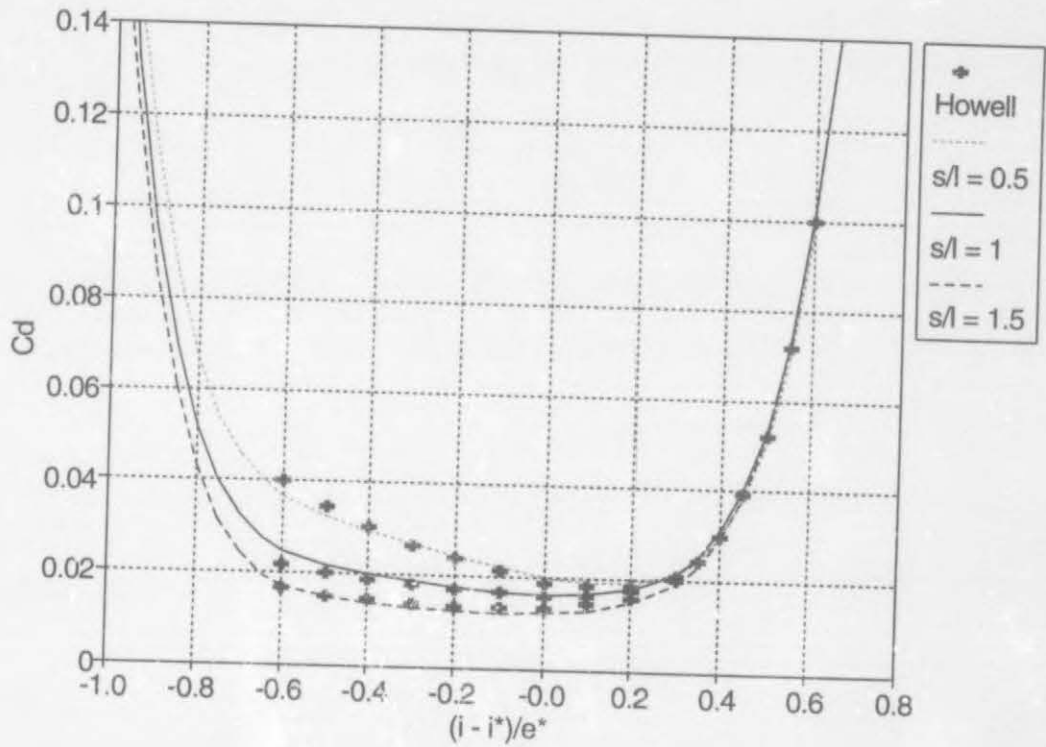


Figure 6.3: Howell's off-design cascade profile drag correlation with polynomial curve fit

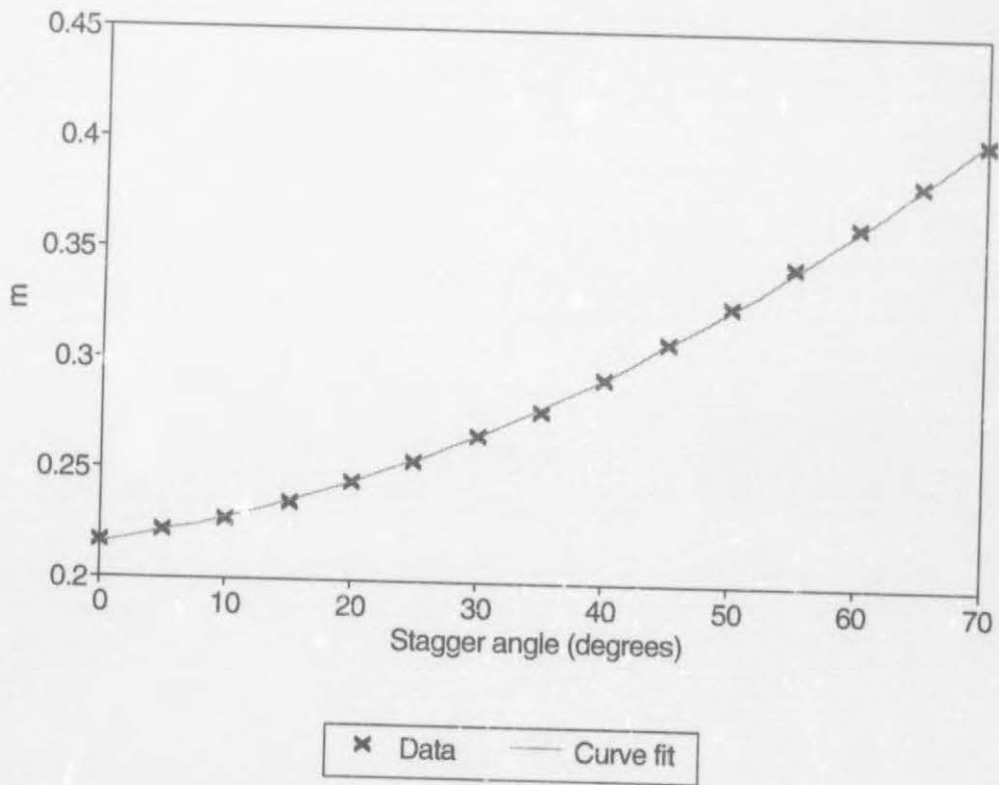


Figure 6.4: Carter's deviation rule for circular arc with polynomial curve fit

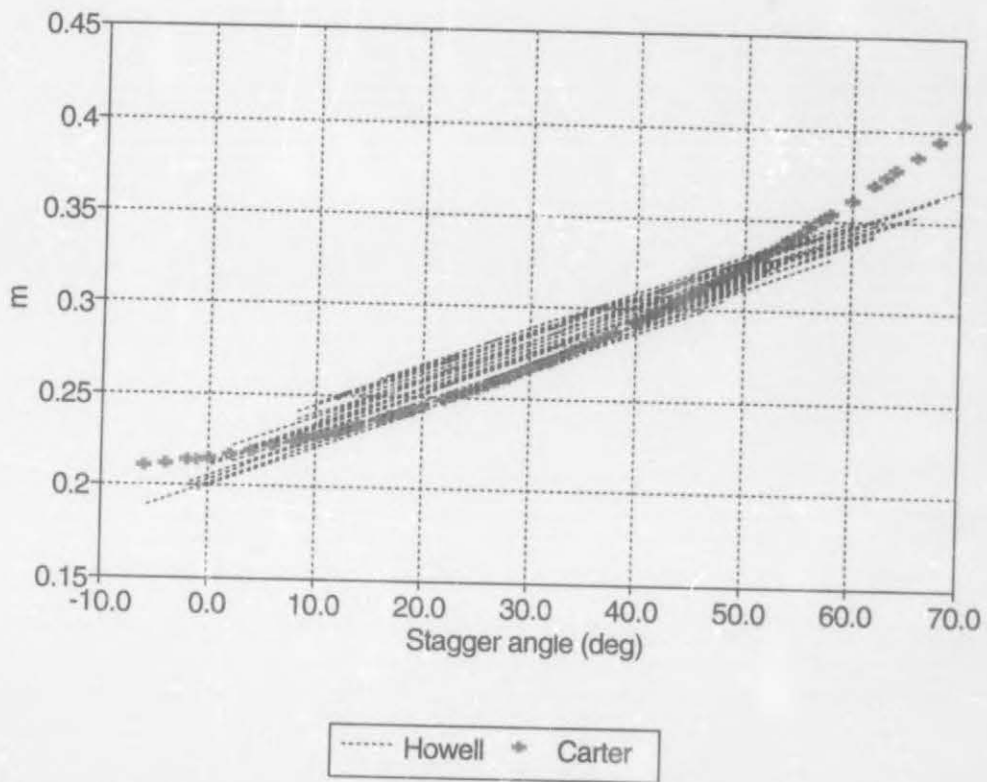


Figure 6.5: Comparison of values of m from Carter's deviation rule and Howell's correlation for the NACA cascade test data

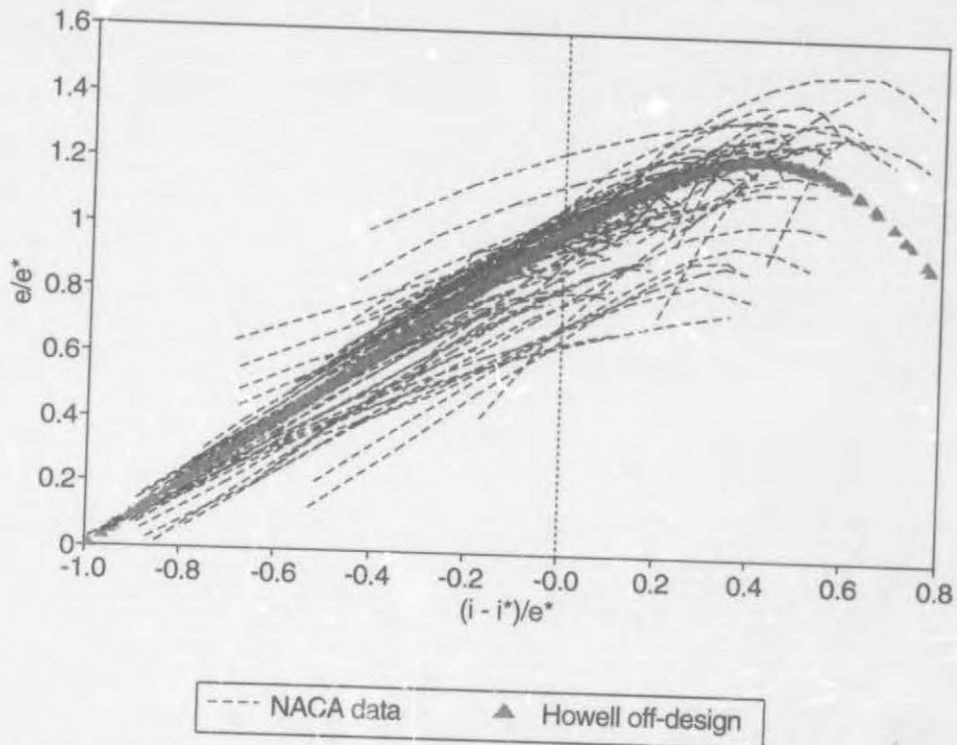


Figure 6.6: NACA cascade test data non-dimensionalised to Howell's off-design correlation using Howell's deviation rule for ϵ^*

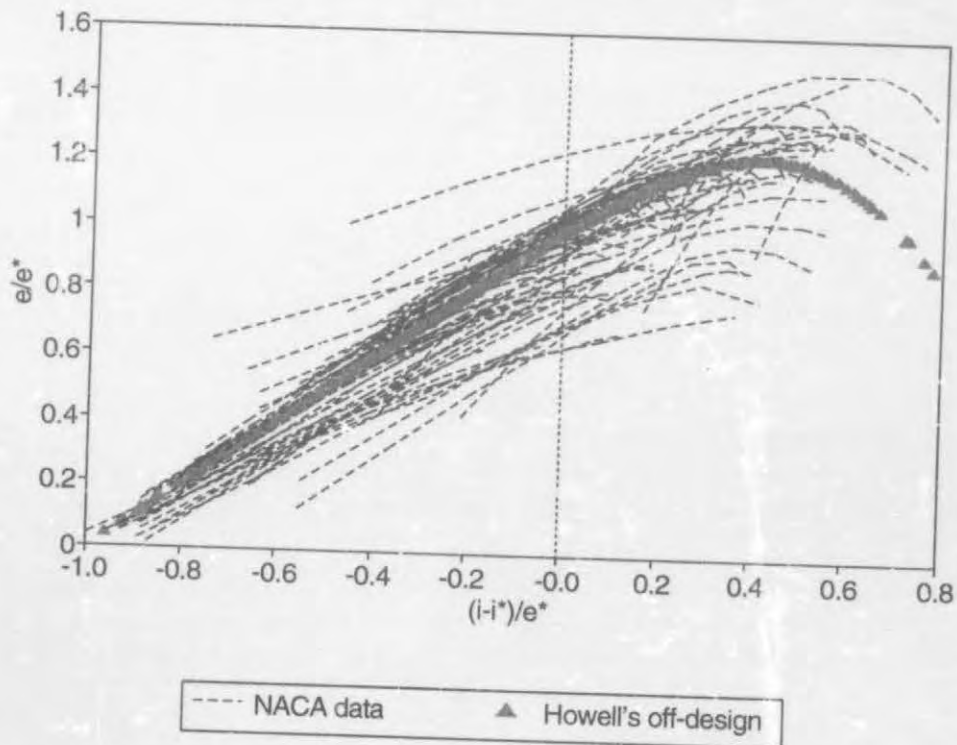


Figure 6.7: NACA cascade test data non-dimensionalised to Howell's off-design correlation using Carter's deviation rule for ϵ^*

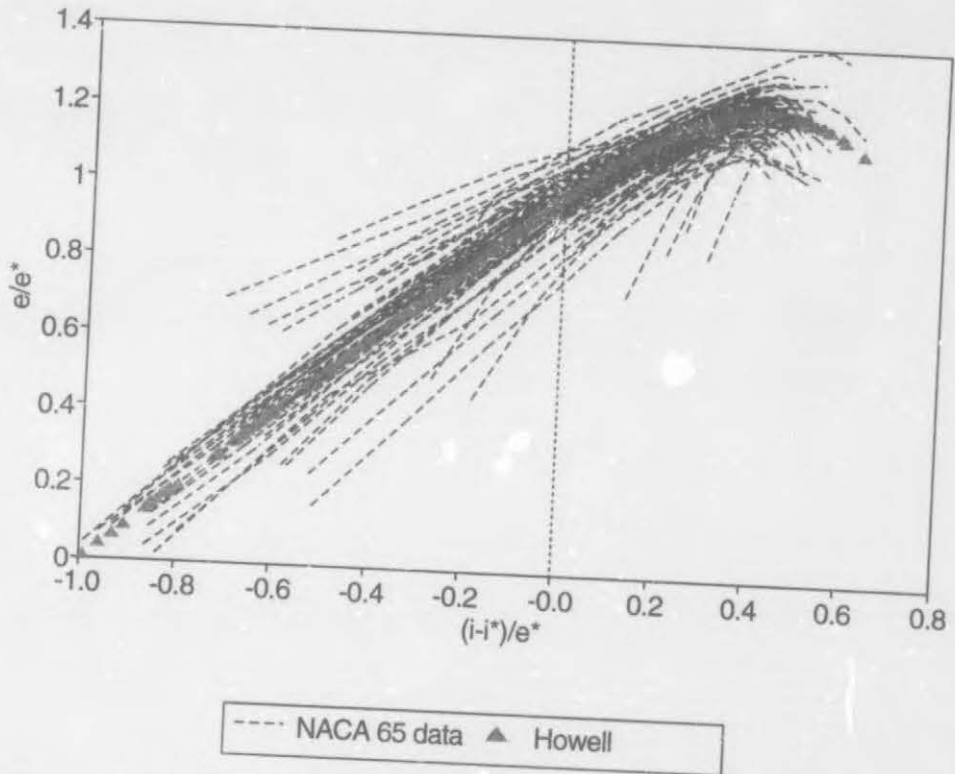


Figure 6.8: NACA cascade test data non-dimensionalised to Howell's off-design correlation and adjusted by the C_1 and C_2 factor correlations

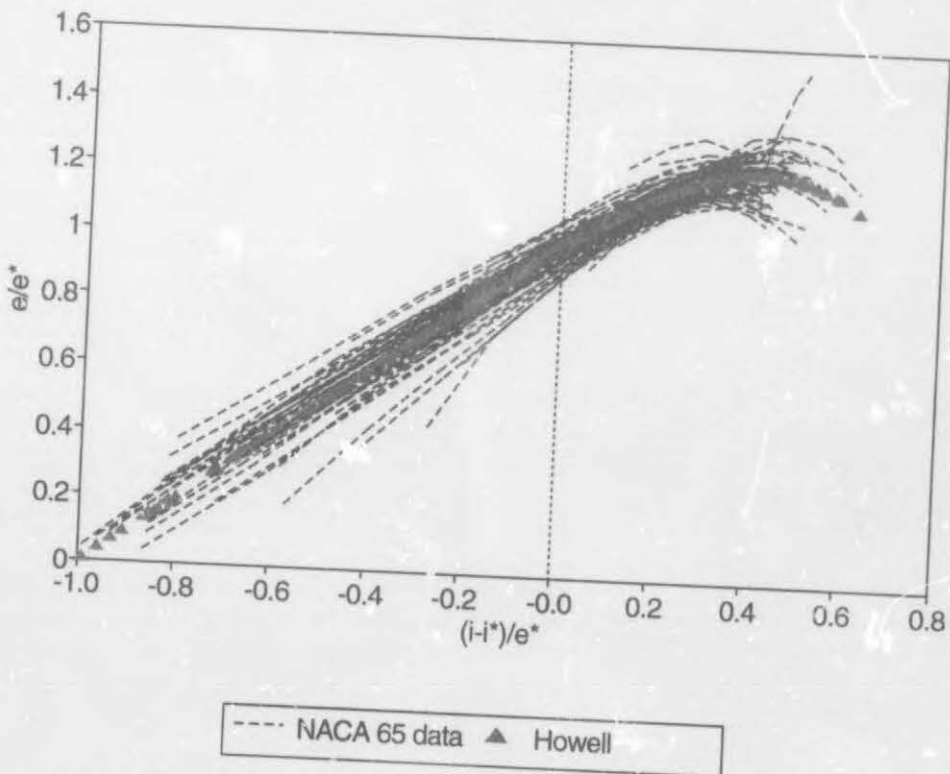


Figure 6.9: NACA cascade test data non-dimensionalised to Howell's off-design correlation and adjusted by the C_1 and C_2 factor and M gradient correlations

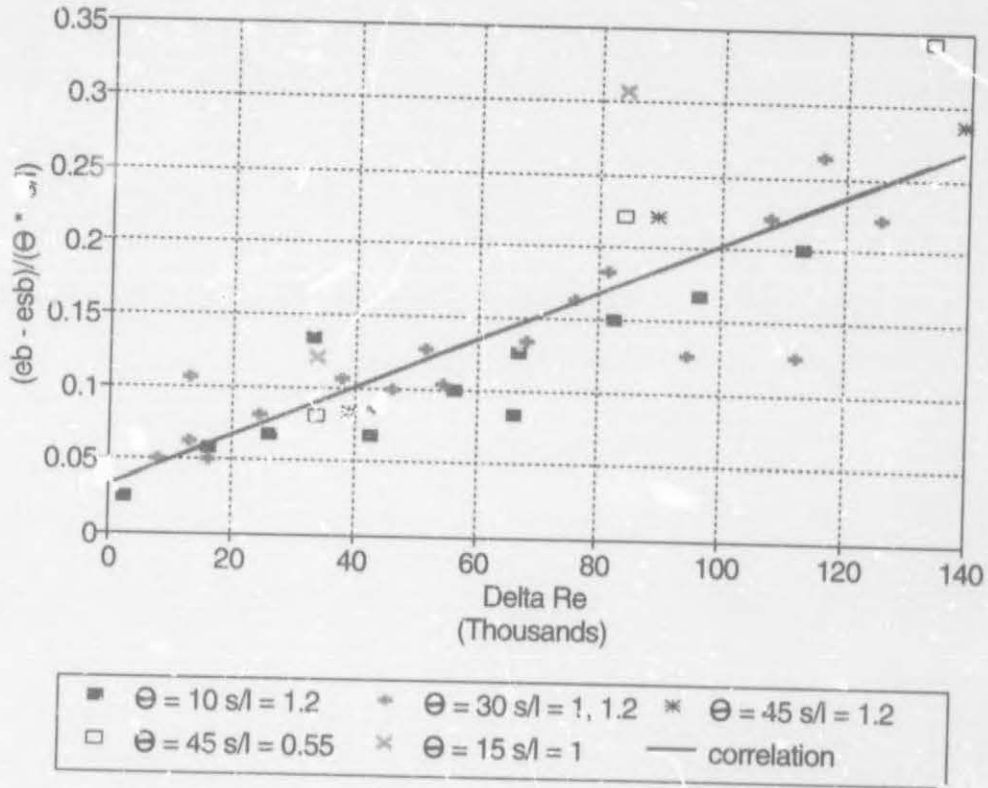


Figure 6.10: Initial correlation applied to the low Reynolds number ϵ data of Roberts

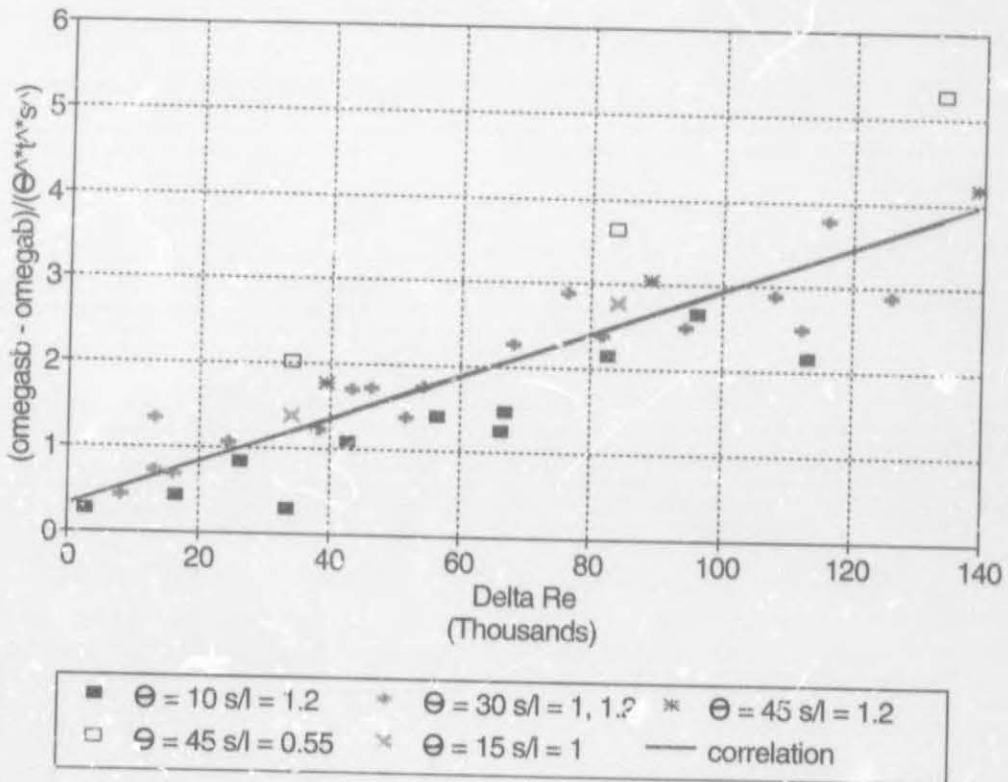


Figure 6.11: Initial correlation applied to the low Reynolds number $\bar{\omega}$ data of Roberts

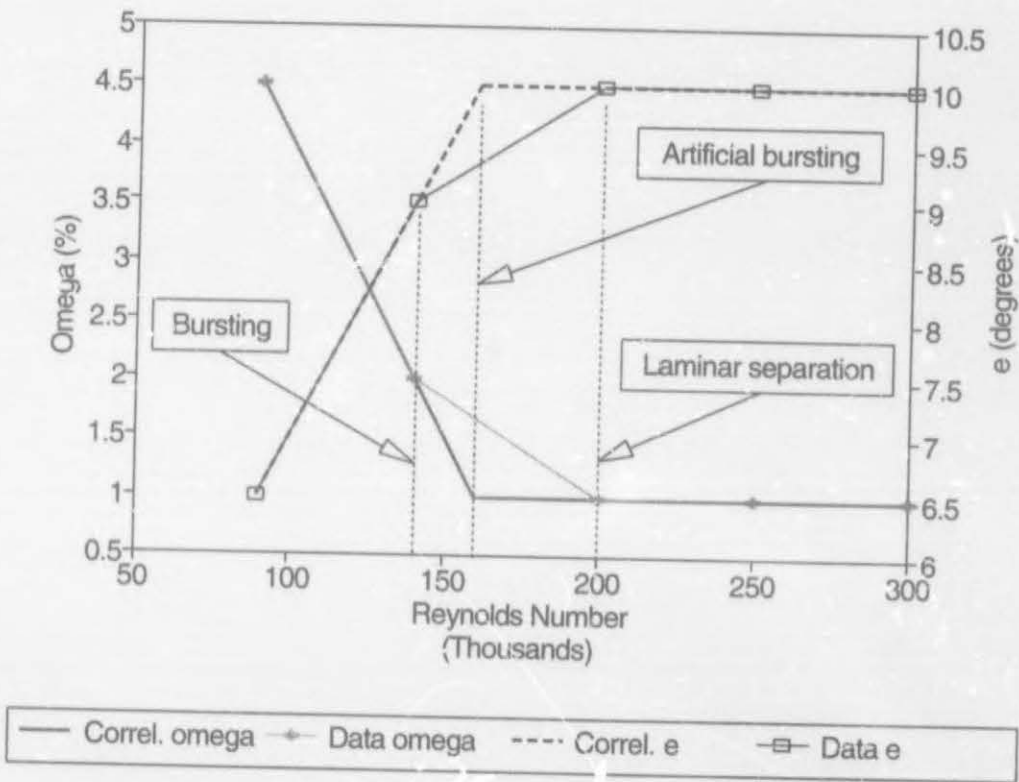


Figure 6.12: Definition of "artificial" bursting Reynolds number

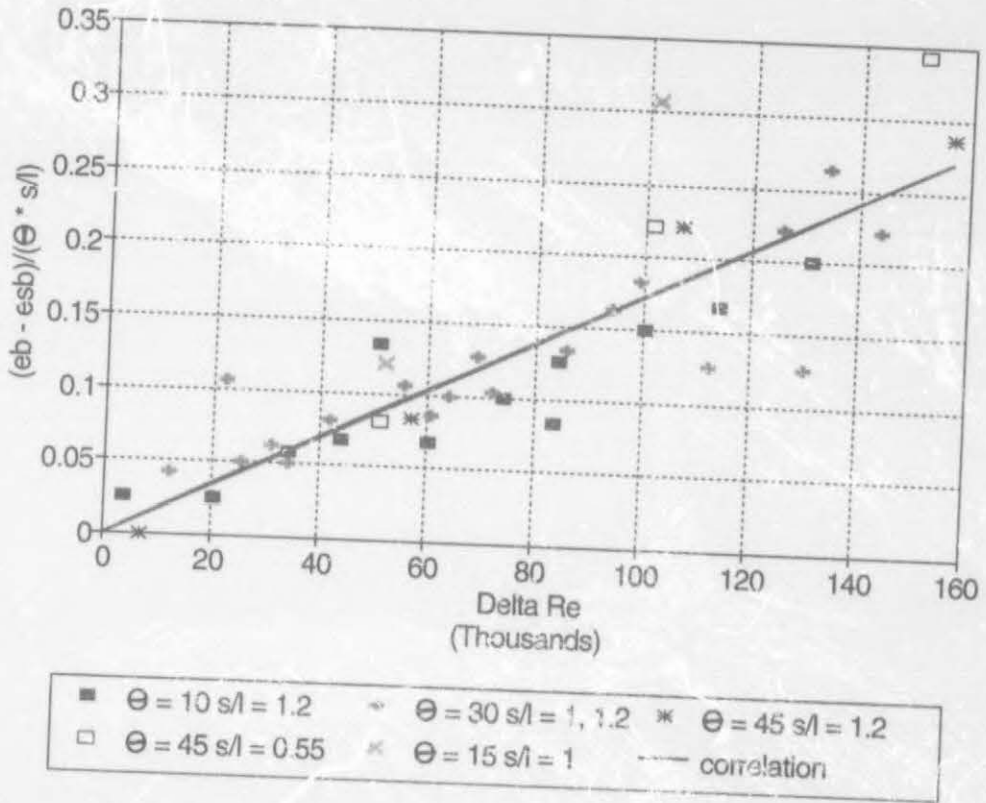


Figure 6.13: Final correlation applied to the low Reynolds number ε data of Roberts

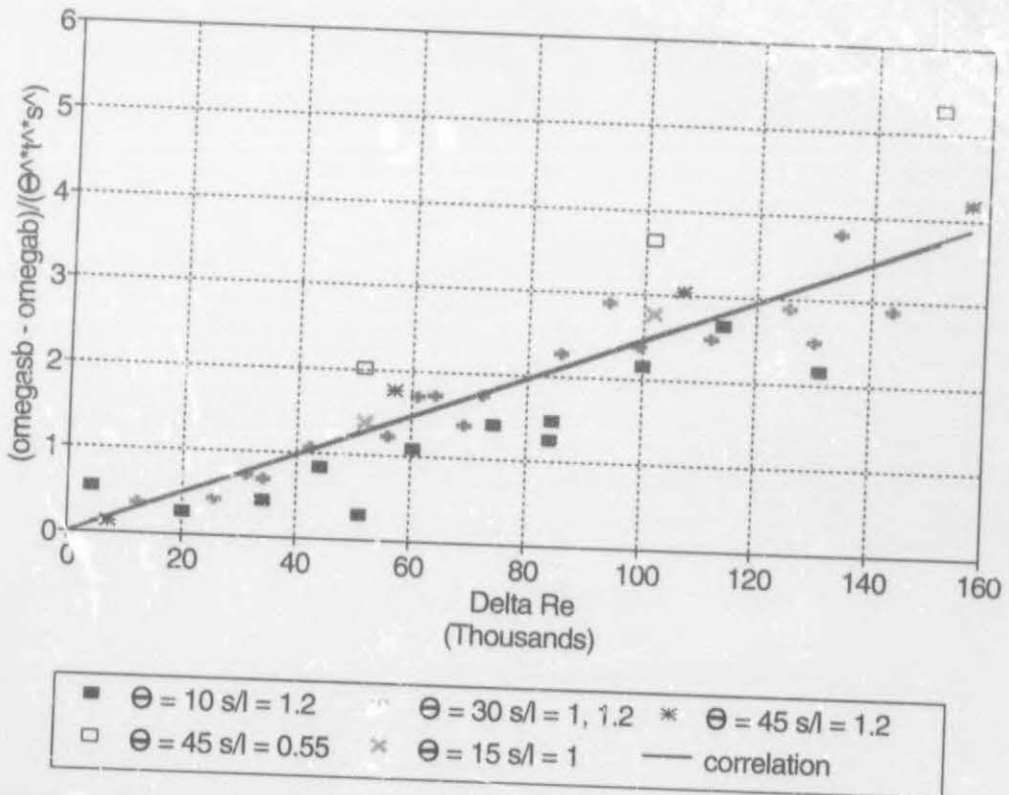


Figure 6.14: Final correlation applied to the low Reynolds number $\bar{\omega}$ data of Roberts

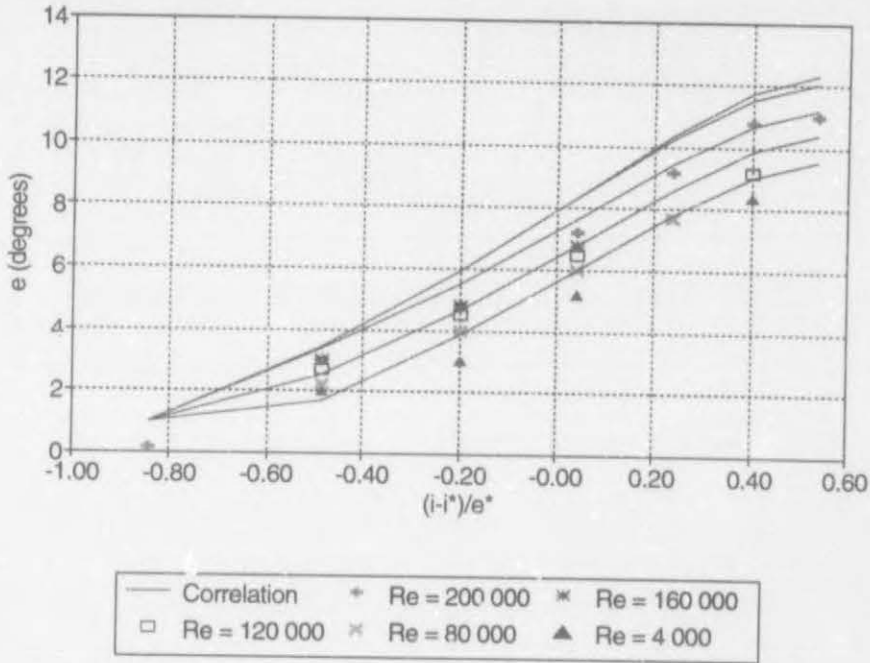


Figure 6.15: Comparison of ϵ as function of non-dimensionalised incidence and Reynolds number, Re_c , between data of Roberts and prediction of H2 correlation combined with modified correlation of Roberts, for NACA 65-4(A10)10 profiles in cascade: $s/l = 1.2$, $\beta_1 = 60^\circ$, $TF \sim 0.006$

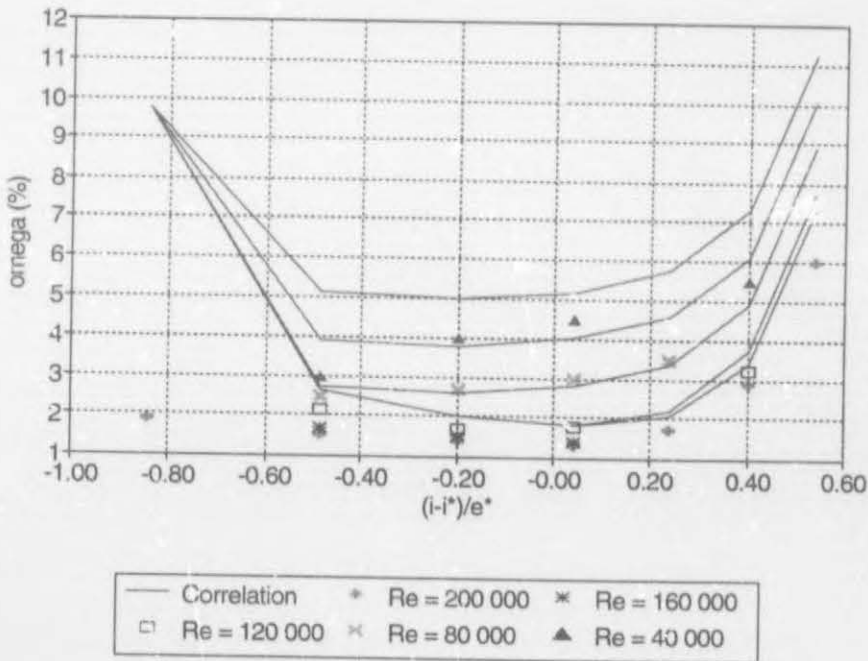


Figure 6.16: Comparison of $\bar{\omega}$ as function of non-dimensionalised incidence and Reynolds number, Re_c , between data of Roberts and prediction of H2 correlation combined with modified correlation of Roberts, for NACA 65-4(A10)10 profiles in cascade: $s/l = 1.2$, $\beta_1 = 60^\circ$, $TF \sim 0.006$

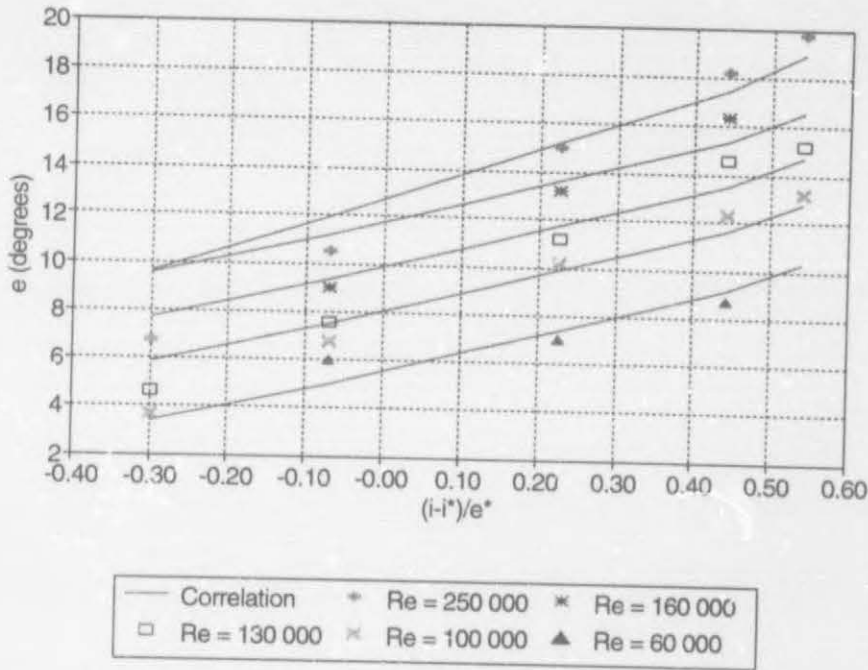


Figure 6.17: Comparison of ϵ as function of non-dimensionalised incidence and Reynolds number, Re_c , between data of Roberts and prediction of H2 correlation combined with modified correlation of Roberts, for NACA 65-12(A10)10 profiles in cascade: $s/l = 1.2$, $\beta_1 = 60^\circ$, $TF \sim 0.006$

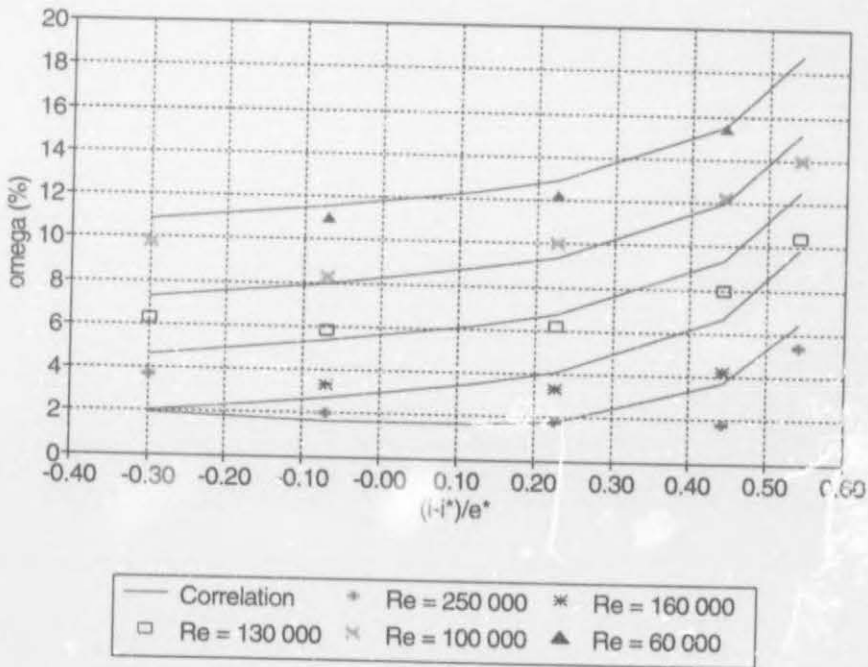


Figure 6.18: Comparison of $\bar{\omega}$ as function of non-dimensionalised incidence and Reynolds number, Re_c , between data of Roberts and prediction of H2 correlation combined with modified correlation of Roberts, for NACA 65-12(A10)10 profiles in cascade: $s/l = 1.2$, $\beta_1 = 60^\circ$, $TF \sim 0.006$

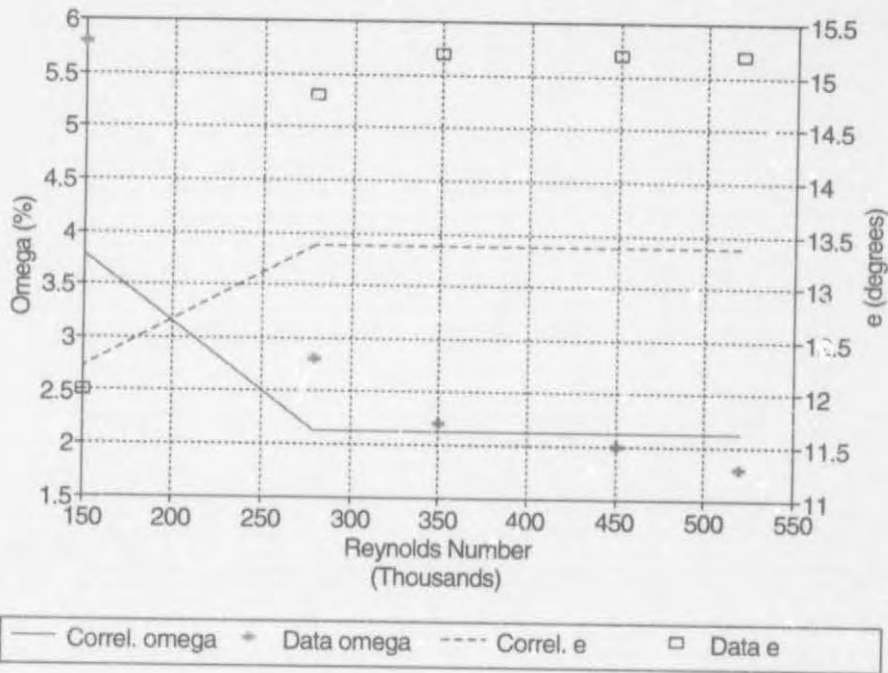


Figure 6.19: Comparison of ϵ and $\bar{\omega}$ as function of Reynolds number, Re_c , between data of Roberts and prediction of H2 correlation combined with modified correlation of Roberts, for NACA 65-12(A2T8b)10 profiles in cascade: $s/l = 1.0$, $\beta_1 = 60^\circ$, $\gamma = 50.4^\circ$, $TF \sim -0.006$

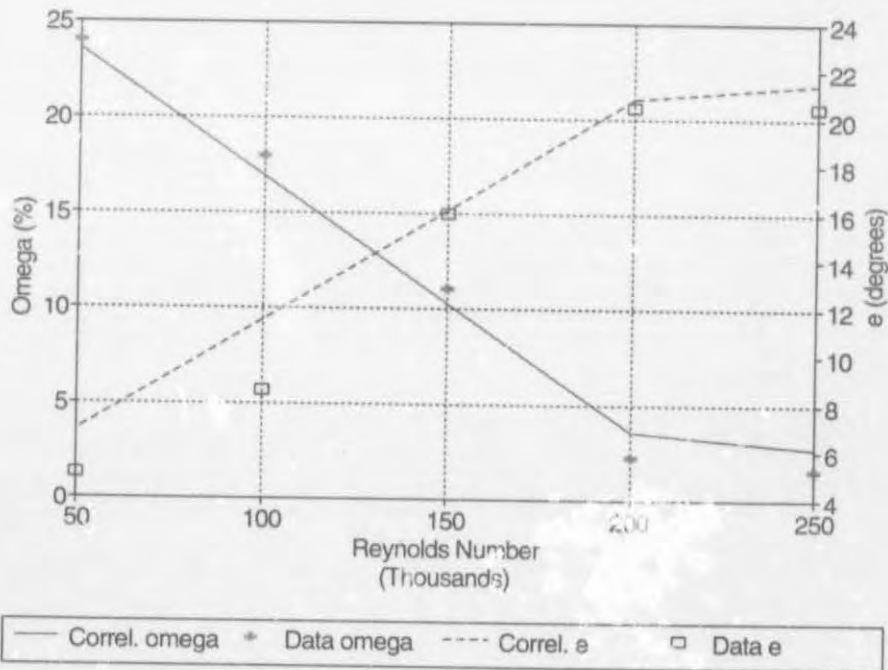


Figure 6.20: Comparison of ϵ and $\bar{\omega}$ as function of Reynolds number, Re_c , between data of Roberts and prediction of H2 correlation combined with modified correlation of Roberts, for NACA 65-18(A10)10 profiles in cascade: $s/l = 1.2$, $\beta_1 = 60^\circ$, $\gamma = 45^\circ$, $TF \sim -0.006$

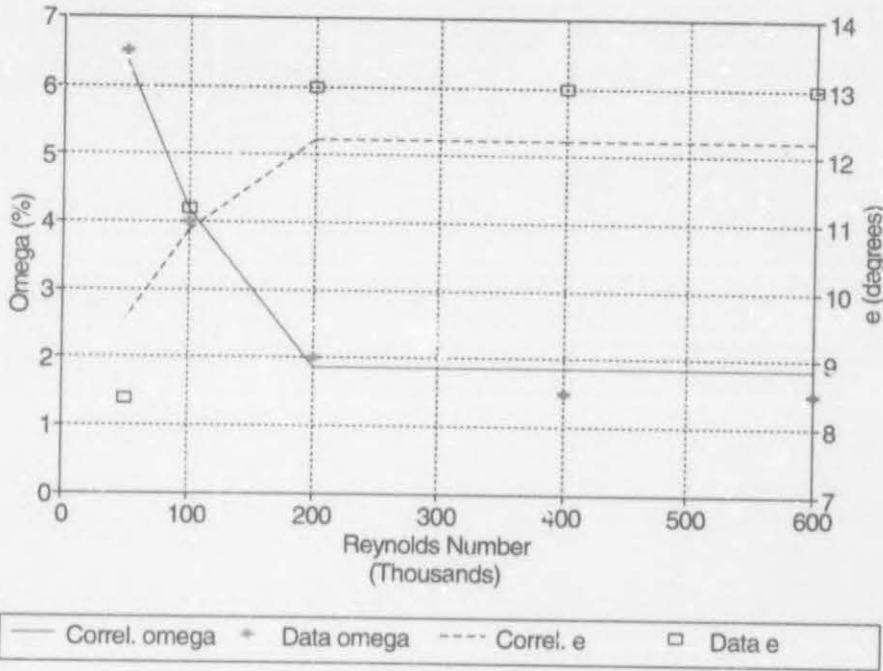


Figure 6.21: Comparison of ϵ and $\bar{\omega}$ as function of Reynolds number, Re_c , between data of Roberts and prediction of H2 correlation combined with modified correlation of Roberts, for NACA 65-6(A10)12 profiles in cascade: $s/l = 1.0$, $\beta_1 = 50^\circ$, $\gamma = 40^\circ$, $Tu < 0.01$, TF assumed ~ 0.006

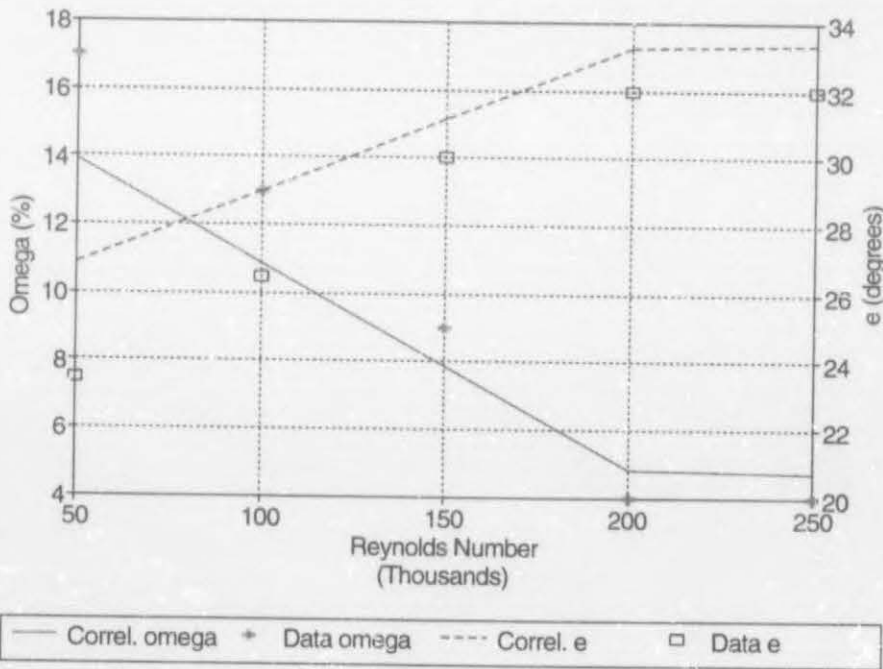


Figure 6.22: Comparison of ϵ and $\bar{\omega}$ as function of Reynolds number, Re_c , between data of Roberts and prediction of H2 correlation combined with modified correlation of Roberts, for NACA 65-18(A10)10 profiles in cascade: $s/l = 0.55$, $\beta_1 = 60^\circ$, $\gamma = 37.5^\circ$, $TF \sim 0.006$

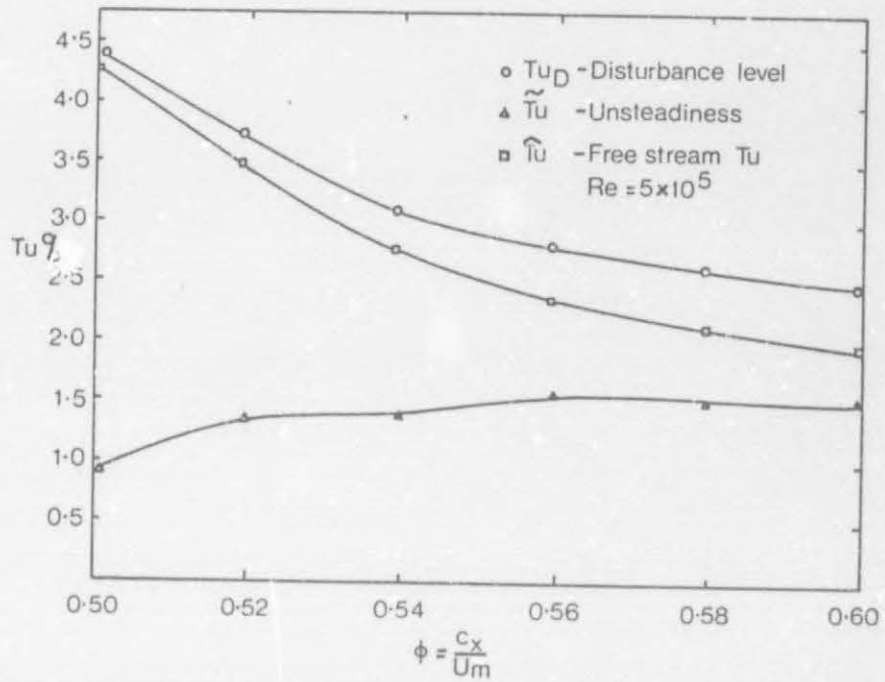


Figure 7.1: Variation of turbulence level with flowrate for a single stage compressor

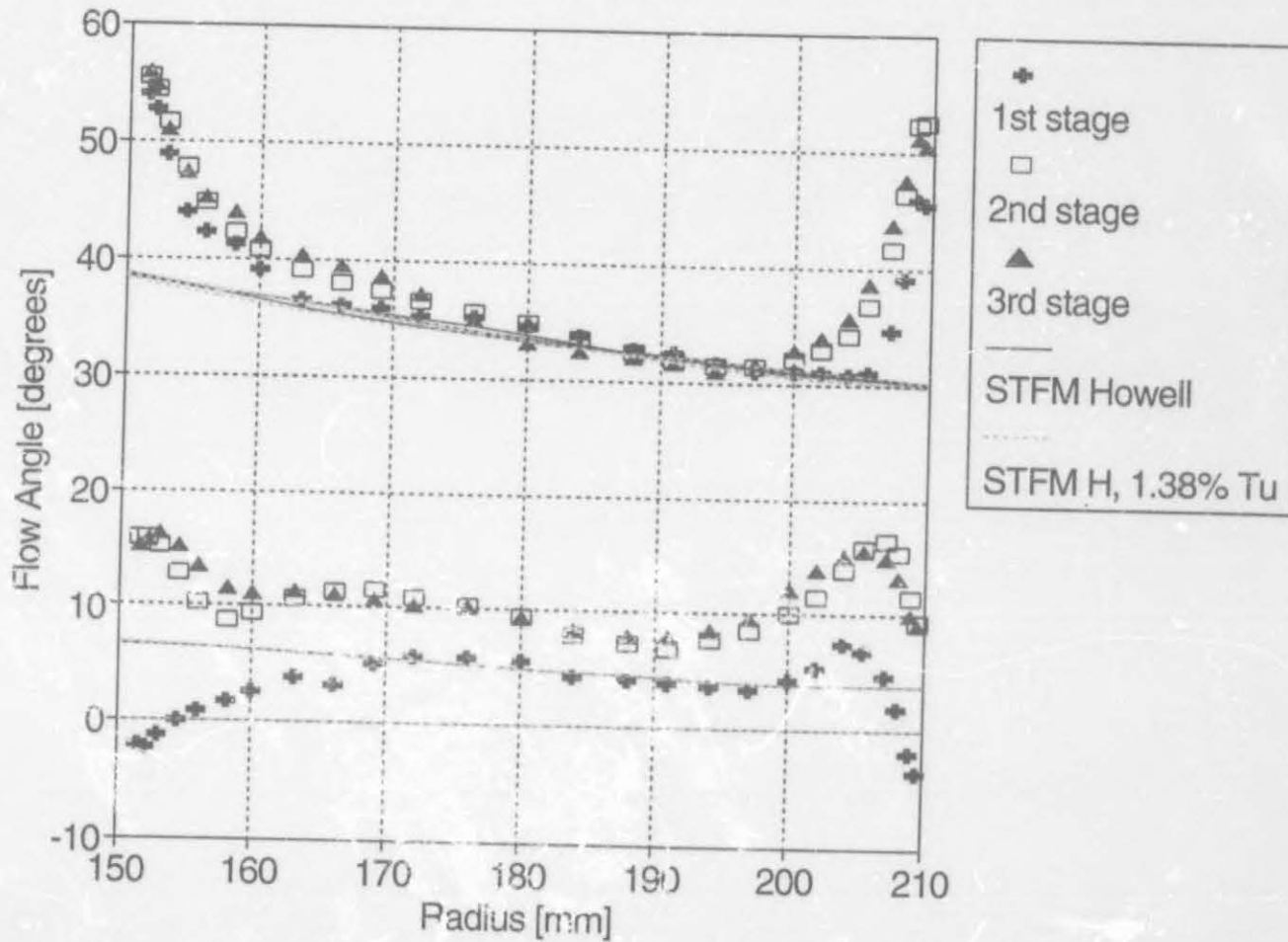


Figure 7.2: Flow angle profiles at near-design flowrate: 2.54 kg/s. Comparison between experimental data and STFM predictions using Howell's method with and without correction of Roberts

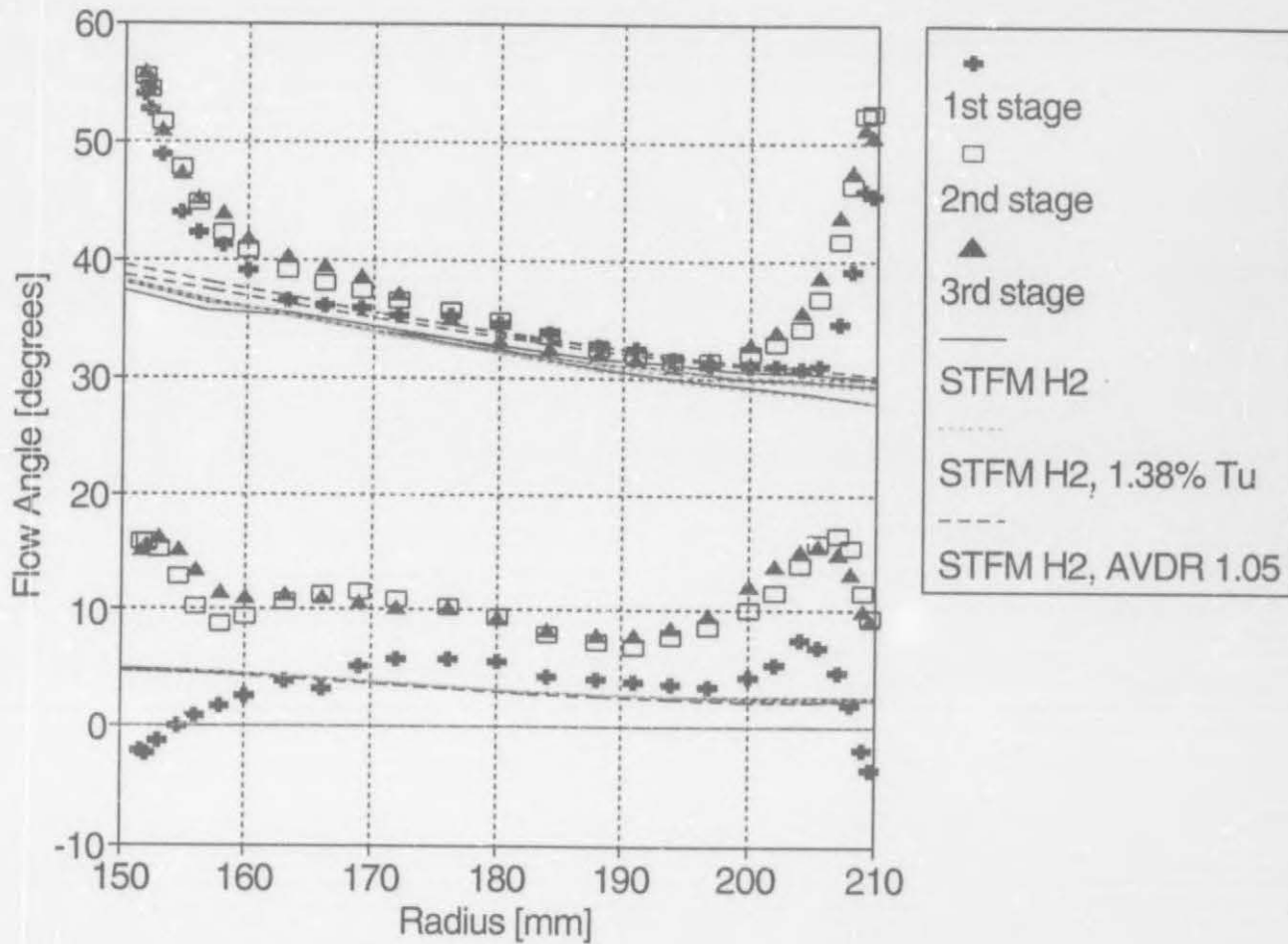


Figure 7.3: Flow angle profiles at near-design flowrate: 2.54 kg/s. Comparison between experimental data and STFM predictions using H2 and H2 with correction of Roberts (with and without AVDR correction)

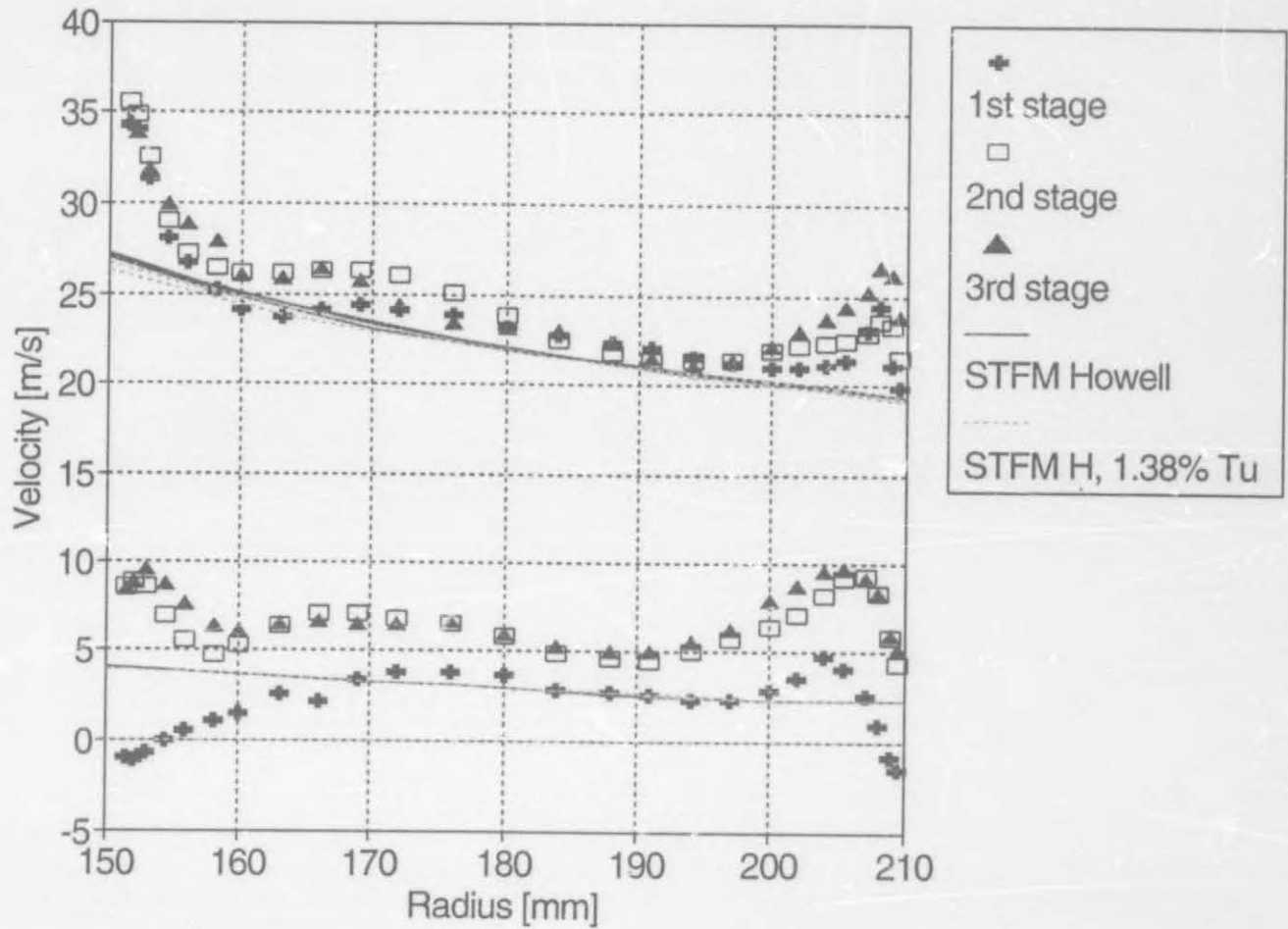


Figure 7.4: Tangential velocity profiles at near-design flowrate: 2.54 kg/s. Comparison between experimental data and STFM predictions using Howell's method with and without correction of Roberts

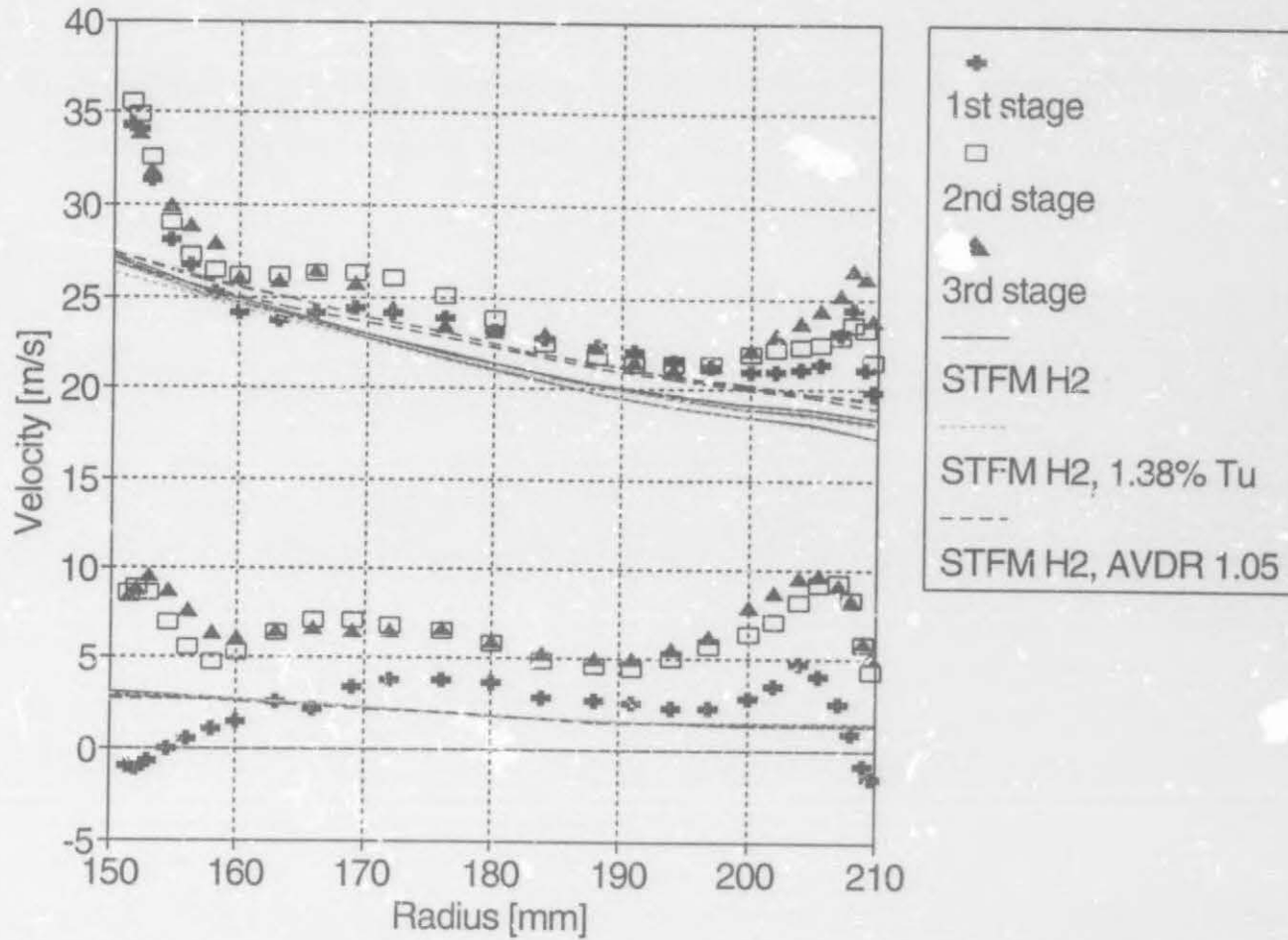


Figure 7.5: Tangential velocity profiles at near-design flowrate: 2.54 kg/s. Comparison between experimental data and STFMs predictions using H2 and H2 with correction of Roberts (with and without AVDR correction)

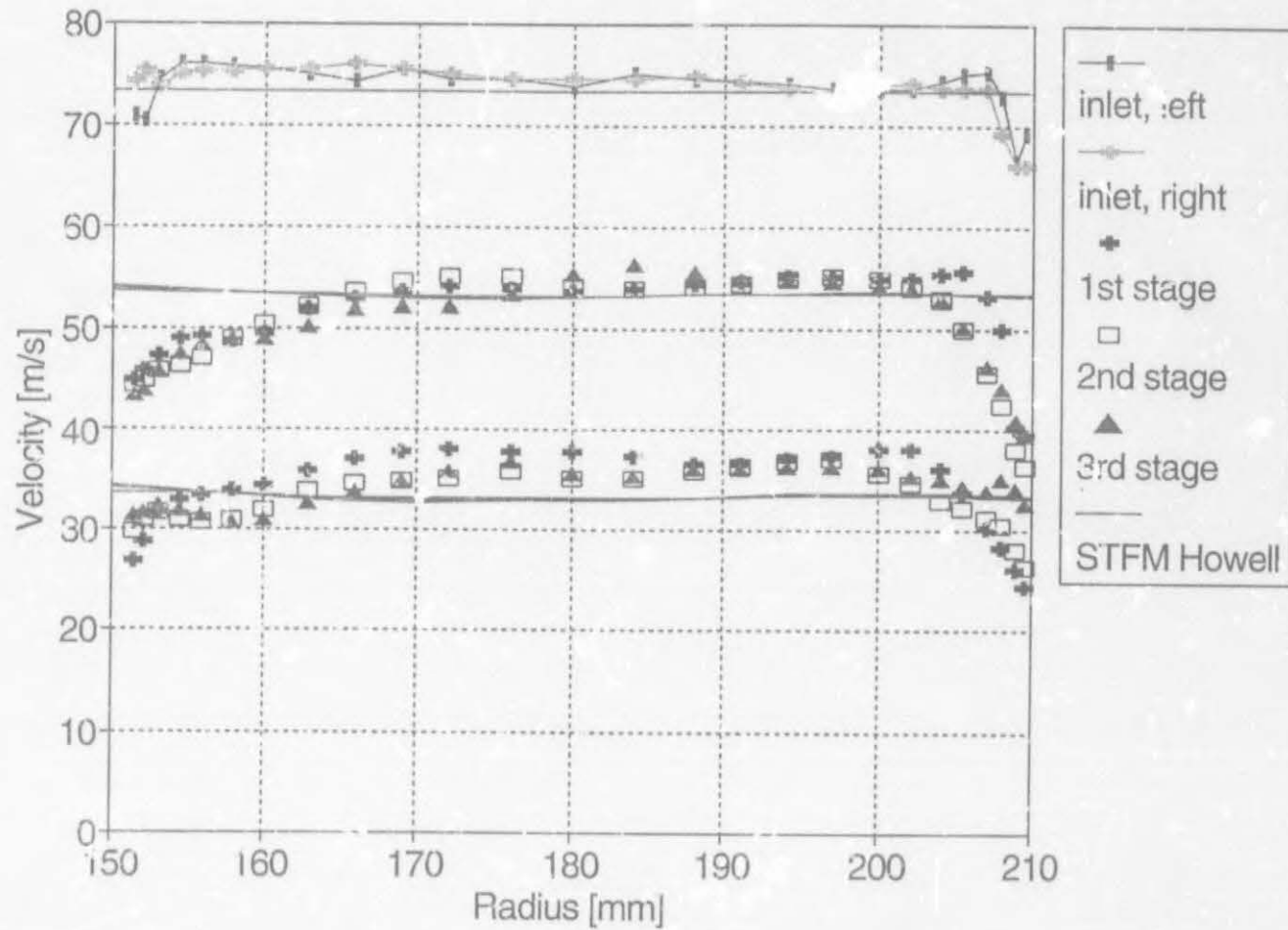


Figure 7.6: Axial velocity profiles at near-design flowrate: 2.54 kg/s. (Zeroes of inlet and rotor rows have been staggered by 40 and 20 m/s, respectively). Comparison between experimental data and STFM predictions using Howell's method

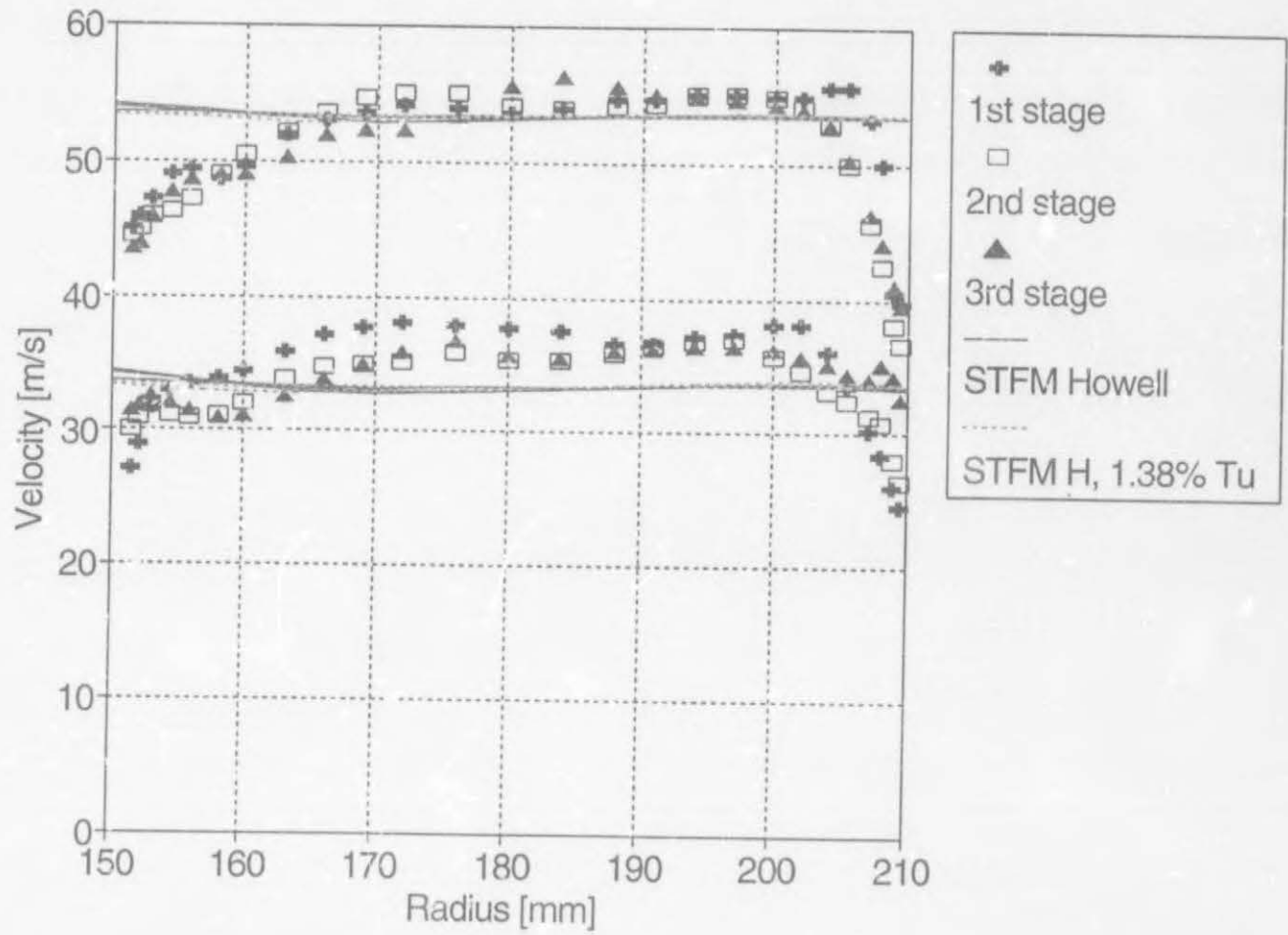


Figure 7.7: Axial velocity profiles at near-design flowrate: 2.54 kg/s. (Zeroes of rotor rows have been staggered by 20 m/s). Comparison between experimental data and STFM predictions using Howell's method with and without correction of Roberts

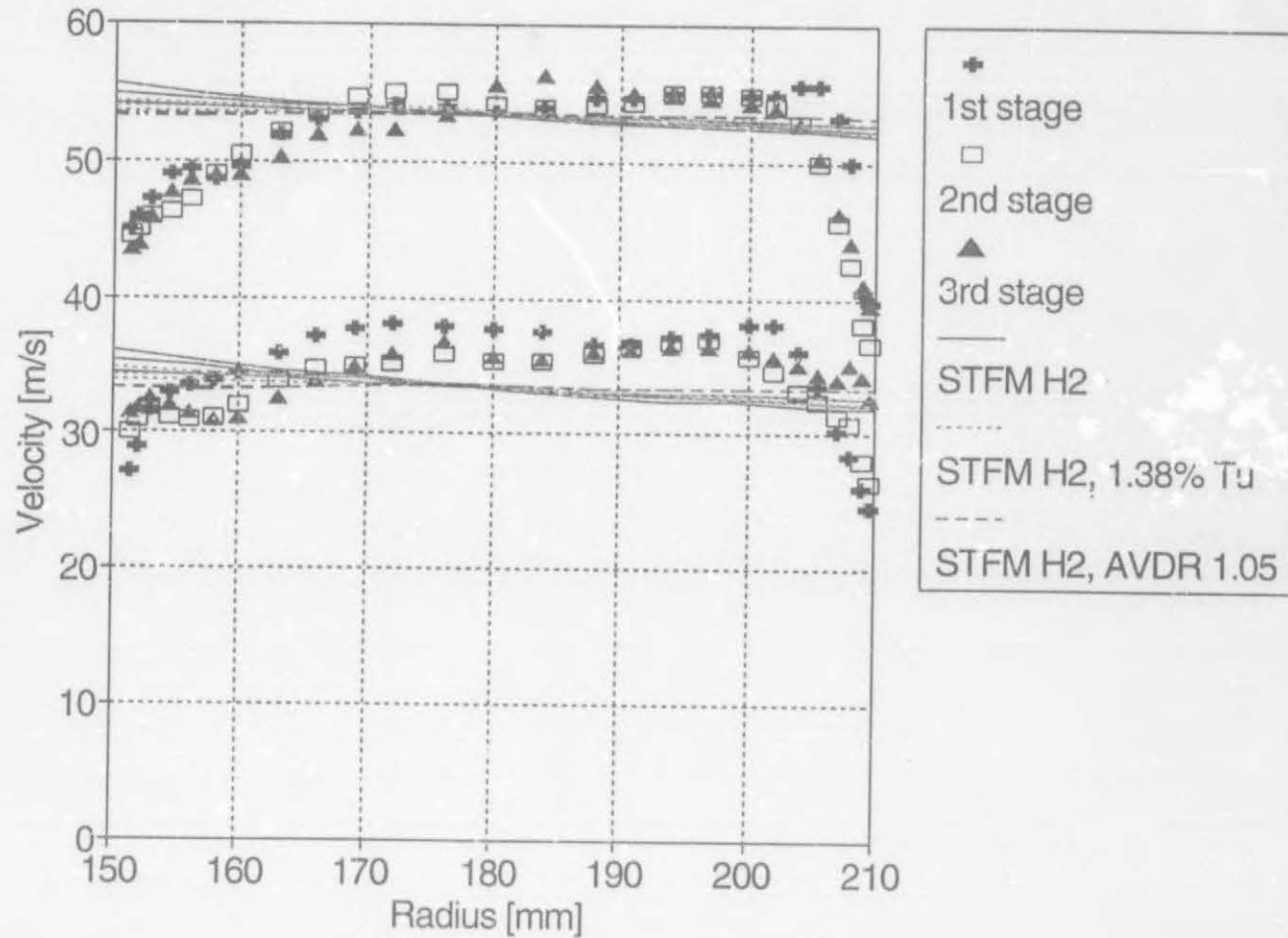
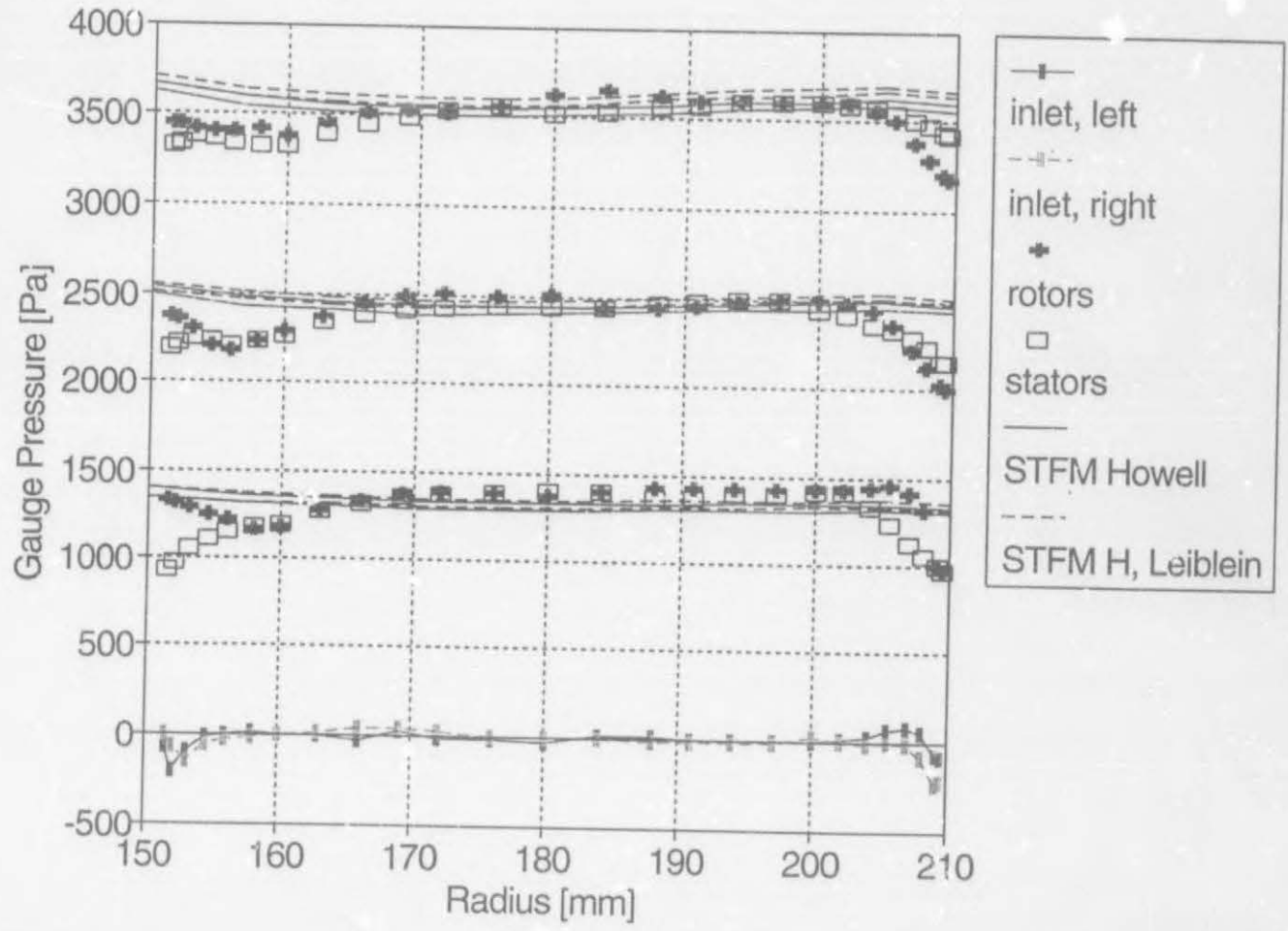


Figure 7.8: Axial velocity profiles at near-design flowrate: 2.54 kg/s. (Zeroes of rotor rows have been staggered by 20 m/s). Comparison between experimental data and STFM predictions using H2 and H2 with correction of Roberts (with and without AVDR correction)



- 159 -

Figure 7.9: Total pressure profiles (relative to inlet mass average) at near-design flowrate: 2.54 kg/s. Comparison between experimental data and STFM predictions using Howell's methods, using Howell's and Lieblein's ρ profile loss models

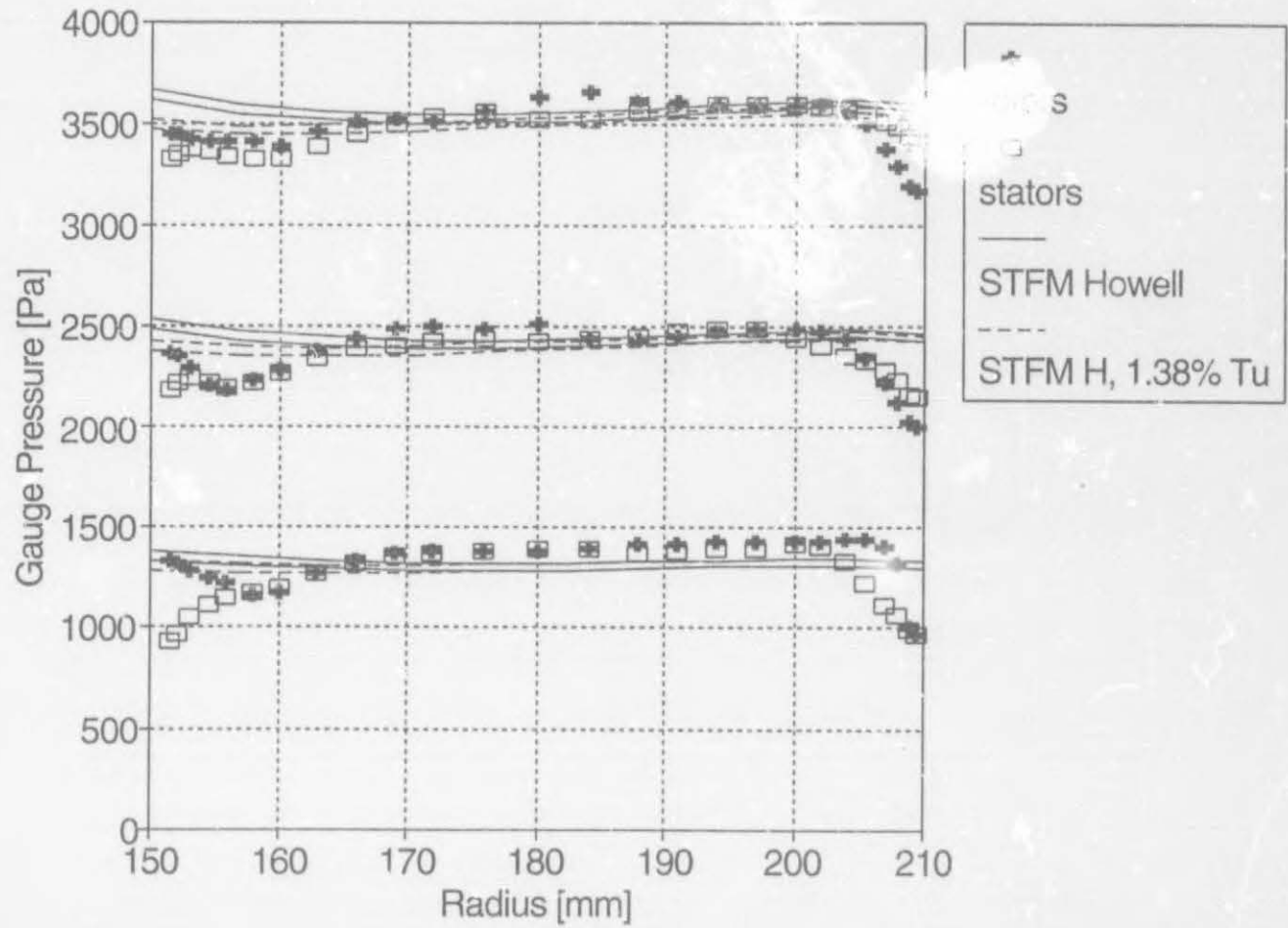


Figure 7.10: Total pressure profiles (relative to inlet mass average) at near-design flowrate: 2.54 kg/s. Comparison between experimental data and STFM predictions using Howell's method with and without correction of Roberts

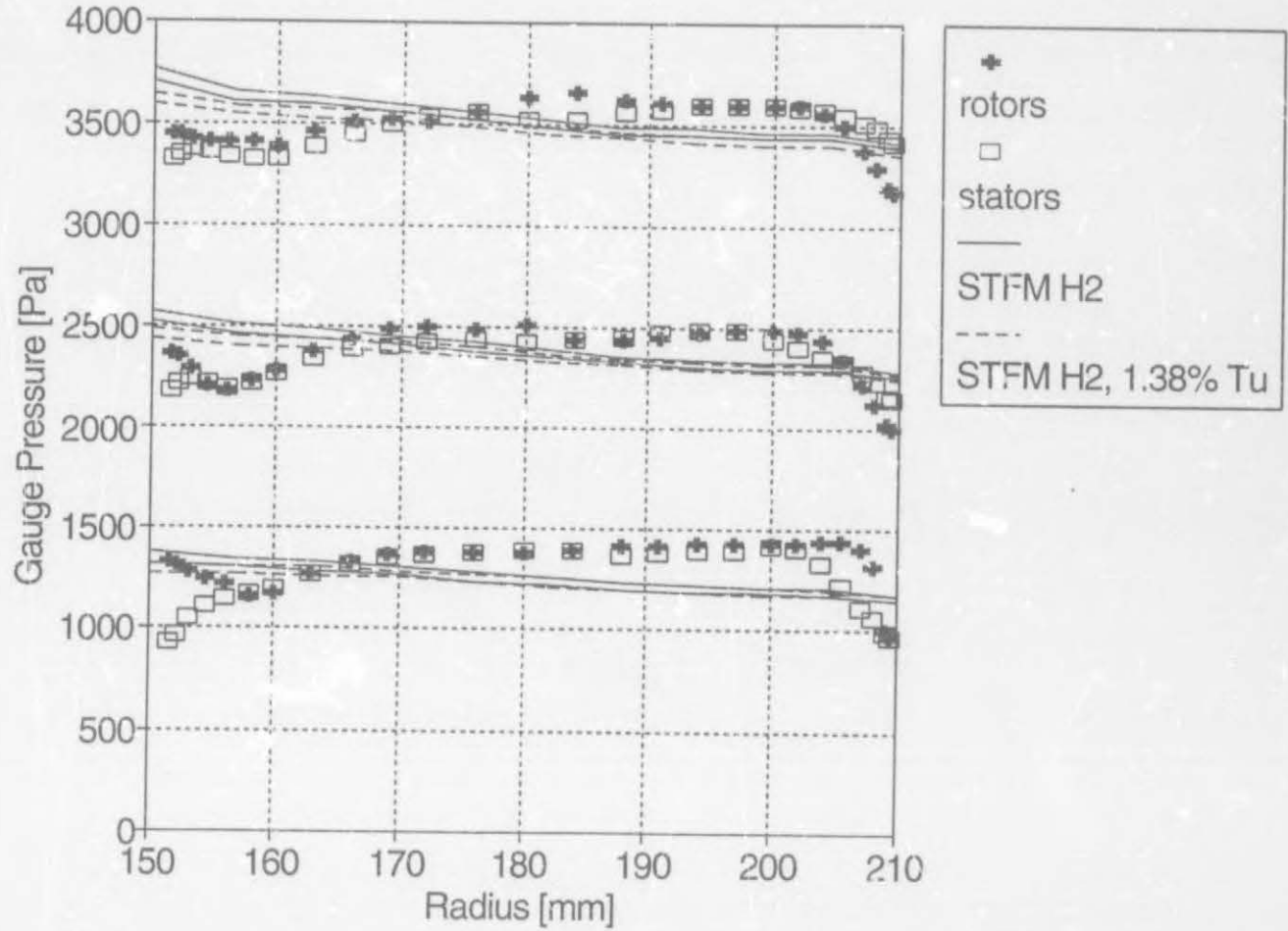


Figure 7.11: Total pressure profiles (relative to inlet mass average) at near-design flowrate: 2.54 kg/s. Comparison between experimental data and STFM predictions using H2 with and without correction of Roberts

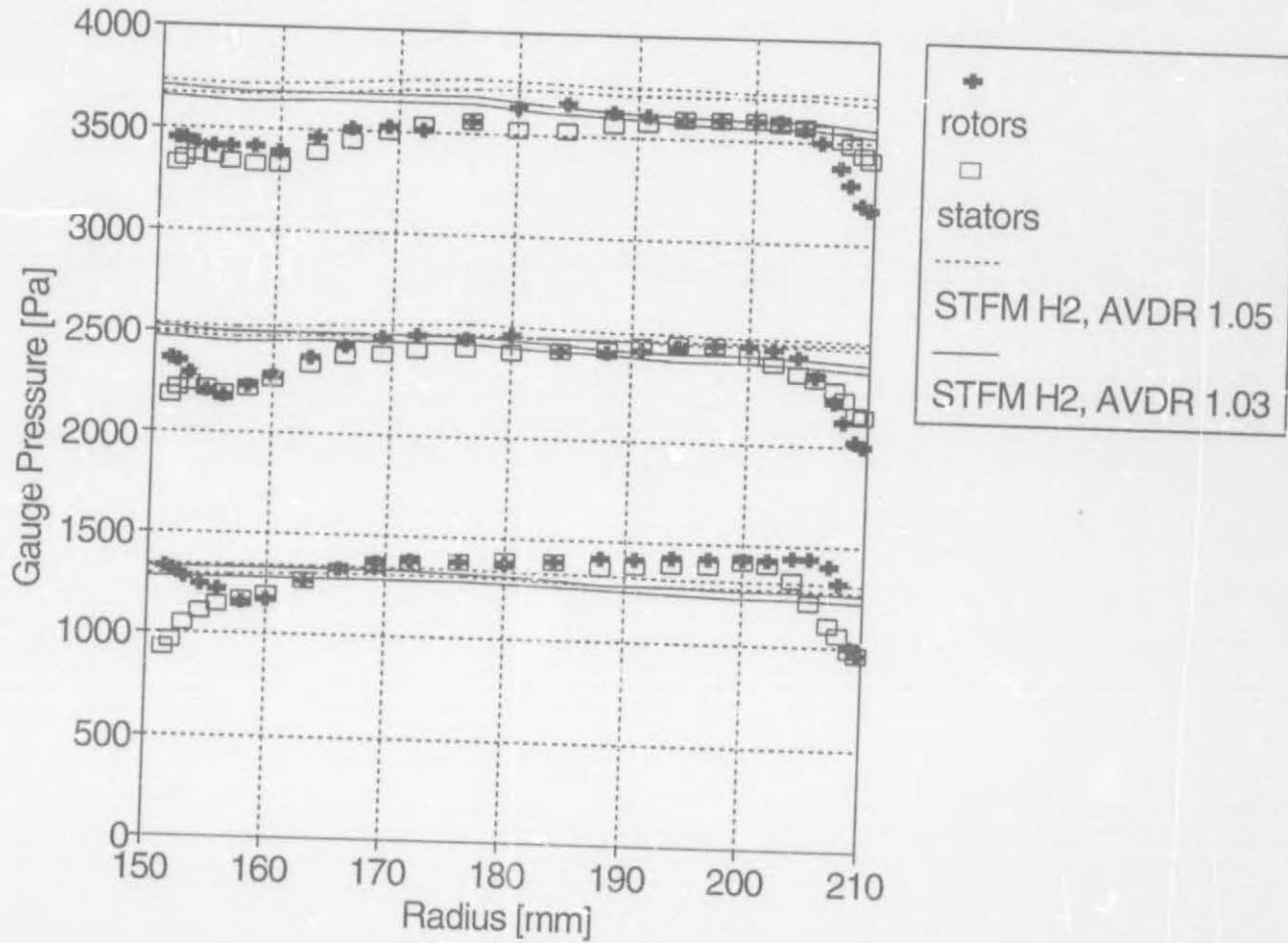


Figure 7.12: Total pressure profiles (relative to inlet mass average) at near-design flowrate: 2.54 kg/s. Comparison between experimental data and STFMs predictions using H2 with correction of Roberts and AVDR correction for two values

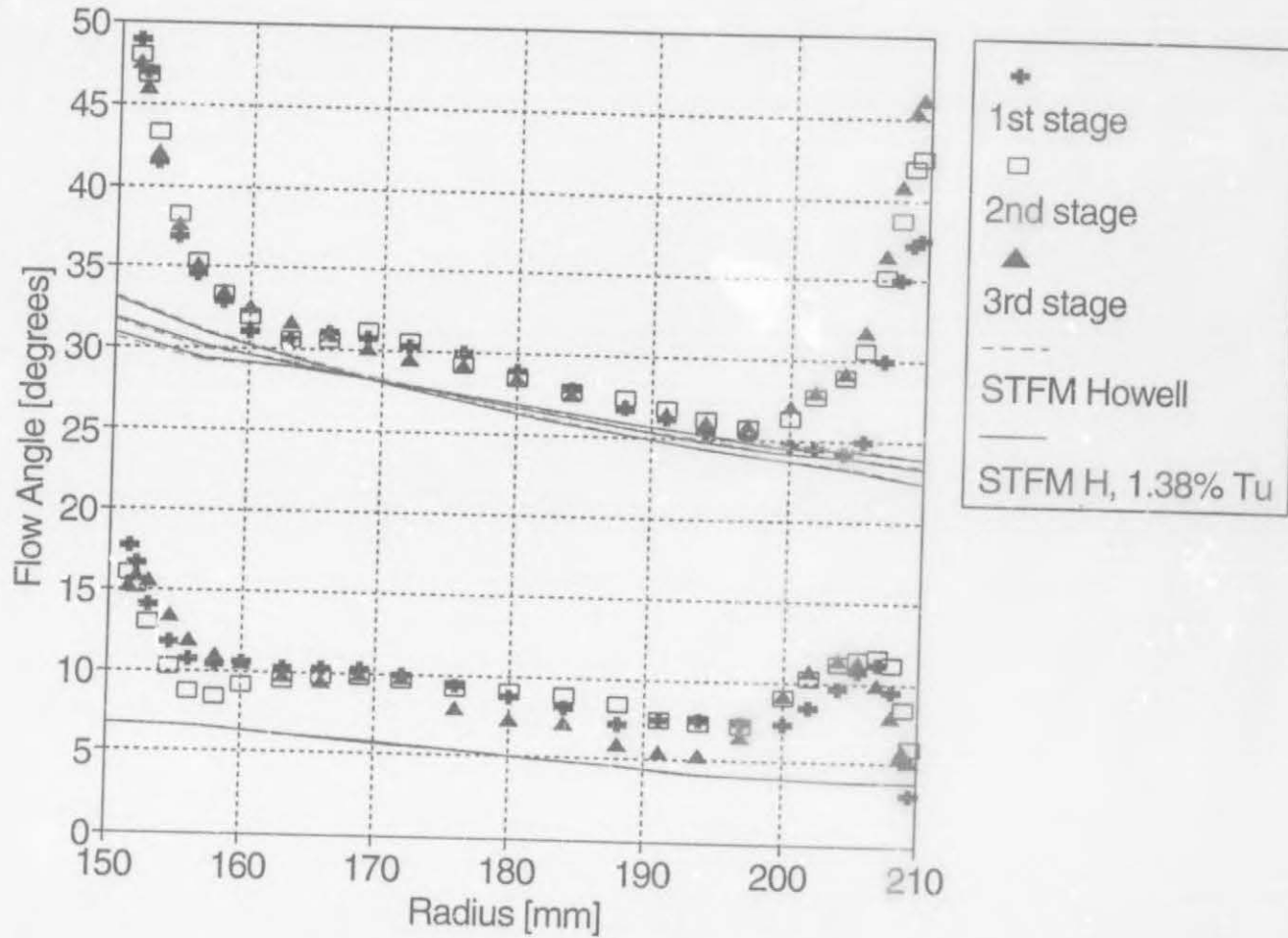


Figure 7.13: Flow angle profiles at near-choke flowrate: 2.80 kg/s. Comparison between experimental data and STFM predictions using Howell's method with and without correction of Roberts

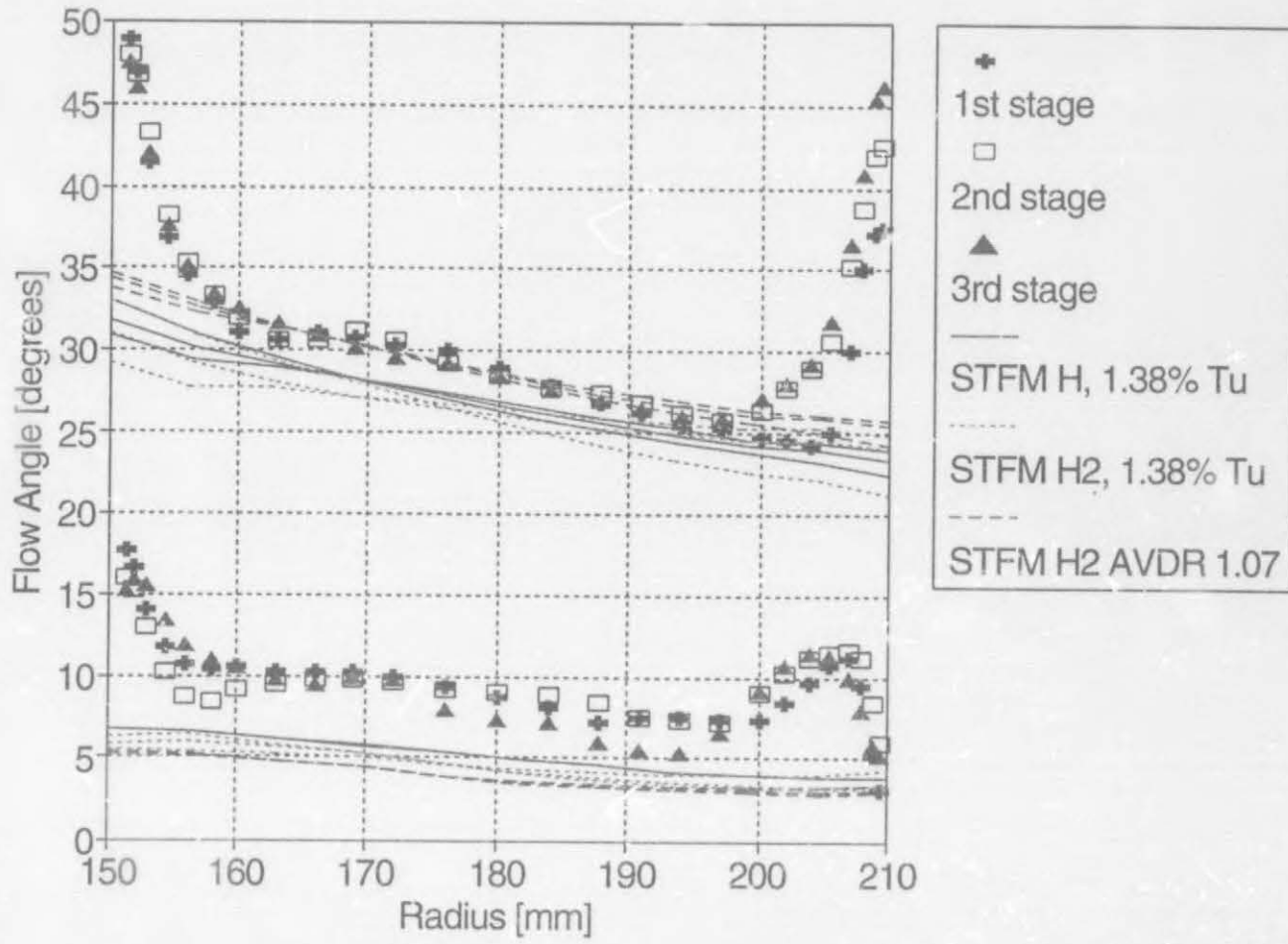


Figure 7.14: Flow angle profiles at near-choke flowrate: 2.80 kg/s. Comparison between experimental data and STFM predictions using correction of Roberts with Howell's method and H2 (with and without AVDR correction)

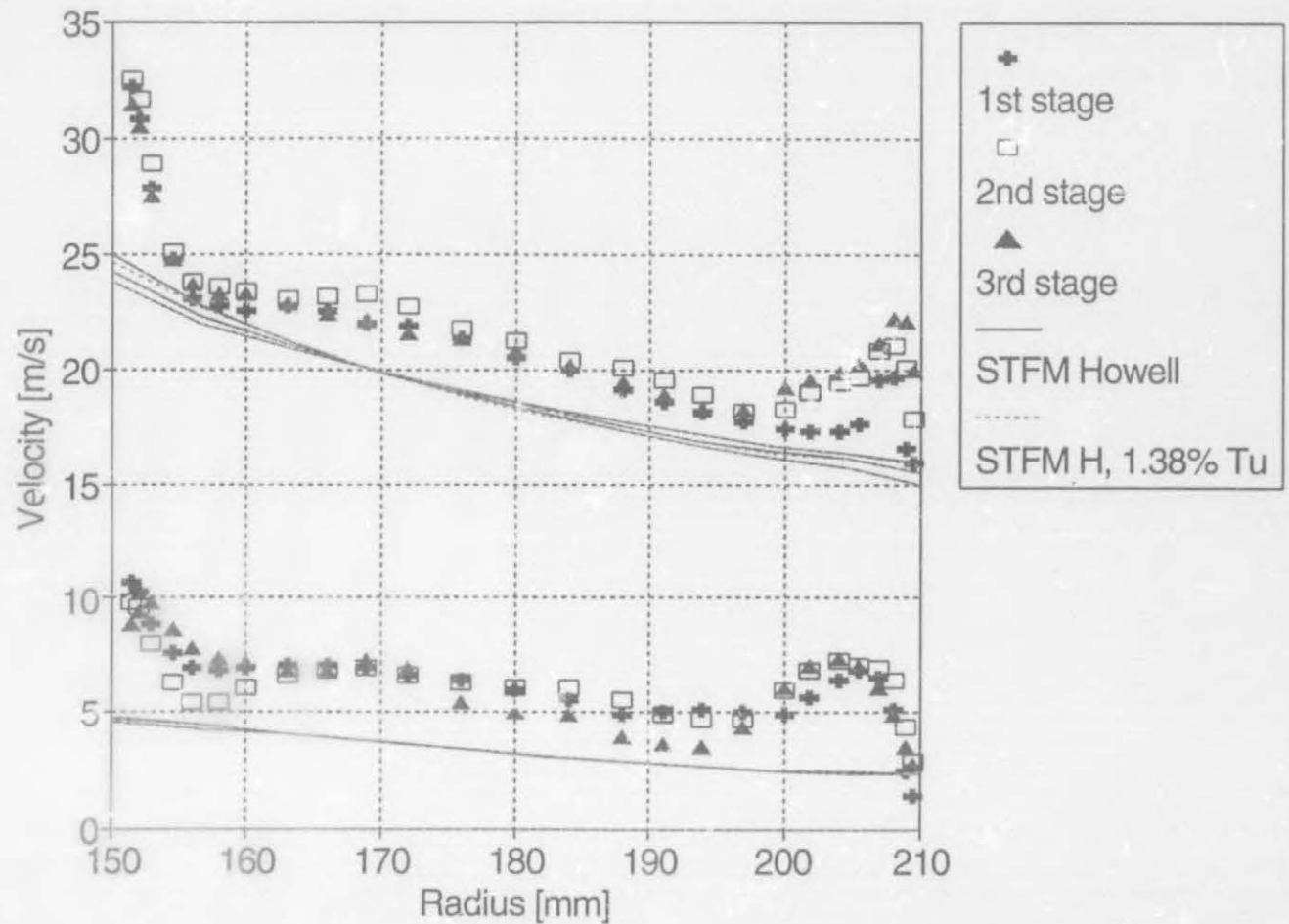


Figure 7.15: Tangential velocity profiles at near-choke flowrate: 2.80 kg/s. Comparison between experimental data and STFM predictions using Howell's method with and without correction of Roberts

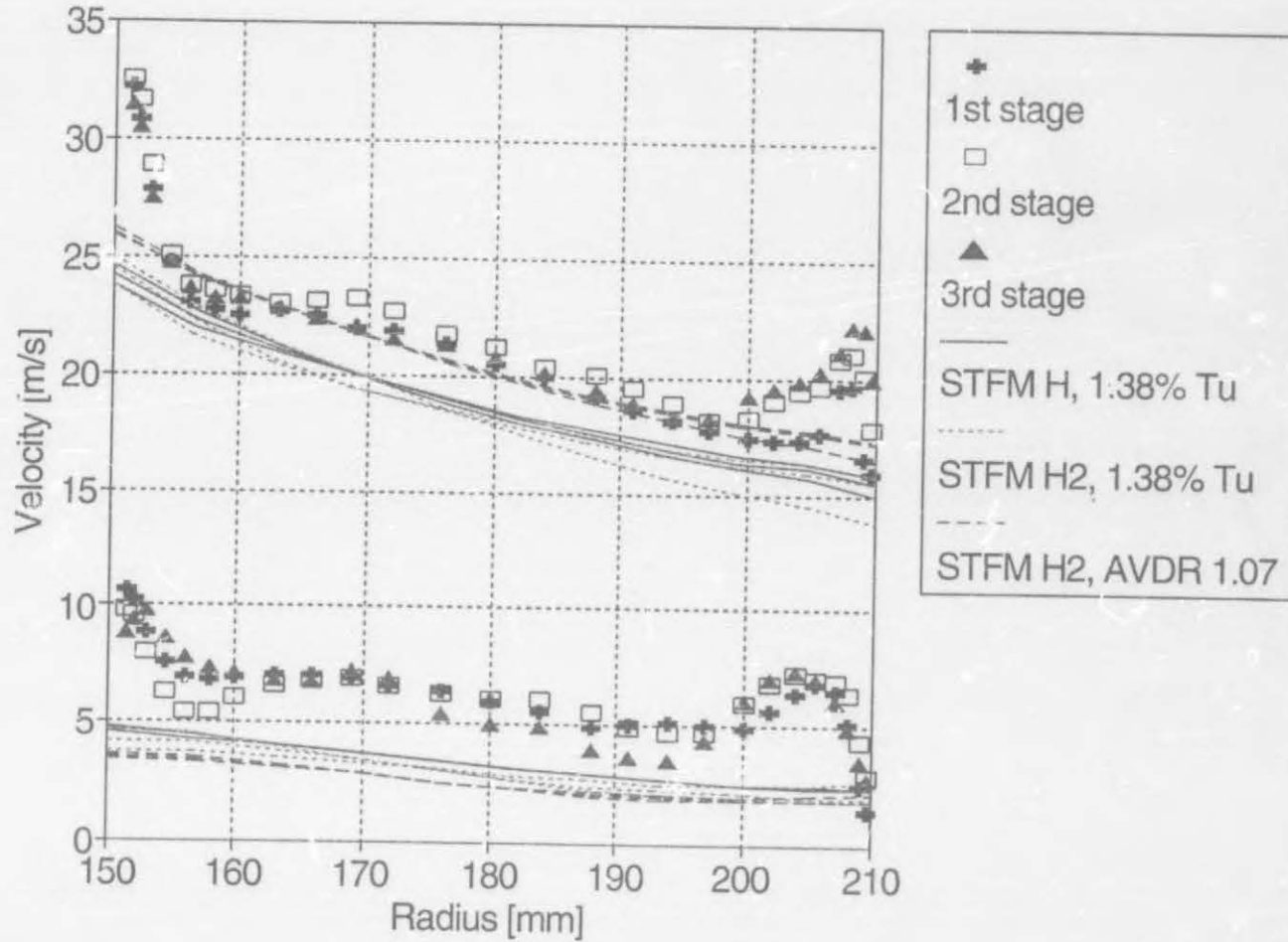


Figure 7.16: Tangential velocity profiles at near-choke flowrate: 2.80 kg/s. Comparison between experimental data and STFM predictions using correction of Roberts with Howell's method and H2 (with and without AVDR correction)

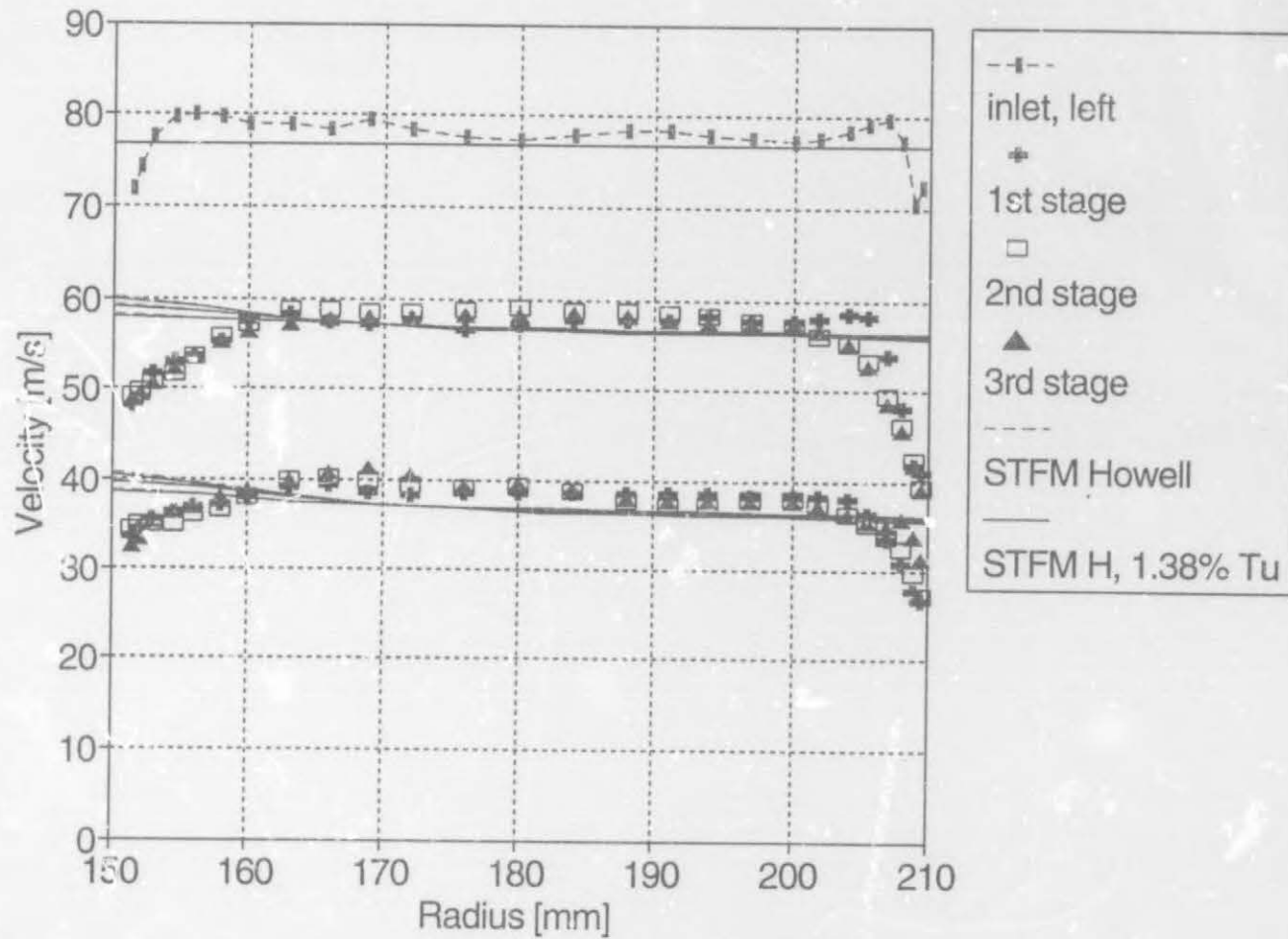
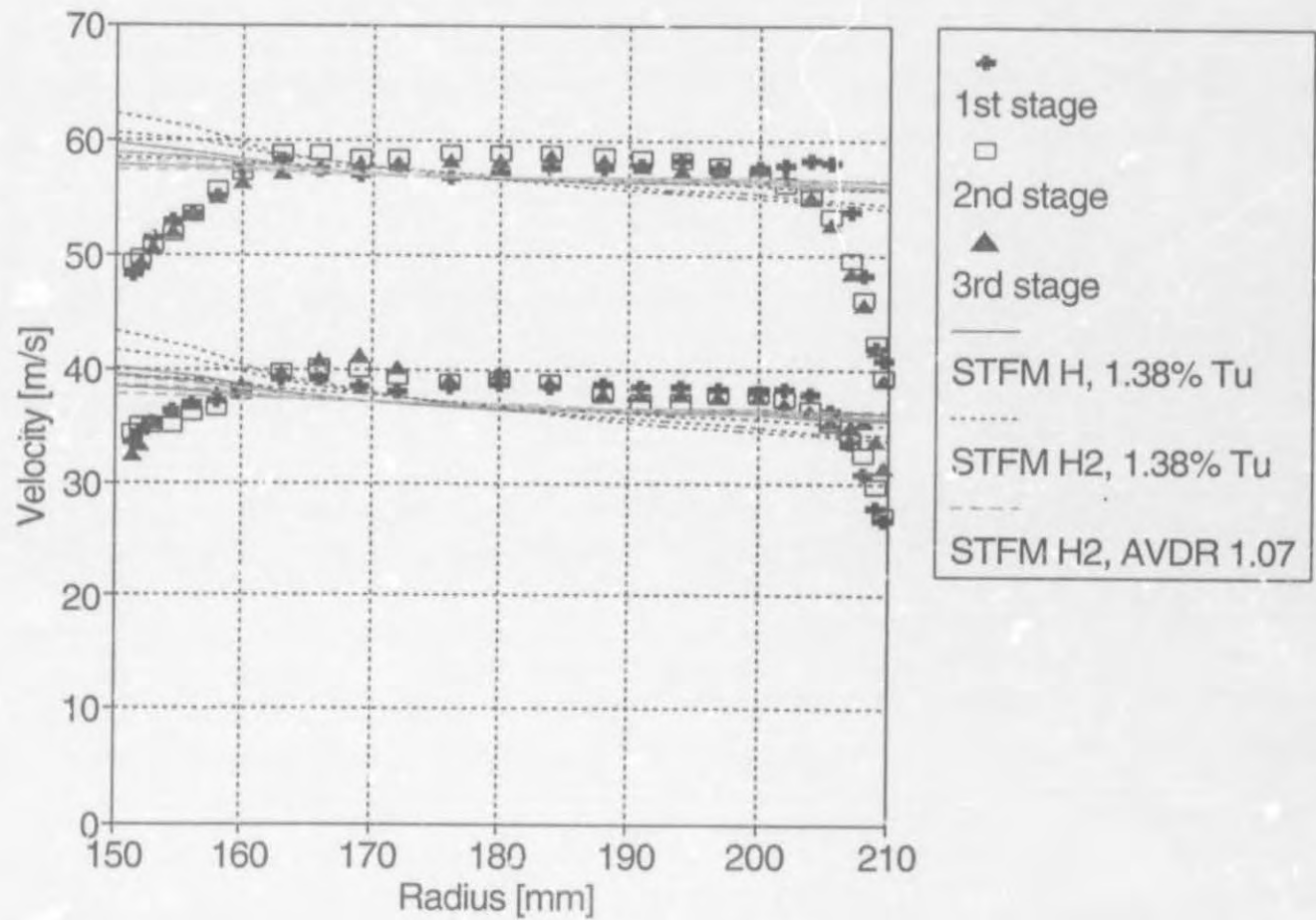


Figure 7.17: Axial velocity profiles at near-choke flowrate: 2.80 kg/s. (Zeroes of inlet and rotor rows have been staggered by 40 and 20 m/s respectively). Comparison between experimental data and STFM predictions using Howell's method with and without correction of Roberts



- 168 -

Figure 7.18: Axial velocity profiles at near-choke flowrate: 2.80 kg/s. (Zeroes of rotor rows have been staggered by 20 m/s). Comparison between experimental data and STFM predictions using correction of Roberts with Howell's method and H2 (with and without AVDR correction)

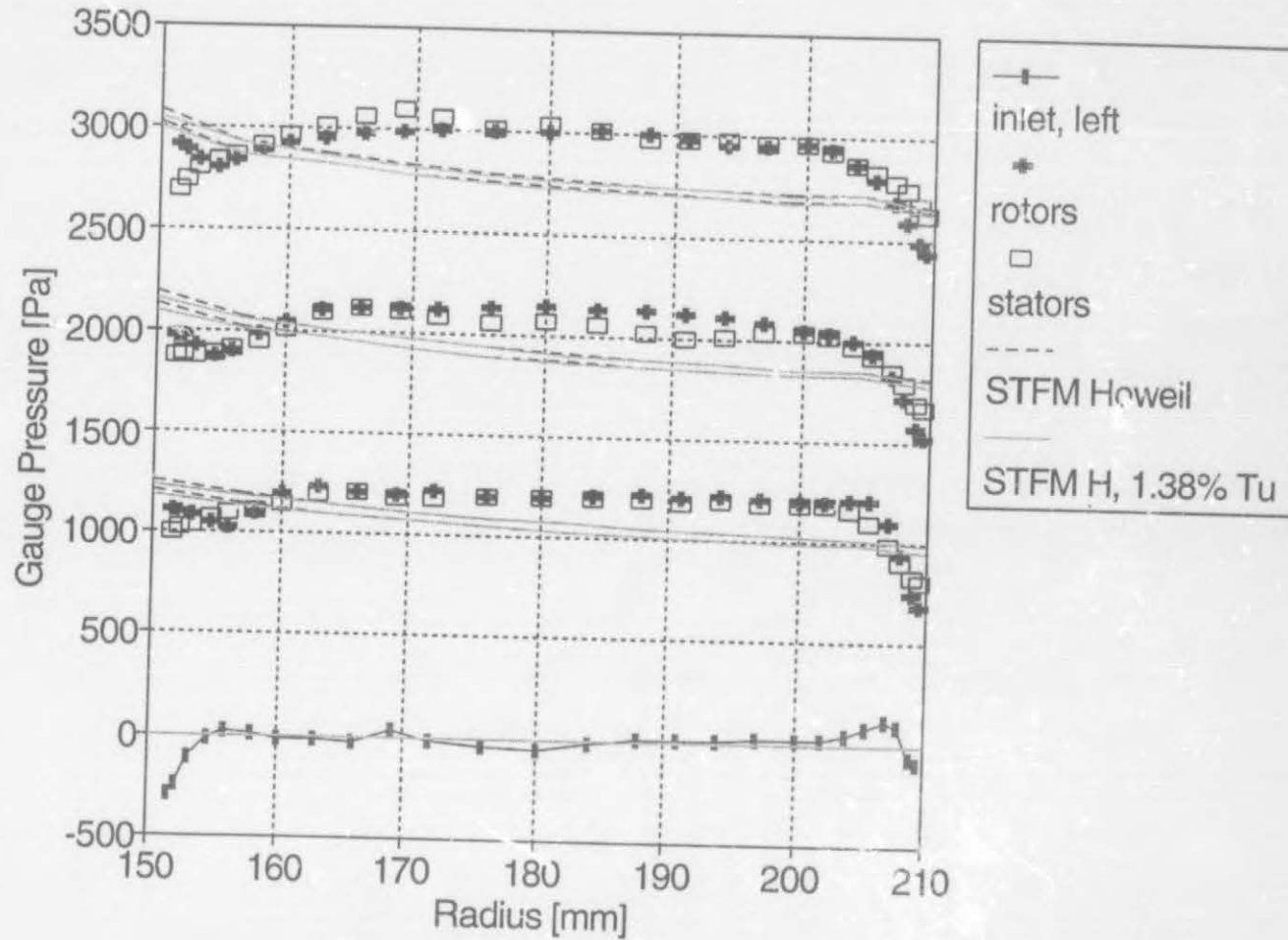


Figure 7.19: Total pressure profiles (relative to inlet mass average) at near-choke flowrate: 2.80 kg/s. Comparison between experimental data and STFM predictions using Howell's method with and without correction of Roberts

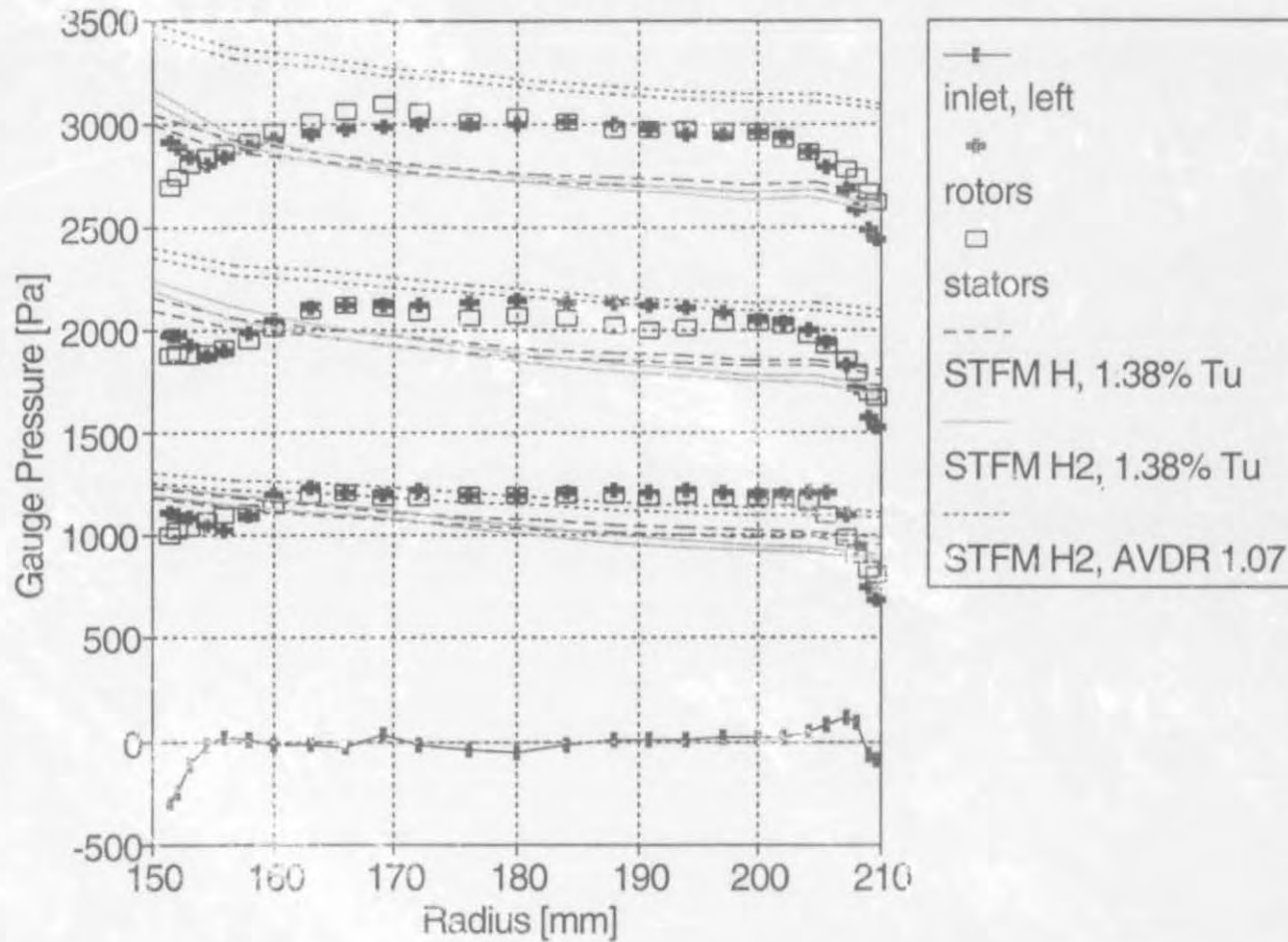


Figure 7.20: Total pressure profiles (relative to inlet mass average) at near-choke flowrate: 2.80 kg/s. Comparison between experimental data and STFM predictions using correction of Roberts with Howell's method and H2 (with and without AVDR correction)

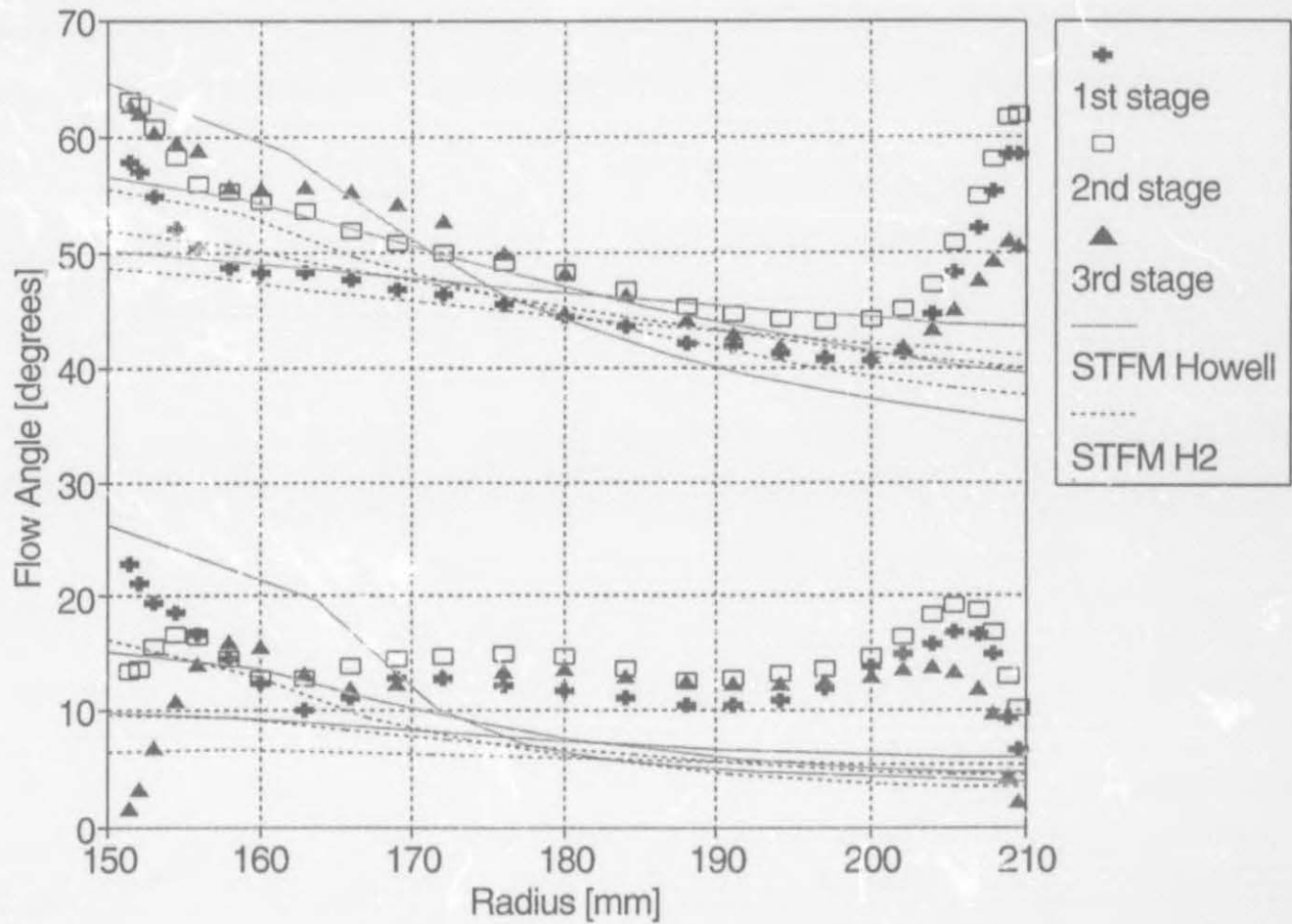


Figure 7.21: Flow angle profiles at near-surge flowrate: 1.99 kg/s. Comparison between experimental data and STFM predictions, with \hat{i}_{adj} limited to 0.6, using Howell's method and H2

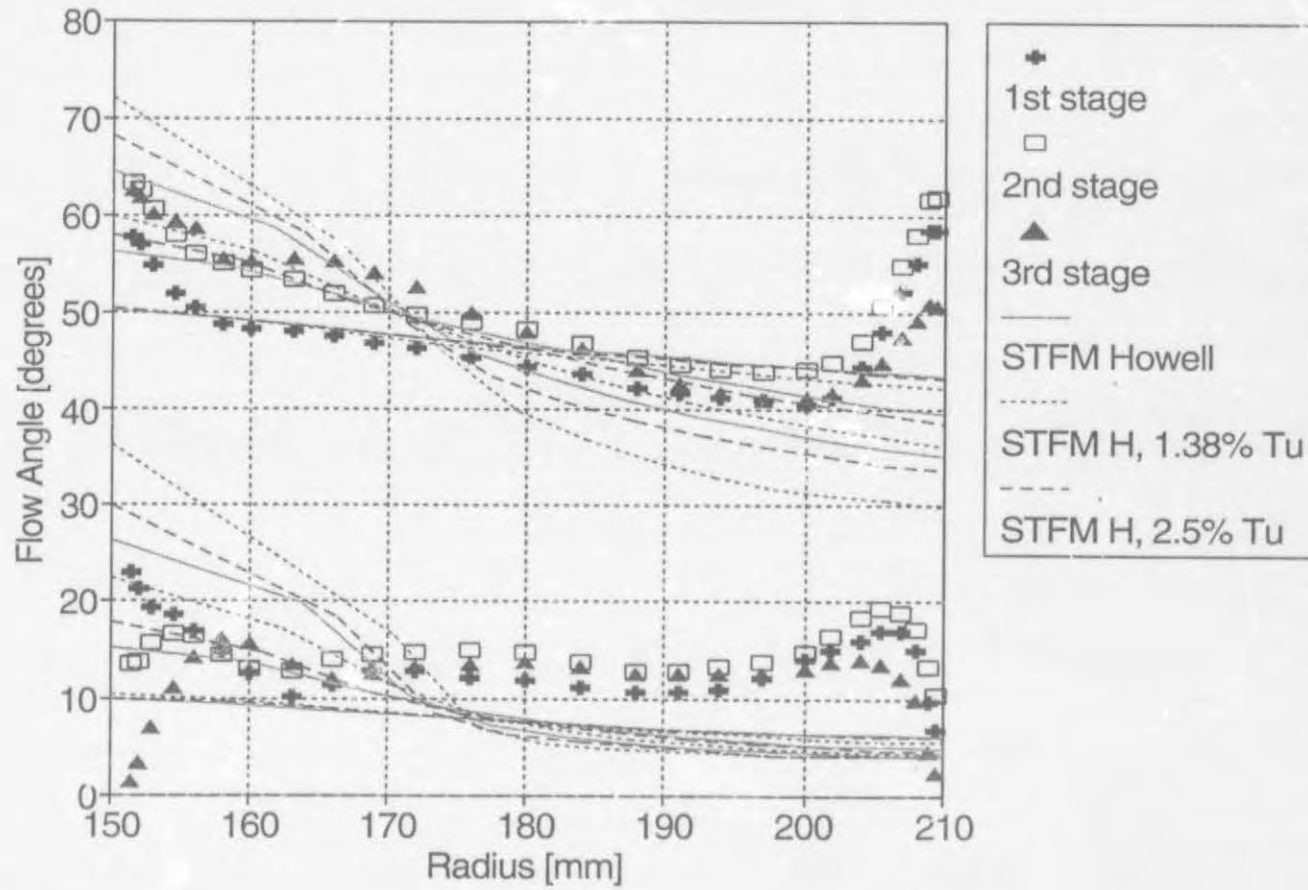


Figure 7.22: Flow angle profiles at near-surge flowrate: 1.99 kg/s. Comparison between experimental data and STFM predictions, with \hat{i}_{adj} limited to 0.6, using Howell's method without and then with the correction of Roberts at two levels of Tu

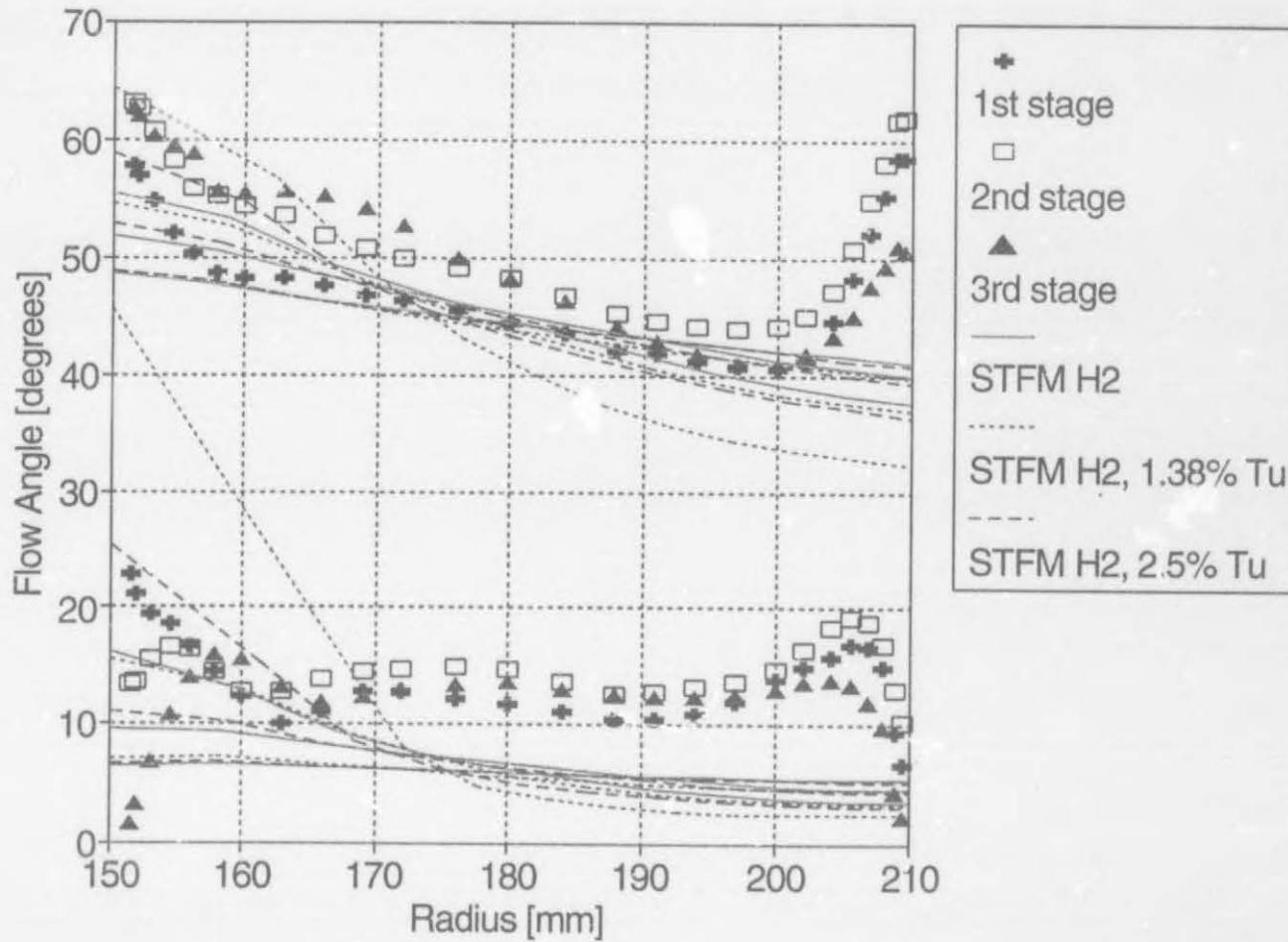


Figure 7.23: Flow angle profiles at near-surge flowrate: 1.99 kg/s. Comparison between experimental data and STFM predictions, with \hat{i}_{adj} limited to 0.6, using H2 without and then with the correction of Roberts at two levels of Tu

- 173 -

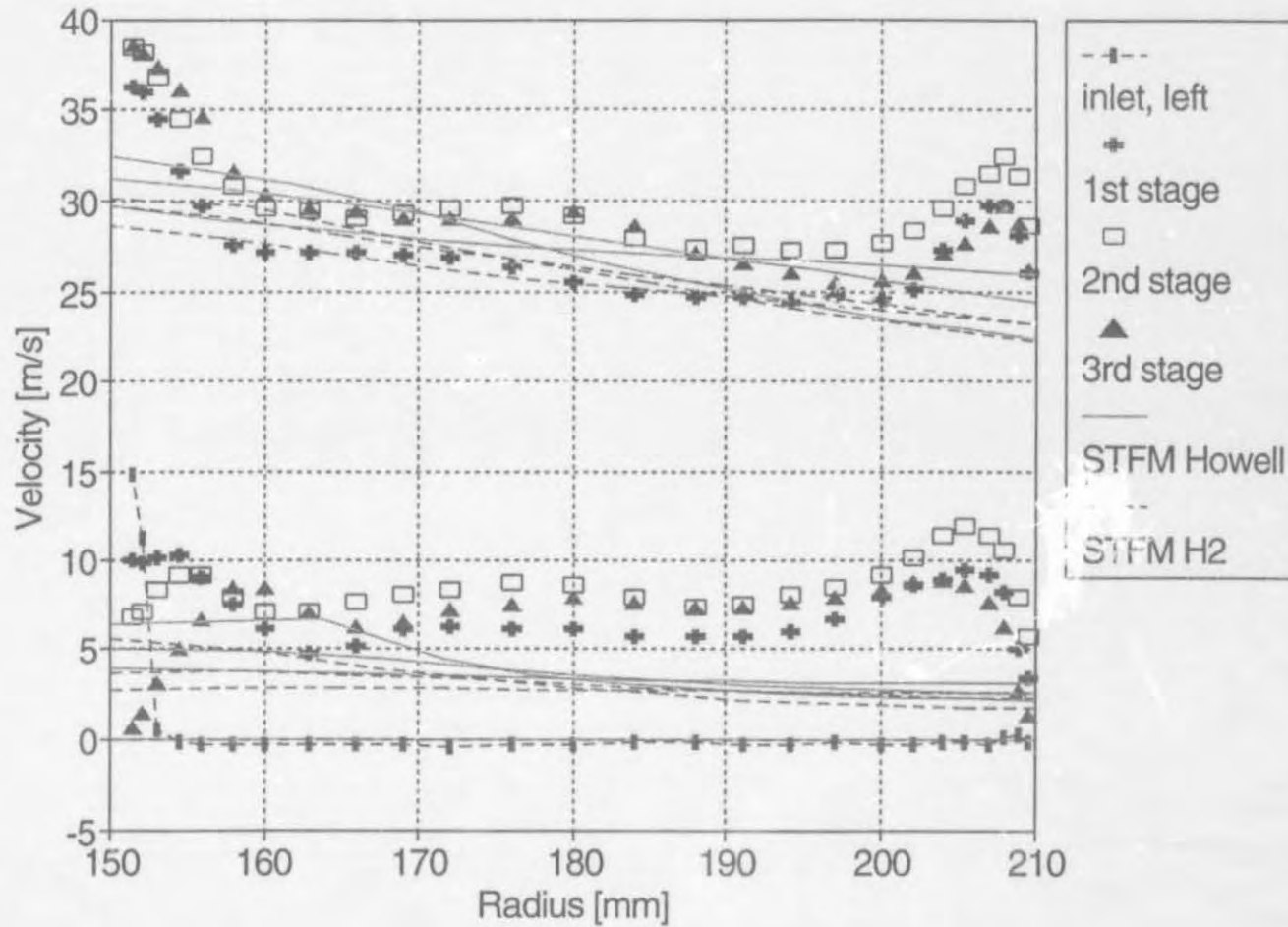


Figure 7.24: Tangential velocity profiles at near-surge flowrate: 1.99 kg/s. Comparison between experimental data and STFM predictions, with \hat{i}_{adj} limited to 0.6, using Howell's method and H2

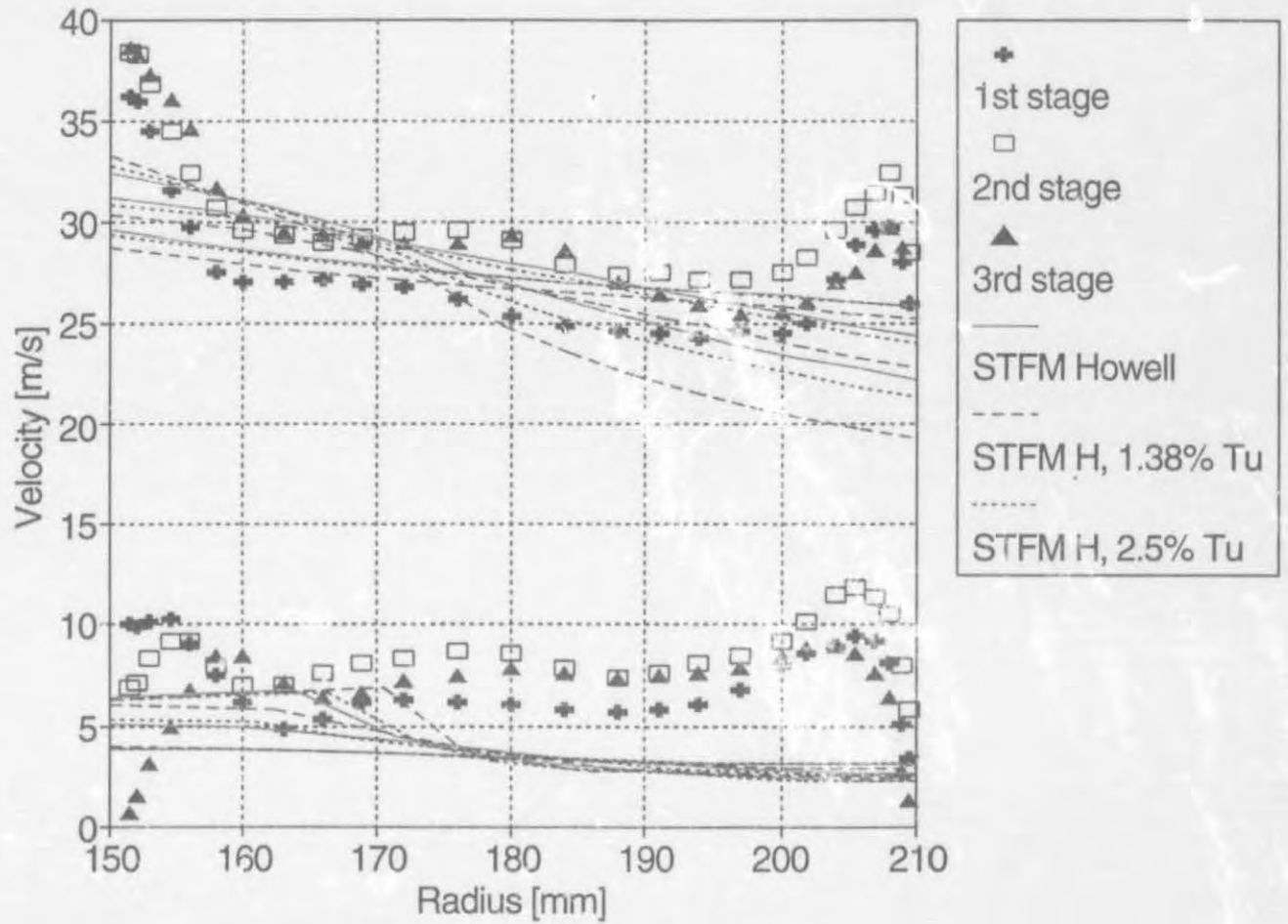


Figure 7.25: Tangential velocity profiles at near-surge flowrate: 1.99 kg/s. Comparison between experimental data and STFM predictions, with \hat{i}_{adj} limited to 0.6, using Howell's method without and then with the correction of Roberts at two levels of Tu

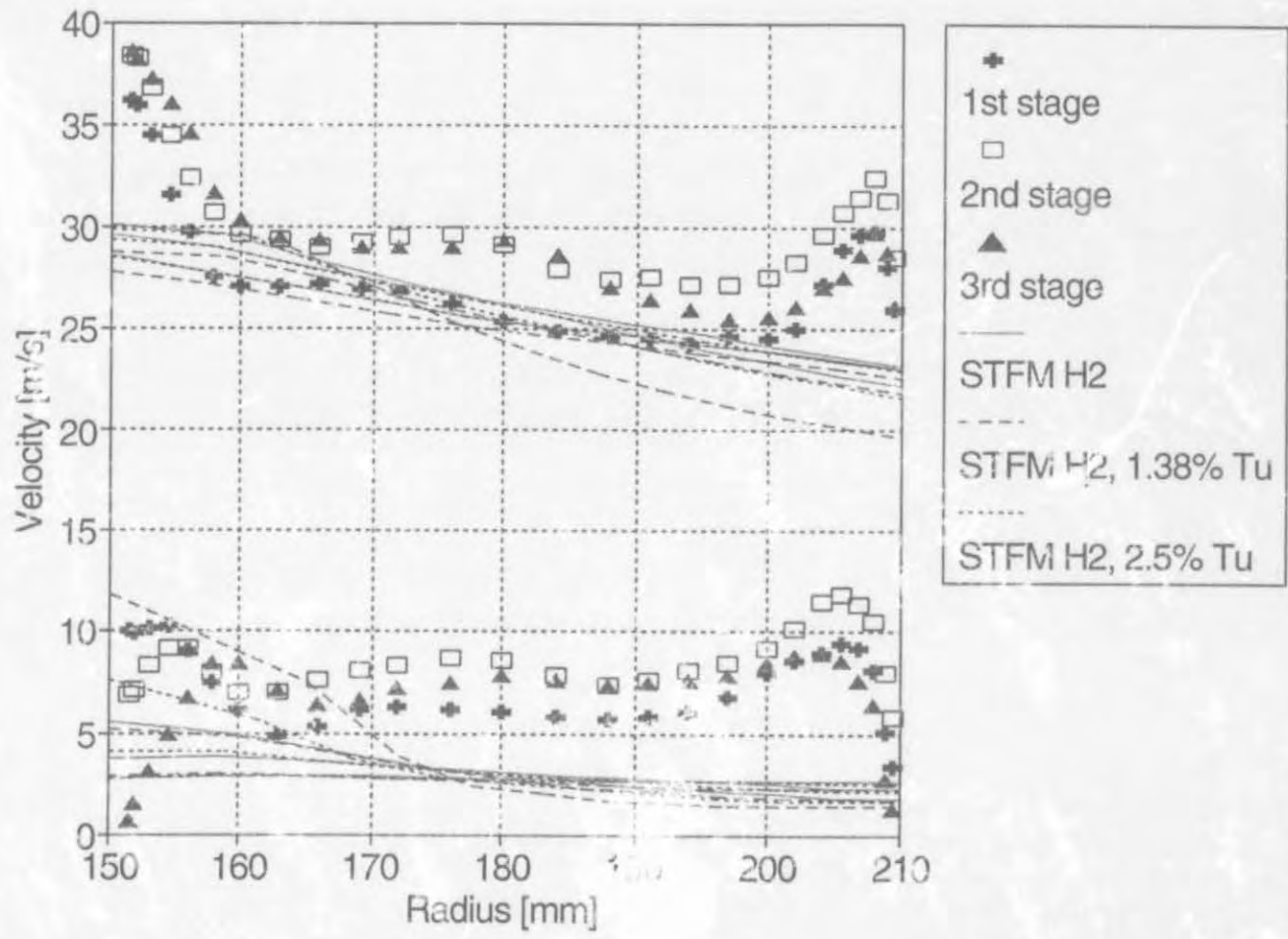


Figure 7.26: Tangential velocity profiles at near-surge flowrate: 1.99 kg/s. Comparison between experimental data and STFM predictions, with \hat{i}_{adj} limited to 0.6, using H2 without and then with the correction of Roberts at two levels of Tu

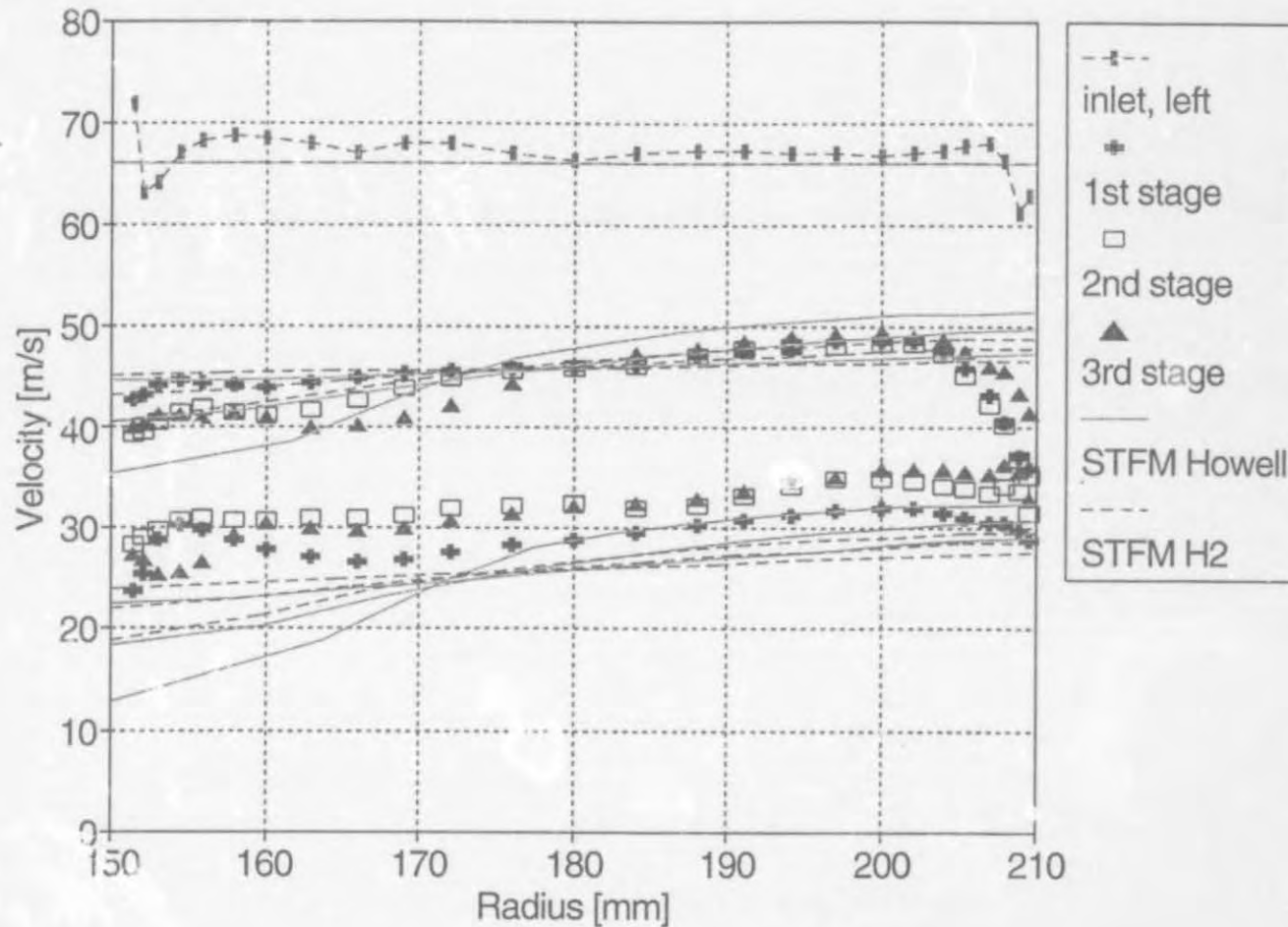


Figure 7.27: Axial velocity profiles at near-surge flowrate: 1.99 kg/s. (Zeroes of inlet and rotor rows have been staggered by 40 and 20 m/s respectively). Comparison between experimental data and STFM predictions, with \hat{i}_{adj} limited to 0.6, using Howell's method and H2

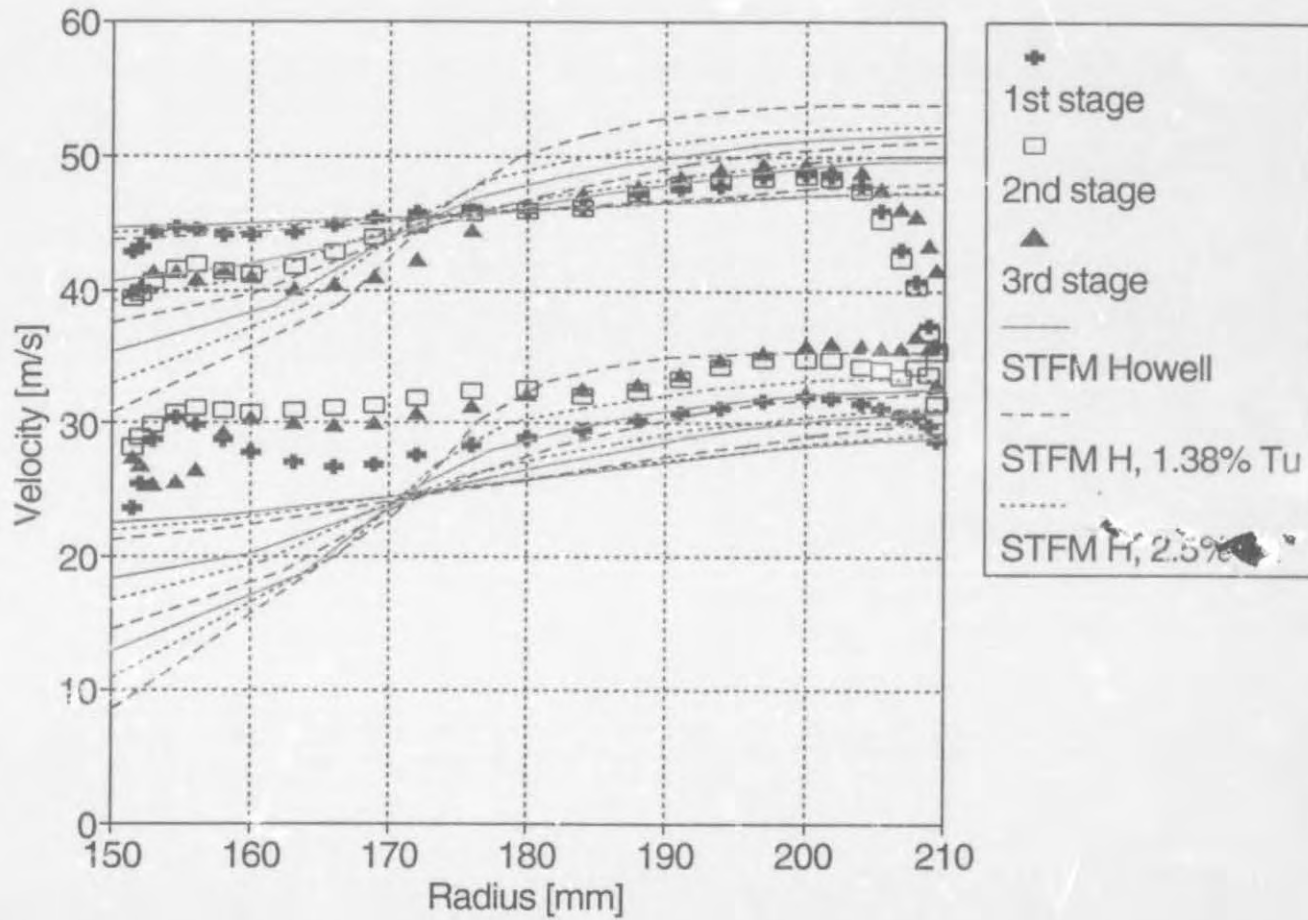


Figure 7.28: Axial velocity profiles at near-surge flowrate: 1.99 kg/s. (Zeroes of inlet and rotor rows have been staggered by 40 and 20 m/s respectively). Comparison between experimental data and STFM predictions, with \hat{i}_{adj} limited to 0.6, using Howell's method without and then with the correction of Roberts at two levels of Tu

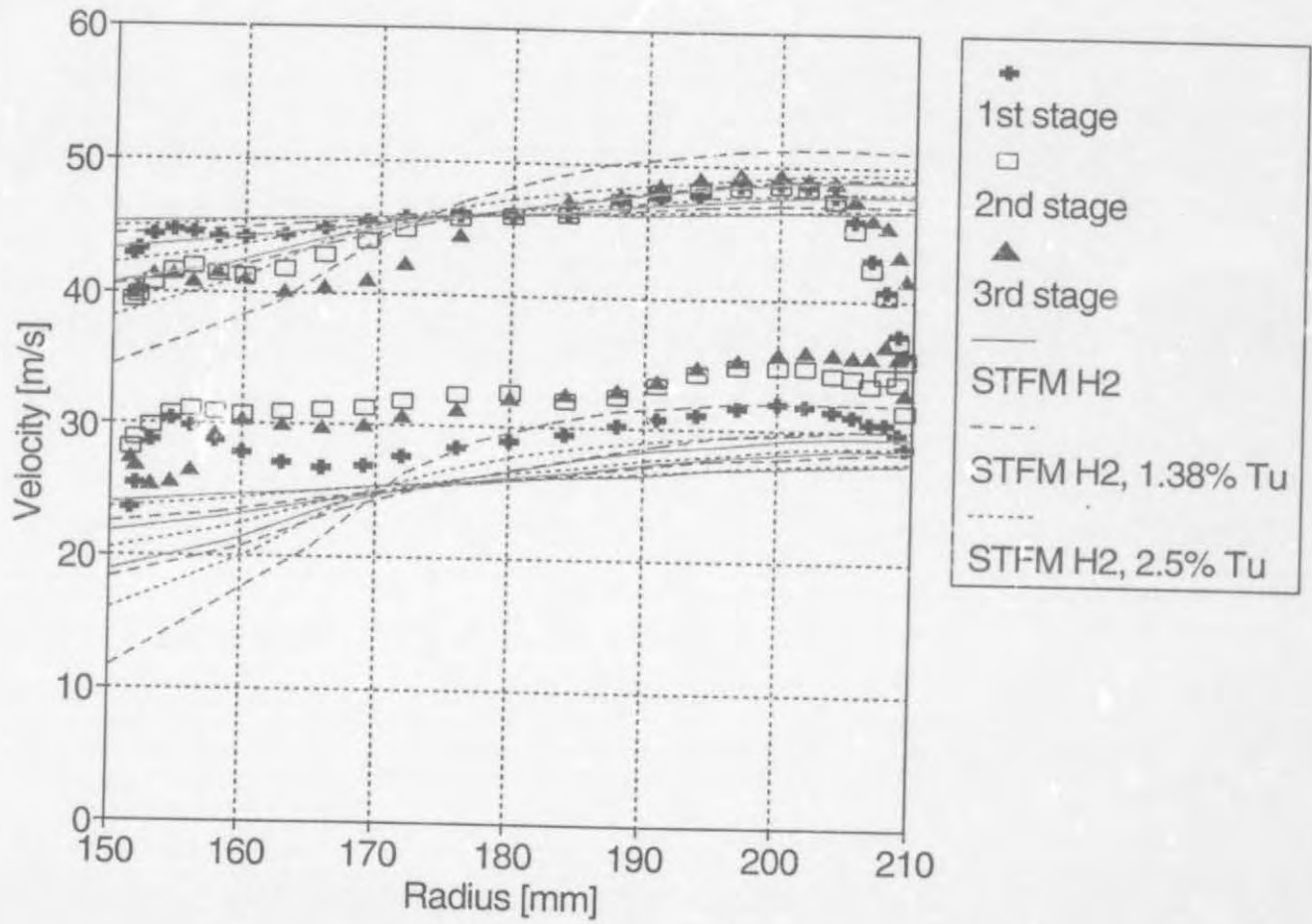


Figure 7.29: Axial velocity profiles at near-surge flowrate: 1.99 kg/s. (Zeroes of rotor rows have been staggered by 20 m/s). Comparison between experimental data and STFMs H2 predictions, with \hat{i}_{adj} limited to 0.6, using H2 without and then with the correction of Roberts at two levels of Tu

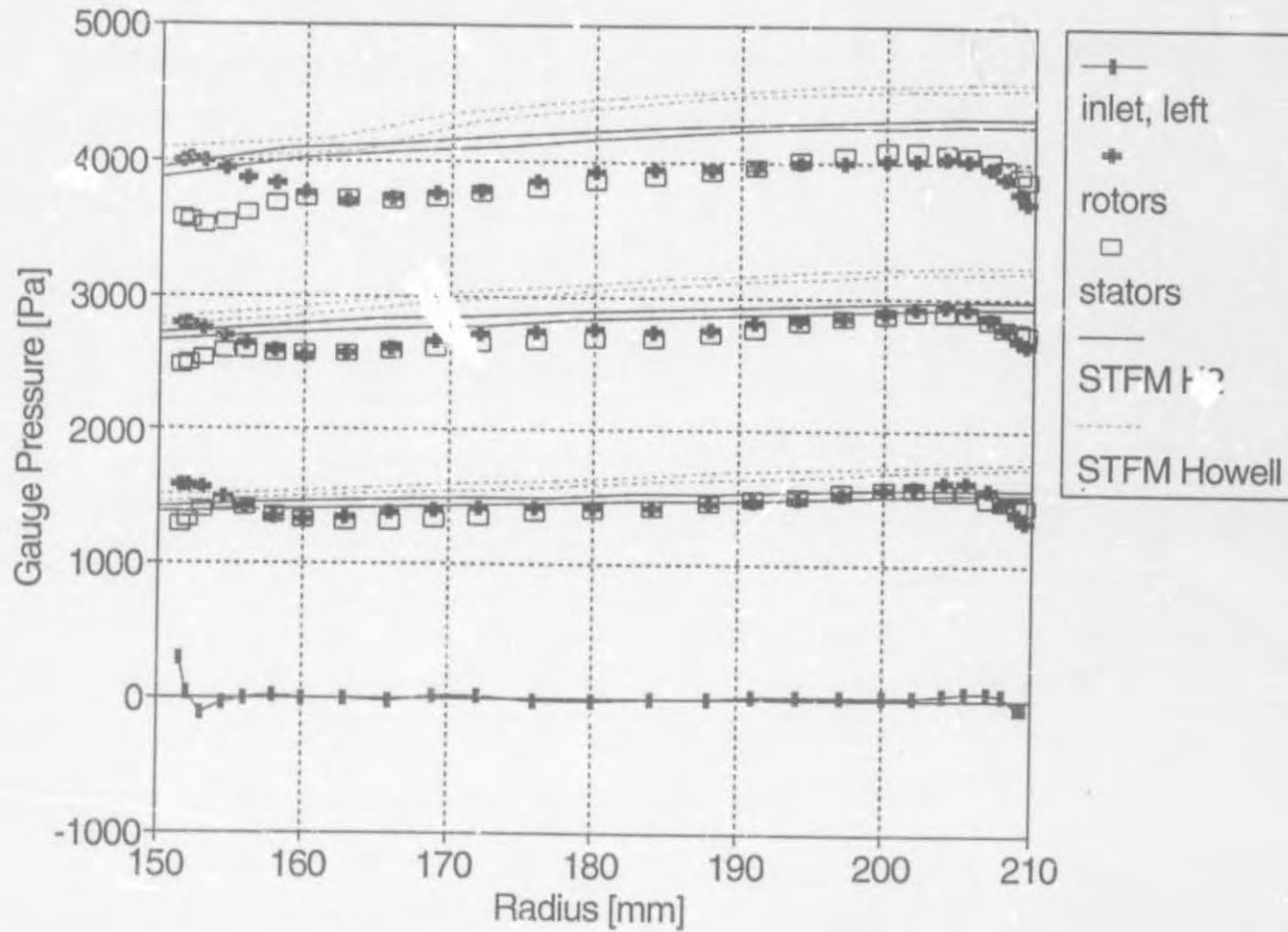


Figure 7.30: Total pressure profiles (relative to inlet mass average) at near-surge flowrate: 1.99 kg/s. Comparison between experimental data and STFMs predictions, with \hat{i}_{adj} limited to 0.6, using Howell's method and H2

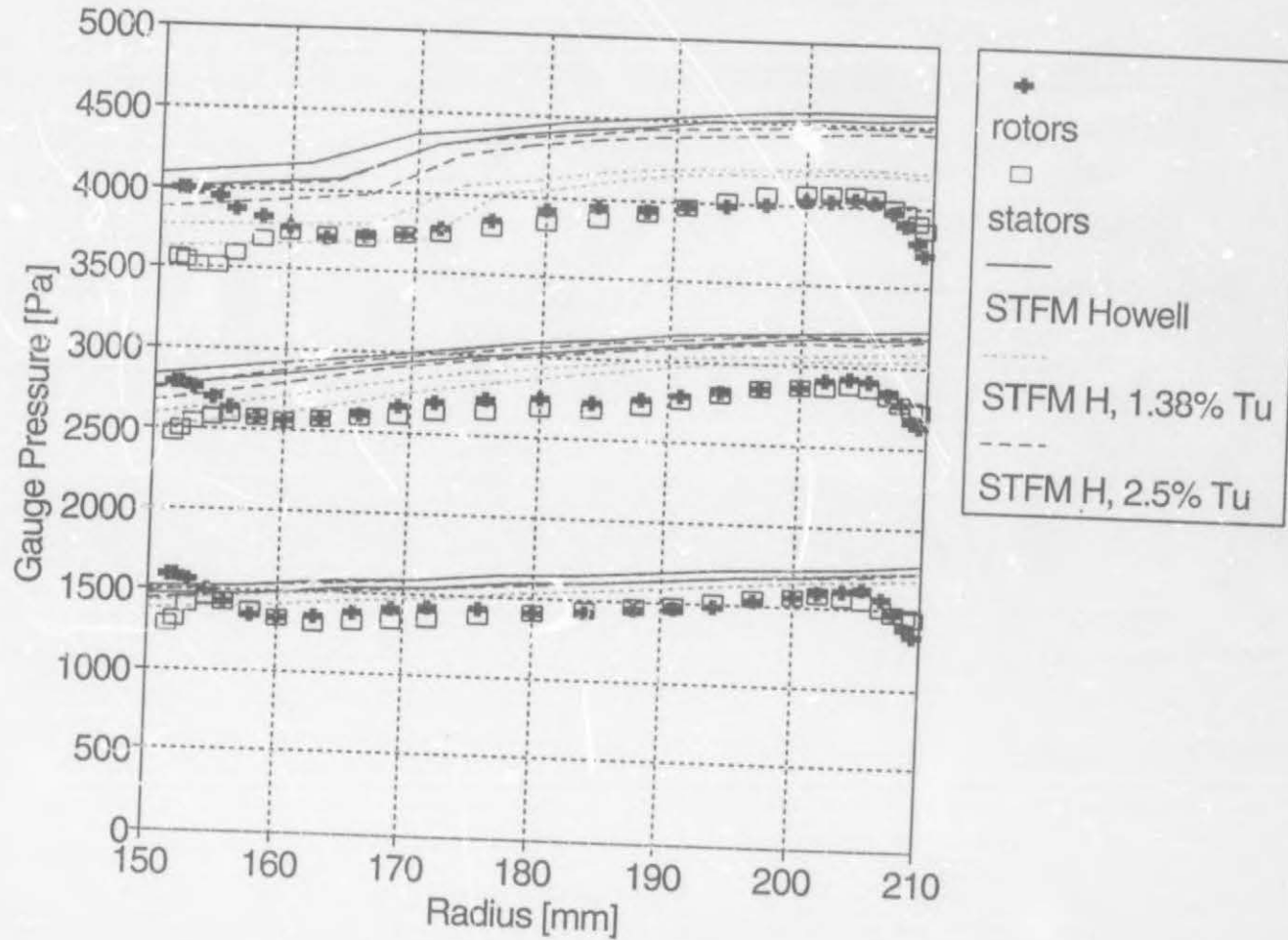


Figure 7.31: Total pressure profiles (relative to inlet mass average) at near-surge flowrate: 1.99 kg/s. Comparison between experimental data and STFM predictions, with \hat{i}_{adj} limited to 0.6, using Howell's method without and then with the correction of Roberts at two levels of Tu

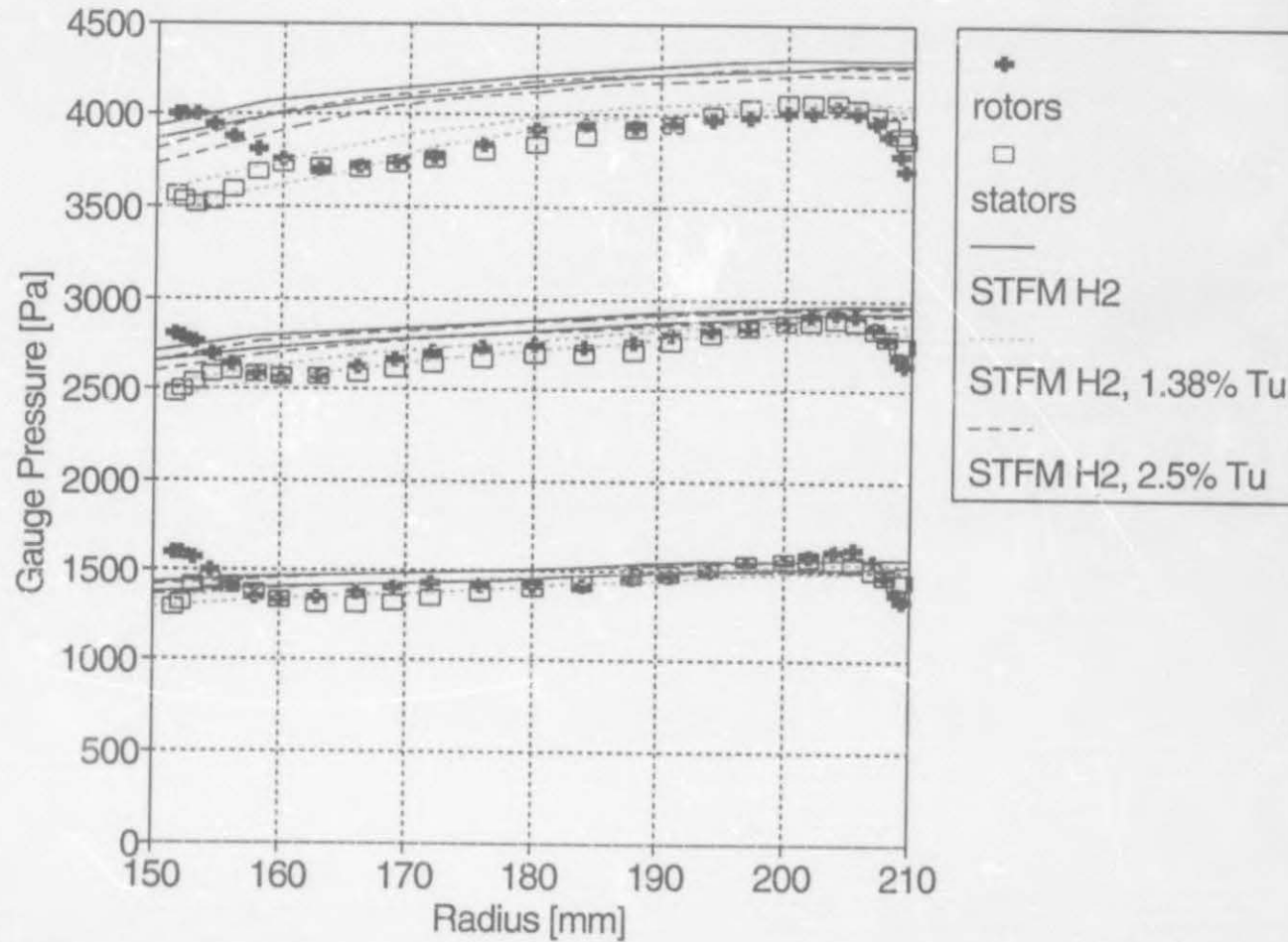


Figure 7.32: Total pressure profiles (relative to inlet mass average) at near-surge flowrate: 1.99 kg/s. Comparison between experimental data and STFM predictions, with \hat{i}_{adj} limited to 0.6, using H2 without and then with the correction of Roberts at two levels of Tu

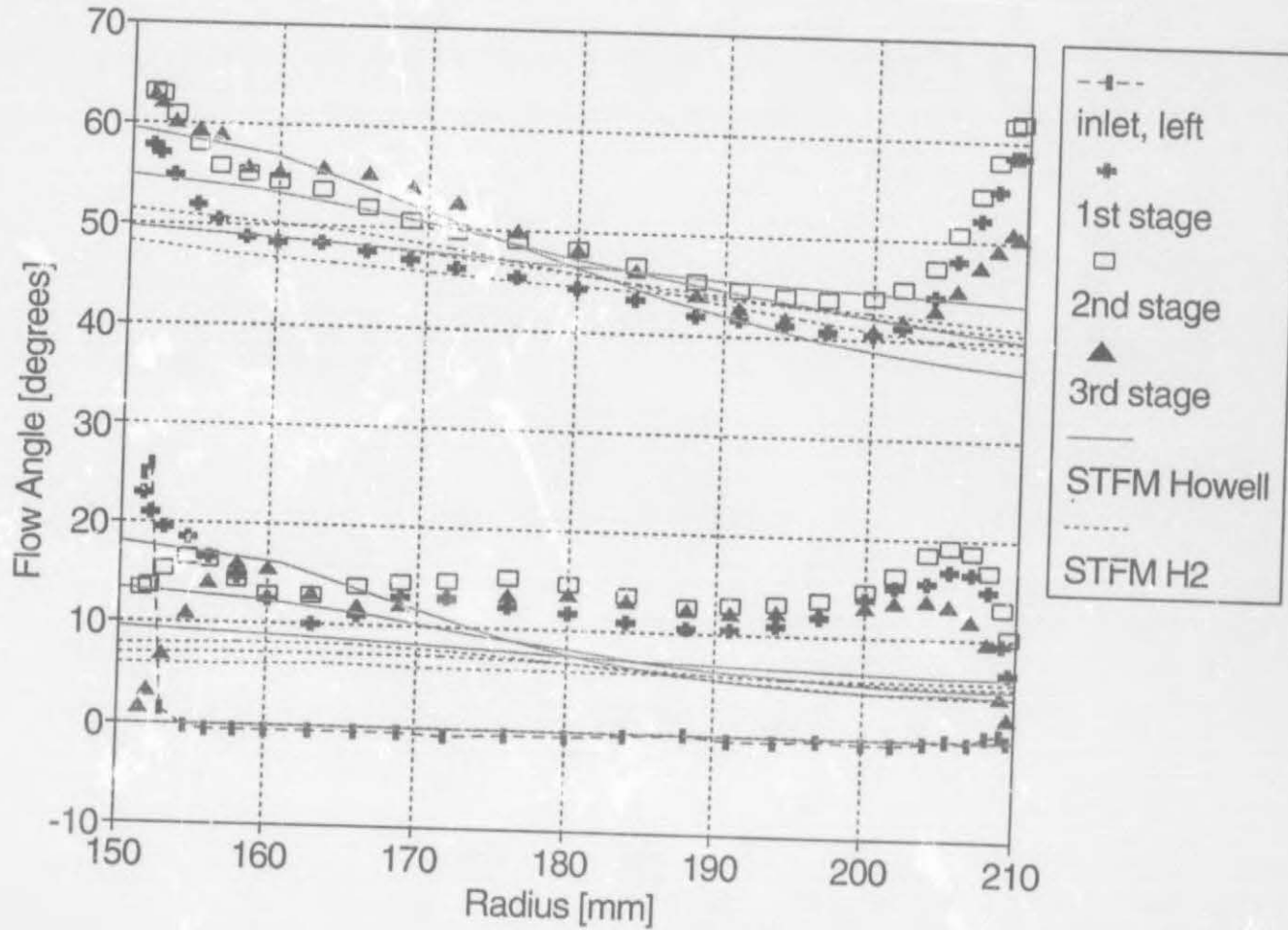


Figure 7.33: Flow angle profiles at near-surge flowrate: 1.99 kg/s. Comparison between experimental data and STFM predictions, with \hat{i}_{adj} limited to 0.4, using Howell's method and H2

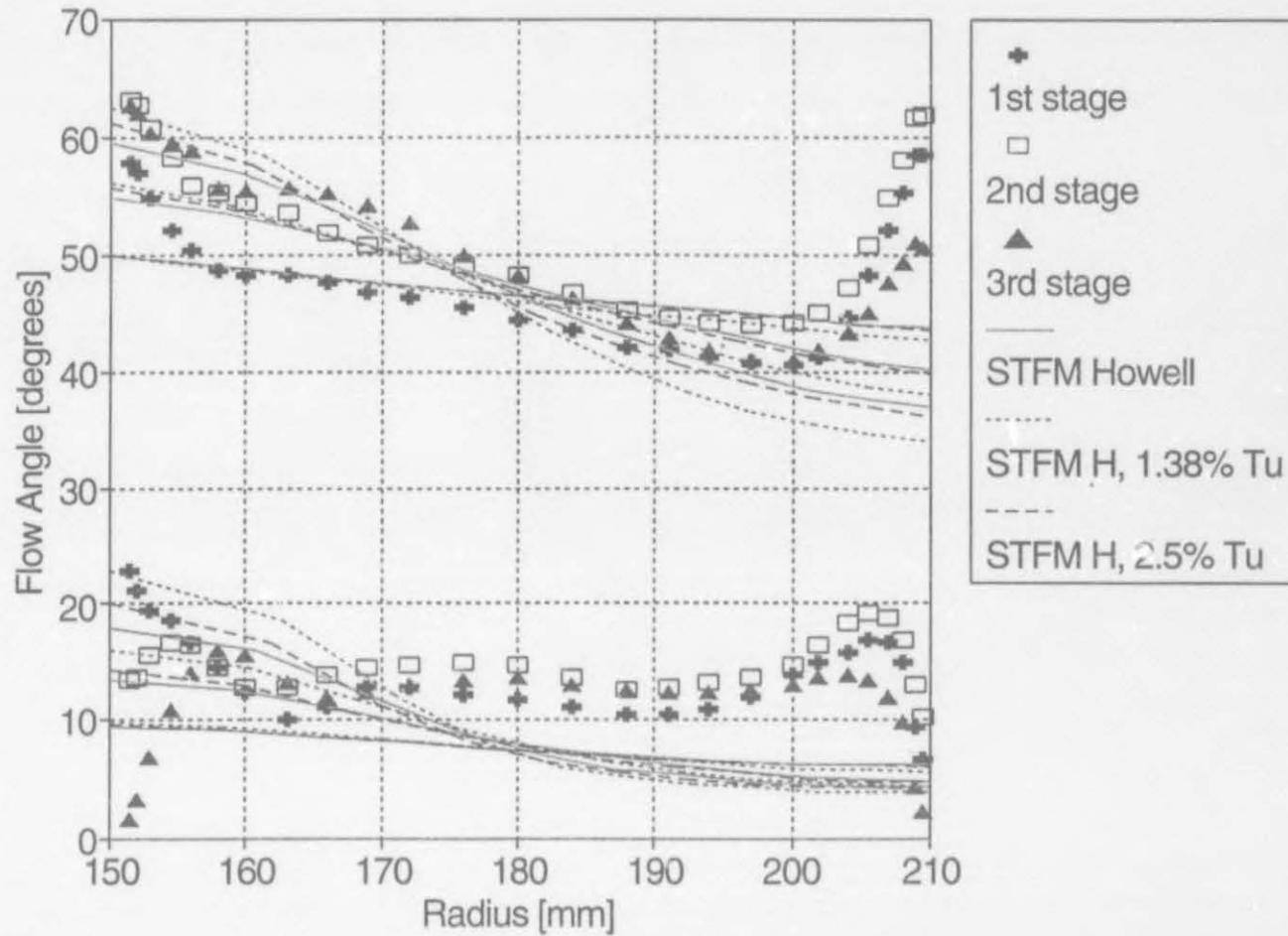


Figure 7.34: Flow angle profiles at near-surge flowrate: 1.99 kg/s. Comparison between experimental data and STFMs predictions, with \hat{i}_{adj} limited to 0.4, using Howell's method without and then with the correction of Roberts at two levels of Tu

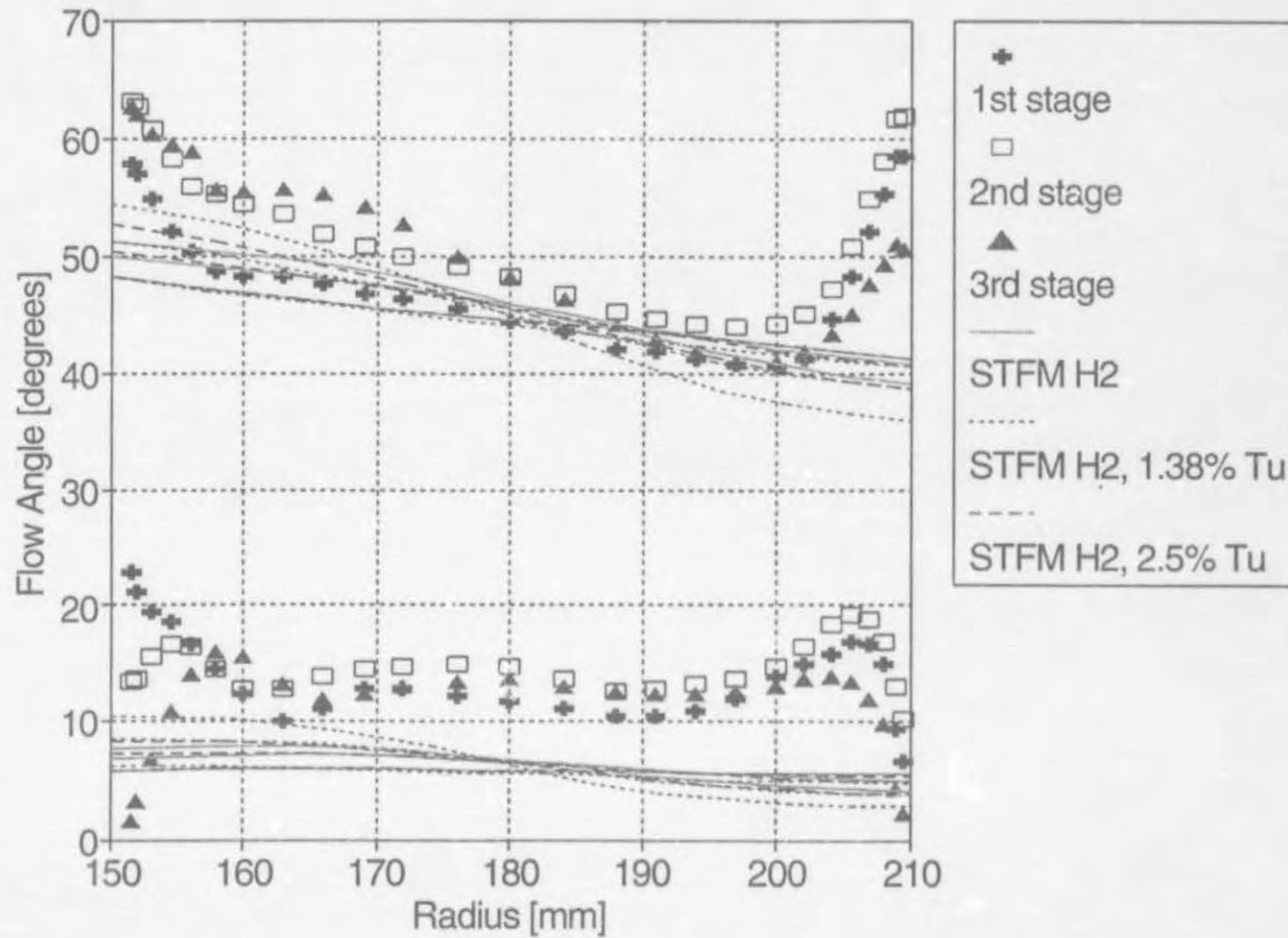


Figure 7.35: Flow angle profiles at near-surge flowrate: 1.99 kg/s. Comparison between experimental data and STFMs predictions, with \hat{i}_{adj} limited to 0.4, using H2 without and then with the correction of Roberts at two levels of Tu

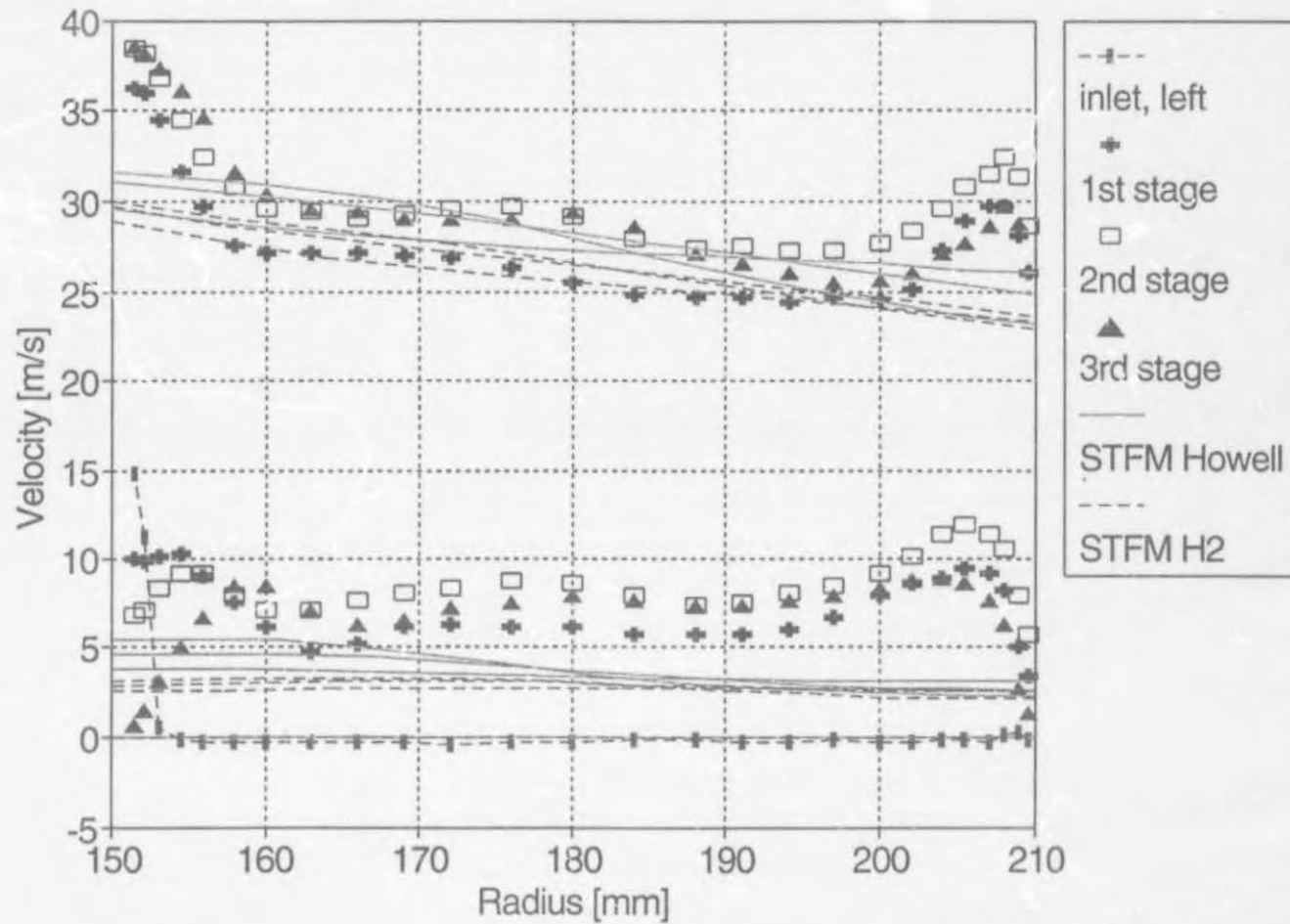


Figure 7.36: Tangential velocity profiles at near-surge flowrate: 1.99 kg/s. Comparison between experimental data and STFM predictions, with \hat{i}_{adj} limited to 0.4, using Howell's method and H2

- 186 -

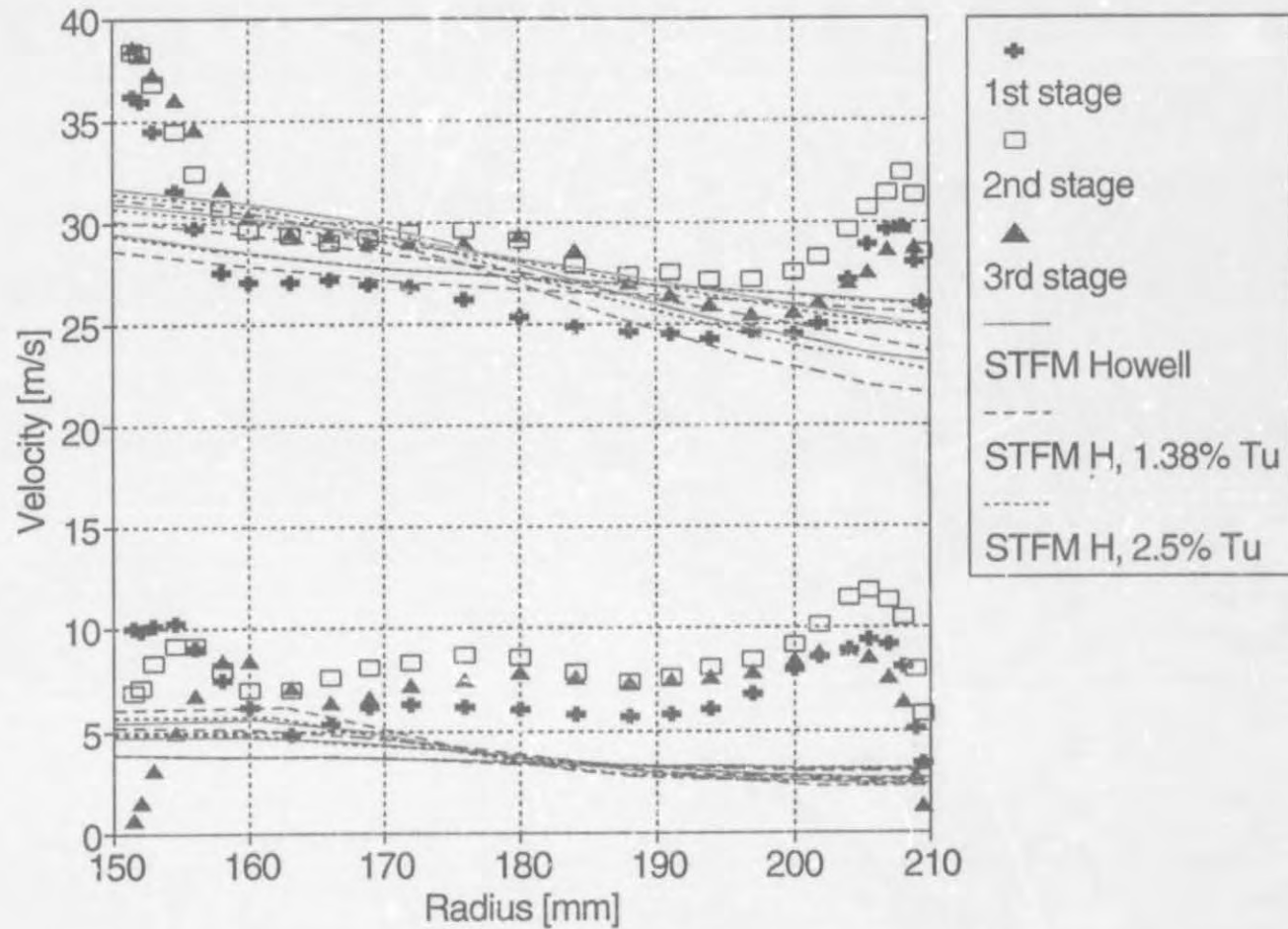


Figure 7.37: Tangential velocity profiles at near-surge flowrate: 1.99 kg/s. Comparison between experimental data and STFM predictions, with \hat{i}_{adj} limited to 0.4, using Howell's method without and then with the correction of Roberts at two levels of Tu

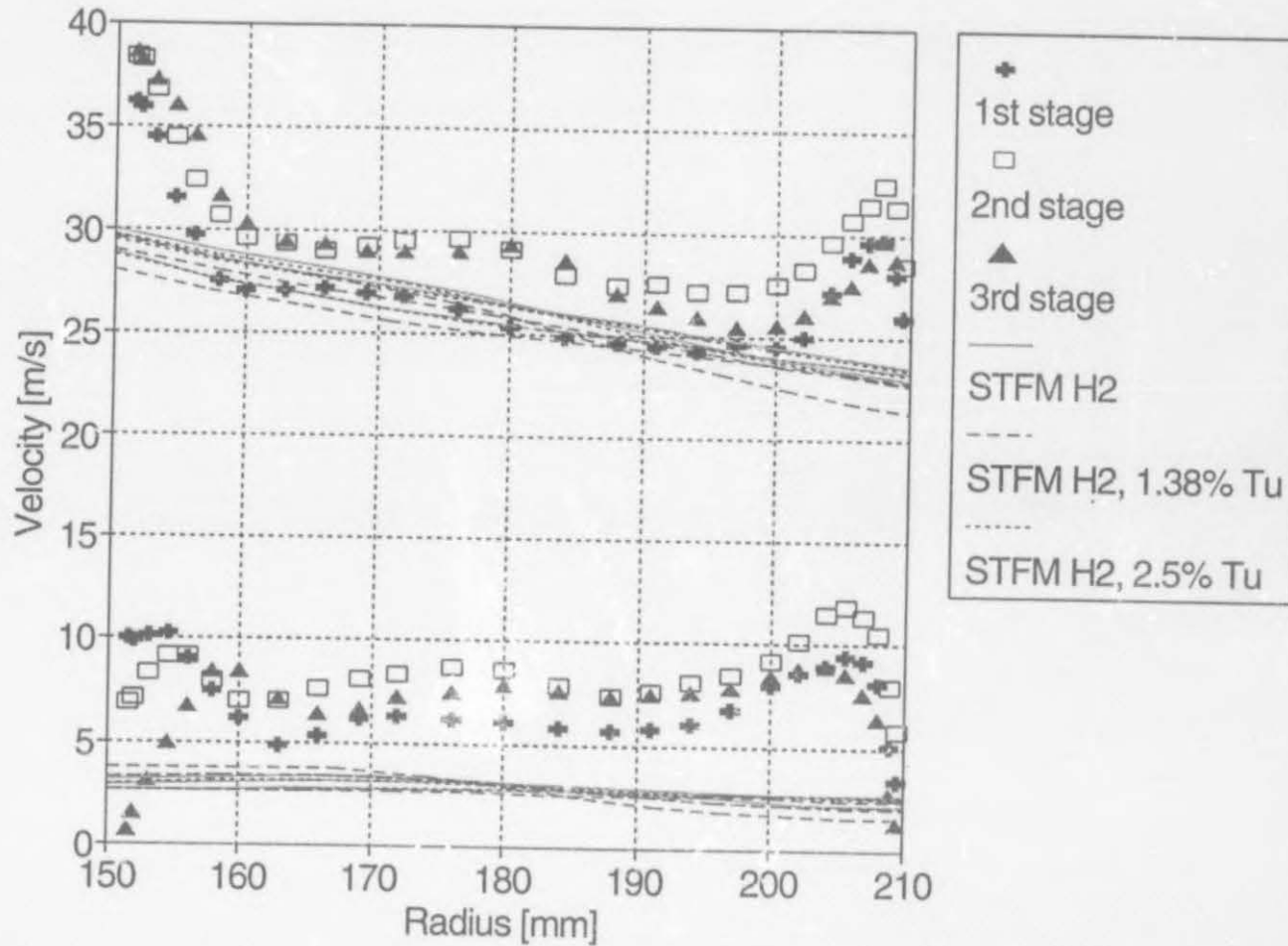


Figure 7.38: Tangential velocity profiles at near-surge flowrate: 1.99 kg/s. Comparison between experimental data and STFM predictions, with \hat{i}_{adj} limited to 0.4, using H2 without and then with the correction of Roberts at two levels of Tu

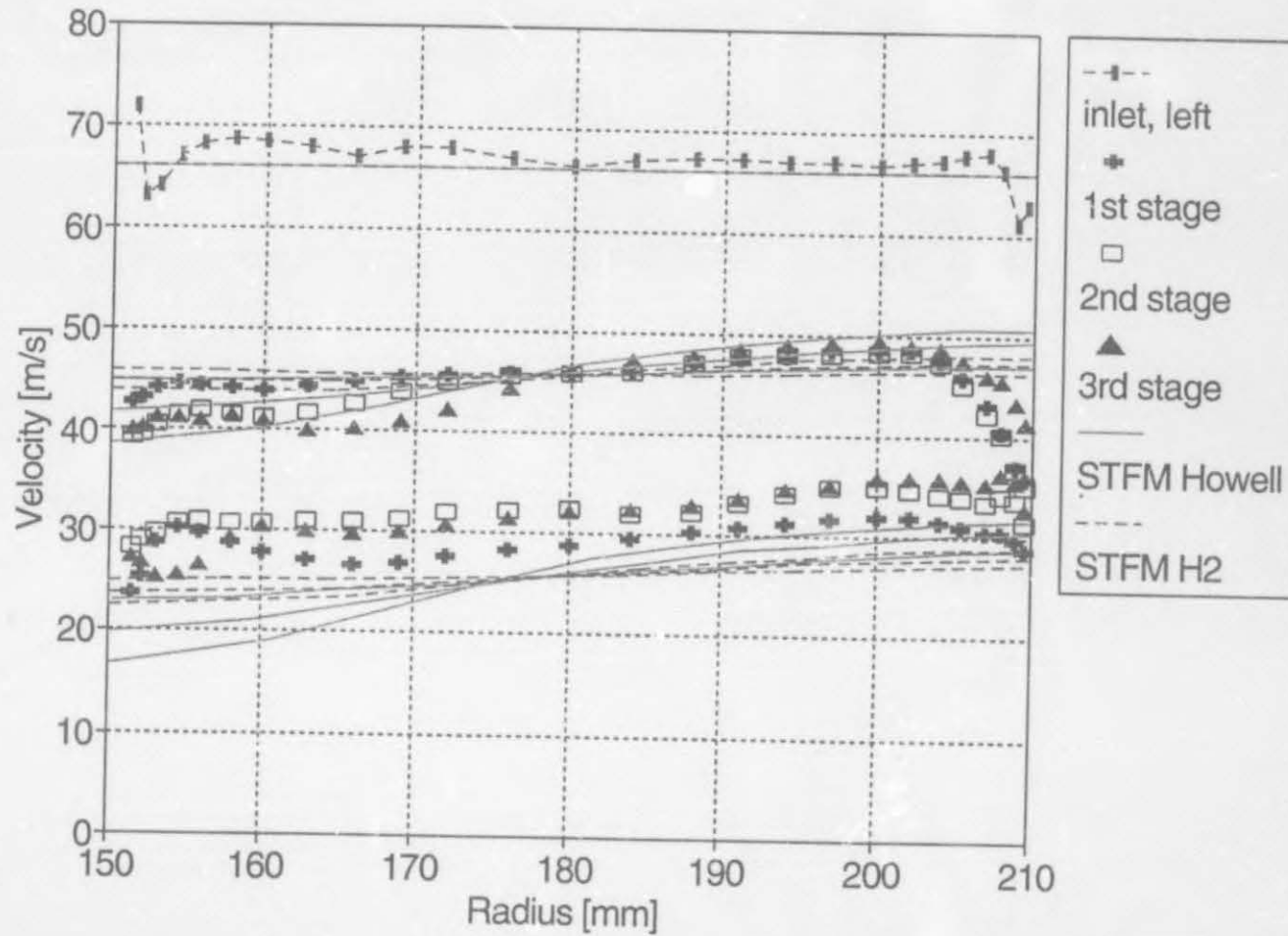


Figure 7.39: Axial velocity profiles at near-surge flowrate: 1.99 kg/s. (Zeroes of inlet and rotor rows have been staggered by 40 and 20 m/s respectively). Comparison between experimental data and STFM predictions, with \hat{i}_{adj} limited to 0.4, using Howell's method and H2

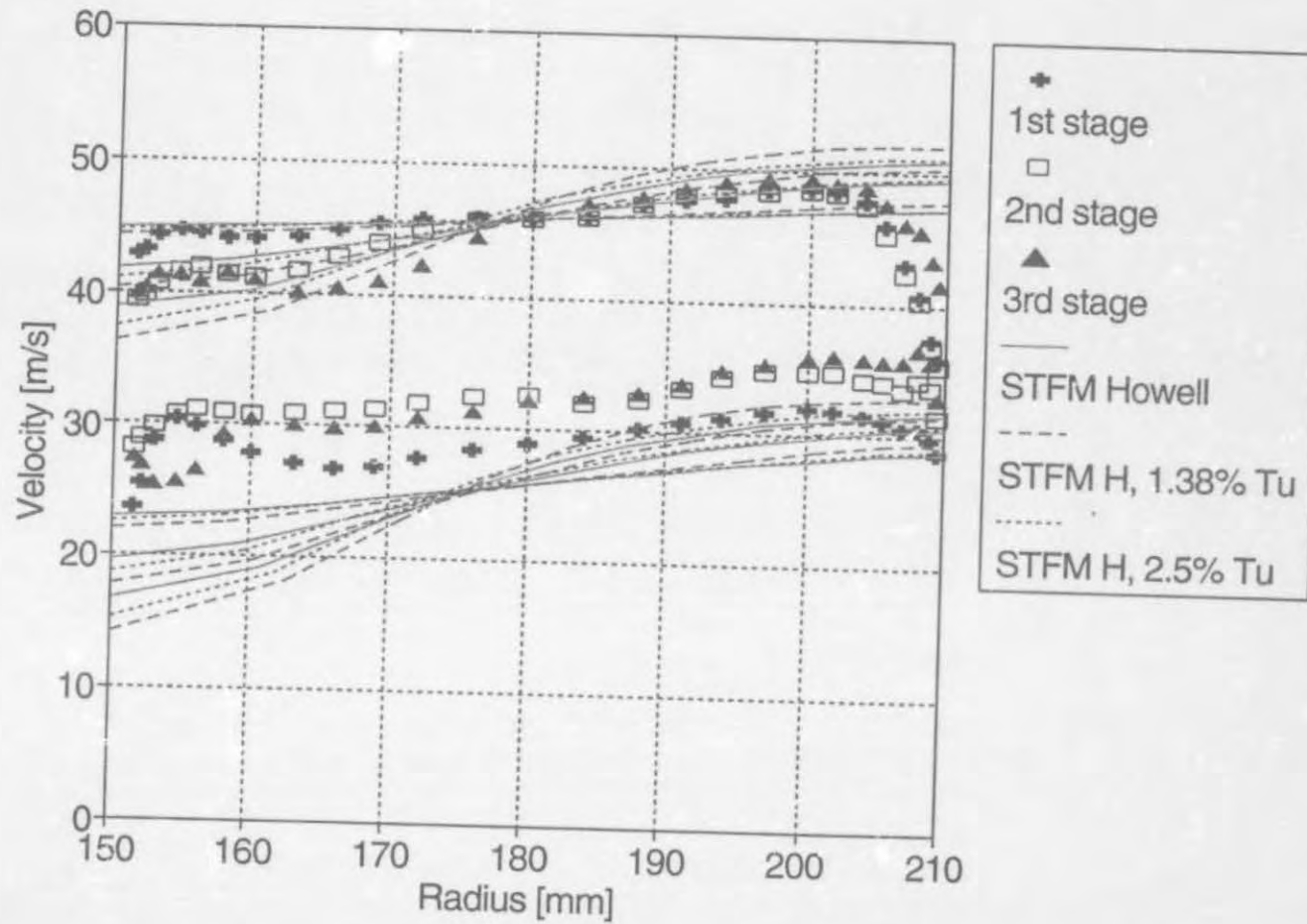


Figure 7.40: Axial velocity profiles at near-surge flowrate: 1.99 kg/s. (Zeroes of inlet and rotor rows have been staggered by 40 and 20 m/s respectively). Comparison between experimental data and STFM predictions, with \hat{i}_{adj} limited to 0.4, using Howell's method without and then with the correction of Roberts at two levels of Tu

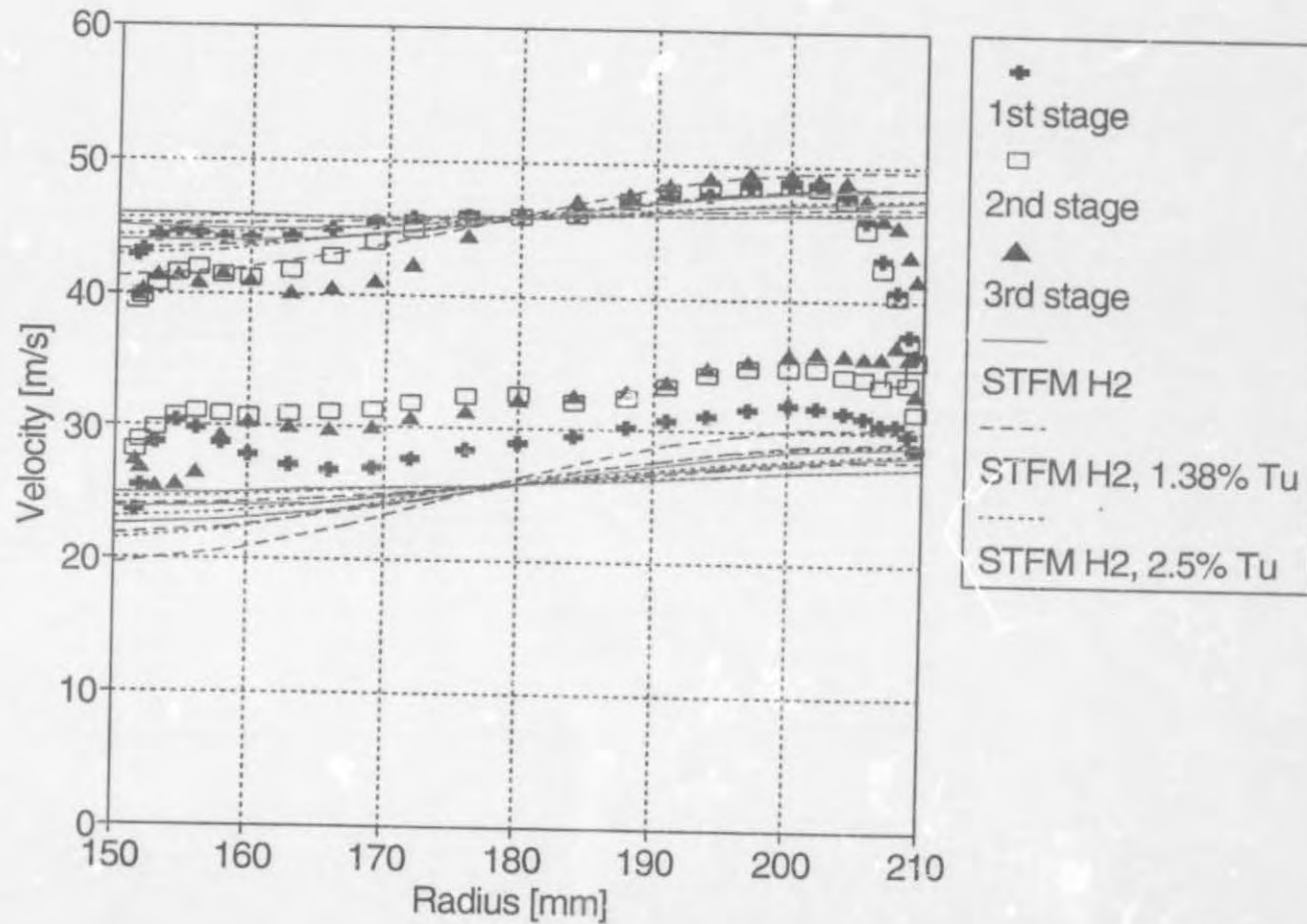


Figure 7.41: Axial velocity profiles at near-surge flowrate: 1.99 kg/s. (Zeroes of rotor rows have been staggered by 20 m/s). Comparison between experimental data and STFMs H2, with \hat{i}_{adj} limited to 0.4, using H2 without and then with the correction of Roberts at two levels of Tu

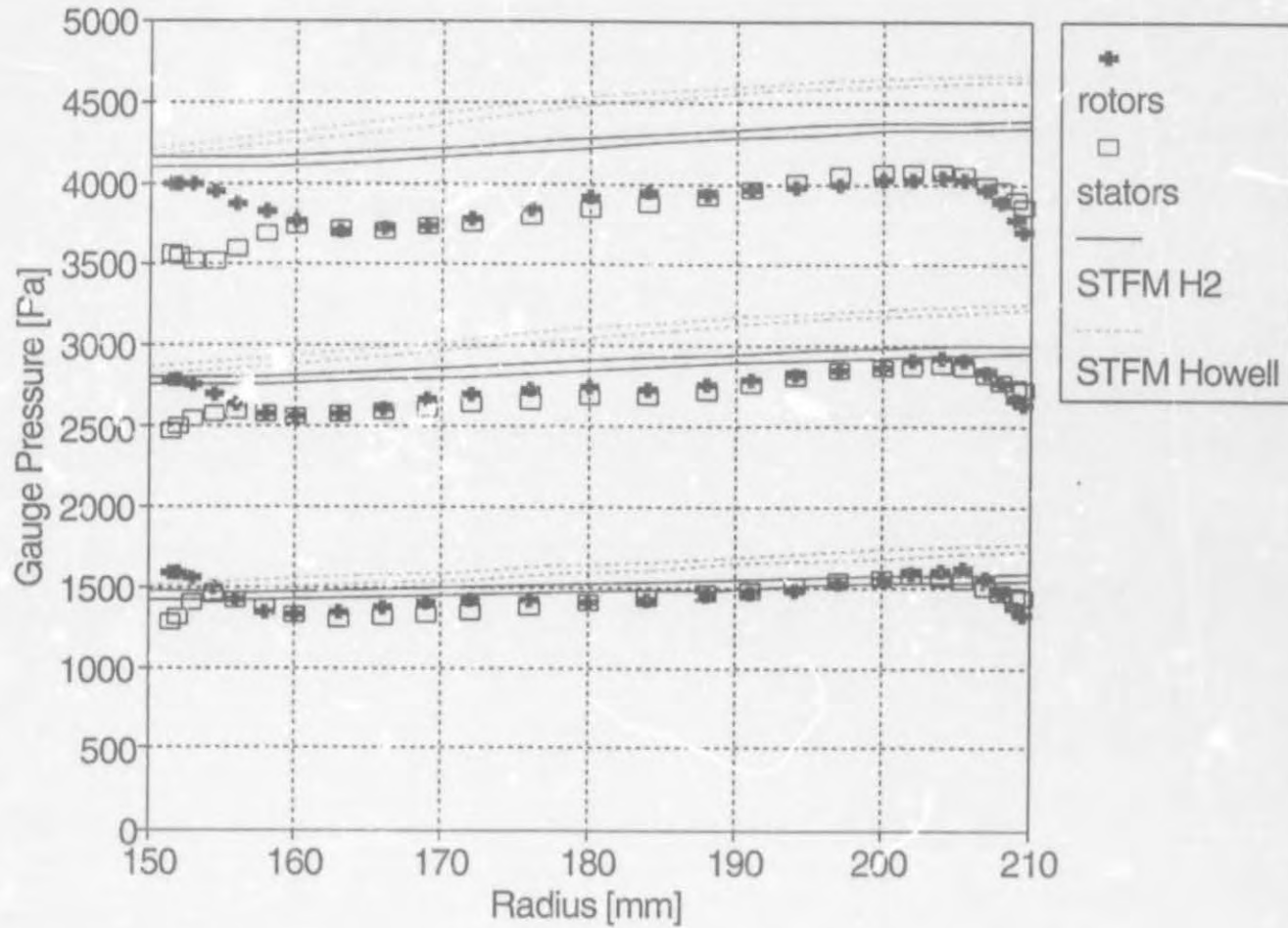


Figure 7.42: Total pressure profiles (relative to inlet mass average) at near-surge flowrate: 1.99 kg/s. Comparison between experimental data and STFM predictions, with \hat{i}_{adj} limited to 0.4, using Howell's method and H2

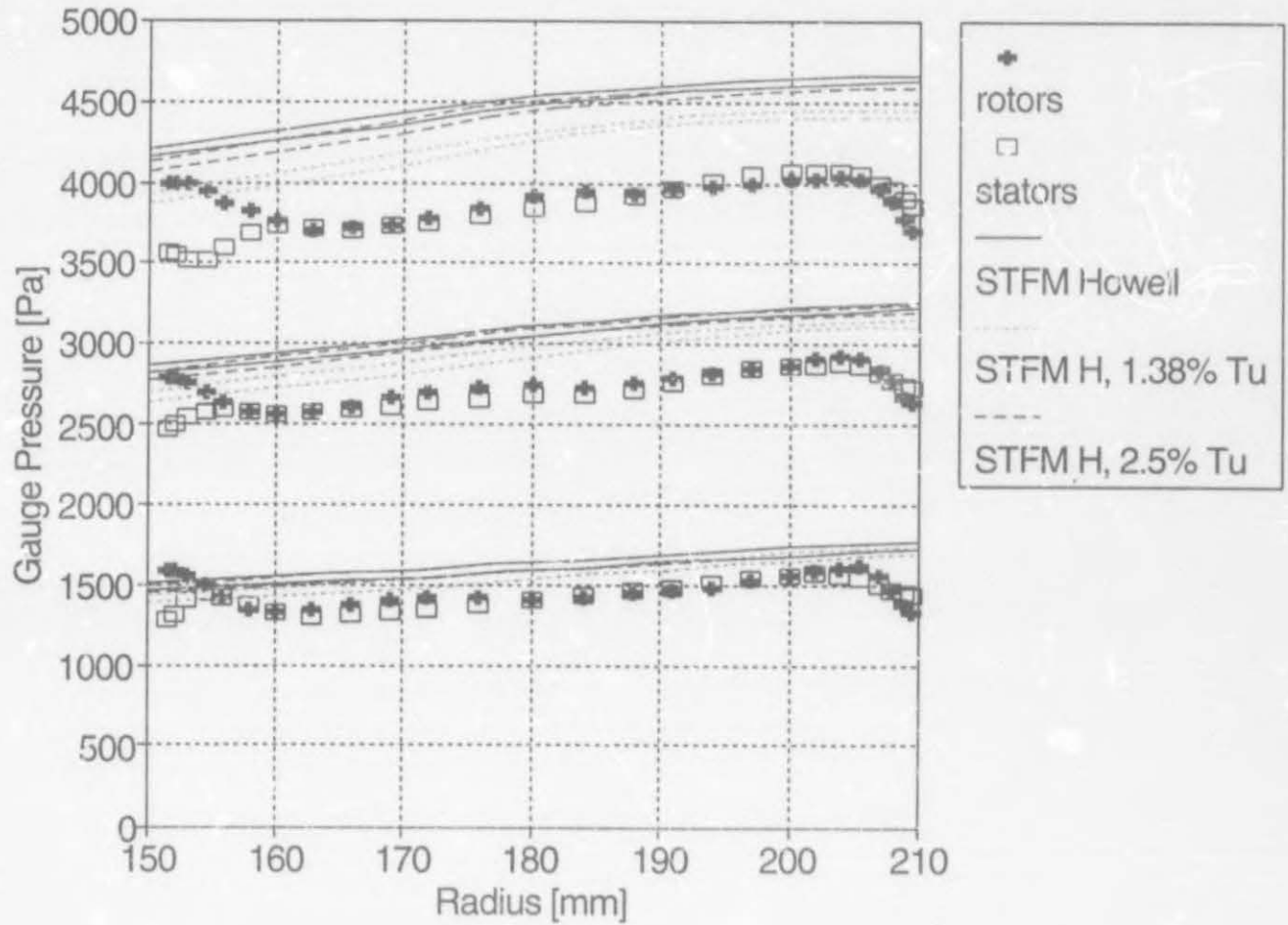


Figure 7.43: Total pressure profiles (relative to inlet mass average) at near-surge flowrate: 1.99 kg/s. Comparison between experimental data and STFM predictions, with \hat{i}_{adj} limited to 0.4, using Howell's method without and then with the correction of Roberts at two levels of Tu

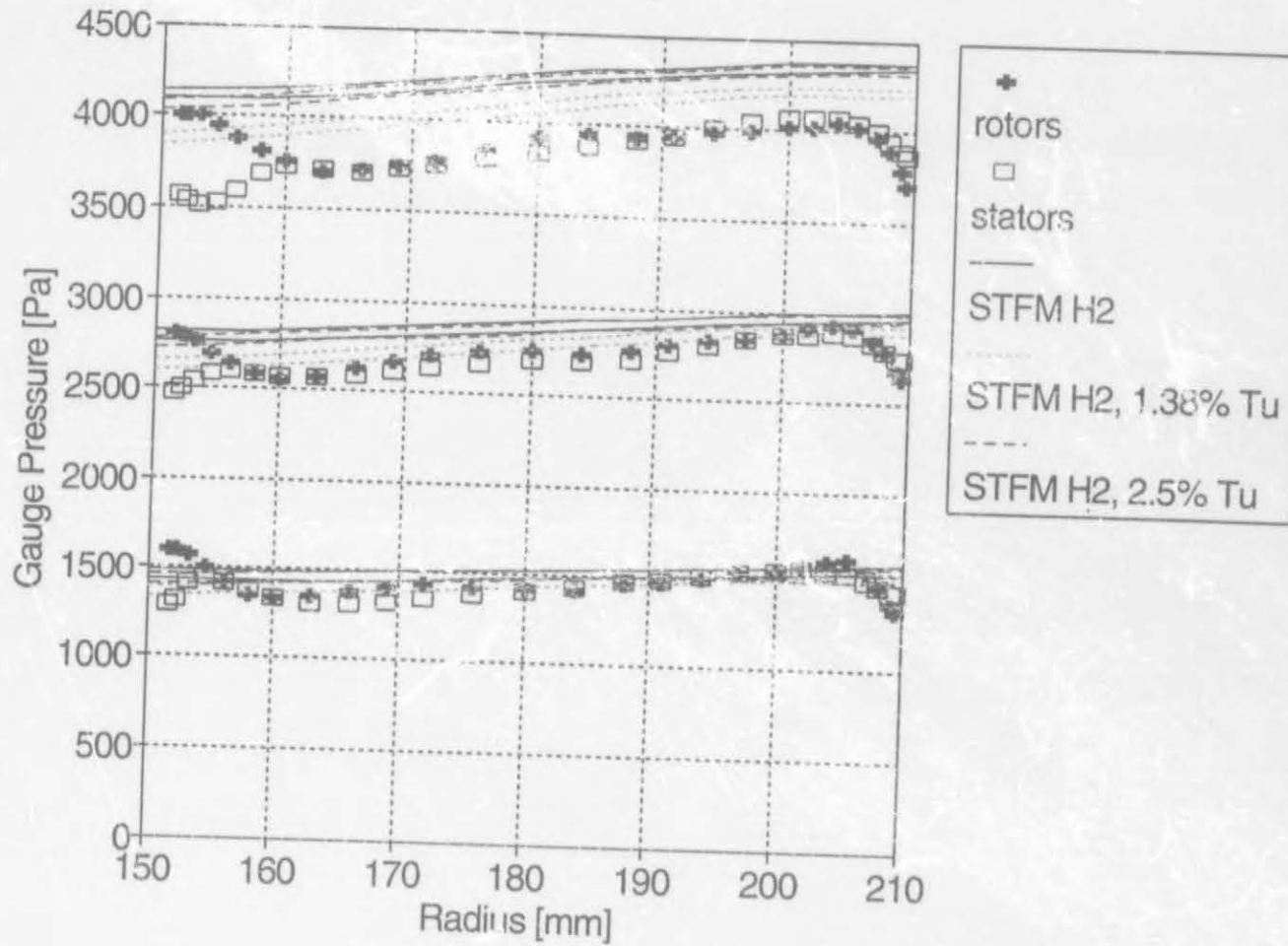


Figure 7.44: Total pressure profiles (relative to inlet mass average) at near-surge flowrate: 1.99 kg/s. Comparison between experimental data and STFMs predictions, with \hat{i}_{adj} limited to 0.4, using H2 without and then with the correction of Roberts at two levels of Tu

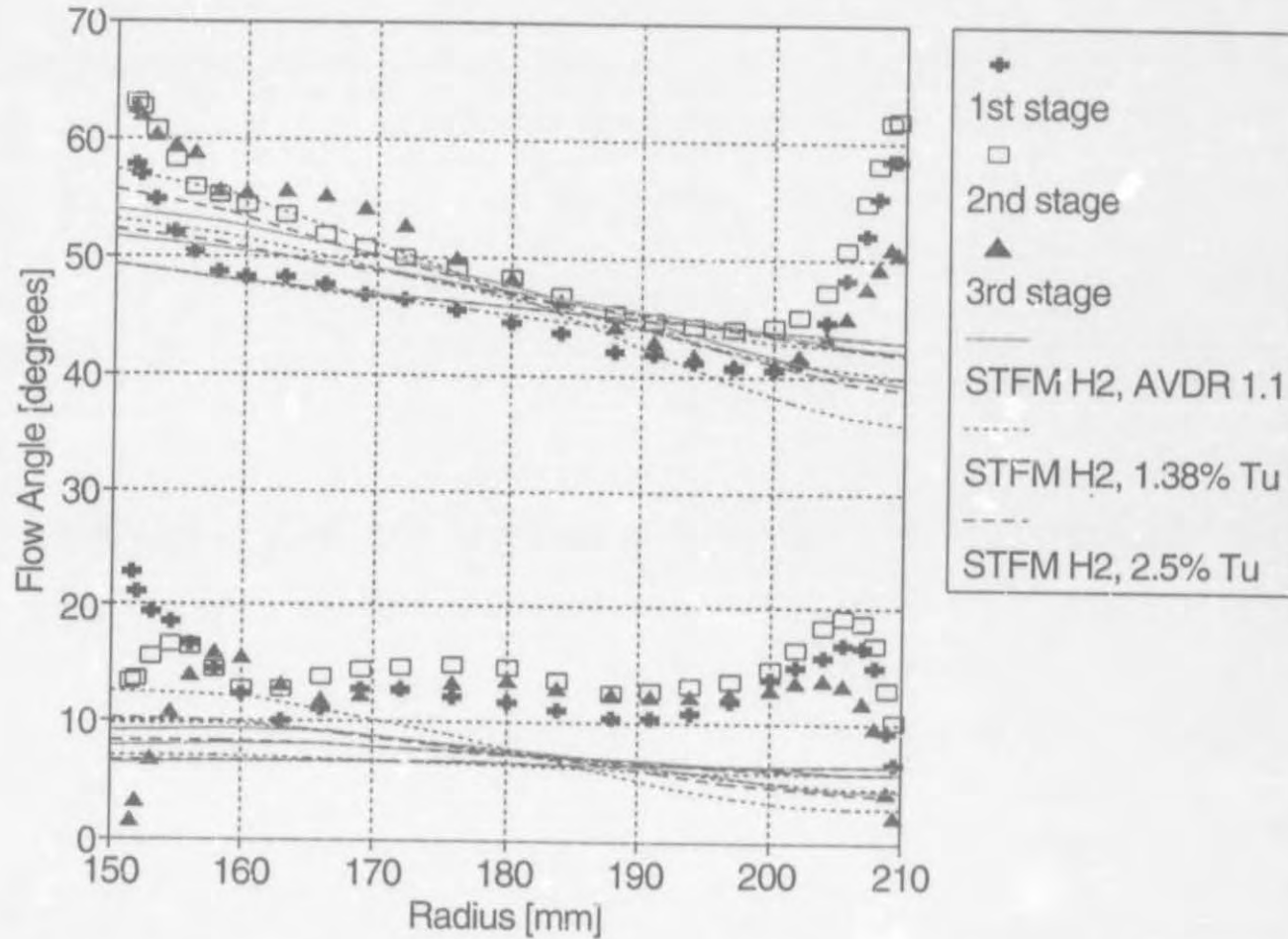


Figure 7.45: Flow angle profiles at near-surge flowrate: 1.99 kg/s. Comparison between experimental data and STFM predictions, with \hat{i}_{adj} limited to 0.4, using H2 with AVDR correction, without and then with the correction of Roberts at two levels of Tu

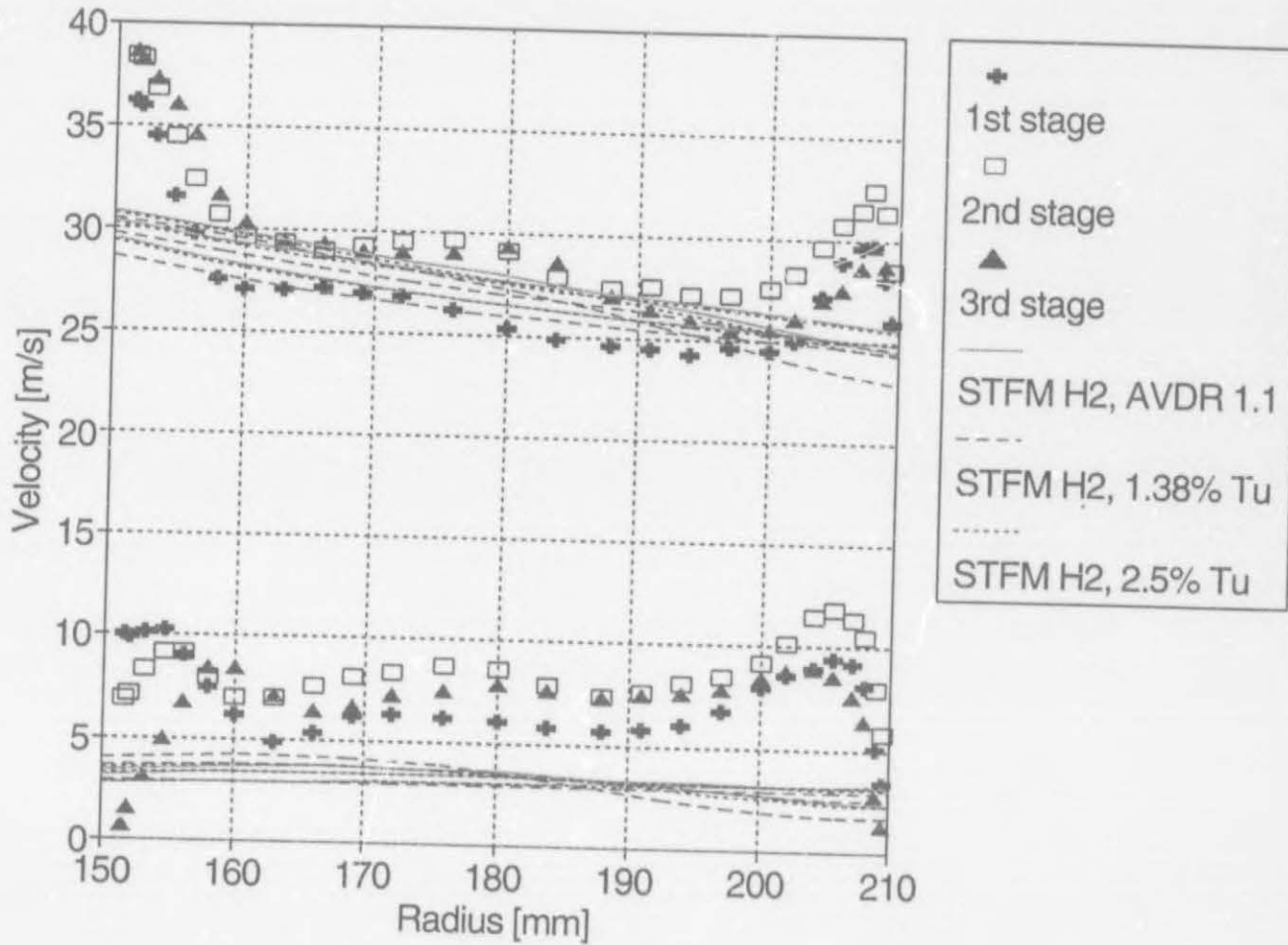


Figure 7.46: Tangential velocity profiles at near-surge flowrate: 1.99 kg/s. Comparison between experimental data and STFM predictions, with \hat{i}_{adj} limited to 0.4, using H2 with AVDR correction, without and then with the correction of Roberts at two levels of Tu

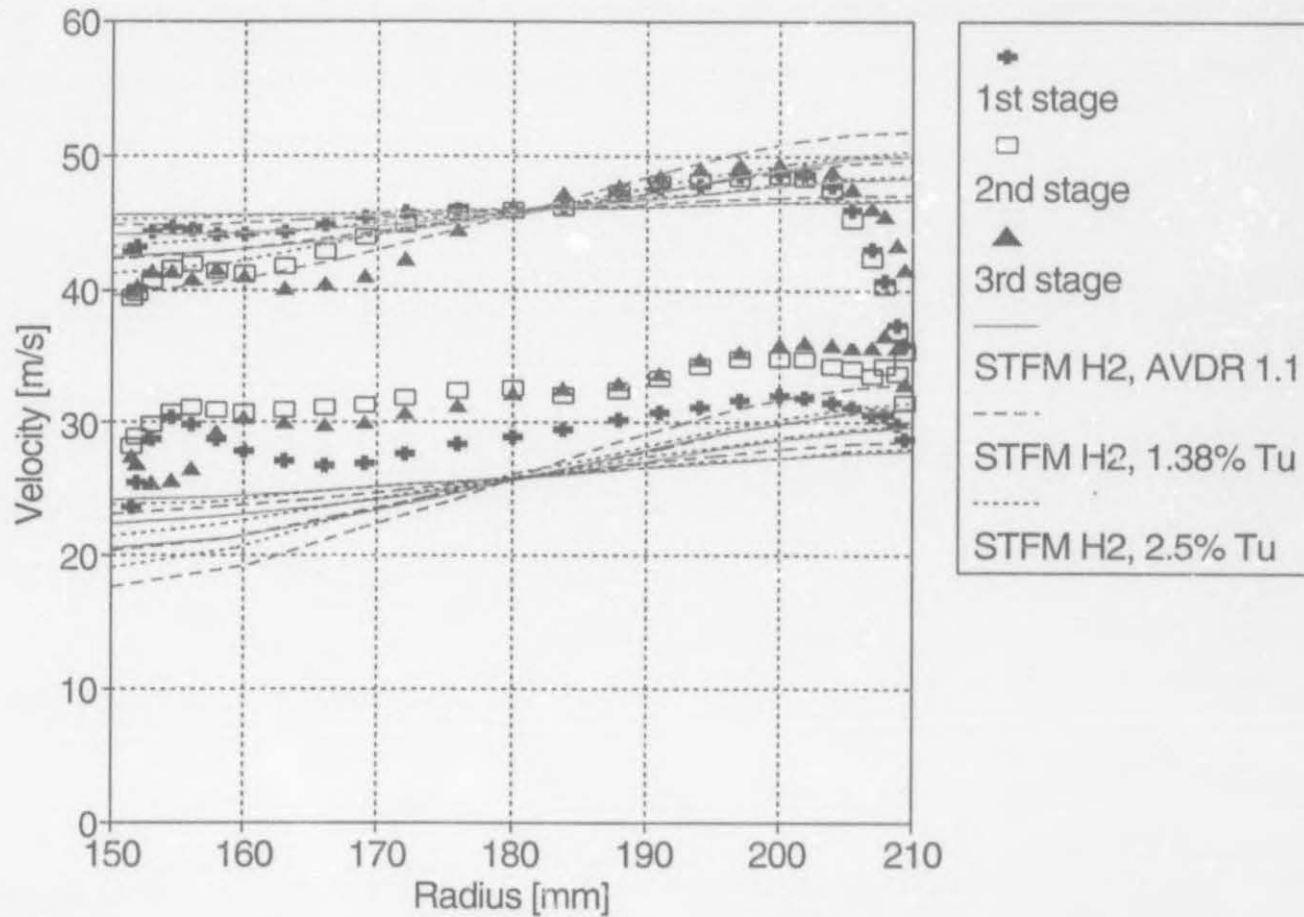


Figure 7.47: Axial velocity profiles at near-surge flowrate: 1.99 kg/s. (Zeroes of rotor rows have been staggered by 20 m/s). Comparison between experimental data and STFM predictions, with \hat{i}_{adj} limited to 0.4, using H2 with AVDR correction, without and then with the correction of Roberts at two levels of Tu

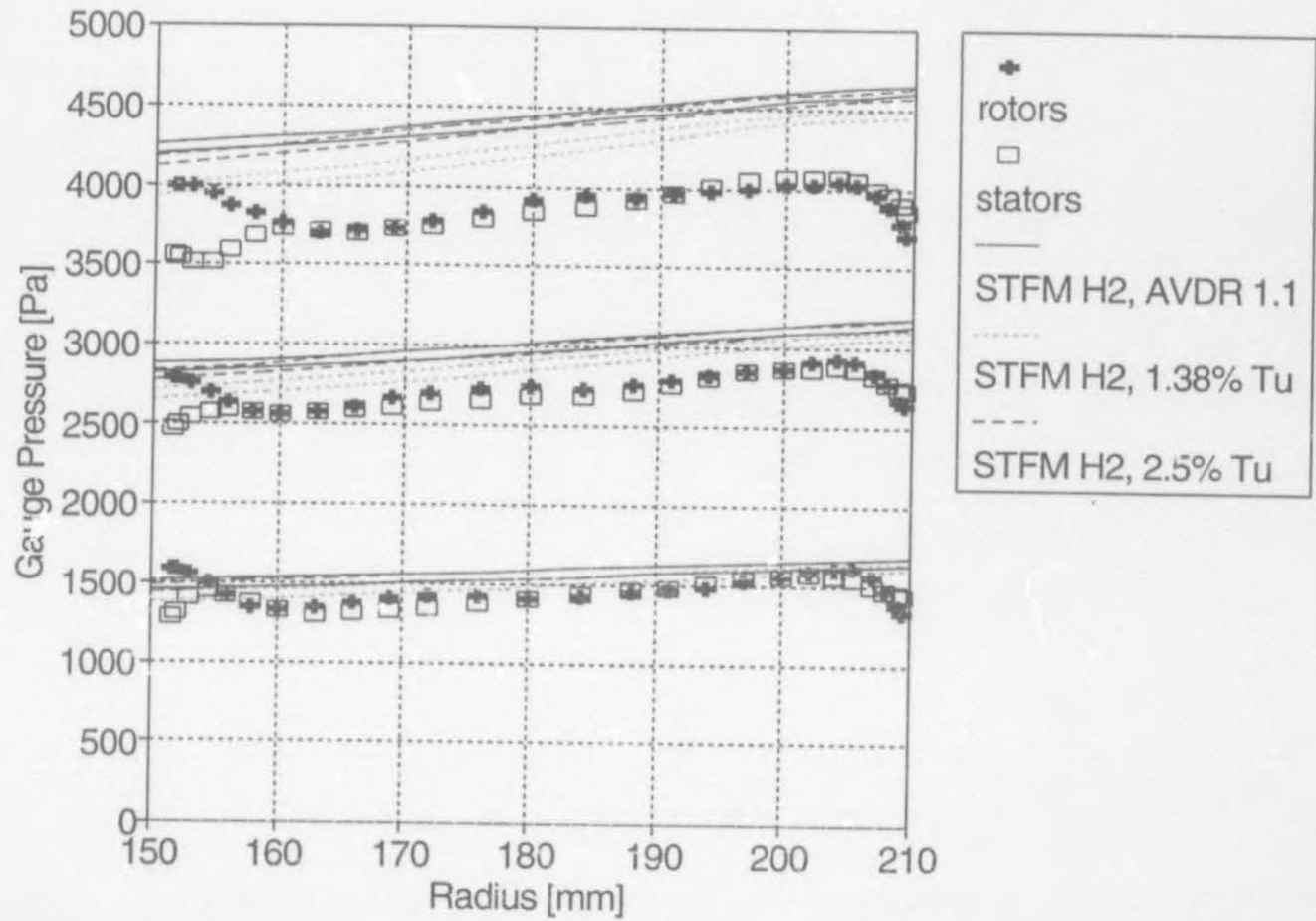


Figure 7.48: Total pressure profiles (relative to inlet mass average) at near-surge flowrate: 1.99 kg/s. Comparison between experimental data and STFM predictions, with \hat{i}_{adj} limited to 0.4, using H2 with AVDR correction, without and then with the correction of Roberts at two levels of Tu

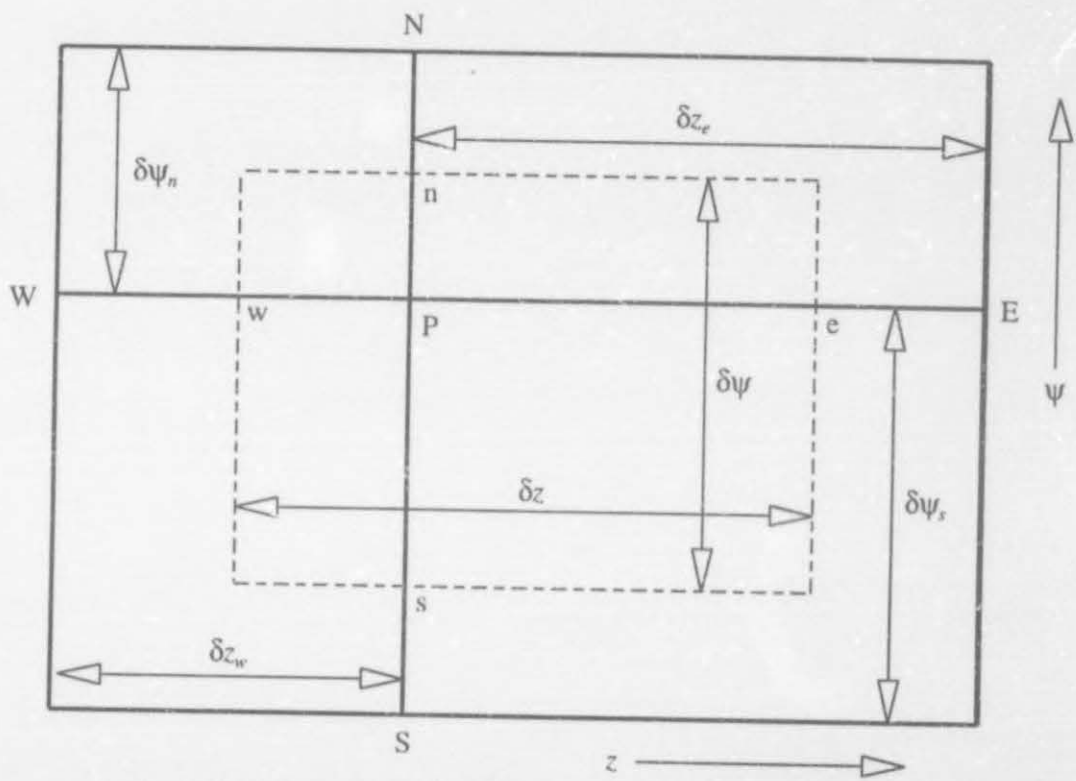


Figure B.1: Nomenclature and discretisation grid of Gravenstein